COSEISMIC DEFORMATION OBSERVED WITH RADAR INTERFEROMETRY: GREAT EARTHQUAKES AND ATMOSPHERIC NOISE

A Dissertation

Presented to the Faculty of the Graduate School

of Cornell University

in Partial Fulfillment of the Requirements for the Degree of

Doctor of Philosophy

by

Chelsea Phipps Scott

January 2017

COSEISMIC DEFORMATION OBSERVED WITH RADAR INTERFEROMETRY: GREAT EARTHQUAKES AND ATMOSPHERIC NOISE

Chelsea Phipps Scott, Ph.D.

Cornell University 2017

Spatially dense maps of coseismic deformation derived from Interferometric Synthetic Aperture Radar (InSAR) datasets result in valuable constraints on earthquake processes. The recent increase in the quantity of observations of coseismic deformation facilitates the examination of signals in many tectonic environments associated with earthquakes of varying magnitude. Efforts to place robust constraints on the evolution of the crustal stress field following great earthquakes often rely on knowledge of the earthquake location, the fault geometry, and the distribution of slip along the fault plane. Well-characterized uncertainties and biases strengthen the quality of inferred earthquake source parameters, particularly when the associated ground displacement signals are near the detection limit. Well-preserved geomorphic records of earthquakes offer additional insight into the mechanical behavior of the shallow crust and the kinematics of plate boundary systems. Together, geodetic and geologic observations of crustal deformation offer insight into the processes that drive seismic cycle deformation over a range of timescales.

In this thesis, I examine several challenges associated with the inversion of earthquake source parameters from SAR data. Variations in atmospheric humidity, temperature, and pressure at the timing of SAR acquisitions result in spatially correlated phase delays that are challenging to distinguish from signals of real ground deformation. I characterize the impact of atmospheric noise on inferred earthquake source parameters following elevation-dependent

atmospheric corrections. I analyze the spatial and temporal variations in the statistics of atmospheric noise from both reanalysis weather models and InSAR data itself. Using statistics that reflect the spatial heterogeneity of atmospheric characteristics, I examine parameter errors for several synthetic cases of fault slip on a basin-bounding normal fault. I show a decrease in uncertainty in fault geometry and kinematics following the application of atmospheric corrections to an event spanned by real InSAR data, the 1992 M5.6 Little Skull Mountain, Nevada, earthquake. Finally, I discuss how the derived workflow could be applied to other tectonic problems, such as solving for interseismic strain accumulation rates in a subduction zone environment.

I also study the evolution of the crustal stress field in the South American plate following two recent great earthquakes along the Nazca- South America subduction zone. I show that the 2010 M_w 8.8 Maule, Chile, earthquake very likely triggered several moderate magnitude earthquakes in the Andean volcanic arc and backarc. This suggests that great earthquakes modulate the crustal stress field outside of the immediate aftershock zone and that far-field faults may pose a heightened hazard following large subduction earthquakes. The 2014 M_w 8.1 Pisagua, Chile, earthquake reopened ancient surface cracks that have been preserved in the hyperarid forearc setting of northern Chile for thousands of earthquake cycles. The orientation of cracks reopened in this event reflects the static and likely dynamic stresses generated by the recent earthquake. Coseismic cracks serve as a reliable marker of permanent earthquake deformation and plate boundary behavior persistent over the million-year timescale. This work on great earthquakes suggests that InSAR observations can play a crucial role in furthering our understanding of the crustal mechanics that drive seismic cycle processes in subduction zones.

BIOGRAPHICAL SKETCH

Chelsea Phipps Scott was born in Falls Church, Virginia, in 1988 to Jeffrey Scott and Peggy Phipps. Growing up, Chelsea explored many parts of the world as her family moved to Illinois, New Jersey, Belgium, and Pennsylvania. Chelsea has fond memories of living in Belgium. She remembers knitting a blue and purple humpty- dumpty doll in her second grade class. She spent many afternoons building different k'nex toys with her friends. Favorites included a roller coaster, a Ferris wheel, and several racecars. Chelsea and her brother, Michael, enjoyed playing outside and exploring nearby ponds and farms near Bruxelles/ Brussel/ Brussels together. Chelsea also learned to speak French, which turned out to be great preparation for speaking small amounts of Spanish with a funny accent in South America many years later.

In high school when Chelsea's family lived in a suburb of Philadelphia, Chelsea dreamed of being a veterinarian and got a weekend job working at a local vet clinic. She excitedly learned about veterinary care for many animals including some unusual pets like iguanas, ferrets, and birds of prey. Although she enjoyed her job, Chelsea was dissuaded from a career where she would work with animals with sharp teeth.

Chelsea attended Carleton College in Northfield, Minnesota. She quickly learned to enjoy the cold weather and took-up cross-country skiing in Carleton's beautiful arboretum. When the ice finally melted after her first Minnesota winter, Chelsea joined Carleton's rowing club. By the end of the (short) season, the team was good enough to keep the boat from hitting the riverbank. Later in college, Chelsea spent many Saturday evenings learning how to ballroom dance.

As a freshman and sophomore, Chelsea took science classes in a variety of subjects. After taking a course in tectonics and exploring the exciting geologic history of the northern shore of Lake Superior, Chelsea decided to major in geology. Chelsea continued to enjoy taking

physics and math courses. She spent several weeks designing and modeling a small k'nex trebuchet with a couple of classmates. After the medieval war machine successfully knocked over several Einstein doll targets, Chelsea decided to also major in physics.

For her senior thesis in geology, Chelsea worked with Sarah Titus (professor at Carleton College) and studied deformation along a paleo ridge-transform intersection in the Troodos Ophiolite, Cyprus. In this project, Chelsea demagnetized many small gabbroic cores at the Institute for Rock Magnetism at the University of Minnesota. Chelsea also developed a mathematical model to describe how rocks deform in a ridge-transform setting. Chelsea accepted a yearlong position following graduation to serve as a research assistant at Carleton, where she continued to develop this project. This year was very influential in Chelsea's choice to pursue a career in science.

The following year, Chelsea headed to back east to the tropical metropolis of Ithaca, New York to attend Cornell University. She joined Rowena Lohman's group as a graduate student in active tectonics and geodesy. This thesis highlights much of this academic journey. She learned how to produce and interpret colorful maps with rainbow-like patterns that illustrate how the surface of the Earth deforms in an earthquake. A significant portion of Chelsea's thesis focuses on the mitigation of a key source of noise in InSAR data. Other work focuses on two recent great earthquakes in Chile. She spent two weeks mapping surface deformation in the Chilean forearc produced by the 2014 Pisagua earthquake with Rick Allmendinger. She appreciated how field observations of surface strain gave her additional insight into the deformation signals in SAR imagery.

At Cornell, Chelsea also co-led multiple outreach activities with fellow graduate students Veronica Prush, Holly Taylor, Andrea Aguirre, and Erin Camp. Most outreach activities were aimed at middle and high school girls through a program called, Expand Your Horizons. Several of the workshops focused on seismology. Students learned how to locate earthquakes (with some help) that were recorded on the analog seismometer in Snee Hall. Students also

acted out an earthquake location triangulation exercise on a grid that filled the entire classroom. They played parts of the earthquake, p-waves, s-waves, and seismic stations. They calculated where the (blind-folded) earthquake occurred with surprisingly good accuracy.

Outside of academic life, Chelsea enjoyed exploring Ithaca. She met Barnaby Levin (her sweetheart) in Cornell's Engineering Quad during their first week of graduate school. They explored the many gorges, parks, and vineyards of the Finger Lakes region together. Barnaby embraced the upstate NY winters and learned to cross-country ski with Chelsea. Chelsea also enjoyed running up and down the many hills in Ithaca. She even ran two half-marathons in Philadelphia with fellow EAS graduate students.

After Chelsea graduates from Cornell, she will start an NSF postdoctoral fellowship at Arizona State University where she will work with Ramón Arrowsmith. She will incorporate the skills she learned in InSAR and structural geology in graduate school to study earthquake processes with a focus on shallow fault slip.

My thesis is dedicated to my grandparents,

Betty and Richard Phipps &

Lorraine and Richard Scott.

ACKNOWLEDGEMENTS

There many people who have shared their scientific expertise, philosophy, mentorship, and friendship with me over the past years. First and foremost, I would like to thank my advisor, Rowena Lohman. Rowena accepted me into her active tectonics group five years ago. Rowena has since taught me an enormous amount about geodesy and earthquakes. She also encouraged discussion of a large variety of scientific questions and approaches for solving inverse problems. She set a high standard for scientific talks and written work, and provided feedback on how to meet those expectations. She welcomed my exploration of scientific topics that were a step outside of her typical research focus. I also very much appreciated Rowena's open discussion about academic and non-academic life.

About half way through my graduate career, Richard Allmendinger invited me to investigate the surface strain produced by a great earthquake in Chile. In the field, Rick discussed approaches of connecting field observations to a broader understanding of tectonics. I very much appreciated our discussions back in Ithaca about exploring multiple hypotheses to questions that were often at the intersection of geodesy and structural geology. Rick shared his wisdom: "Interesting data do not fit your model." I hope to incorporate this philosophy in my scientific work in the years to come.

Paul Dawson taught a graduate course in solid mechanics during my first semester at Cornell. This was one of the most challenging and rewarding courses I took at Cornell. I would like to thank Paul for multiple excellent questions over the years that pushed me to develop a deeper understanding of several topics related to my research.

There are many other Cornell faculty that deserve a very sincere word of thanks. Terry Jordan shared her deep knowledge and excitement for surface processes and hydrology of the Atacama Desert over many discussions about InSAR imagery in northern Chile. Matthew Pritchard provided critical and kind feedback at weekly group meetings and in several EAS

courses. Suzanne Kay led the Friday afternoon Andes seminars, which proved to be a great environment to learn about giving effective scientific presentations and to get really useful feedback on research from a broad audience. She taught the fielding mapping course, which was a excellent opportunity to see faults in the field. I would like to thank Muawia Barazangi for pushing me to consider and present my research in terms of broad scientific questions. Muawia led exciting discussions about seismograms recorded in Snee Hall and often reminded me that it is never too late to become a seismologist (sorry Muawia). Alan Zehnder taught a fascinating course on fracture mechanics and very patiently answered many questions.

In addition, faculty at other universities strengthened my work. Patricia Alvarado (Universidad Nacional de San Juan, Argentina) shared her seismic analyses and interpretation of the Salta earthquake. Gabriel González (Universidad Católica del Norte, Chile) and Jack Loveless (Smith College) offered their expertise and editorial comments on the coseismic crack project. Greg Hoke (Syracuse University) offered insight on SAR coherence imagery in northern Chile.

I would like to thank many Cornell graduate students for friendship and scientific discussions over the past years. I thank Francisco Delgado for sharing a lab with me for the past four years and for many engaging conversations about InSAR and deformation models. Holly Taylor shared much excitement and many woes as we both learned to use process InSAR data during our first year of graduate school. Scott Henderson and Veronica Prush provided very positive camaraderie in the lab and patiently helped me trouble shoot a variety of InSAR processing issues. Felipe Aron was always up for discussion about deformation processes and kindly introduced me to many students at conferences. Andrew Melkonian showed me how to work with optical imagery and produce maps of pixel offsets, which supported work on the 2014 Pisagua earthquake sequence. Bill Barnhart, Jennifer Jay, Chris Siron, Ben Valentino and Kyle Murray, in addition to many of the above people, asked questions in different contexts that pushed me to gain a deeper understanding of my work and present

my results more clearly.

I would like to acknowledge a variety of sources for funding during my Ph.D. Rowena Lohman generously funded me from with grants from the American Chemical Society Petroleum Research Fund, the National Science Foundation (EAR-0911464 & EAR-1358573), the National Aeronautics and Space Administration (NNX10AQ80G S01), and the Southern California Earthquake Center (12096). NSF RAPID grant 1443410 to Richard Allmendinger funded the 2014 fieldwork in northern Chile. Additionally, I am grateful to the Department of Earth and Atmospheric Sciences for the Sidney Kauffman travel funds throughout my graduate career and for the McMullen graduate fellowship for full funding during the 2015-2016 academic year. I am thankful for support from the Gubbels fund, which funded my attendance at the Cornell Field course in Argentina. The Engineering College at Cornell provided Teaching Assistant training and funding as I served as the TA for Satellite-Based Remote Sensing taught by Rowena Lohman.

My enthusiasm for geology and early skill set was developed at Carleton College. I would like to thank Sarah Titus (Geology Department) for sharing her passion for geology in tectonics and structural geology courses. She invited me to work with her to study deformation in the Troodos Ophiolite of Cyprus for both my undergraduate thesis and a year following graduation. This was a fantastic opportunity to participate in tectonics research and learn about quantitative approaches for modeling rock deformation. In addition, I also thank Joshua Davis (Mathematics department) for very critical and constructive feedback on code development, as well as for many discussions on mathematical approaches for describing the deformation of geological structures. Other Carleton faculty including Bill Titus, Melissa Eblen-Zayas, Cameron Davidson, Sam Patterson, Jack Goldfeather, and Mark Krusemeyer taught classes that pushed my intellectual development in a variety of ways.

My undergraduate summers supported and broadened my undergraduate course work. I would like to thank Justin Revenaugh for teaching me about techniques to image the

structure of the deep Earth as part of the Research Experience for Undergraduates (REU) program at the University of Minnesota. I would like to thank the many scientists that ran the Summer of Applied Geophysical Experience (SAGE) in Sante Fe, New Mexico, for a fantastic field course. I have the honor of being a second-generation attendee of this course, as Rowena Lohman also attended it.

I would like to thank my entire family for years of encouragement, support, and inspiration. My Mom encouraged me to pursue the subjects I was most passionate about. She built k'nex structures with me (see biography), which got me in an engineering mind-set at a young age. I very much appreciate my Mom's continued excitement about science. My Dad discussed many scientific topics with me over the years, beginning with, 'what is an atom?'. These discussions peaked my interest and curiosity in science beginning at a young age. My brother, Michael, provided much laughter and fun as we were growing up. My grandparents and aunts always have supported me immensely over the years. My uncle Jack shared his enthusiasm for nerdy engineering toys with me beginning long ago.

And finally, I would like to thank my best friend, Barnaby Levin for daily companionship, friendship, laughs, home-made dinners, and support since we met five years ago in Cornell's Engineering Quad as (lost) first-year graduate students. Among the many things I have learned in graduate school: Sometimes it can be very good to be lost.

Table of Contents

List of Tables

List of Figures

LIST OF SYMBOLS

General Synthetic Aperture Radar (SAR) quantities	
Γ	Interferometric correlation
λ	Wavelength
ρ	Distance between the satellite and the ground
ΔR	Pixel size in range
R_{az}	Pixel size in azimuth
L	Length of antenna
Δf_{BW}	Band-width of the radar signal
c	Speed of light
Linear Algebra terms	
$\mathbf{G}$	Matrix of Green's functions
$\mathbf{G}_w$	Matrix of weighted Green's functions
$\mathbf{L}$	Regularization matrix
$\mathbf{N}$	Data resolution matrix
$\mathbf{C}_d$	Data covariance matrix
m	Model parameters
d	Data
d_w	Weighted data
ξ	Weighting parameter
Empirical Correction of Atmospheric Noise	
$\Delta\phi_i$	Phase delay at the ith pixel
$K'_{\Delta\phi}$	Constant relating elevation to interferometric phase
α	Power law coefficient
h_o	Elevation above which atmospheric properties are assumed constant
h_i	Elevation at the i^{th} pixel
r_i	Polynomial ramp parameter
W_{ij}	Weighting term
Smoothing in Spatially Variable Atmospheric Corrections: $_jR_i$ Approach	
d_o	Data: Signal from the stratified component of the atmosphere
d_o^*	Smoothed data
n_i	ith noise realization
n_i^*	Smoothed ith noise realization
$_or_o$	Regularization error
$_jr_i^n$	Perturbation error

CHAPTER 1

INTRODUCTION AND BACKGROUND

1.1 Introduction

Fault scarps, volcanoes, and mountain belts across the Earth's surface are evidence that active tectonic forces are continually reshaping the landscape. Earthquakes, which deform the Earth's upper crust on timescales of tens of seconds, give researchers a window into the processes that produce surface deformation during the different portions of the seismic cycle. On longer timescales, the evidence of earthquake activity preserved in the landscape is indicative of tectonic behavior over multiple seismic cycles and offers additional insight into the constitutive laws that govern how the Earth deforms. Ultimately, geodetic observations spanning earthquakes contribute to an understanding of the style of plate boundary deformation, the physical processes that drive the seismic cycle, and the hazards posed to communities near active faults.

Interferometric Synthetic Aperture Radar (InSAR) is a remote sensing technique that allows researchers to image static displacements of the Earth's surface. InSAR imagery provides spatially dense observations of the growth of geologic structures in the near and far- field (e.g., Bürgmann et al., 2000) during the co-, post-, and interseismic portions of the seismic cycle (e.g., Pollitz et al., 2001; Simons et al., 2002; Fialko, 2006). These observations, combined with inverse modeling, allow researchers to infer quantities of tectonic interest including earthquake magnitude, fault geometry, and the depth extent of the seismogenic zone (e.g., Delouis et al., 2002; Lohman et al., 2002; Wright et al., 2003). While much of this previous work involved displacement signals with large spatial scales (few to 10's of km), recent increases in the availability of SAR datasets enable detailed characterization of

smaller-scale features such as surface ruptures, soil liquefaction, and infrastructure damage (e.g., Fielding et al., 2005; Ishitsuka et al., 2012; Plank, 2014). This contributes to a deeper understanding of the response of the shallowest portion of the crust to fault motion.

In this thesis, I solve for earthquake source parameters from InSAR observations and interpret patterns of coseismic strain in terms of the mechanics of plate boundary deformation. This work represents efforts to better quantify the uncertainty in InSAR- inferred earthquake source parameters due to the presence of atmospheric noise. Signals introduced by the delay of the radar signal traveling through the troposphere result in significant errors in the inferred ground displacement (e.g., Berrada Baby et al., 1988; Bürgmann et al., 2000; Hanssen, 2001) and a degradation of scientists' abilities to gain insight on earthquake processes. A key frontier in InSAR science involves the strengthening of constraints on ground displacement with estimates of the atmospheric phase delay from weather models. I develop an approach to assess the inferred earthquake source parameter uncertainties before and after elevation-dependent empirical atmospheric corrections. This analysis reveals both the robustness of inferred earthquake source parameters and shortcomings of correction approaches that do not account for the spatial variation in atmospheric properties. Further, a similar workflow could be applied to illustrate the data quantity required to infer parameters with errors below certain thresholds for processes that are challenging to study, such as interseismic strain accumulation and uplift associated with low-slip rate faults.

In addition, I study the connection between great earthquakes ($M_w \geq 8$) along the South America- Nazca subduction zone plate boundary and the coseismic release of strain in the overriding South American plate. The 2010 M_w8.8 Maule earthquake of central Chile ruptured 500 km of the plate boundary with a maximum slip of $\sim$15 m (e.g., Hayes, 2010). The earthquakes in the Andean backarc and volcanic arc that were triggered by the Maule event offer insight into the stress field evolution following the large release of interseismically

accumulated strain. Backarc faults are likely to become active following a great earthquake, particularly if they are already in an advanced portion of their seismic cycle. Changes in static Coulomb stress are likely to trigger events in the near- field that may be additionally controlled by regional magmatic systems (Pritchard et al., 2013).

The 2014 M_w 8.1 Pisagua earthquake of northern Chile offers opportunity to examine the behavior of subduction zone systems over both a single earthquake and the million-year timescale. The surrounding hyperarid Atacama Desert creates a unique environment that supports the preservation of surface cracks over thousands of earthquake cycles (Rech et al., 2003; Loveless et al., 2005, 2009; Baker et al., 2013). The variation in orientation of cracks reopened in 2014 over the ∼200 km rupture length is consistent with strain axes inferred from static displacements of the 2014 event and therefore also likely dynamic stresses generated by the passage of seismic waves (Loveless et al., 2009). This suggests that repeated great earthquakes largely control crack orientation in the forearc landscape. Further, cracks serve as a record of long-term tectonic behavior and significantly lengthen the record of great earthquakes beyond the decadal timescale provided by geodetic datasets.

1.1.1 Outline

Chapter 1 serves an introduction to many of the methodologies applied throughout this thesis. I outline basic InSAR processing techniques and introduce inverse methods used to invert for earthquakes source parameters. I describe characteristics of atmospheric noise and present comparisons of the atmospheric contribution inferred from weather models to InSAR data itself.

Chapter 2 focuses on the portion of uncertainty on earthquake source parameters inferred

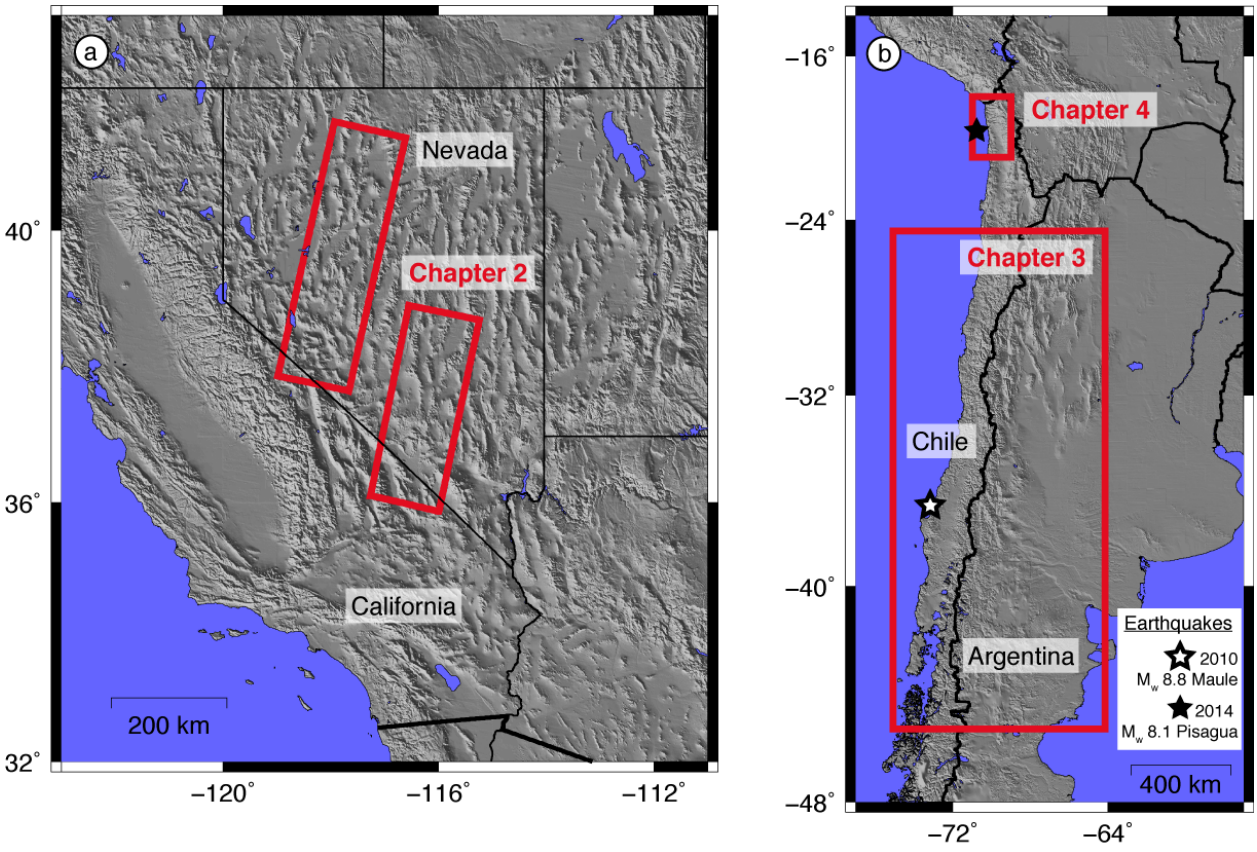

Figure 1.1: Areas of study highlighted on shaded relief maps. (a) Map of western North America showing the two interferogram tracks studied in Chapter 2. (b) Map of South America highlighting the GCMT locations of the great earthquakes and the regions of study described in Chapters 3 and 4.

from InSAR datasets that is introduced by the tropospheric delay of the radar signal. The synthetic realizations of atmospheric noise are based on an analysis of the amplitude and spatial characteristics of noise from the turbulent and stratified components of the atmosphere. I develop a Monte Carlo approach to calculate error bounds and biases on earthquake source parameters. The application of the approach to several synthetic earthquake examples along a basin-bounding fault in central Nevada (Figure 1.1a) illustrates the impact of atmospheric noise in cases with a high degree of correlation between deformation and topography. The atmospheric corrections improve the quality of inferred parameters of 1992 M5.6 Little Skull mountain, Nevada, earthquake. This chapter was published in the Journal of Geophysical

Research: Solid Earth with Rowena Lohman as coauthor.

Chapter 3 focuses on several upper crustal earthquakes in the Andean volcanic and backarc that were likely triggered by the 2010 M_w 8.8 Maule, Chile, earthquake (Figure 1.1b). The inferred earthquake locations and fault geometries benefit from the high spatial resolution observations of deformation from InSAR datasets, and error bounds reflect the presence of atmospheric and ionospheric noise. The focal mechanisms of the far-field earthquakes are consistent with late Cenozoic kinematics inferred from regional faults. The near-field event is consistent with triggering following an increase in the static Coulomb stress due to the great 2010 Maule earthquake. This chapter was published in the Journal of South American Earth Sciences. Rowena Lohman and Matt Pritchard provided invaluable discussion and editorial comments. Patricia Alvarado and Gerado Sánchez processed and analyzed the seismic data.

Chapter 4 focuses on the surface strain produced by the 2014 M_w 8.1 Pisagua, northern Chile, earthquake that ruptured a segment of the South America- Nazca plate boundary (Figure 1.1b). The 2014 earthquake reopened ancient surface cracks along 200 km of coast length. The consistency in strain orientation inferred from cracks reopened in 2014 and coseismic geodetic displacements suggests that the reopened cracks are a measure of the static strain release and permanent coseismic deformation. Evidence of high coseismic ground shaking from the very large surficial crack openings suggests that dynamic stresses also exert control on the characteristics of the reopened cracks. This chapter has been published in Geology with Richard Allmendinger, Gabriel González, and Jack Loveless as coauthors who provided very valuable discussions, significant collaboration in the field, and editorial comments on the manuscript.

There are several appendixes that support some of the main themes in this thesis. Ap-

pendix A is the Supporting Information for Chapter 2 published with the main manuscript. Appendix B outlines the ${}_j\mathrm{R}_i$ method used to derive empirical corrections of atmospheric noise with statistically non-stationary characteristics in InSAR data, as described in Chapter 2. Appendix C is the Supporting Information for Chapter 4 and was published with the main manuscript. Appendix D focuses on the InSAR record (or the lack thereof) of ancient coseismic cracks reopened during the 2014 M_w 8.1 Pisagua, Chile, earthquake.

1.2 InSAR background

Spatially dense observations from SAR datasets enable researchers to remotely examine surface characteristics, topography, ground deformation, and characteristics of the atmosphere. Here, I briefly describe the process required to produce an interferogram based on radar imagery acquired on a spaceborne satellite (Figure 1.2) and the resulting sensitivity of the produced imagery to a variety of physical processes.

1.2.1 Formation of an interferogram

Individual SAR images include information about both the phase and amplitude of the radar signal emitted and reflected back to the satellite. Each pixel in the SAR imagery contains information about the surface characteristics at the spatial resolution of meters to several tens of meters. The amplitude (Figure 1.3a) largely reflects the roughness and slope of the ground surface. Surfaces that are rough at the wavelength of the radar signal appear bright, because they scatter energy back to the satellite. Smooth surfaces such as lakes and paved roads reflect the microwave energy away from the satellite and appear dark. The phase associated with single acquisitions appears random: Each pixel contains contribution from a large set of ground scatterers whose interaction with the radar signal is controlled by the microwave wavelength (centimeters to a few tens of centimeters) that is significantly lower than the spatial dimension of the individual pixel.

An interferogram is constructed by multiplying the phase in one image with the complex conjugate of the second image. The phase in the resulting interferogram is often spatially coherent and represents the contribution from a variety of physical processes that all impact the travel time of the radar signal between the satellite and the ground, as discussed in the

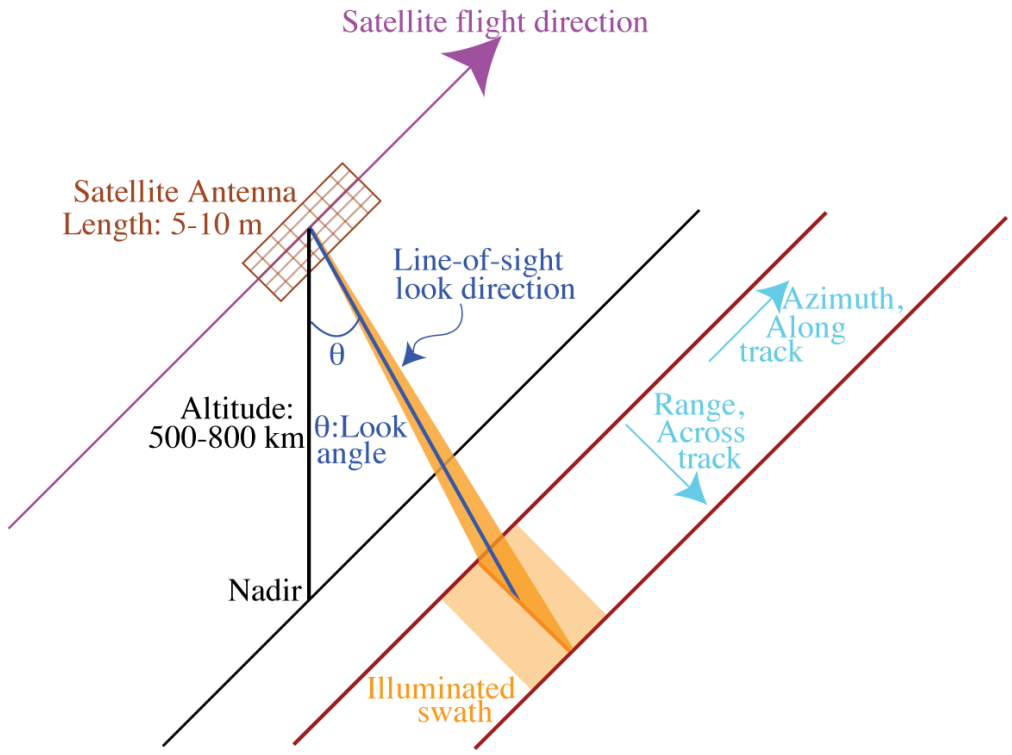

Figure 1.2: Geometry of a SAR satellite. SAR satellites orbit the Earth in a low Earth orbit at altitudes ranging from 500 to 800 km. The satellite is an active instrument, as it emits and receives radar signals. The sideways look-angle results in a combined sensitivity to vertical and horizontal static displacement, although the near-vertical look direction of many satellites results in a greater sensitivity to vertical deformation. Controls on the dimension of the pixel size in range and azimuth are described in Section 1.2.5.

following section. Coherence (Figure 1.3c) is a measure of the similarity in the reflective properties of the surface between SAR acquisitions (e.g., Zebker and Villasenor, 1992; Rosen et al., 2000) and is commonly used as a measure of data quality (e.g., Wei and Sandwell, 2010). Coherence values vary between 0 and 1, and higher values indicate a greater similarity in ground characteristics between acquisitions. When coherence is totally lost, the phase between neighboring pixels appears random and tracking ground deformation becomes very challenging (e.g., Funning et al., 2007; Feng et al., 2010).

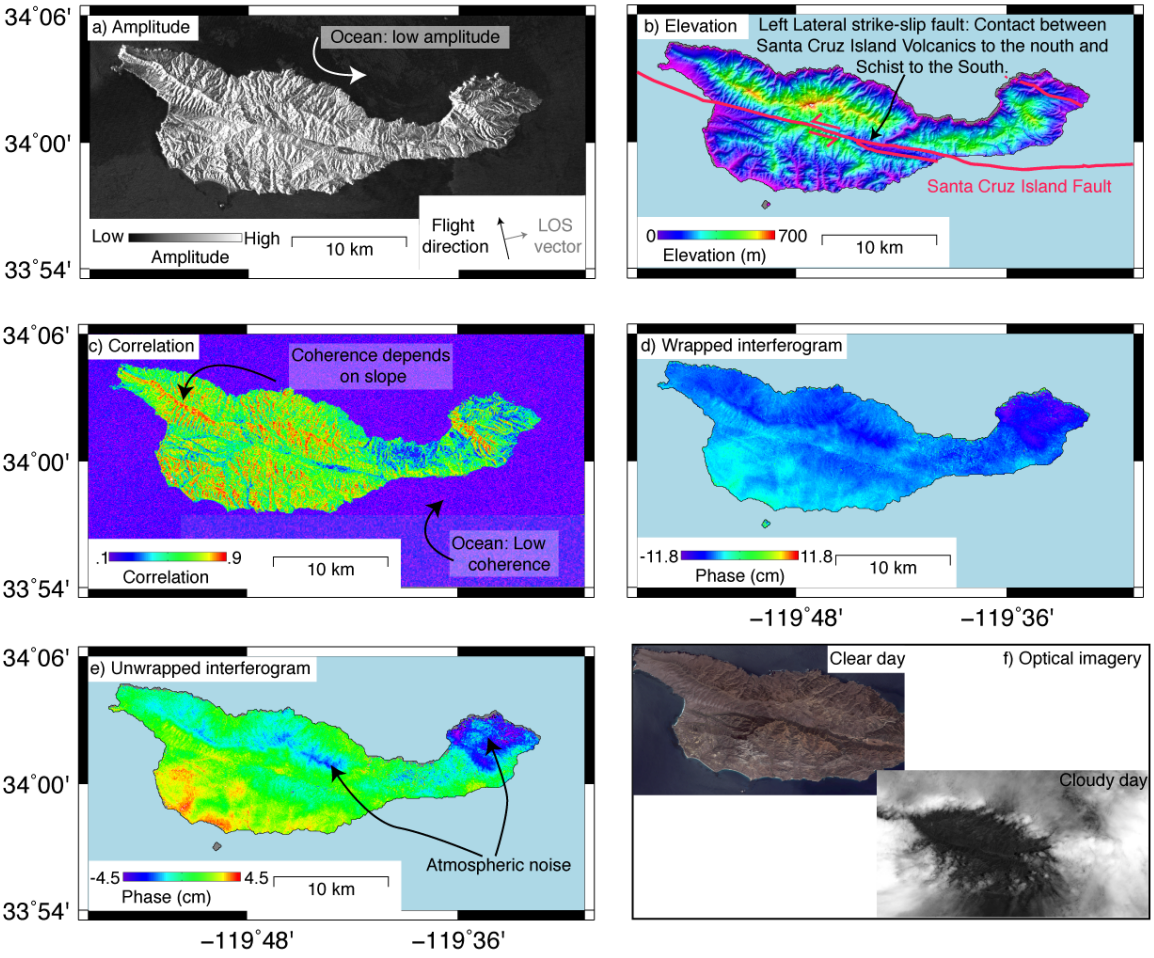

Figure 1.3: InSAR over the Santa Cruz Island, Channel Islands of southern California. The interferogram is from the ALOS satellite and spans February 20, 2007- May 23, 2007. (a) Amplitude. Line-of-sight (LOS) vector shows the satellite look direction. (b) Elevation with shaded relief map highlighting the left-lateral Santa Cruz Island fault. (c) Correlation. (d) Wrapped interferogram. (e) Unwrapped interferogram highlighting the presence of atmospheric noise that is approximately correlated with topography. (f) Two examples of optical imagery showing a diversity of weather patterns over the Santa Cruz Island that contribute to atmospheric noise in SAR data (e).

1.2.2 Contributions to interferometric phase

Below, I briefly describe several major contributors to the interferometric phase. The phase in an interferogram is equal to the differential phase associated with the two SAR acquisitions. As described the below, phase across an interferogram contains information about the displacement of the surface ground, as well as a variety of other physical phenomena that alter the propagation of the radar signal. In the case that the radar signal is sensitive only to the displacement of the ground surface, the phase (ϕ) is equal to:

$$\phi = \frac{4\pi}{\lambda}(\rho_2 - \rho_1), \tag{1.1}$$

where λ is the wavelength of the microwave signal, and ρ_1 and ρ_2 are the distances between the ground and the satellite at the first and second acquisitions, respectively. The signal in an individual interferogram may be reported as phase with units of radians or as displacement often with units of centimeters or meters.

Ground displacement: The interferometric phase includes contribution from changes in the position of the ground's surface in the near-vertical satellite line-of-sight direction. Deformation sources include fault slip (e.g., Massonnet et al., 1994), volcanic inflation (e.g., Pritchard and Simons, 2002), anthropogenic pumping of water and hydrocarbons (e.g., Amelung et al., 1999), and seasonal or long- term changes in the storage of water in aquifers (e.g., Watson et al., 2002; Lanari et al., 2004).

Atmospheric characteristics: The velocity of the radar signal traveling in the atmosphere is controlled by the atmospheric water vapor content, pressure, and temperature (e.g., Berrada Baby et al., 1988; Bürgmann et al., 2000; Rosen et al., 2000). Variations in the atmospheric characteristics at the timing of the two SAR acquisitions used to construct an interferogram result in spatially coherent noise that is challenging to distinguish from signals

that reflect the real displacement of the Earth's surface. Because the noise contribution from the turbulent component of the atmosphere is not correlated over temporal scales greater than a day (Emardson, 2003), the impact of atmospheric noise can be partially mitigated by averaging many interferograms together (e.g., Zebker et al., 1997). However, averaging the contribution from the seasonally dependent stratified component of the atmosphere can introduce biases in the inferred deformation rates if the data acquisitions are not uniformly distributed across the seasons (e.g., Doin et al., 2009; Barnhart and Lohman, 2013a). Efforts to correct atmospheric noise are described in more detail in Section 1.4 and Chapter 3.

Ionosphere: The phase is rotated in the electrically changed ionosphere by an amount that scales with the total electron count along the propagation path and inversely with the square of the signal frequency (e.g., Gray et al., 2000). Typical observed effects include azimuth streaks and decorrelation of the phase imagery. Ionospheric noise is often strongest in polar regions but also impacts data in over low and mid-latitude areas (Wegmuller et al., 2006; Pi et al., 2011).

Topography: When the distance separating SAR satellites (i.e., baseline) at the time of acquisition above a given point is non-zero, the phase is sensitive to topography. For instance, the Shuttle Radar Topography Mission took advantage of this feature to generate a digital elevation model (DEM) at a resolution of 1 arc second (Farr et al., 2007), by recording the reflected radar return at two separate antennae separated by a boom of known length. For studies focusing on tectonic deformation, the effect of topography must be removed with a pre-existing DEM when the baseline is non-zero.

Satellite position: When satellite positions differ by more than an amount known as the critical baseline, the set of scatterers in individual pixels do not add meaningfully and the

differential phase is incoherent. The critical baseline ($B_{\perp,crit}$) scales as,

$$B_{\perp,crit} \propto \frac{\lambda}{\Delta R}, \tag{1.2}$$

where ΔR is the range resolution. For the European Remote Sensing (ERS) satellite, $B_{\perp,crit}$ is 1.1 km. For the Advanced Land Observing Satellite (ALOS), $B_{\perp,crit}$ varies between 6.5 km and 13 km for different observation modes. For each of these platforms, space agencies were typically able to control position to within a hundred meters.

Errors in satellite position: Errors in our knowledge of satellite orbits result in long wavelength signals (Massonnet and Feigl, 1998; Fattahi and Amelung, 2014) that are typically modeled using polynomial ramps. Error on position varies from meter to centimeter scale for the older (e.g., ERS, Envisat, ALOS) and for the more recently launched satellites (e.g., TerraSAR-X, Sentinel), respectively (e.g., Eineder et al., 2003; Yoon et al., 2009). These errors in position result in strain rate uncertainties of 0.5 to 1.5 mm yr^{-1} 100 km^{-1} for older satellites and 0.2 to 0.5 mm yr^{-1} 100 km^{-1} for the recent satellites (Fattahi and Amelung, 2014). Orbital errors pose a major limitation for accurate inferences of long wavelength deformation signals that are of interest to researchers studying great earthquakes and interseismic loading (e.g., Fialko, 2006; Bekaert et al., 2015).

Ground characteristics: The microwave signal interacts with the surface layer and shallowest subsurface volume. Nolan and Fatland (2003) attribute variations in phase across agricultural areas to varying depths of interaction between the radar signal and the uppermost soil layer. Njoku and Kong (1977) propose that the dielectric constant of the soil largely controls this interaction. Guneriussen et al. (2001) demonstrate that the accumulation of dry snow between SAR acquisitions introduces coherent measurements of apparent surface displacement.

Satellite	Wavelength	Orbit Altitude	Mission dates
ERS-1	5.67 cm (C-band)	783 km	17 July 1991-10 March 2000
ERS-2	5.67 cm (C-band)	780 km	21 April 1995- 5 Sept' 2011
Envisat	5.67 cm (C-band)	782 km	1 March 2002-8 April 2012
ALOS	23.62 cm (L-band)	691 km	24 Jan' 2006- 12 May 2011
TerraSAR-X	3.11 cm (X-band)	514 km	Launched: 15 June 2007
Sentinel-1A	5.67 cm (C-band)	693 km	Launched: 3 April 2014

Table 1.1: List of SAR satellites discussed in this thesis. ERS: European Remote Sensing, Envisat: Environmental Satellite, ALOS: Advanced Land Observing Satellite. Note this is not a complete list of SAR satellites currently in orbit.

1.2.3 Filtering and phase unwrapping

Researchers often apply a filter to decrease the phase noise in wrapped SAR imagery. Goldstein and Werner (1998) develop an adaptive filtering algorithm where the spatial scale of the applied band-pass filter varies as a function of the local coherence in the interferogram. Often, filtering eases the process of unwrapping (see below) and improves estimates of surface displacement. This is particularly important when an interferogram is used as input into an earthquake source inversion (Chapters 2 and Chapter 3: Scott et al., 2014; Scott and Lohman 2016). However, the application of a filter decreases the effective spatial resolution of SAR imagery and therefore may not benefit studies focused on resolving fine- scale features in surface deformation patterns (Chapter 4: Scott et al., 2016).

The phase values within an interferogram are necessarily only known to modulo 2π - larger displacements will be "wrapped", with cycles that range from 0 to 2π. When an interferogram is unwrapped (Figure 1.3e), the phase contains information about ground displacement without the modulo 2π ambiguity. Unwrapping correctly is challenging, particularly if the

signal lacks continuity in the presence of decorrelation or high phase gradients associated with large topographic relief or surface displacement. Multiple approaches exist for phase unwrapping. The branch-cut method (Goldstein et al., 1988) isolates potential errors likely to result from phase noise and only unwraps relatively "clean" portions of the interferogram. The Statistical-Cost, Network- Flow Algorithm for Phase Unwrapping (Chen and Zebker, 2001) treats unwrapping as a probability estimation problem and attempts to identify the unwrapped phase surface that meets certain *a priori* criteria (e.g., smoothness).

1.2.4 Pixel offsets

Sub-pixel offset techniques offer an alternative approach to the calculation of surface displacements from SAR datasets. Displacement vectors in the range and the azimuth directions are calculated following an automated measurement of the offset between surface features in two sets of radar imagery. More formally, this task is often approached as a cross-correlation of the amplitude imagery. Pixel offset techniques are commonly applied when the surface displacements are high and are no longer resolvable with the methods described above. Typical applications often include earthquakes (e.g., Fielding et al., 2013), glaciers (e.g., Melkonian et al., 2014), and landslides (e.g., Singleton et al., 2014).

1.2.5 Spatial and temporal resolution

The resolution (spatial and temporal) achievable with satellite-based InSAR observations strongly controls the types of problems that can be addressed. The temporal resolution is limited by the frequency of data acquisition. Satellites repeat flight-orbits with weekly to monthly frequency, although imagery is not acquired at each pass due to limitations in the

transmission of large datasets from the satellite to the ground. Below, I describe the controls on the spatial resolution of SAR datasets.

Azimuth ("along track"): For a conventional radar system, the antenna footprint (R_{az}) dimension is:

$$R_{az} = \frac{\rho\lambda}{L}, \tag{1.3}$$

where L is the length of antennae. For the ALOS satellite ρ=695 km, λ= 23.6 cm, L=8.9 m, and the dimension of the ground footprint is $\sim$18 km. The spatial resolution of meters to tens of meters is achieved by synthesizing a larger antenna from many echoes that illuminate a single target. The SAR resolution is limited by the length of time a target is in view, which is directly controlled by the antenna length.

Range ("across track"): The resolution in range (ΔR) is expressed as,

$$\Delta R = \frac{c}{2\Delta f_{BW}}, \tag{1.4}$$

where c is the speed of light and Δf_{BW} is the range bandwidth of the radar signal. Variations in topography further impact the pixel dimension. The pixel is foreshortened and the amplitude is high when the line-of-sight vector is oriented sub-parallel to the vector normal to the topographic slope. Similarly, pixels along slopes that face away from the satellite look-direction have lower amplitude and larger ground dimension. Areas are shadowed when the topographic slope is steeper than the line-of-sight look vector, which can vary between 20^o and 50^o.

Interaction depth: The extent to which the radar signal is scattered, attenuated, or reflected along an interface boundary depends on the dielectric constants of the interacting materials, scatterer geometry, terrain slope, and radar wavelength. Over a forest, a C-band (λ= 5.6 cm) signal may interact with the uppermost canopy, while an L-band signal samples

lower levels of the vegetation and the underlying forest bottom (e.g., Prush and Lohman, 2014). The depth of interaction of the radar signal within the subsurface is largely controlled by the soil moisture content. Wet and dry materials have significantly differing dielectric constants, which largely control the interaction between the microwave signal and the shallow subsurface. Nolan and Fatland (2003) show that a change in volumetric water content from 1% to 40% alters the interaction depth from 50 cm to 4 cm for L-band wavelengths. This sensitivity to subsurface structure facilitates the mapping of buried paleo-rivers and drainage channels in hyperarid climates with SAR datasets (e.g., Schaber et al., 1986; Dabbagh et al., 1997; Grandjean et al., 2006).

1.3 Imaging earthquake deformation

InSAR observations of surface displacement and inverse theory techniques together create a powerful toolbox that geodesists use to image portions of the seismic cycle and ultimately understand the processes that produce surface deformation. For example, InSAR observations of coseismic deformation are used to place precise constraints on earthquake location and fault geometry (e.g., Massonnet et al., 1994; Simons et al., 2002). The postseismic signal reveals the upper mantle response to seismically driven stress changes (e.g., Pollitz et al., 2001) that can support comparisons between geologic and geodetic deformation rates (e.g., Gourmelen and Amelung, 2005). InSAR imagery illustrates the interseismic partition of deformation along neighboring faults (e.g., Fialko, 2006) and along-strike variations in the stress accumulation rate (e.g., Tong et al., 2013). The InSAR phase is additionally sensitive to aseismic activity, which may exceed the coseismic activity (e.g., Barnhart and Lohman, 2013b) or trigger moderate-sized earthquakes (e.g., Lohman and McGuire, 2007).

In this section, I focus on techniques employed to analyze earthquake deformation. Solving for subsurface fault geometry from static ground displacements is commonly framed as an inverse problem as illustrated in Figure 1.4. SAR data are sensitive to coseismic ground displacements measured in the near-vertical SAR line-of-sight. The model parameters of interest often include fault location, depth, strike, dip, rake, and slip magnitude. The Green's functions impose the physics of problem, and for the case of a slip inversion problem, relate the slip on a fault patch of known geometry to displacement along the Earth's surface.

Constraining subsurface processes from ground deformation is challenging for several reasons. First, slip on a set of faults with different orientations is likely to produce ground deformation consistent with the SAR observations– the solution is non-unique. Second, the InSAR phase is sensitive to a variety of signals including those from the tectonic signal of

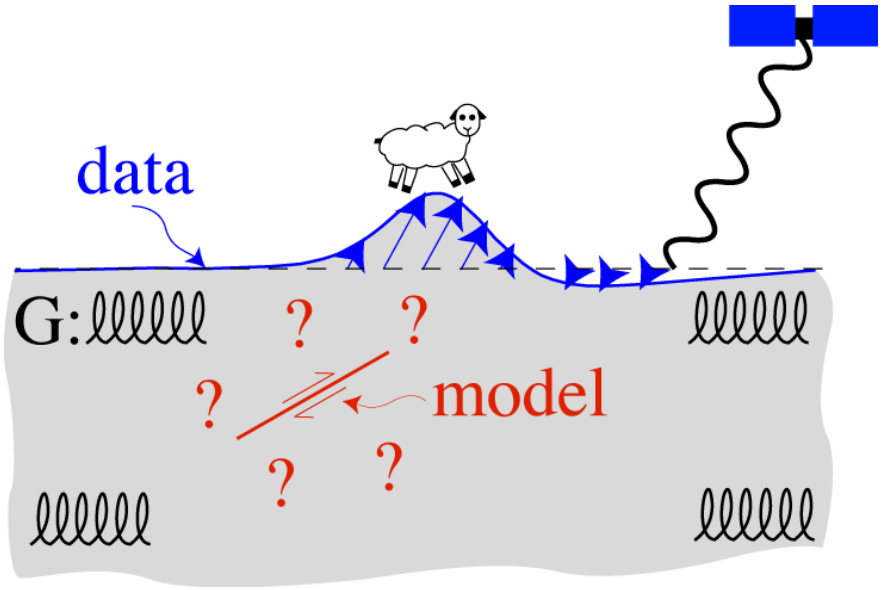

Figure 1.4: Cartoon illustrating the set-up of an inverse problem used to solve for fault geometry from surface displacements in SAR datasets. The data in blue are the ground displacements in the near-vertical SAR line-of-sight. The model parameters describe the geometry of the fault that generated the ground displacement. The Green's functions (**G**) relate slip along the fault patch to ground displacement. The crust is represented as an elastic half-space (Okada, 1985). This simplistic representation of the crust is insensitive the effect of anelastic deformation and material heterogeneities, which may be particularly significant near the fault (e.g., Oskin et al., 2012; Vallage et al., 2015). Note the cartoon is not drawn to scale.

interest, as well as seasonal uplift and subsidence, land-use changes, variations in atmospheric properties, and satellite position. Constraints on tectonic deformation are strengthened with knowledge of the likely contribution from each of these signal types. Third, models of deformation processes and subsurface structure do not capture the complexity of the real Earth. The researcher must optimize between the complexity required to solve the problem of interest, and that permitted by the known structural heterogeneities and the available computational resources.

1.3.1 Earthquake source inversions as inverse problems

The inversion for the magnitude of fault slip is linear, because slip on a fault patch with a known geometry scales linearly with the produced surface deformation. Because changes in fault geometry impact both the shape and magnitude of the surface deformation signal, the fault geometry is non-linearly related to the surface deformation. The full inversion for the earthquake source geometry and the magnitude of fault slip is treated as a non-linear inversion for fault geometry with a nested linear inversion for the magnitude of fault slip. The optimal fault geometry is associated with the lowest the root-mean-square residual between the real InSAR observations and the synthetic ground displacements produced by slip on the associated fault. Significant challenges associated with the inversion for fault geometry are posed the multi-dimensionality of the parameter space and by the non-uniqueness of the inferred fault geometry.

Solving for the magnitude of fault slip

In the linear component of the earthquake source inversion problem, the magnitude of slip is optimized for a given fault geometry. Mathematically, the forward problem is expressed as,

$$\mathbf{G}m = d, \tag{1.5}$$

where $\mathbf{G}$ is a matrix of Green's functions relating the magnitude of fault slip to the surface deformation. m is the set of model parameters that include slip on the fault plane and polynomial terms that account for long wavelength errors in satellite position (e.g., Massonnet and Feigl, 1998; Fattahi and Amelung, 2014) and atmospheric noise (e.g., Bürgmann et al., 2000). d is the set of surface displacement observations that are often spatially averaged from millions to hundreds of data points to make the inversion computationally feasible (e.g.,

Lohman et al., 2005). When the linear component of the inverse problem is not weighted and no regularization is applied, the model solution takes the form,

$$m = (\mathbf{G}^T\mathbf{G})^{-1}\mathbf{G}^T d. \tag{1.6}$$

Solving for fault geometry

The inversion for fault geometry (e.g., fault location, depth, strike, dip, and rake) from surface displacements is a non-linear problem and is approached as a large set of forward problems. In each forward problem, the specific fault geometry is selected based on a search of the non-linear parameter space. A simple, but thorough grid search of the multi-dimensional parameter space is very computationally expensive. The neighborhood algorithm (Sambridge, 1999) offers an alternative approach and searches the parameter space in an efficient manner. The approach includes an iterative global search that focuses in areas that performed better in earlier iterations. The resulting ensemble of tested fault geometries and their ability to produce surface deformation consistent with the observations provides information about the broadness of minima and possible trade-offs between inferred fault parameters.

1.3.2 Examples: Uniform slip

For smaller earthquakes where variations in slip along the fault plane are poorly constrained, researchers typically solve for fault slip that is uniform across the fault plane. Figure 1.5a illustrates the synthetic ground deformation produced by uniform slip along a 60^o dipping normal fault in an elastic half-space. The yellow lobe indicates ground subsidence or line-of-sight extension. The small blue lobe illustrates uplift or line-of-sight shortening. Synthetic noise mimicking the contribution from the stratified and turbulent components

of the atmosphere is added to the deformation signal in Figure 1.5b. I treat the signal in Figure 1.5b as observations of the surface displacement produced by slip on a fault with an unknown geometry and invert for the fault geometry using the process outlined above. Figure 1.5c shows the surface deformation in the line-of-sight produced by slip on the optimized fault plane, which closely matches the deformation signal prior to the addition of noise (Figure 1.5a). This inversion also facilitates the prediction of the displacement in the vertical, north- south, and east-west directions associated with the optimized fault model. The spatially coherent features in the residual between the input observations and the predicted displacement signal (Figure 1.5d) are largely due to the presence of atmospheric noise.

Trade-offs in the inferred fault parameters occur when one parameter cannot be retrieved independently of a second parameter. Common trade-offs in fault slip inversions include slip magnitude and fault width (Wright et al., 2003), location and mechanism (Lohman et al., 2002), as well as fault dip and depth. The impact of the trade-off between fault slip and width can be mitigated by imposing slip magnitude from fault-slip dimension scaling laws (Wright et al., 2003) or that the fault plane be square (Lohman et al., 2002). Further, the use of data acquired on both ascending and descending satellite flights improves constraints on the three-dimensional deformation field and earthquake source parameters (e.g., Lohman et al., 2002; Wright et al., 2004).

1.3.3 Examples: Distributed slip

In distributed slip models, the fault plane is divided into multiple fault patches. The inferred coseismic fault slip is allowed to vary along strike and with depth. For larger earthquakes, the inferred variations in slip are likely better able to capture complexity in earthquake processes and further our understanding of the mechanical properties of faults

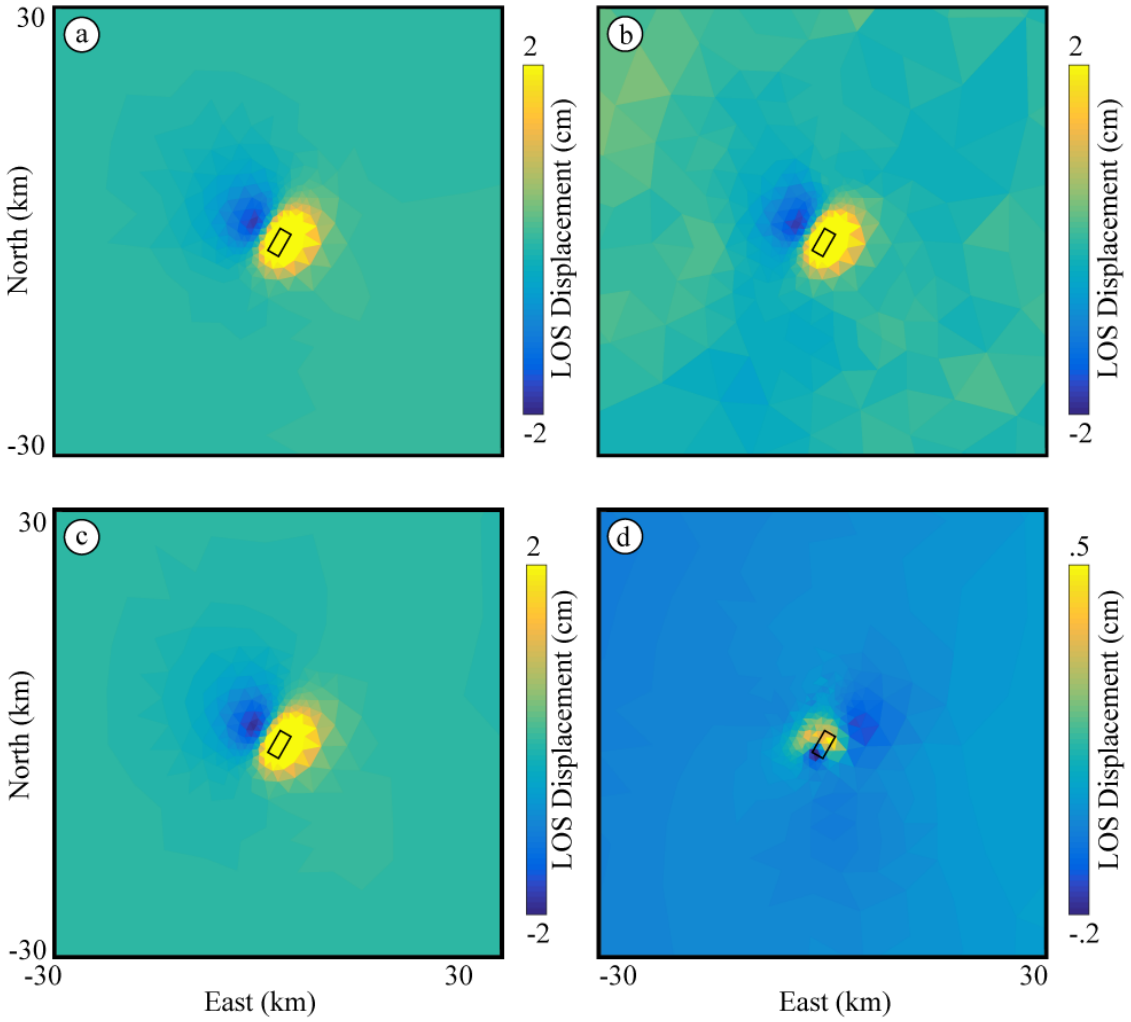

Figure 1.5: Source inversion of the displacement signal associated with a synthetic M_w 5.5 earthquake. (a) The surface displacement field generated by slip along a 60^o dipping normal fault. The black box outlines the fault plane. The triangular pixels reflect the spatial averaging of original imagery with a greater spatial resolution. (b) Synthetic atmospheric noise added to the signal in (a). (c) Predicted deformation in the SAR line-of-sight based on the optimized fault geometry from (b). The black box is the inferred fault plane. (d) Residual deformation signal, calculated by subtracting the predicted displacement signal (c) from the data that includes both the input surface displacement and a realization of atmospheric noise (b).

(e.g., Pritchard et al., 2006; Fielding et al., 2009; Delouis et al., 2010; Elliott et al., 2012).

Due to the non-uniqueness of the inferred fault geometry and challenges associated with the simultaneous inversion for both fault geometry and slip magnitude, inversions for distributed slip often rely on *a priori* knowledge of the fault geometry. For moderate-sized earthquakes, the fault geometry is typically optimized with an initial model of uniform slip on a single fault patch. For great and megathrust earthquakes in subduction zones, the fault plane geometry is often inferred from global models of subduction zone fault geometry (Figure 1.6; Hayes et al., 2012; Gusman et al., 2015). Subsequent research often focuses on constraining variations in slip along the fault plane that are supported by the available geodetic observations (e.g., Barnhart and Lohman, 2010). Commonly, the slip distribution is penalized for unsupported variations in fault slip by applying some form of Tikhonov regularization (e.g., Menke, 1989; Aster et al., 2013). In this case, the preferred model minimizes the norm,

$$||\mathbf{G}m - d||_2^2 + \xi^2||\mathbf{L}m||_2^2. \tag{1.7}$$

$\mathbf{L}$ is a matrix that imposes the regularization, and ξ is the regularization weighting factor. Minimum norm constraints minimize the amplitude of fault slip and are imposed by setting $\mathbf{L}$ equal to the identity matrix. These constraints are often applied to damp fault slip in areas where no quality data are available. When $\mathbf{L}$ is the finite difference approximation to the Laplacian operator, smoothing constraints penalize against abrupt gradients in the slip distribution.

The regularization weighting factor is often optimized in one of two ways. The L-curve method results in a solution that balances between the residual surface deformation and the complexity in the underlying source model. The ideal weighting factor lies at the corner of an L-shaped curve when the model semi-norm ($||\mathbf{L}m||$) is plotted versus the residual

($||\mathbf{G}m - d||$). This approach requires making a somewhat selective choice of the curve corner. Alternatively, the ${}_jR_i$ method (Lohman, 2004; Lohman and Simons, 2005; Barnhart and Lohman, 2010) ideally results in a source model that predicts surface displacement that is minimally impacted by noise but also captures the true complexity in the observations. This method can be automated and benefits from the fact that the choice of smoothing is driven by the actual complexity and structure of the observed data. I describe the ${}_jR_i$ method in Appendix B.

1.3.4 Complementary datasets

Geodetic and geophysical datasets

The integration of InSAR observations with other geophysical datasets results in stronger constraints on earthquake processes. The high spatial resolution of ground displacements acquired with SAR datasets facilitates the placement of strong constraints on the distribution of surface deformation. For moderate-magnitude earthquakes particularly in remote areas, InSAR observations are often considered a 'ground-truth' for earthquake location (e.g., Weston et al., 2012), which may be critical for the identification of the active fault. Further, InSAR observations offer valuable constraints on fault orientation (e.g., Funning et al., 2007; Weston et al., 2012). In contrast, error in earthquake location from seismic datasets is commonly 10 to 50 km, particularly when only global or regional networks are available (e.g., Weston et al., 2011; Devlin et al., 2012).

Because constraints on earthquake timing from InSAR datasets are limited by the timing of data acquisitions (usually weekly to monthly), seismic and GPS datasets are often used to constrain earthquake timing. When seismic networks are dense, seismic waveforms are

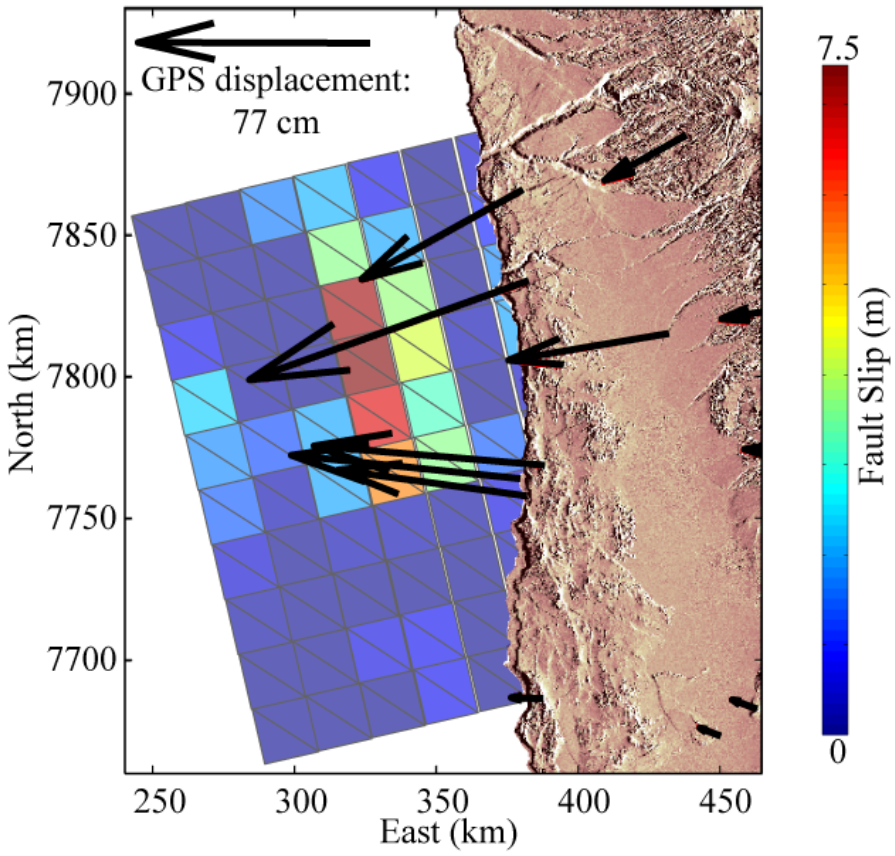

Figure 1.6: Distributed fault slip for the 2014 M_w 8.1 Pisagua, Chile, earthquake from Gusman et al. (2015). Data used to produce the slip model include horizontal and vertical GPS displacements, and tsunami waveforms. Black arrows show the horizontal displacement measured at GPS stations that are part of the Integrated Plate Boundary Observatory Chile (IPOC), the International Associated Laboratory, and the Central Andean Tectonic Observatory Geodetic Array projects (Schurr et al., 2014).

sensitive to patterns of rupture development, including rupture directivity and the temporal variation in moment release, as well as the migration of earthquake sequences (e.g., Amelung and Bell, 2003; Prejean, 2004; Kundu et al., 2012; Sevilgen et al., 2012; Schurr et al., 2014). The daily position estimates of continuous Global Positioning System (GPS) stations allows for the distinction between co- and early post-seismic deformation (e.g., Gonzalez-Ortega et al., 2014).

InSAR observations are insensitive to off- shore deformation (Figure 1.6), because the radar signal reflects off the water surface and does not interact with the seafloor bottom. Therefore studies focusing on great and megathrust earthquakes may be augmented with seismic waveforms, tsunami height observations (e.g., Lorito et al., 2011; Gusman et al., 2015), and measurements of seafloor displacement from bathymetry datasets (e.g., Fujiwara et al., 2011). The pre- and post- earthquake bathymetry datasets from the 2011 M_w 9.1 Tohoku reveal significant shallow slip near the trench, which has important consequences for our understanding of the frictional properties of the up-dip portion of subduction zone thrust faults (Fujiwara et al., 2011; Ide et al., 2011; Scholz, 2014).

Geodetic and geologic datasets

Geodetic and geologic observations of deformation offer complementary insight into the relationship between surface deformation and the physical processes that govern subduction zone processes. InSAR and GPS observations constrain surface deformation during the past several decades. While the span of the geodetic record is less than the 100- 150 year length of the seismic cycle in northern Chile (e.g., Comte and Pardo, 1991), for example, geodetic data have recorded interseismic deformation (Béjar-Pizarro et al., 2013), as well as the coseismic and post-seismic signals associated with several great earthquakes (Hayes et al.,

2014; Schurr et al., 2014; Duputel et al., 2015). These observations place strong constraints on the surface deformation during different segments of the seismic cycle that can be used to explore possible segmentation of the plate boundary system and depth-dependent variations in frictional properties along the main thrust fault (e.g., Melbourne et al., 2002; Chlieh et al., 2004; Métois et al., 2012; Métois et al., 2013). Results necessarily reflect deformation associated with a short segment of a seismic cycle– they lack sensitivity to deformation over a full seismic cycle and potential variations in tectonic behavior over several seismic cycles.

Paleoseismic, geomorphic, and geologic observations are indicative of plate boundary behavior over several to hundreds of seismic cycles. In many subduction environments, features of interest include tsunami deposits (e.g., Atwater and Moore, 1992), uplifted coastal terraces (e.g., Matsuda et al., 1978), and upper plate faults (e.g., Arriagada et al., 2011; Farías et al., 2011). These features give insight into the size and timing of past earthquakes, as well as controls on tectonic behavior over many seismic cycles (e.g., Nanayama et al., 2003; Loveless et al., 2005; Dawson and Stewart, 2007; Baker et al., 2013). However, interpreting permanent structures in terms of seismic cycle behavior remains challenging. Several approaches have focused on understanding the relationship between permanent forearc structures active in recent great earthquakes and the kinematics of those great earthquakes inferred from geodetic datasets (e.g., Aron et al., 2013; Scott et al., 2016).

1.4 Atmospheric Noise in InSAR data

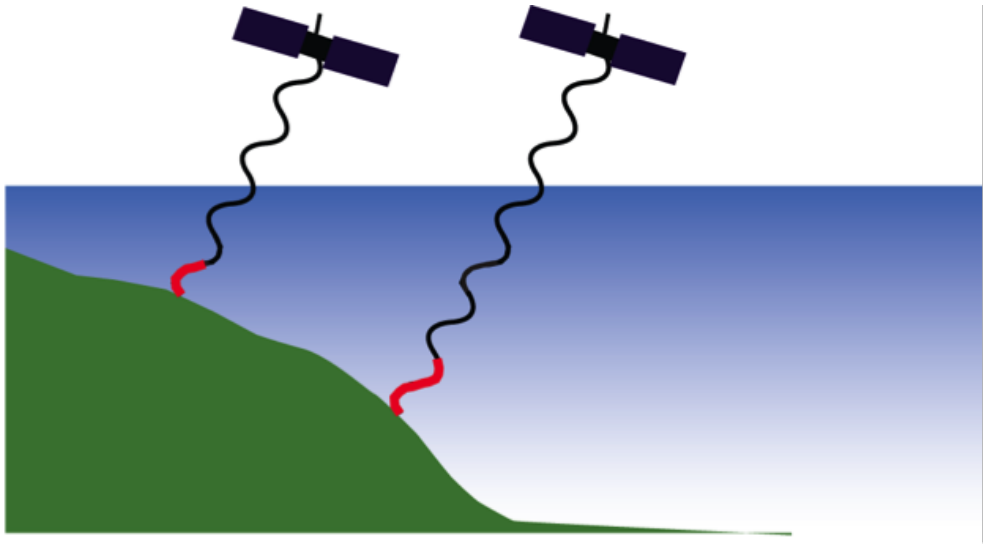

Figure 1.7: Cartoon illustrating the impact of the vertical stratification of the atmosphere on topographically correlated noise in InSAR data. Variations in atmospheric characteristics impact of the speed of traveling microwave radar signal. The radar signal samples more of the troposphere above areas of low elevation and accumulates additional delay relative to areas of higher elevation.

Changes in atmospheric humidity, temperature, and pressure impact the speed of the radar signals as they travel through the troposphere (e.g., Berrada Baby et al., 1988) as shown in Figure 1.7. Variations in atmospheric delay result in spurious signals in InSAR datasets that pose a major challenge to efforts to infer ground deformation rates (e.g., Bürgmann et al., 2000). Atmospheric noise corrections may decrease the impact of the noise on inferred earthquake source parameters (e.g., Onn and Zebker, 2006; Cavalié et al., 2007; Doin et al., 2009). Statistics of atmospheric noise characteristics support the understanding of the quality of tectonic parameters inferred from InSAR datasets (e.g., Hanssen, 2001; Emardson, 2003; Lohman and Simons, 2005). In this section, I describe characteristics of atmospheric noise and make comparisons between the InSAR phase delay in several interferograms and the expected atmospheric phase delay inferred from a reanalysis weather model.

The total atmospheric delay is commonly described in terms of turbulent and stratified components (Hanssen, 2001). Turbulent mixing of the atmosphere results from horizontal and vertical variations in the water vapor content over both flat and mountainous areas. The turbulent contribution in InSAR data is spatially correlated over distances of ∼20 km (Lohman and Simons, 2005). Because the characteristics of atmospheric turbulence are not correlated over time-scales greater than a day (Emardson, 2003), averaging many interferograms reduces the impact of the turbulent component of the atmosphere (e.g., Zebker et al., 1997). Weather models, which can be useful for predicting the contribution from the stratified component of the atmosphere, sample atmospheric characteristics at spatial and temporal scales that are too coarse to effectively capture and correct the turbulent component of atmospheric noise (e.g., Jolivet et al., 2014).

Vertical stratification of air pressure, temperature, and water vapor result in phase delays that are approximately correlated with topography (e.g., Bürgmann et al., 2000) as shown in Figure 1.8. For the ease of modeling, the stratified delay is sometimes further separated into wet and dry components. The dry delay scales linearly with the difference in total air pressure in the atmosphere. The wet delay scales with water vapor partial pressure and inversely with temperature. Because the amplitude of the stratified delay is commonly seasonally dependent, a simple averaging of many interferograms can bias inferred rates if the seasonality is poorly sampled by the set of acquisitions (e.g., Doin et al., 2009; Barnhart and Lohman, 2013a).

Atmospheric noise in InSAR datsets is challenging to separate from signals associated with real ground uplift and subsidence. For example, observations of long-wavelength coseismic and interseisimic deformation in subduction zone environments are biased by atmospheric noise, which has power at the same spatial scales (e.g., Lin et al., 2010; Fournier et al., 2011; Remy et al., 2011; Béjar-Pizarro et al., 2013; Bekaert et al., 2015; Jolivet et

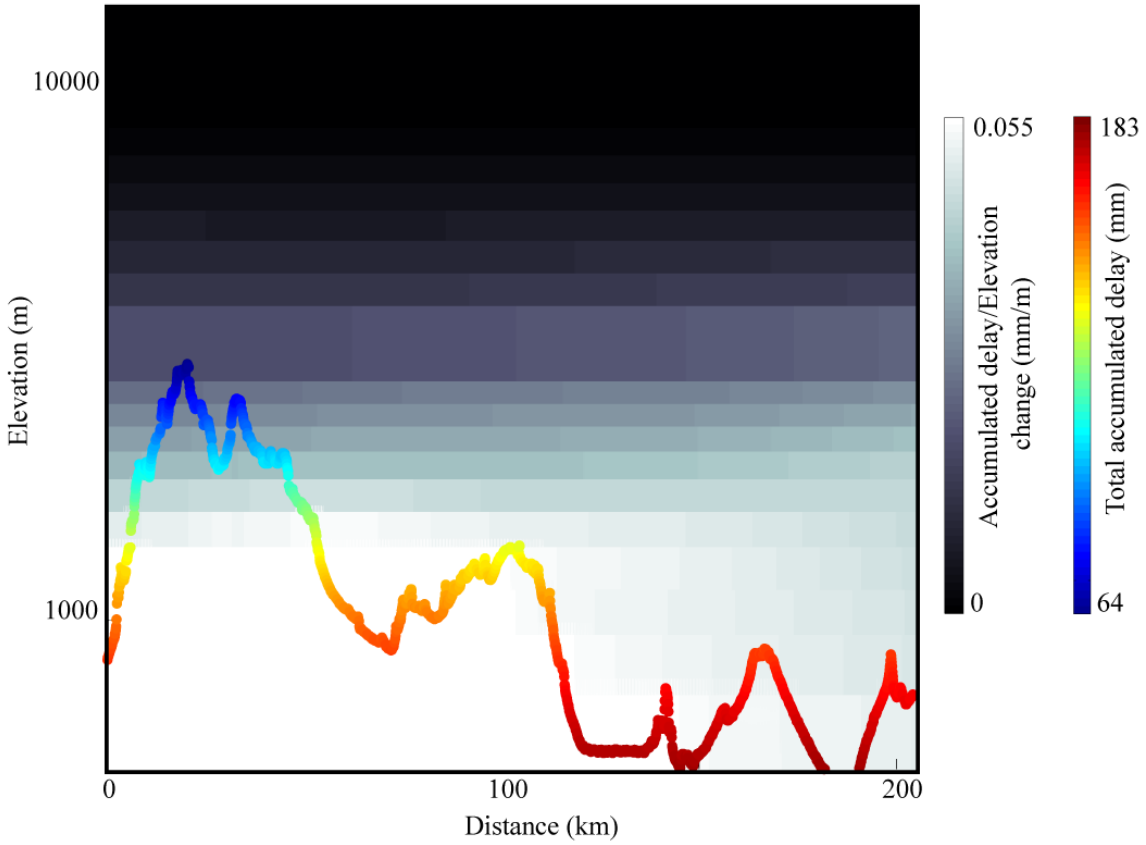

Figure 1.8: Atmospheric contribution to InSAR data across the San Bernardino mountains, California. The shaded grey background illustrates the accumulated delay of the of the radar signal in multiple elevation bands in the troposphere. The rainbow line outlines topography colored by the delay of the radar signal from the satellite to the ground surface. Note that during a single acquisition, the delay is strictly positive and only differences between two dates results in negative values. This figure was created using the Python based Atmospheric Phase Screen Estimation software package (PyAPS) produced by Jolivet et al. (2011) with constraints on atmospheric characteristics from the North America Regional Reanalysis model (NARR; Mesinger et al., 2006) .

al., 2014). A significant amount of research is focused on correcting the noise contribution from the stratified component of the atmosphere with one of two types of approaches. In the first, an empirical fit or set of fits between topography and phase is removed from the interferogram (e.g., Cavalié et al., 2007; Elliott et al., 2008; Tymofyeyeva and Fialko, 2015). In the second, atmospheric constraints from external datasets, such as weather models, are used to infer the atmospheric contribution (e.g., Doin et al., 2009). Because the characteristics of the atmosphere vary over short spatial and temporal scales, residual atmospheric signals persist following the application of atmospheric corrections (e.g., Jolivet et al., 2011). An understanding of the impact of the residual atmospheric noise on the inferred tectonic parameters can strengthen constraints on seismic cycle processes from SAR observations.

1.4.1 Atmospheric delay from Global Atmospheric Models (GAM)

Global Atmospheric Models (GAM) provide meteorological constraints on atmospheric pressure, temperature, and humidity that are used to statistically evaluate and correct the atmospheric contribution to InSAR data. The ERA40 reanalysis (Uppala et al., 2005), the European Centre for Medium-Range Weather Forecasts (ECMWF), and the North American Regional Reanalysis weather model (NARR; Mesinger et al., 2006) are meteorological models used to correct InSAR datasets. This section focuses on results from the NARR weather model, which produces relatively high spatial and temporal resolution analyses of weather characteristics in North America.

The Python based Atmospheric Phase Screen Estimation software package (PyAPS; Jolivet et al., 2014) generates atmospheric corrections based on NARR-inferred meteorological properties modeled at 29 pressure levels every 3 hours along a 32 km grid spacing. The PyAPS workflow is shown in Figure 1.9. The atmospheric reanalysis results are translated

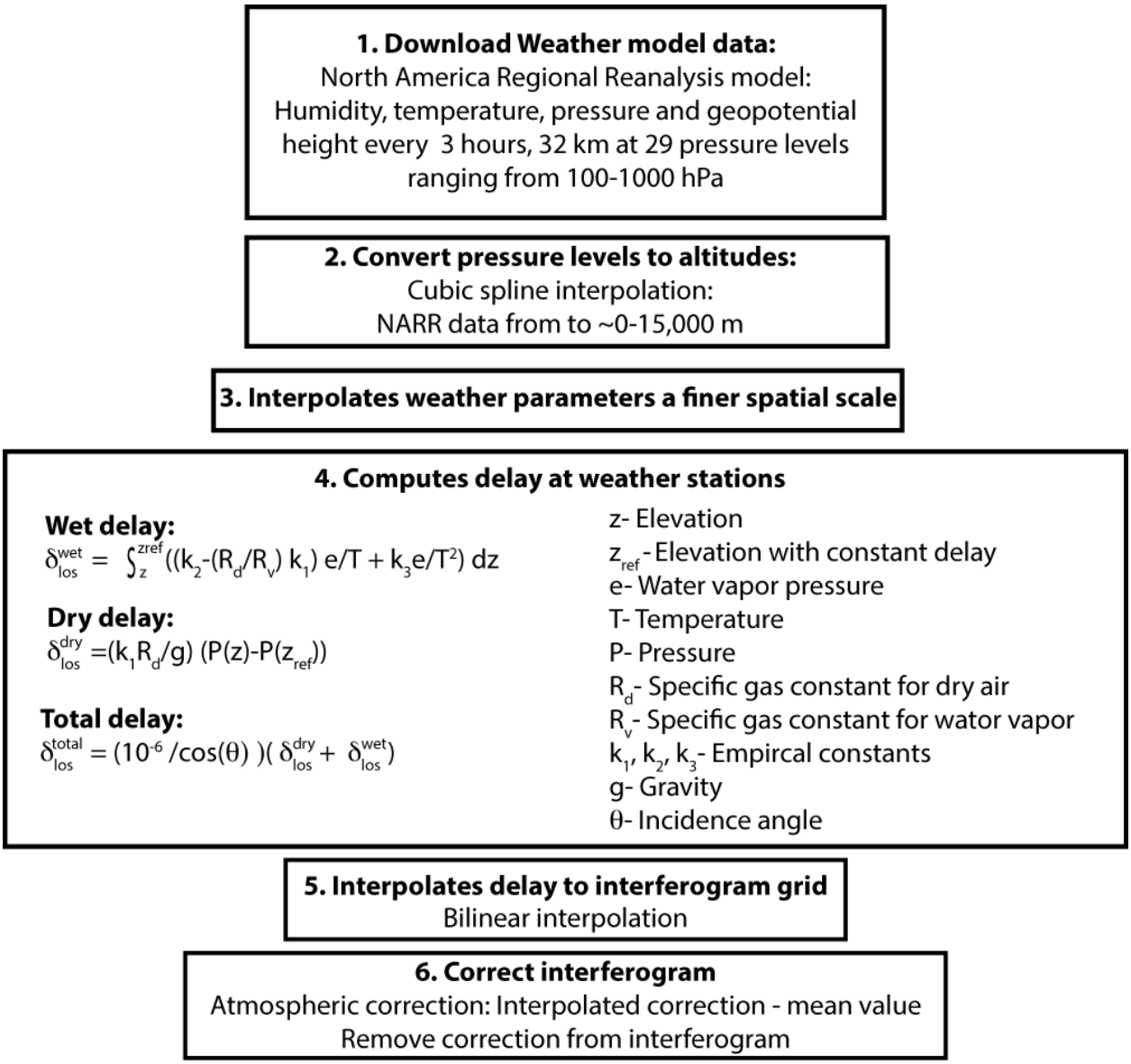

Figure 1.9: Workflow developed by Jolivet et al. (2011) and implemented PyAPS to correct the atmospheric signal in InSAR data with the North America Regional Reanalysis (NARR) weather model. Note this figure is not modified from earlier publications.

to microwave signal delay by the integration of the total delay through the troposphere, which is itself calculated from several empirical constants and constraints on weather characteristics.

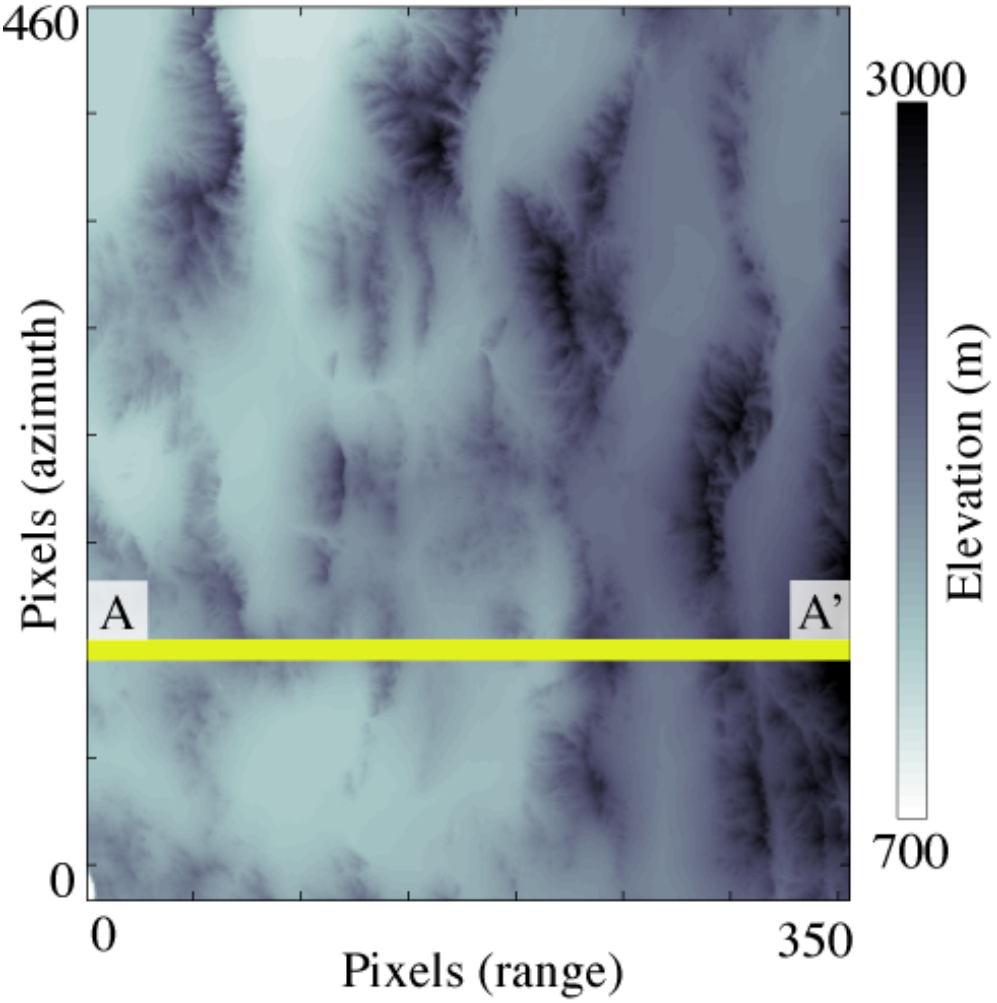

Figure 1.10: Digital elevation model for Envisat Track 213, Frame 2817 show in Figures 1.11 and 1.12. The A-A' transect spans the profile in Figure 1.13.

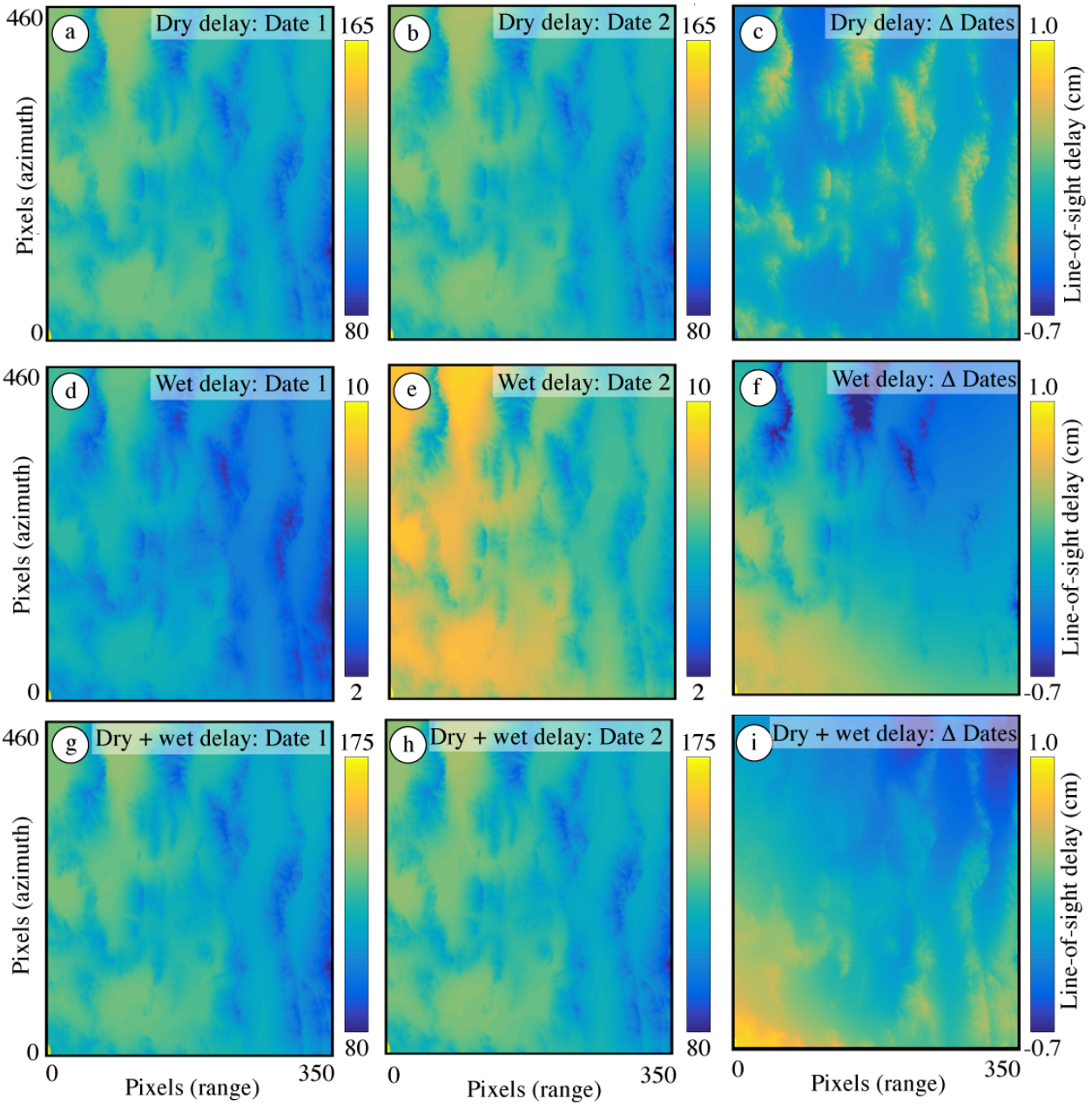

Figure 1.11: Maps illustrating atmospheric delays predicted from the NARR weather model. The first row shows the dry delay for (a) September 23, 2008 and (b) August 4, 2009, and (c) the delay difference between the respective dates. The second and third rows show the wet and total delay, respectively. Interferometric phase is sensitive only to the difference in total delay, shown in (i).

1.4.2 Comparisons of phase delay

The wet and dry atmospheric delays for individual dates are always positive and decrease with elevation. The dry delay associated with the two dates shown in Figure 1.11 varies between 80 cm and 165 cm. Because the dry delay for these two dates is almost identical, the contribution to an interferogram (difference in delay) is less than 2 cm. In contrast, the amplitude of the wet delay for individual dates is less than 10 cm but varies significantly between these two dates. For this set of date pairs, the interferometric phase contribution from both delay types is similar (Figure 1.11i).

I compare the observed phase delay in four real interferograms to the expected delay based on the NARR weather model in Figure 1.12. The first two rows illustrate cases where the NARR-predicted delay matches the long wavelength and topographically correlated signal observed in the InSAR data. For these cases, the atmospheric correction improves data quality. The third row shows an example where the NARR-predicted delay is lower in amplitude than the InSAR signal and has relatively little impact on data quality. The fourth row illustrates a case where the phase delay predicted from the NARR weather model differs significantly from the InSAR observations. For this case, the correction results in additional errors in the inferred deformation and decreases data quality. These cases together illustrate a varied utility of weather model corrections and importantly show that the application of weather models to correct atmospheric noise may decrease data quality.

In many cases, even when the NARR correction fits the long wavelength InSAR signal (e.g., Figure 1.12a-c), the corrections are generally unable to reproduce the smaller spatial scale signals. For the case shown in Figure 1.13, the NARR delay matches the InSAR contribution associated with the ridges and the long wavelength the ramp. However, the correction does not predict the observed phase delays between ridges that appears to be

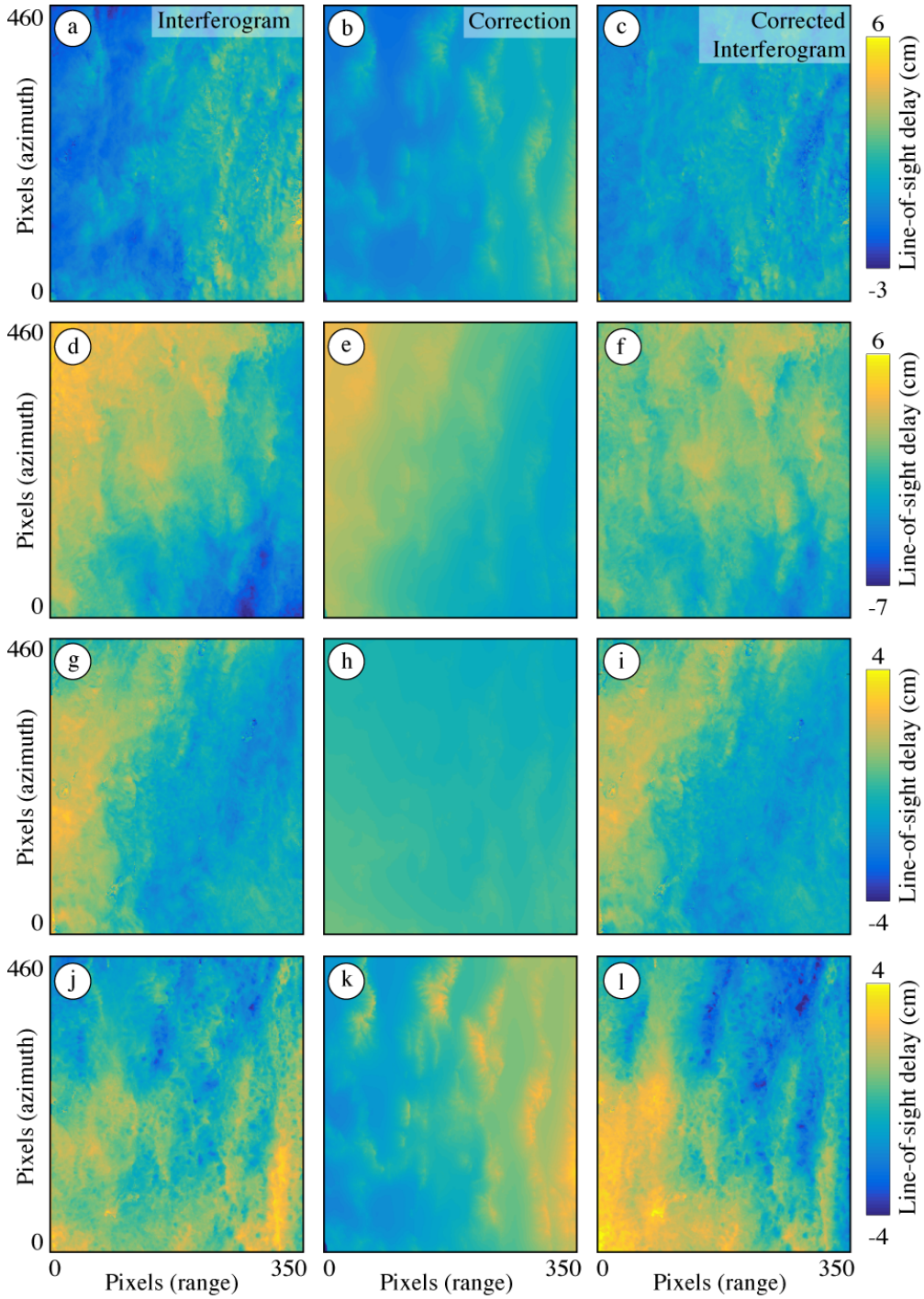

Figure 1.12: A comparison of atmospheric phase delays inferred from InSAR data and the NARR weather model. From top to bottom, the rows show delay spanning May 11, 2010-June 15, 2010; July 15, 2008-August 19, 2008; September 9, 2008-August 4, 2009; May 26, 2009-June 30, 2009. The columns from left to right show the interferogram, the NARR-inferred correction, and the corrected interferogram.

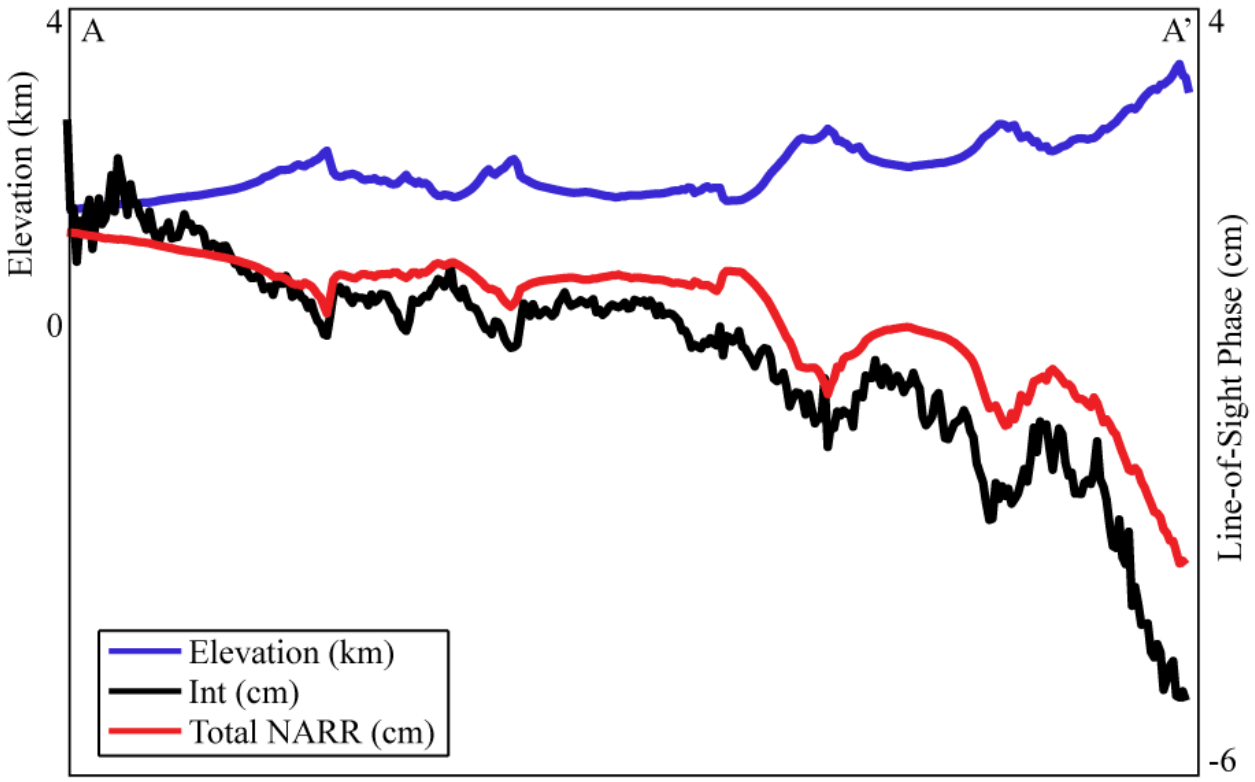

Figure 1.13: Profiles showing elevation (blue), interferometric phase (black), and NARR correction (red) for an interferogram spanning May 2, 2006- November 13, 2007. Profile location is shown in Figure 1.10.

anomalously large relative to the present topography. This suggests that even when the inferred atmospheric characteristics are accurate enough to predict the long wavelength contribution, turbulent features persist at smaller spatial scales and are not easily corrected with atmospheric characteristics inferred from weather models.

1.4.3 Concluding thoughts

This work demonstrates that the improvement to data quality from corrections based on atmospheric characteristics from the NARR weather model is variable. The differing quality of corrections from a single weather model may reflect the possibility that atmospheric char-

acteristics change at different speeds. Several authors have demonstrated that the amplitude of the stratified delay varies seasonally (e.g., Doin et al., 2009; Barnhart and Lohman, 2013a). A more extensive but similar dataset to the one analyzed here could be used to explore the possibility that the quality of delay predicted from the weather model also varies seasonally.

Future work may also focus on characterizing the spatial scales where atmospheric corrections from weather models are likely to improve data quality. These spatial scales are likely to reflect the spatial resolution of the weather model. As demonstrated here, even when weather models predict the long wavelength atmospheric signal in InSAR data, they fail to produce the shorter spatial-scale signals likely associated with atmospheric turbulence. Corrections based on a weather model may not significantly improve constraints associated with a moderate-magnitude earthquake whose spatial footprint is much smaller than the grid spacing of the weather model. In contrast, the corrections may improve constraints associated with long wavelength signals in subduction zone environments. Knowledge of the utility of atmospheric corrections at different spatial scales can inform researchers of the most useful atmospheric correction for different types of tectonic problems and the expected improvement to data quality.

1.5 References

Amelung, F., and J. Bell (2003), Interferometric synthetic aperture radar observations of the 1994 Double Spring Flat, Nevada, earthquake (M5.9): Main shock accompanied by triggered slip on a conjugate fault, Journal of Geophysical Research, 108(B9), doi:10.1029/2002JB001953.

Amelung, F., D. L. Galloway, J. W. Bell, H. A. Zebker, and R. J. Laczniak (1999), Sensing the ups and downs of Las Vegas: InSAR reveals structural control of land subsidence and aquifer-system deformation, Geology, 27(6), 483, doi:10.1130/0091-7613(1999)027<0483:STUADO>2.3.CO;2.

Aron, F., R. W. Allmendinger, J. Cembrano, G. González, and G. Yáñez (2013), Permanent fore-arc extension and seismic segmentation: Insights from the 2010 Maule earthquake, Chile: Journal of Geophysical Research: Solid Earth, 118(2), 724-739, doi:10.1029/2012JB009339.

Arriagada, C. et al. (2011), Nature and tectonic significance of co-seismic structures associated with the Mw 8.8 Maule earthquake, central-southern Chile forearc, Journal of Structural Geology, 33(5), 891-897, doi:10.1016/j.jsg.2011.03.004.

Atwater, B. F., and A. L. Moore (1992), A Tsunami About 1000 Years Ago in Puget Sound, Washington, Science, 258(5088), 1614-1617, doi:10.1126/science.258.5088.1614.

Baker, A., R. W. Allmendinger, L. A. Owen, and J. A. Rech (2013), Permanent deformation caused by subduction earthquakes in northern Chile, Nature Geoscience, 6(6), 492-496, doi:10.1038/ngeo1789.

Barnhart, W. D., and R. B. Lohman (2010), Automated fault model discretization for inversions for coseismic slip distributions, Journal of Geophysical Research, 115(B10), doi:10.1029/2010JB007545.

Barnhart, W. D., and R. B. Lohman (2013a), Characterizing and estimating noise in InSAR and InSAR time series with MODIS: Geochemistry, Geophysics, Geosystems, 14(10), 4121-4132, doi:10.1002/ggge.20258.

Barnhart, W. D., and R. B. Lohman (2013b), Phantom earthquakes and triggered aseismic creep: Vertical partitioning of strain during earthquake sequences in Iran: Geophysical Research Letters, 40(5), 819-823, doi:10.1002/grl.50201.

Béjar-Pizarro, M., A. Socquet, R. Armijo, D. Carrizo, J. Genrich, and M. Simons (2013), Andean structural control on interseismic coupling in the North Chile subduction zone, Nature Geoscience, 6(6), 462-467, doi:10.1038/ngeo1802.

Bekaert, D. P. S., A. Hooper, and T. J. Wright (2015), A spatially variable power law tropospheric correction technique for InSAR data, Journal of Geophysical Research: Solid Earth, doi:10.1002/2014JB011558.

Berrada Baby, H., P. Golé, and J. Lavergnat (1988), A model for the tropospheric excess path length of radio waves from surface meteorological measurements, Radio Science, 23(6), 1023-1038, doi:10.1029/RS023i006p01023.

Bürgmann, R., P. A. Rosen, and E. J. Fielding (2000), Synthetic Aperture Radar Interferometry to Measure Earth's Surface Topography and Its Deformation, Annual Review of Earth and Planetary Sciences, 28(1), 169-209, doi:10.1146/annurev.earth.28.1.169.

Cavalié, O., M.-P. Doin, C. Lasserre, and P. Briole (2007), Ground motion measurement in the Lake Mead area, Nevada, by differential synthetic aperture radar interferometry time series analysis: Probing the lithosphere rheological structure, Journal of Geophysical Research, 112(B3), doi:10.1029/2006JB004344.

Chen, C. W., and H. A. Zebker (2001), Two-dimensional phase unwrapping with use of statistical models for cost functions in nonlinear optimization, Journal of the Optical Society of America A, 18(2), 338, doi:10.1364/JOSAA.18.000338.

Chlieh, M., J. B. de Chabalier, J. C. Ruegg, R. Armijo, R. Dmowska, J. Campos, and K. L. Feigl (2004), Crustal deformation and fault slip during the seismic cycle in the North Chile subduction zone, from GPS and InSAR observations, Geophysical Journal International, 158(2), 695-711, doi:10.1111/j.1365-246X.2004.02326.x.

Comte, D., and M. Pardo (1991), Reappraisal of great historical earthquakes in the northern Chile and southern Peru seismic gaps, Natural Hazards, 4(1), 23-44, doi: 10.1007/ BF00126557.

Dabbagh, A. E., K. G. Al-Hinai, and M. Asif Khan (1997), Detection of sand-covered geologic features in the Arabian Peninsula using SIR-C/X-SAR data, Remote Sensing of Environment, 59(2), 375-382, doi:10.1016/S0034-4257(96)00160-5.

Delouis, B., D. Giardini, P. Lundgren, and J. Salichon (2002), Joint Inversion of InSAR, GPS, Teleseismic, and Strong-Motion Data for the Spatial and Temporal Distribution of Earthquake Slip: Application to the 1999 Izmit Mainshock, Bulletin of the Seismological Society of America, 92(1), 278-299, doi:10.1785/ 0120000806.

Delouis, B., J.-M. Nocquet, and M. Vallée (2010), Slip distribution of the February 27, 2010 Mw = 8.8 Maule Earthquake, central Chile, from static and high-rate GPS, InSAR, and broadband teleseismic data, Geophysical Research Letters, 37(17), doi:10.1029/2010GL043899.

Devlin, S., B. L. Isacks, M. E. Pritchard, W. D. Barnhart, and R. B. Lohman (2012),

Depths and focal mechanisms of crustal earthquakes in the central Andes determined from teleseismic waveform analysis and InSAR: Tectonics, 31(2), doi:10.1029/2011TC002914.

Doin, M.-P., C. Lasserre, G. Peltzer, O. Cavalié, and C. Doubre (2009), Corrections of stratified tropospheric delays in SAR interferometry: Validation with global atmospheric models, Journal of Applied Geophysics, 69(1), 35-50, doi:10.1016/j.jappgeo.2009.03.010.

Eineder, M., H. Runge, E. Boerner, R. Bamler, N. Adam, B. Schattler, H. Breit, and S. Suchandt (2003), SAR Interferometry with TerraSAR-X, Proc. of Fringe 2003 Workshop, Frascati, Italy.

Elliott, J. R., J. Biggs, B. Parsons, and T. J. Wright (2008), InSAR slip rate determination on the Altyn Tagh Fault, northern Tibet, in the presence of topographically correlated atmospheric delays, Geophysical Research Letters, 35(12), doi:10.1029/2008GL033659.

Elliott, J. R., E. K. Nissen, P. C. England, J. A. Jackson, S. Lamb, Z. Li, M. Oehlers, and B. Parsons (2012), Slip in the 2010-2011 Canterbury earthquakes, New Zealand: Journal of Geophysical Research: Solid Earth, 117(B3), doi:10.1029/2011JB008868.

Emardson, T. R. (2003), Neutral atmospheric delay in interferometric synthetic aperture radar applications: Statistical description and mitigation, Journal of Geophysical Research, 108(B5), doi:10.1029/2002JB001781.

Farías, M., D. Comte, S. Roecker, D. Carrizo, and M. Pardo (2011), Crustal extensional faulting triggered by the 2010 Chilean earthquake: The Pichilemu Seismic Sequence, Tectonics, 30(6), doi:10.1029/2011TC002888.

Farr, T. G. et al. (2007), The Shuttle Radar Topography Mission, Reviews of Geophysics, 45(2), doi:10.1029/2005RG000183. Fattahi, H., and F. Amelung (2014), InSAR uncertainty due to orbital errors, Geophysical Journal International, 199(1), 549-560, doi:10.1093 /gji/ggu276.

Feng, G., E. A. Hetland, X. Ding, Z. Li, and L. Zhang (2010), Coseismic fault slip of the 2008 M w 7.9 Wenchuan earthquake estimated from InSAR and GPS measurements: Geophysical Research Letters, 37(1), doi:10.1029/2009GL041213.

Fialko, Y., D. Sandwell, M. Simons, and P. Rosen (2005), Three-dimensional deformation caused by the Bam, Iran, earthquake and the origin of shallow slip deficit, Nature, 435(7040), 295-299, doi:10.1038/nature03425.

Fialko, Y. (2006), Interseismic strain accumulation and the earthquake potential on the southern San Andreas fault system, Nature, 441(7096), 968-971, doi:10.1038/nature04797.

Fielding, E. J., M. Talebian, P. A. Rosen, H. Nazari, J. A. Jackson, M. Ghorashi, and

R. Walker (2005), Surface ruptures and building damage of the 2003 Bam, Iran, earthquake mapped by satellite synthetic aperture radar interferometric correlation, Journal of Geophysical Research, 110(B3), doi:10.1029/2004JB003299.

Fielding, E. J., P. R. Lundgren, R. Bürgmann, and G. J. Funning (2009), Shallow fault-zone dilatancy recovery after the 2003 Bam earthquake in Iran, Nature, 458(7234), 64-68, doi:10.1038/nature07817.

Fielding, E. J., P. R. Lundgren, T. Taymaz, S. Yolsal-Cevikbilen, and S. E. Owen (2013), Fault-Slip Source Models for the 2011 M 7.1 Van Earthquake in Turkey from SAR Interferometry, Pixel Offset Tracking, GPS, and Seismic Waveform Analysis, Seismological Research Letters, 84(4), 579-593, doi:10.1785/0220120164.

Fournier, T., M. E. Pritchard, and N. Finnegan (2011), Accounting for Atmospheric Delays in InSAR Data in a Search for Long-Wavelength Deformation in South America, IEEE Transactions on Geoscience and Remote Sensing, 49(10), 3856-3867, doi:10.1109/TGRS.2011.2139217.

Fujiwara, T., S. Kodaira, T. No, Y. Kaiho, N. Takahashi, and Y. Kaneda (2011), The 2011 Tohoku-Oki Earthquake: Displacement Reaching the Trench Axis, Science, 334(6060), 1240-1240, doi:10.1126/science.1211554.

Funning, G. J., B. Parsons, and T. J. Wright (2007), Fault slip in the 1997 Manyi, Tibet earthquake from linear elastic modelling of InSAR displacements, Geophysical Journal International, 169(3), 988-1008, doi:10.1111/j.1365-246X.2006.03318.x.

Goldstein, R. M., and C. L. Werner (1998), Radar interferogram filtering for geophysical applications, Geophysical Research Letters, 25(21), 4035- 4038, doi:10.1029/1998GL900033.

Goldstein, R. M., H. A. Zebker, and C. L. Werner (1988), Satellite radar interferometry: Two-dimensional phase unwrapping, Radio Science, 23(4), 713-720, doi:10.1029/RS023i004p00713.

Gonzalez-Ortega, A., Y. Fialko, D. Sandwell, F. Alejandro Nava-Pichardo, J. Fletcher, J. Gonzalez-Garcia, B. Lipovsky, M. Floyd, and G. Funning (2014), El Mayor-Cucapah (Mw 7.2) earthquake: Early near-field postseismic deformation from InSAR and GPS observations: Journal of Geophysical Research: Solid Earth, 119(2), 1482-1497, doi:10.1002/2013JB010193.

Gourmelen, N., and F. Amelung (2005), Postseismic Mantle Relaxation in the Central Nevada Seismic Belt, Science, 310(5753), 1473-1476, doi:10.1126/science.1119798.

Grandjean, G., P. Paillou, N. Baghdadi, E. Heggy, T. August, and Y. Lasne (2006), Surface and subsurface structural mapping using low frequency radar: A synthesis of the

Mauritanian and Egyptian experiments, Journal of African Earth Sciences, 44(2), 220-228, doi:10.1016/j.jafrearsci.2005.10.015.

Gray, A. L., K. E. Mattar, and G. Sofko (2000), Influence of ionospheric electron density fluctuations on satellite radar interferometry, Geophysical Research Letters, 27(10), 1451-1454, doi:10.1029/2000GL000016.

Guneriussen, T., K. Hogda, H. Johnson, and I. Lauknes (2001), InSAR for estimating in snow water equivalent of dry snow, IEEE Geoscience and Remote Sensing Letters, 2101-2108.

Hanssen, R. (2001), Radar Interferometry: Data Interpretation and Error Analysis, Kluwer Academic Press, Dordrecht.

Hayes, G. P. (2010), Finite Fault Model: Updated Result of the Feb 27, 2010 Mw 8.8 Maule, Chile Earthquake, USGS: Earthquake Hazards Program.

Hayes, G. P., D. J. Wald, and R. L. Johnson (2012), Slab1.0: A three-dimensional model of global subduction zone geometries, Journal of Geophysical Research, 117(B1), doi:10.1029/2011JB008524.

Hayes, G. P., M. W. Herman, W. D. Barnhart, K. P. Furlong, S. Riquelme, H. M. Benz, E. Bergman, S. Barrientos, P. S. Earle, and S. Samsonov (2014), Continuing megathrust earthquake potential in Chile after the 2014 Iquique earthquake, Nature, 512(7514), 295-298, doi:10.1038/nature13677.

Ide, S., A. Baltay, and G. C. Beroza (2011), Shallow Dynamic Overshoot and Energetic Deep Rupture in the 2011 Mw 9.0 Tohoku-Oki Earthquake, Science, 332(6036), 1426-1429, doi:10.1126/science.1207020.

Ishitsuka, K., T. Tsuji, and T. Matsuoka (2012), Detection and mapping of soil liquefaction in the 2011 Tohoku earthquake using SAR interferometry, Earth, Planets and Space, 64(12), 1267-1276, doi:10.5047/eps.2012.11.002.

Jolivet, R., P. S. Agram, N. Y. Lin, M. Simons, M.-P. Doin, G. Peltzer, and Z. Li (2014), Improving InSAR geodesy using Global Atmospheric Models, Journal of Geophysical Research: Solid Earth, 119(3), 2324-2341, doi:10.1002/2013JB010588.

Kundu, B., D. Legrand, K. Gahalaut, V. K. Gahalaut, P. Mahesh, K. A. Kamesh Raju, J. K. Catherine, A. Ambikapthy, and R. K. Chadha (2012), The 2005 volcano-tectonic earthquake swarm in the Andaman Sea: Triggered by the 2004 great Sumatra-Andaman earthquake: Tectonics, 31(5), doi:10.1029/2012TC003138.

Lanari, R., P. Lundgren, M. Manzo, and F. Casu (2004), Satellite radar interferometry time series analysis of surface deformation for Los Angeles, California: Geophysical Research

Letters, 31(23), doi:10.1029/2004GL021294.

Lin, Y. N., M. Simons, E. A. Hetland, P. Muse, and C. DiCaprio (2010), A multiscale approach to estimating topographically correlated propagation delays in radar interferograms, Geochemistry Geophysics Geosystems, 11(9), doi:10.1029/2010GC003228.

Lohman, R. (2004), The inversion of geodetic data for earthquake parameters, Ph.D Thesis, California Institute of Technology.

Lohman, R. B., and J. J. McGuire (2007), Earthquake swarms driven by aseismic creep in the Salton Trough, California, Journal of Geophysical Research, 112(B4), doi:10.1029/2006JB004596.

Lohman, R. B., and M. Simons (2005), Some thoughts on the use of InSAR data to constrain models of surface deformation: Noise structure and data downsampling: Geochemistry, Geophysics, Geosystems, 6(1), doi:10.1029/2004GC000841.

Lohman, R. B., M. Simons, and B. Savage (2002), Location and mechanism of the Little Skull Mountain earthquake as constrained by satellite radar interferometry and seismic waveform modeling, Journal of Geophysical Research, 107(B6), doi:10.1029/2001JB000627.

Lorito, S., F. Romano, S. Atzori, X. Tong, A. Avallone, J. McCloskey, M. Cocco, E. Boschi, and A. Piatanesi (2011), Limited overlap between the seismic gap and coseismic slip of the great 2010 Chile earthquake, Nature Geoscience, 4(3), 173-177, doi:10.1038/ngeo1073.

Loveless, J. P., G. D. Hoke, R. W. Allmendinger, G. González, B. L. Isacks, and D. A. Carrizo (2005), Pervasive cracking of the northern Chilean Coastal Cordillera: New evidence for forearc extension, Geology, 33(12), 973, doi:10.1130/G22004.1.

Loveless, J. P., R. W. Allmendinger, M. E. Pritchard, J. L. Garroway, and G. González (2009), Surface cracks record long-term seismic segmentation of the Andean margin, Geology, 37(1), 23-26, doi:10.1130/G25170A.1.

Massonnet, D., and K. L. Feigl (1998), Radar interferometry and its application to changes in the Earth's surface, Reviews of Geophysics, 36(4), 441-500, doi:10.1029/ 97RG03139.

Massonnet, D., K. Feigl, M. Rossi, and F. Adragna (1994), Radar interferometric mapping of deformation in the year after the Landers earthquake, Nature, 369(6477), 227-230, doi:10.1038/369227a0.

Matsuda, T., Y. Ota, M. Ando, and N. Yonekura (1978), Fault mechanism and recurrence time of major earthquakes in southern Kanto district, Japan, as deduced from coastal terrace data, Geological Society of America Bulletin, 89(11), 1610, doi:10.1130/0016-7606(1978)89 $\leq$ 1610:FMARTO $\geq$ 2.0.CO;2.

Melbourne, T. I., F. H. Webb, J. M. Stock, and C. Reigber (2002), Rapid postseismic transients in subduction zones from continuous GPS, Journal of Geophysical Research: Solid Earth, 107(B10), ETG 10-1-ETG 10-10, doi:10.1029/2001JB000555.

Melkonian, A. K., M. J. Willis, and M. E. Pritchard (2014), Satellite-derived volume loss rates and glacier speeds for the Juneau Icefield, Alaska, Journal of Glaciology, 60(222), 743-760, doi:10.3189/2014JoG13J181.

Mesinger, F. et al. (2006), North American Regional Reanalysis, Bulletin of the American Meteorological Society, 87(3), 343-360, doi:10.1175/BAMS-87-3-343.

Métois, M., A. Socquet, and C. Vigny (2012), Interseismic coupling, segmentation and mechanical behavior of the central Chile subduction zone, Journal of Geophysical Research: Solid Earth, 117(B3), doi:10.1029/2011JB008736.

Métois, M., A. Socquet, C. Vigny, D. Carrizo, S. Peyrat, A. Delorme, E. Maureira, M.-C. Valderas-Bermejo, and I. Ortega (2013), Revisiting the North Chile seismic gap segmentation using GPS-derived interseismic coupling, Geophysical Journal International, 194(3), 1283-1294, doi:10.1093/gji/ggt183.

Nanayama, F., K. Satake, R. Furukawa, K. Shimokawa, B. F. Atwater, K. Shigeno, and S. Yamaki (2003), Unusually large earthquakes inferred from tsunami deposits along the Kuril trench, Nature, 424(6949), 660-663, doi:10.1038/nature01864.

Nolan, M., and D. R. Fatland (2003), Penetration depth as a DInSAR observable and proxy for soil moisture, IEEE Transactions on Geoscience and Remote Sensing, 41(3), 532-537, doi:10.1109/TGRS.2003.809931.

Njoku, E. G., and J.-A. Kong (1977), Theory for passive microwave remote sensing of near-surface soil moisture, Journal of Geophysical Research, 82(20), 3108-3118, doi:10.1029/JB082i020p03108.

Onn, F., and H. A. Zebker (2006), Correction for interferometric synthetic aperture radar atmospheric phase artifacts using time series of zenith wet delay observations from a GPS network, Journal of Geophysical Research, 111(B9), doi:10.1029/2005JB004012.

Oskin, M. E. et al. (2012), Near-Field Deformation from the El Mayor-Cucapah Earthquake Revealed by Differential LIDAR, Science, 335(6069), 702- 705, doi:10.1126/science.1213778.

Pi, X., A. Freeman, B. Chapman, P. Rosen, and Z. Li (2011), Imaging ionospheric inhomogeneities using spaceborne synthetic aperture radar: Journal of Geophysical Research: Space Physics, 116(A4), doi:10.1029/2010JA016267.

Plank, S. (2014), Rapid Damage Assessment by Means of Multi-Temporal SAR: A Comprehensive Review and Outlook to Sentinel-1, Remote Sensing, 6(6), 4870-4906, doi:10.3390/rs6064870.

Pollitz, F. F., C. Wicks, and W. Thatcher (2001), Mantle Flow Beneath a Continental Strike-Slip Fault: Postseismic Deformation After the 1999 Hector Mine Earthquake, Science, 293(5536), 1814-1818, doi:10.1126/science.1061361.

Prejean, S. G. (2004), Remotely Triggered Seismicity on the United States West Coast following the Mw 7.9 Denali Fault Earthquake, Bulletin of the Seismological Society of America, 94(6B), S348-S359, doi:10.1785/0120040610.

Pritchard, M. E., and M. Simons (2002), A satellite geodetic survey of large-scale deformation of volcanic centres in the central Andes, Nature, 418(6894), 167-171, doi:10.1038/nature00872.

Pritchard, M. E., C. Ji, and M. Simons (2006), Distribution of slip from 11 Mw$>$ 6 earthquakes in the northern Chile subduction zone, Journal of Geophysical Research, 111(B10), doi:10.1029/2005JB004013.

Pritchard, M. E., J. A. Jay, F. Aron, S. T. Henderson, and L. E. Lara (2013), Subsidence at southern Andes volcanoes induced by the 2010 Maule, Chile earthquake, Nature Geoscience, 6(8), 632-636, doi:10.1038/ngeo1855.

Prush, V., and R. Lohman (2014), Forest Canopy Heights in the Pacific Northwest Based on InSAR Phase Discontinuities across Short Spatial Scales, Remote Sensing, 6(4), 3210-3226, doi:10.3390/rs6043210.

Rech, J. A., J. Quade, and W. S. Hart (2003), Isotopic evidence for the source of Ca and S in soil gypsum, anhydrite and calcite in the Atacama Desert, Chile, Geochimica et Cosmochimica Acta, 67(4), 575-586, doi:10.1016/S0016-7037(02)01175-4.

Remy, D., M. Falvey, S. Bonvalot, M. Chlieh, G. Gabalda, J.-L. Froger, and D. Legrand (2011), Variability of atmospheric precipitable water in northern Chile: Impacts on interpretation of InSAR data for earthquake modeling, Journal of South American Earth Sciences, 31(2-3), 214-226, doi:10.1016/j.jsames.2011.01.003.

Rosen, P. A., S. Hensley, I. R. Joughin, F. K. Li, S. N. Madsen, E. Rodriguez, and R. M. Goldstein (2000), Synthetic aperture radar interferometry, Proceedings of the IEEE, 88(3), 333-382, doi:10.1109/5.838084.

Sambridge, M. (1999), Geophysical inversion with a neighbourhood algorithm-I. Searching a parameter space, Geophysical Journal International, 138(2), 479-494, doi:10.1046/j.1365-246X.1999.00876.x.

Schaber, G., J. McCauley, C. Breed, and G. Olhoeft (1986), Shuttle Imaging Radar: Physical Controls on Signal Penetration and Subsurface Scattenng in the Eastern Sahara, IEEE Transactions on Geoscience and Remote Sensing, GE-24(4), 603-623, doi: 10.1109/TGRS.1986.289677.

Scholz, C. H. (2014), The Rupture Mode of the Shallow Large-Slip Surge of the Tohoku-Oki Earthquake, Bulletin of the Seismological Society of America, 104(5), 2627-2631, doi: 10.1785/0120140130.

Schurr, B. et al. (2014), Gradual unlocking of plate boundary controlled initiation of the 2014 Iquique earthquake, Nature, 512(7514), 299-302, doi:10.1038/nature13681.

Scott, C., R. Lohman, M. Pritchard, P. Alvarado, and G. Sánchez (2014), Andean earthquakes triggered by the 2010 Maule, Chile (Mw 8.8) earthquake: Comparisons of geodetic, seismic and geologic constraints, Journal of South American Earth Sciences, 50, 27-39, doi:10.1016/j.jsames.2013.12.001.

Scott, C., and R. Lohman (2016), Sensitivity of earthquake source inversions to atmospheric noise and corrections of InSAR data: Atmospheric corrections of InSAR data, Journal of Geophysical Research: Solid Earth, doi:10.1002/2016JB012969.

Scott, C. P., R. W. Allmendinger, G. González, and J. P. Loveless (2016), Coseismic extension from surface cracks reopened by the 2014 Pisagua, northern Chile, earthquake sequence, Geology, G37662.1, doi:10.1130/G37662.1.

Sevilgen, V., R. S. Stein, and F. F. Pollitz (2012), Stress imparted by the great 2004 Sumatra earthquake shut down transforms and activated rifts up to 400 km away in the Andaman Sea, Proceedings of the National Academy of Sciences, 109(38), 15152-15156, doi:10.1073/pnas.1208799109.

Simons, M., Y. Fialko, and L. Rivera (2002), Coseismic Deformation from the 1999 Mw 7.1 Hector Mine, California, Earthquake as Inferred from InSAR and GPS Observations, Bulletin of the Seismological Society of America, 92(4), 1390-1402, doi:10.1785/0120000933.

Singleton, A., Z. Li, T. Hoey, and J.-P. Muller (2014), Evaluating sub-pixel offset techniques as an alternative to D-InSAR for monitoring episodic landslide movements in vegetated terrain, Remote Sensing of Environment, 147, 133-144, doi:10.1016/j.rse.2014.03.003.

Tong, X., D. T. Sandwell, and B. Smith-Konter (2013), High-resolution interseismic velocity data along the San Andreas Fault from GPS and InSAR, Journal of Geophysical Research: Solid Earth, 118(1), 369-389, doi:10.1029/2012JB009442.

Tymofyeyeva, E., and Y. Fialko (2015), Mitigation of atmospheric phase delays in InSAR data, with application to the eastern California shear zone, Journal of Geophysical Research:

Solid Earth, 120(8), 5952-5963, doi:10.1002/2015JB011886.

Uppala, S. M. et al. (2005), The ERA-40 re-analysis, Quarterly Journal of the Royal Meteorological Society, 131(612), 2961-3012, doi:10.1256/qj.04.176.

Vallage, A., Y. Klinger, R. Grandin, H. S. Bhat, and M. Pierrot-Deseilligny (2015), Inelastic surface deformation during the 2013 Mw 7.7 Balochistan, Pakistan, earthquake, Geology, G37290.1, doi:10.1130/G37290.1.

Watson, K. M., Y. Bock, and D. T. Sandwell (2002), Satellite interferometric observations of displacements associated with seasonal groundwater in the Los Angeles basin, Journal of Geophysical Research, 107(B4), doi:10.1029/2001JB000470.

Wegmuller, U., C. Werner, T. Strozzi, and A. Wiesmann (2006), Ionospheric Electron Concentration Effects on SAR and INSAR, pp. 3731-3734, IEEE.

Wei, M., and D. Sandwell (2010), Decorrelation of L-Band and C-Band Interferometry Over Vegetated Areas in California, IEEE Transactions on Geoscience and Remote Sensing, 48(7), 2942-2952, doi:10.1109/TGRS.2010.2043442.

Weston, J., A. M. G. Ferreira, and G. J. Funning (2011), Global compilation of interferometric synthetic aperture radar earthquake source models: 1. Comparisons with seismic catalogs, Journal of Geophysical Research, 116(B8), doi:10.1029/2010JB008131.

Weston, J., A. M. G. Ferreira, and G. J. Funning (2012), Systematic comparisons of earthquake source models determined using InSAR and seismic data, Tectonophysics, 532-535, 61-81, doi:10.1016/j.tecto.2012.02.001.

Wright, T. J., Z. Lu, and C. Wicks (2003), Source model for the M w 6.7, 23 October 2002, Nenana Mountain Earthquake (Alaska) from InSAR, Geophysical Research Letters, 30(18), doi:10.1029/2003GL018014.

Wright, T. J., B. Parsons, and Z. Lu (2004), Toward mapping surface deformation in three dimensions using InSAR, Geophysical Research Letters, 31(1), doi:10.1029/2003GL018827.

Yoon, Y. T., M. Eineder, N. Yague-Martinez, and O. Montenbruck (2009), TerraSAR-X Precise Trajectory Estimation and Quality Assessment, IEEE Transactions on Geoscience and Remote Sensing, 47(6), 1859-1868, doi:10.1109/TGRS.2008.2006983.

Zebker, H. A., and J. Villasenor (1992), Decorrelation in Interferometric Radar Echoes, IEEE Transactions on Geoscience and Remote Sensing, 30, 950-959.

Zebker, H. A., P. A. Rosen, and S. Hensley (1997), Atmospheric effects in interferometric synthetic aperture radar surface deformation and topographic maps, Journal of Geophysical

Research, 102(B4), 7547, doi:10.1029/96JB03804.

CHAPTER 2

SENSITIVITY OF EARTHQUAKE SOURCE INVERSIONS TO ATMOSPHERIC NOISE AND CORRECTIONS OF INSAR DATA

2.1 Abstract

Tropospheric phase delays pose a major challenge to InSAR (interferometric synthetic aperture radar)-based studies of tectonic deformation. One approach to the mitigation of effects from tropospheric noise is the application of elevation-dependent corrections based on empirical fits between elevation and interferometric phase. We quantify the effects of corrections with a range of complexity on inferred earthquake source parameters using synthetic interferograms with known atmospheric characteristics. We infer statistical properties of the stratified component of the atmosphere using pressure, temperature, and water vapor data from the North America Regional Reanalysis model over our region of interest in the Basin and Range province of the western United States. The statistics of the simulated atmospheric turbulence are estimated from InSAR and Global Positioning System data. We demonstrate potentially significant improvements in the precision of earthquake magnitude, depth, and dip estimates for several synthetic earthquake focal mechanisms following a correction for spatially variable atmospheric characteristics, relative to cases where the correction is based on a uniform delay versus elevation relationship or where no correction is applied. We apply our approach to the 1992 M_w5.6 Little Skull Mountain, Nevada, earthquake and demonstrate that the earthquake source parameter error bounds decrease in size after applying the atmospheric corrections. Our approach for evaluating the impact of atmospheric noise on inferred fault parameters is easily adaptable to other regions and source mechanisms.

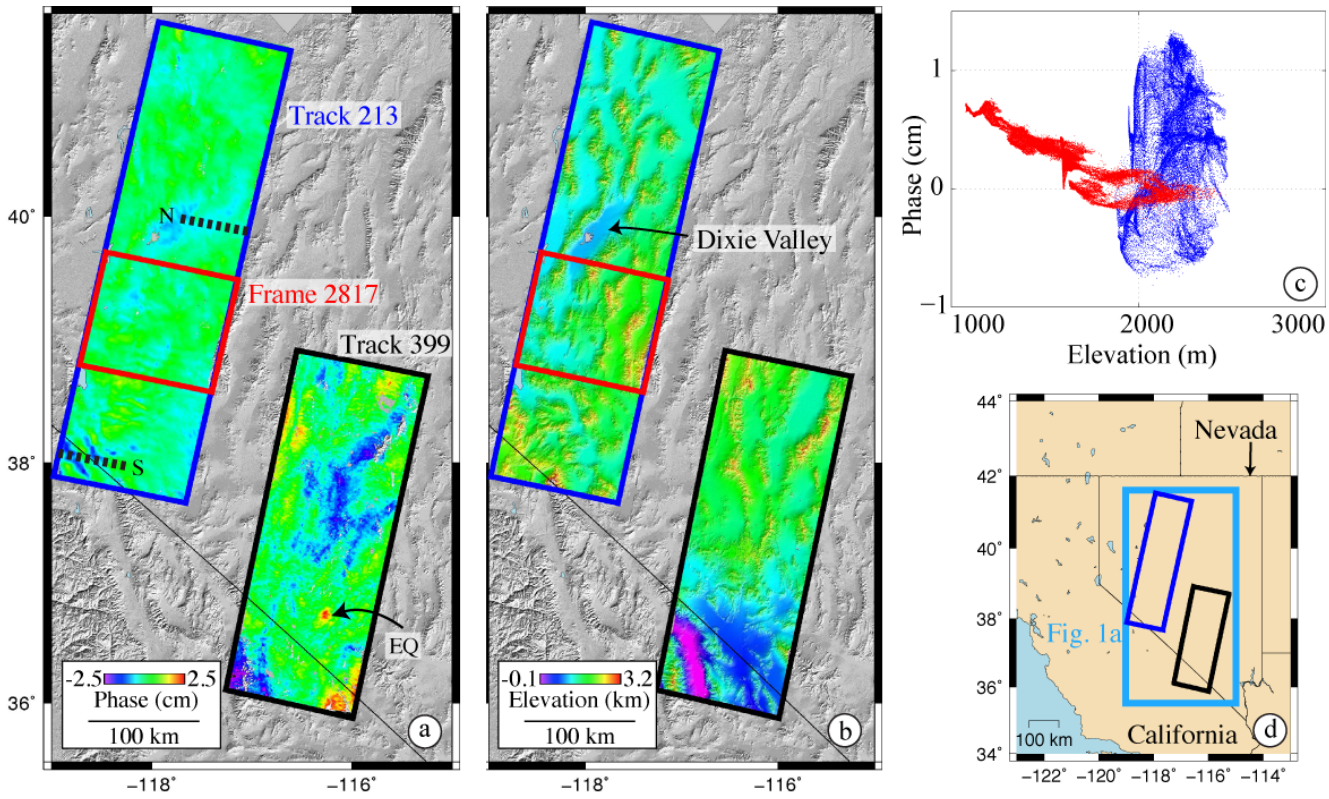

Figure 2.1: (a) Example ERS interferograms: The blue box outlines a tandem interferogram spanning 20-21 November 1995 (Track 213, Frames 2781-2835), and the black box highlights an interferogram that contains the 1992 M_w 5.6 Little Skull Mountain earthquake and spans 24 April 1992 to 18 June 1996 (Track 399, Frames 2835-2871). Note that the interferograms in Figure 2.1a span very different time lengths and seasons, which may account for some of the difference in magnitude of the atmospheric contribution. (b) The colored, shaded relief digital elevation model highlighting the location of Dixie Valley (Figure 2.1d). (c) Phase delay versus elevation across the two dashed transects in Track 213. Note the approximately linear relationship between elevation and phase across the northern transect (red), and the much less well-defined relationship in the south (blue). (d) Regional map showing interferogram locations. Location of profiles are shown in Figure 2.1d.

2.2 Introduction

Characterizing the surface response to earthquakes [e.g., Simons et al., 2002; Amelung and Bell, 2003], postseismic deformation [e.g., Pollitz et al., 2001; Gourmelen and Amelung, 2005], aseismic deformation [e.g., Lohman and McGuire, 2007; Wicks et al., 2011], withdrawal of subsurface fluids [e.g., Amelung et al., 1999; Bell et al., 2008; Argus et al., 2014; Borsa et al., 2014], and geothermal energy production [e.g., Fialko and Simons, 2000; Wicks et al., 2001] allows researchers to place constraints on physical properties of the subsurface that are critical to many broader geophysical studies [e.g., Becker et al., 2005; Meade and Hager, 2005; Holt and Shcherbenko, 2013]. The high spatial resolution and near-global coverage of interferometric synthetic aperture radar (InSAR) make it a powerful tool for characterizing subsurface processes [Massonnet et al., 1994; Bürgmann et al., 2000; Hanssen, 2001]. A significant obstacle is posed by signals introduced by the delay of the radar signal traveling through the atmosphere [e.g., Berrada Baby et al., 1988] and the ionosphere. Lateral and temporal variations in humidity, temperature, and pressure of the lower troposphere result in spatially correlated, centimeter-scale signals in InSAR data that are challenging to separate from those of real ground uplift and subsidence. The contribution from the stratified component of the atmosphere scales with elevation, as radar paths between the satellite and low-elevation regions result in interaction with a thicker layer of atmosphere than do paths to high-elevation regions [Bürgmann et al., 2000]. When tectonic strain is spatially correlated with topography, as is commonly the case along subduction zones [e.g., Lin et al., 2010; Fournier et al., 2011; Béjar-Pizarro et al., 2013], basin-bounding faults and volcanic edifices [e.g., Wicks et al., 2002] distinguishing between signals from ground deformation and atmospheric noise are of critical importance.

Research aimed at mitigating the impact of atmospheric noise in InSAR data sets includes

efforts to characterize the statistics of the atmospheric noise [Hanssen, 2001; Emardson, 2003; Lohman and Simons, 2005; Parker et al., 2015], average multiple interferograms together [e.g., Zebker et al., 1997], and correct the atmospheric signal with empirical functions derived from the data itself [e.g., Cavalié et al., 2007; Elliott et al., 2008; Tymofyeyeva and Fialko, 2015] or independent data from other satellites and weather models[e.g., Li et al., 2003; Onn and Zebker, 2006; Doin et al., 2009]. However, the spatial complexity and temporal variability of the atmosphere limit these approaches [e.g., Bekaert et al., 2015b] to some degree, so that inferences from InSAR data still require careful assessment of the remaining noise from the troposphere.

In this study, we isolate the impact of empirical atmospheric corrections on earthquake source parameter inversions through the use of synthetic and real InSAR scenarios. The uncertainty and bias in the retrieved earthquake source parameters indicate the error resulting from atmospheric noise and the relative improvement from empirical atmospheric corrections. We generate synthetic data that include a coseismic deformation signal and realistic atmospheric phase delays. The elevation-dependent atmospheric contribution (i.e., the stratified component) is based on pressure, temperature, and water vapor data from the North America Regional Reanalysis (NARR) Model [Mesinger et al., 2006], and the turbulent characteristics are consistent with our own InSAR data analysis for this region and Global Position System (GPS) observations [e.g., Emardson, 2003]. Our use of synthetic data means that the statistics of the atmospheric noise are known, and the inferred earthquake source parameters are free from errors in the physical source model and other subsurface contributions to the actual ground deformation. We apply our approach to the area of ERS/Envisat Track 213 within the Basin and Range province of the western United States (Figure 2.1). We select the Dixie Valley in central Nevada for our work with synthetic data, because the correlation between the high relief topography and tectonic deformation

creates ideal scenarios to assess the sensitivity of the inferred earthquake parameters to atmospheric noise. Further, this region has experienced large earthquakes along basin-bounding faults in the past, such as the 1954 Dixie Valley earthquake [Slemmons, 1957; Doser, 1986; Bell and Katzer, 1990; Caskey et al., 1996; Hodgkinson et al.,1996; Abbott et al., 2001]. We examine scenarios including shallow and moderate depth crustal earthquakes with a range of source orientations and assess the constraints on earthquake source parameters using three types of atmospheric corrections. We also apply our approach to the 1992 M5.6 Little Skull Mountain earthquake [Walter, 1993; Harmsen, 1994; Meremonte et al., 1995; Smith et al., 2001; Lohman et al., 2002] in southern Nevada and demonstrate the dependence of the fault parameters error bounds on atmospheric noise.

2.3 Atmospheric noise corrections

Several families of approaches have been developed to mitigate the impact of atmospheric noise in InSAR data. Because the turbulent component of the atmospheric contribution is not correlated at temporal scales greater than one day [e.g., Emardson, 2003] averaging many interferograms reduces the impact of atmospheric noise [Zebker et al., 1997]. However, atmospheric signals still persist at some level and result in uncertainty in the inferred deformation rates and earthquake source parameters [e.g., Scott et al., 2014], particularly when the seasonal variations in the atmospheric contribution (Figure 2.2) are unevenly sampled [e.g., Barnhart and Lohman, 2013].

A second approach involves the removal of a best-fit, empirical function between elevation and phase from the interferogram [e.g., Cavalié et al., 2007; Elliott et al., 2008]. For this empirical technique to be effective, the elevation-phase relationship must be relatively

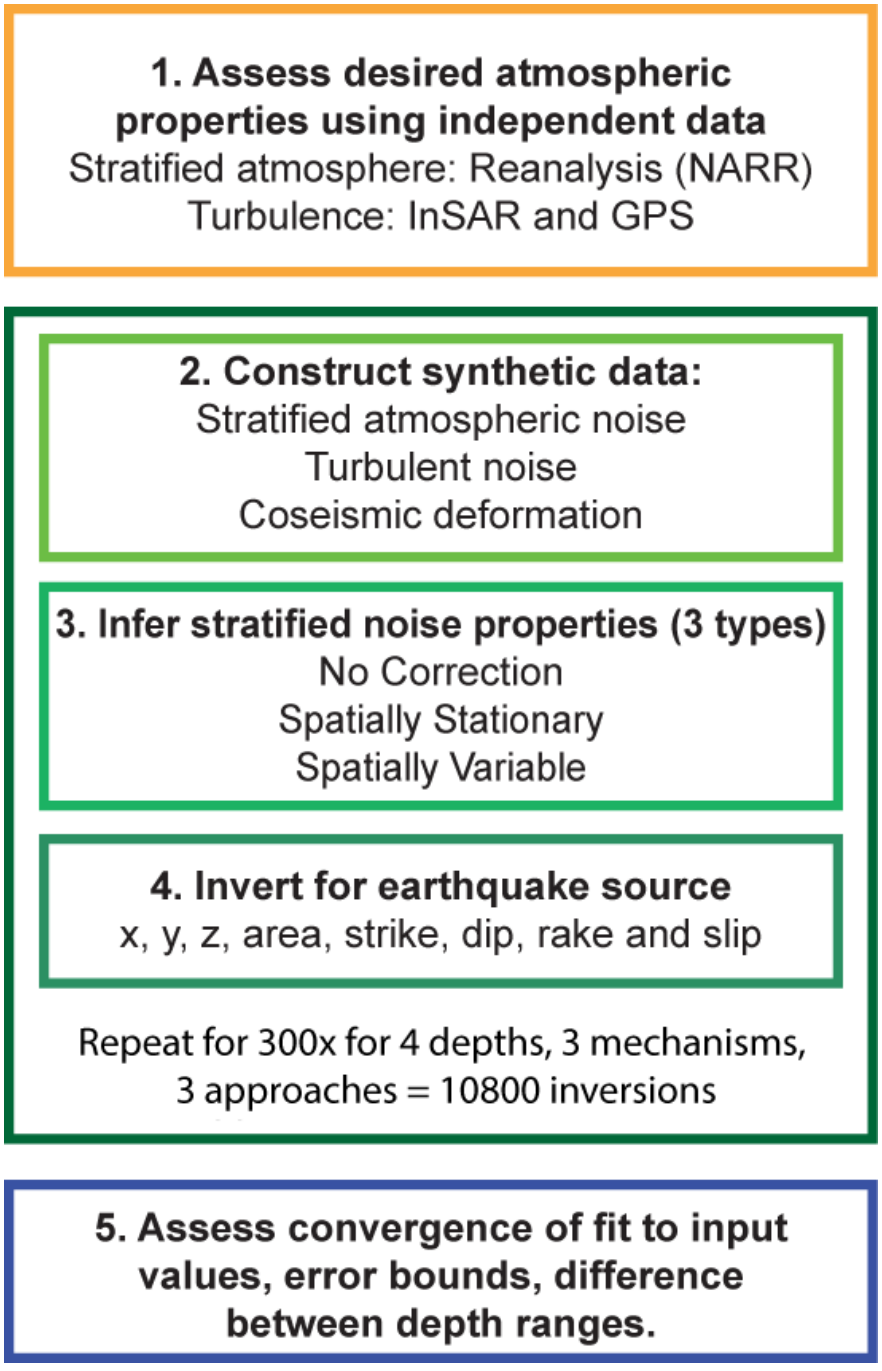

Figure 2.2: Workflow applied to synthetic data developed in this study.

constant over the entire interferogram; i.e., its statistical properties must be spatially stationary. Documented spatial variability in atmospheric characteristics (e.g., Figure 2.1) includes examples where large-scale topography acts as a meteorological barrier near the Caspian Sea [Walters et al., 2013], between the Andean fore arc and volcanic arc [Lin et al., 2010; Fournier et al., 2011], and across smaller-scale features such as single ridges the Mojave Desert, California [Barnhart and Lohman, 2013]. Béjar-Pizarro et al. [2013] and Bekaert et al. [2015a] account for complexity in the atmospheric contribution by removing a spatially variable empirical function between elevation and phase in northern Chile and Acapulco, Mexico, respectively.

In a third set of approaches, researchers use independent observations to characterize and/or remove the atmospheric contribution to interferograms. Global atmospheric models (GAMs) can be used to calculate elevation-dependent and spatially variable atmospheric contributions [e.g., Doin et al., 2009]. This method is effective at correcting atmospheric signals at larger spatial scales and estimating seasonally variable effects [e.g., Doin et al., 2009; Jolivet et al., 2011, 2014]. The relatively coarse spatial (32-100 km) and temporal sampling rate (3-6 h) of GAMs limit their success in the presence of significant turbulence [e.g., Jolivet et al., 2014] and complex weather systems [Doin et al., 2009; Walters et al., 2013] that can vary rapidly over time scales of a few minutes to hours [Onn and Zebker, 2006]. Wet delay estimates recovered from GPS measurements can be effective at mitigating the atmospheric contribution when GPS networks are dense [e.g., Li et al., 2003, 2006; Onn and Zebker, 2006]. Multispectral data from the Moderate Resolution Imaging Spectroradiometer and Medium-Resolution Imaging Spectrometer instruments can provide corrections for daytime synthetic aperture radar (SAR) acquisitions in cloud-free areas [e.g., Li et al., 2003, 2005, 2006, 2009; Liu et al., 2011].

All of the approaches mentioned above have been shown to reduce the level of noise in

individual or sets of interferograms in cases where no ground deformation signal was expected and clearly can be an improvement over cases where no correction is used. However, all suffer from some limitations due to differing temporal and spatial sampling or due to the difference in observation type. Assessment of the efficacy of any particular correction approach, and the identification of any biases that may be introduced (i.e., an elevation-dependent correction will necessarily remove some parts of an actual elevation-dependent ground deformation signal) is critical if we are to place robust constraints on subsurface source models.

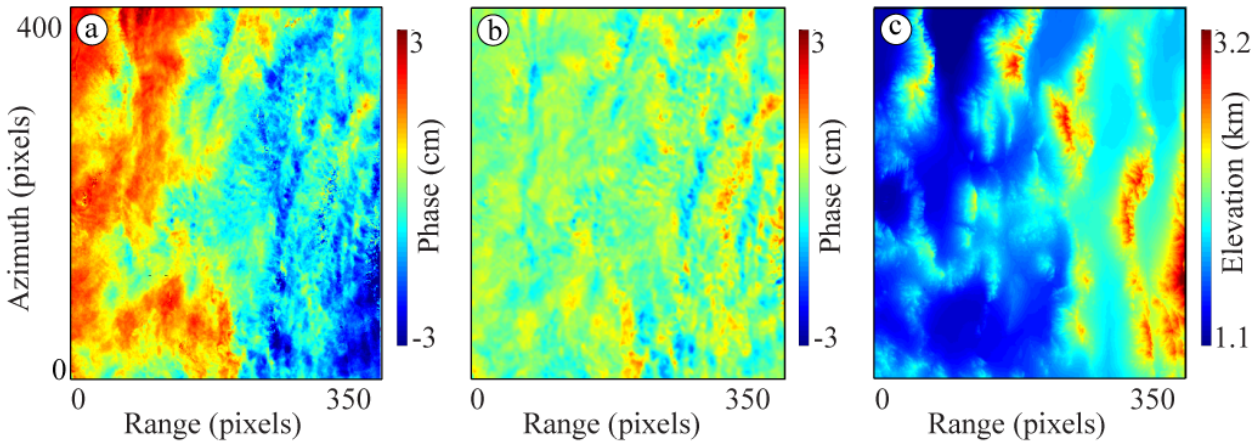

Figure 2.3: Atmospheric turbulence: (a) Envisat interferogram(11 May 2010 to 15 June 2010), covering Track 213, Frame 2817 in Figure 2.1a. (b) Atmospheric turbulence in Figure 2.3 associated by removing a bilinear ramp and a linear fit between elevation and phase, and applying a Gaussian band-pass filter to retain signals between wavelengths of 1-20 km. (c) Digital elevation model.

2.4 Methods

In this section, we describe our workflow for assessing the error introduced by atmospheric noise in earthquake source inversions and improvements resulting from empirical corrections of the noise source (Figure 2.2). We generate realistic atmospheric noise based on statistics retrieved from a weather model, InSAR, and GPS data. The entire synthetic data set used in our analysis includes three components: topographically correlated noise from the stratified component of the atmosphere, atmospheric turbulence, and coseismic deformation. We invert for the topographically correlated noise contribution twice in each case: either assuming that the elevation dependence of the tropospheric delay is spatially constant or variable within an individual interferogram. We solve for the earthquake source parameters from the corrected interferograms to quantify the improvement, remaining uncertainty, and bias in earthquake source parameters following the atmospheric corrections. Finally, we place error bounds on the 1992 M5.6 Little Skull Mountain earthquake source parameters using the approach outlined above.

2.4.1 Synthetic noise: Stratified component of the atmosphere

To generate noise from the stratified component of the atmosphere, we require constraints on the real spatial variability of the atmosphere. The North America Regional Reanalysis (NARR) [Mesinger et al., 2006] model provides estimates of temperature, water vapor partial pressure, and geopotential height at 29 pressure levels at a 32 km grid spacing every 3 h. This coarse spatial sampling is not likely to capture characteristics of the atmospheric turbulence but can provide constraints on the magnitude and variability of the elevation-dependent contribution. We use the Python based Atmospheric Phase Screen Estimation

software package [Jolivet et al., 2011] to extract the accumulated wet and hydrostatic delay at 10 elevations (0 to 4500m in 500m increments) at 18:00 UTC to closely match the timing of the SAR acquisitions, at all days during 2007. We generate a NARR-based covariance matrix on a three-dimensional grid at these elevations and with a 20 km spacing in map view (i.e., slightly denser than the original NARR spacing), by examining the differential, NARR-predicted delay between 182 randomly generated, independent date pairs. We generate the stratified portion of the noise in our synthetic data with realizations of this covariance structure, interpolated onto a grid spacing of 80m (the approximate spacing of the ERS/Envisat data when spatially averaged 4 times in range and 20 times in azimuth) at the known elevation at each pixel (Shuttle Radar Topography Mission [Farr et al., 2007]). Note that we do not impose a specific analytical form to the vertical stratification of the atmosphere (e.g., equation (1)) but are drawing from the real statistical correlations present within the NARR model.

2.4.2 Synthetic noise: Turbulent component of the atmosphere

The spatially correlated atmospheric turbulence [Emardson, 2003; Lohman and Simons, 2005] will also affect the inferred earthquake source parameters. Depending on the magnitude, scale, and topographic relief within a particular interferogram, the effects of turbulence could be much larger or smaller than those that arise from the stratified atmosphere. Previous results from both InSAR and GPS-based studies showed that the turbulent portion of the atmospheric contribution to interferograms often has length scales of $\sim$20 km [e.g., Lohman and Simons, 2005]. We examine Envisat interferograms using 17 acquisitions from Track 213 (Figure 2.3) to quantify the magnitude of the atmospheric turbulence. We isolate the turbulent noise from contributions from the stratified atmosphere and errors in satellite position

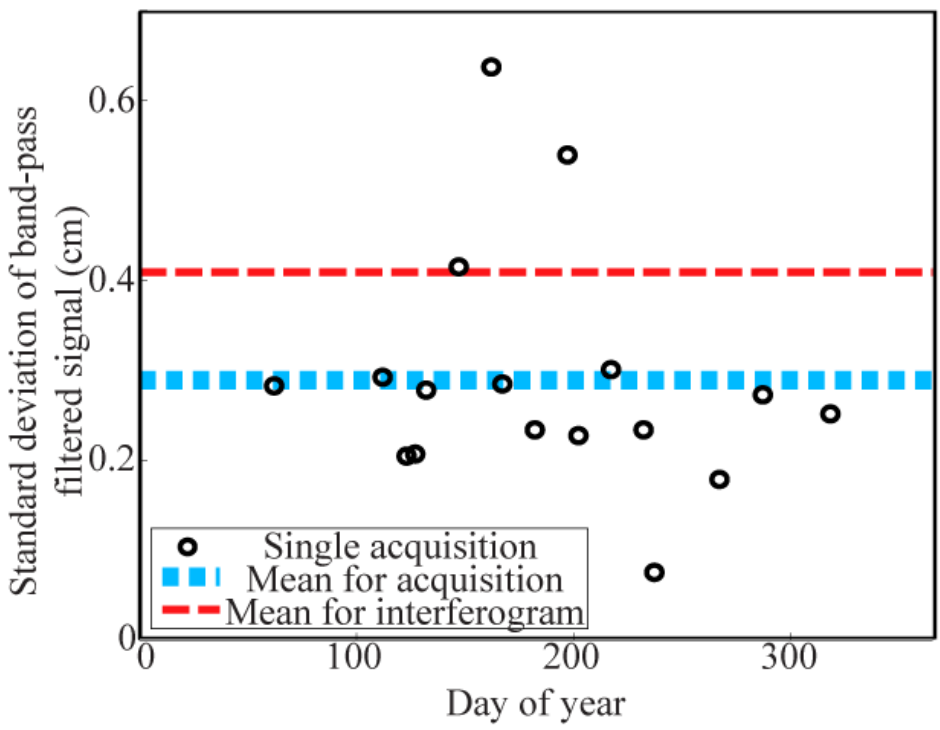

Figure 2.4: The amplitude of the atmospheric turbulence estimated for 17 individual acquisitions from 22 interferograms covering Frame 2817 highlighted in Figure 2.1d. This analysis suggests that 0.4 cm is appropriate for the amplitude of the simulated turbulence. Note the higher amplitude of turbulence in the summer relative to the winter.

[e.g., Massonnet and Feigl, 1998; Fattahi and Amelung, 2014] by subtracting the best-fit bilinear ramp and linear topography-phase function and applying a Gaussian band-pass filter to retain signals at wavelengths of 1-20 km. The spatially averaged variance present in single acquisitions (Figure 2.4, black circles) can be inferred from the set of interferograms, since the spatially averaged variance of a single interferogram should be equal to the sum of the variances of the individual dates that contribute to it. As shown in Figures 2.4 and A.1, 0.4 cm is appropriate for the amplitude of the atmospheric turbulence in our simulations. This result is robust to our choice of a 20 km Gaussian band-pass filter (Figure A.1). Not surprisingly, there is a pronounced seasonality with more turbulence present in the summer than the winter. We do not capture the seasonality of the turbulence in the simulations,

but it could easily be assessed for any particular set of existing SAR acquisition dates [e.g., Barnhart and Lohman, 2013]. Constructing many sets of spatially correlated noise over the entire interferogram at 80m resolution would be very computationally expensive. However, it is standard in earthquake source inversions to preweight the data and the associated design matrix (kernel, or Green's function) by the inverse of the Cholesky factorization of the data covariance matrix [e.g., Harris and Segall, 1987]. If the covariance of atmospheric turbulence is estimated correctly, the effect of the spatially correlated turbulence can be added to the preweighted stratified noise and coseismic signal as white noise with unit variance. Tests on small subsets of the interferogram demonstrated that as expected, this simplification has no effect on the outcome.

2.4.3 Earthquake source

We use a single square dislocation in an elastic half-space [Okada, 1985] to generate synthetic coseismic deformation. We require that the fault plane dimensions and slip be consistent with a M_w 5.7 event and a stress drop of 100 bars [e.g., Stein and Wysession, 2003]. We set the strike to be aligned with the trend of the Stillwater mountain range. Focal mechanisms include 30^o and 60^o dipping normal faults, and a vertical strike-slip fault. We used a range of centroid depths (4 km, 6 km, 8 km, and 10 km) to simulate surface deformation with variable magnitudes and spatial scales. For each case, we choose the earthquake epicenter such that the surface trace of the fault would intersect the same location along the range foothills.

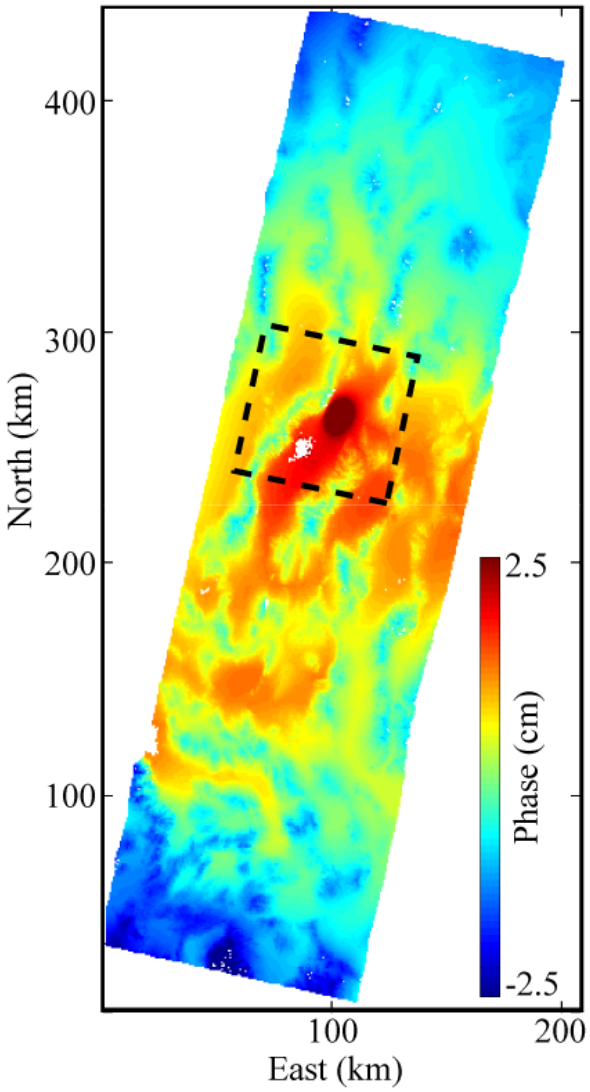

Figure 2.5: (a) An example of a synthetic interferogram containing the topographically correlated component of the atmospheric noise and the coseismic signal. No atmospheric turbulence has been added at this stage. The dashed black box indicates the region masked out during the inversion for the topographically correlated atmospheric noise and the approximate area shown in Figure 2.7. The white regions within the interferogram indicate areas with no data in the digital elevation model. The color scale is chosen to emphasize atmospheric properties- full range is from 2.5 to 10 cm.

2.5 Atmospheric Correction

2.5.1 Phase - elevation relationships

The delay accumulated within the troposphere is often modeled as a non-linear function between elevation and phase [Elliott et al., 2008; Doin et al., 2009; Bekaert et al., 2015a]. For example, Bekaert et al. [2015a] use weather balloon data over Acapulco, Mexico and express the relationship between delay in an interferogram (ϕ) and elevation (h) as:

$$\Delta\phi_i = K'_{\Delta\phi}(h_0 - h_i)^\alpha \tag{2.1}$$

where $\Delta\phi_i$ is the phase delay at the ith pixel, $K'_{\Delta\phi}$ relates the local topographic relief to phase, h_0 is the altitude above which the atmospheric properties are essentially constant in time, h_i is the elevation at the ith pixel, and α is the power law coefficient. We use Eq. 2.1 with $\alpha = 1.4$ and $h_0 = 8$ km from Bekaert et al. [2015a] to correct the atmospheric contribution as described in the following sections.

2.5.2 Inversion assuming spatially constant atmospheric delay

For each set of synthetic data (which contain the stratified and turbulent components of the atmosphere, and the earthquake), we mask out the area containing the earthquake to avoid contaminating the inferred atmospheric signal (dashed box, Figure 2.5). For the case where we assume homogenous atmospheric contribution vs. elevation (using the power-law elevation-phase relationship in Eq. 2.1) over the full interferogram, we simultaneously solve for the atmospheric contribution and a bilinear ramp:

$$\phi_i = K'_{\Delta\phi}(h_0 - h_i)^\alpha + r_1 + r_2 x_i + r_3 y_i + r_4 x_i y_i, \tag{2.2}$$

where $K'_{\Delta\phi}$ and hi are as defined in Eq. 1, r_i are the ramp parameters, and x_i and x_i are the coordinates of the ith point. This approach is similar to what would be performed by most researchers solving for a single elevation vs. phase relationship. We consider the inverse problem,

$$\mathbf{G}m = d \tag{2.3}$$

where $\mathbf{G}$ is a matrix of Green's functions relating the matrix of model parameters, $m = [K'_{\Delta\phi}(h_0 - h_i)^\alpha \quad r_1 \quad r_2 \quad r_3 \quad r_4]^T$ to the n InSAR observations (or synthetic data), $\phi = [\phi_1 \quad \phi_2 \quad \phi_3]^T$, as:

$$\mathbf{G} = \begin{bmatrix} \Delta h_1 & 1 & x_1 & y_1 & x_1 y_1 \\ \Delta h_2 & 1 & x_2 & y_2 & x_2 y_2 \\ \vdots & \vdots & \vdots & \vdots & \vdots \\ \Delta h_n & 1 & x_n & y_n & x_n y_n \end{bmatrix} \tag{2.4}$$

where,

$$\Delta h_i = (h_0 - h_i)^\alpha. \tag{2.5}$$

This scenario is a simple correction of the topographically correlated atmospheric noise and ramp contribution, averaged over the entire interferogram.

2.5.3 Inversion for spatially variable atmospheric delay

The inversion for spatially variable atmospheric contribution, while a much more computationally intensive problem than the spatially homogenous case, may better capture the documented variability in atmospheric contributions. Below, we outline the steps we use to estimate the spatially variable atmospheric contribution.

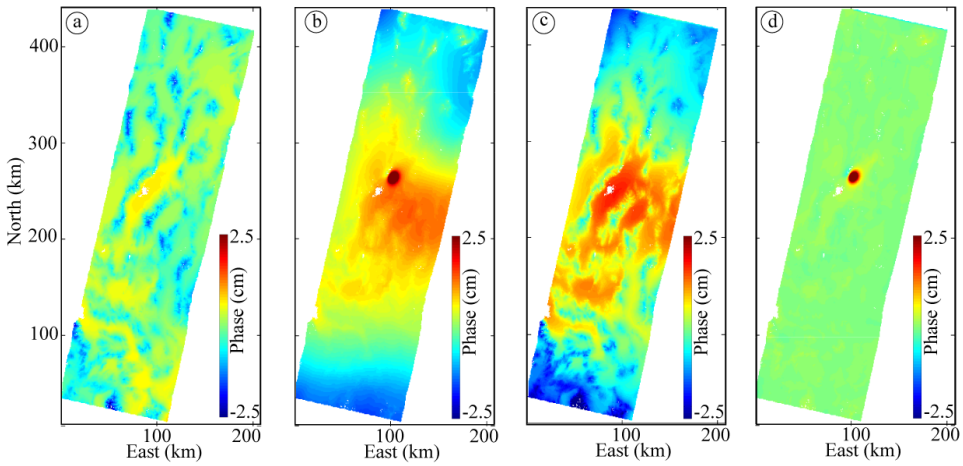

Figure 2.6: (a and c) Corrections and (b and d) residuals associated with the synthetic interferogram shown in Figure 2.5, for the approach associated with constant (a and b) and variable (c and d) atmospheric properties. Color scale as in Figure 2.5.

We invert for the values of $K'_{\Delta\phi}$ at a coarser spacing than the full dataset, which imposes some spatial smoothness on the solution and improves computational efficiency without any appreciable change to the solution (i.e., the coarseness of the inversion spacing trades off with the required amount of Tikhonov regularization). The preferred model minimizes the norm [Menke, 1989; Aster et al., 2013],

$$||\mathbf{G}m - d||_2^2 + \xi^2||\mathbf{L}m||_2^2, \tag{2.6}$$

where $m = [K'_{\Delta\phi 1} \quad K'_{\Delta\phi 2} \quad ... \quad K'_{\Delta\phi j} \quad r_1 \quad r_2 \quad r_3 \quad r_4]^T$, j is the number of locations where we infer the atmospheric delay, L is the Laplacian operator, and ξ is a weighting parameter. G is a sparse n x $(j+4)$ matrix that relates the full set of observations (n) to the smaller number (j) of atmospheric model points through a bilinear interpolation:

$$\mathbf{G} = \begin{bmatrix} W_{11}\Delta h_1 & W_{12}\Delta h_1 & \dots & W_{1j}\Delta h_1 & x_1 & y_1 & x_1y_1 \\ W_{21}\Delta h_2 & W_{22}\Delta h_2 & \dots & W_{2j}\Delta h_2 & x_2 & y_2 & x_2y_2 \\ \vdots & \vdots & \vdots & \vdots & \vdots & \vdots & \vdots \\ W_{n1}\Delta h_n & W_{n2}\Delta h_n & \dots & W_{nj}\Delta h_n & x_n & y_n & x_ny_n \end{bmatrix}, \tag{2.7}$$

The weights W_{ij} are zero except for those corresponding to the four surrounding model points. We optimize ξ using the ${}_jR_i$ method [Lohman, 2004; Lohman and Simons, 2005; Barnhart and Lohman, 2010]. This technique is used to select the weighting parameters by finding a compromise between the regularization error from over-smoothing the signal from the stratified component of the tropospheric noise contribution and perturbation error due to mapping turbulence into the topographic contribution. Better estimates of the spatial statistics of the turbulence improve the selection of the weighting parameter.

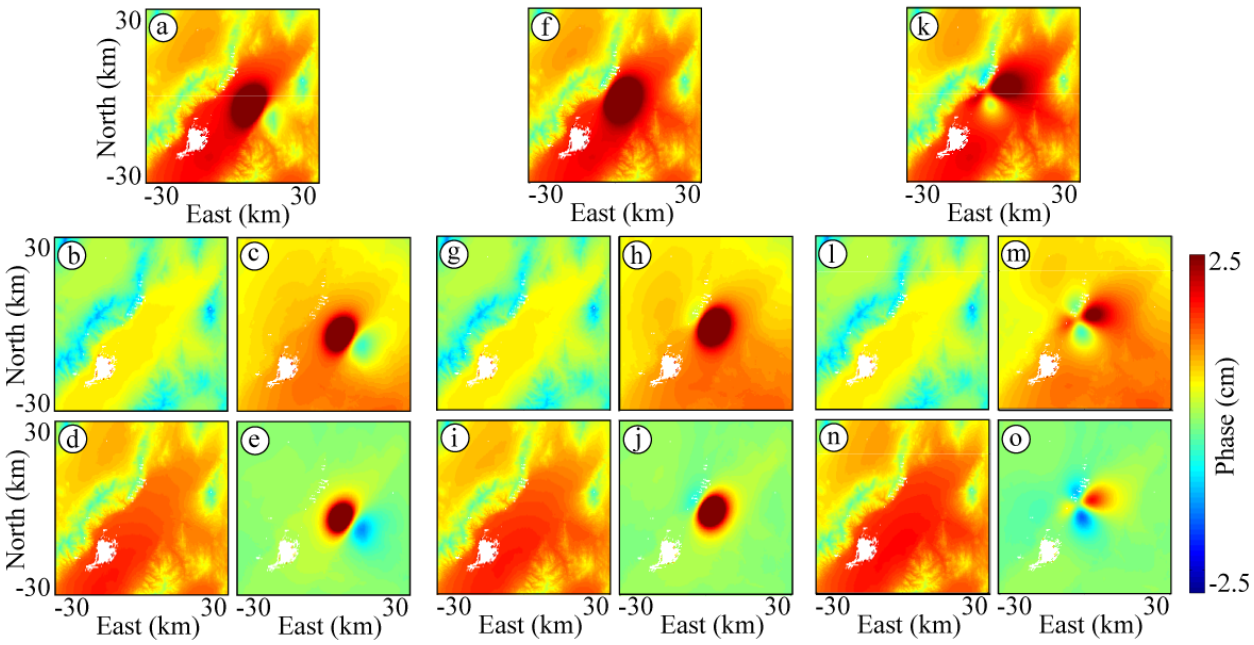

Figure 2.7: Atmospheric correction of a synthetic interferogram. The first row shows the synthetic interferogram containing topographically correlated atmospheric noise and a co-seismic signal from an earthquake along (a) a normal fault with a 30^o dip, (f) a normal fault with a 60^o dip, and (k) a vertical strike-slip fault, all at a 6 km depth. The second row shows (b, g, and l) the constant atmospheric correction and (d, h, and m) the residual, which is used as input into the earthquake inversion. The third row shows the correction for (d, i, and n) the spatially variable atmospheric properties and (e, j, and o) the residual. Color scale as in Figure 2.5.

2.5.4 Invert for earthquake source

We first downsample or average the several millions of data points in the interferogram to several hundreds of points to make the earthquake source parameter inversion computationally less expensive. We use the fault resolution-based algorithm developed by [Lohman and Simons, 2005], with a modification to allow for the use of triangular mesh [McGuire et al., 2015] that substantially decreases the computational cost of the inversion (Figure A.2). We add atmospheric turbulence with the statistical properties described in Section 3.2. We weight the Green's functions and the data (which now include any residual noise from the stratified atmosphere, the turbulent noise, and the coseismic signal) based on the known statistical properties of the turbulence. We search for the best-fit fault geometry (fault dimensions, depth, strike, dip and rake) using the Neighborhood algorithm [Sambridge, 1999] after applying the three types of corrections described above. We perform the inversion 300 times with independent sets of atmospheric noise, and illustrate the convergence of the earthquake source parameters in Figure A.3.

2.5.5 Little Skull Mountain earthquake

We estimate source parameters and error bounds associated with the 1992 M5.6 Little Skull Mountain earthquake [e.g., Lohman et al., 2002] by applying many of the above steps as described in the remainder of this paragraph. We estimate that the amplitude of the atmospheric turbulence present in the coseismic interferogram (Figure 2.1a) to be 0.35 cm after masking out the region surrounding the earthquake and applying the methods described in Section 3.2. We apply the spatially constant and variable atmospheric corrections to the real InSAR data and invert for the earthquake source parameters from the uncorrected

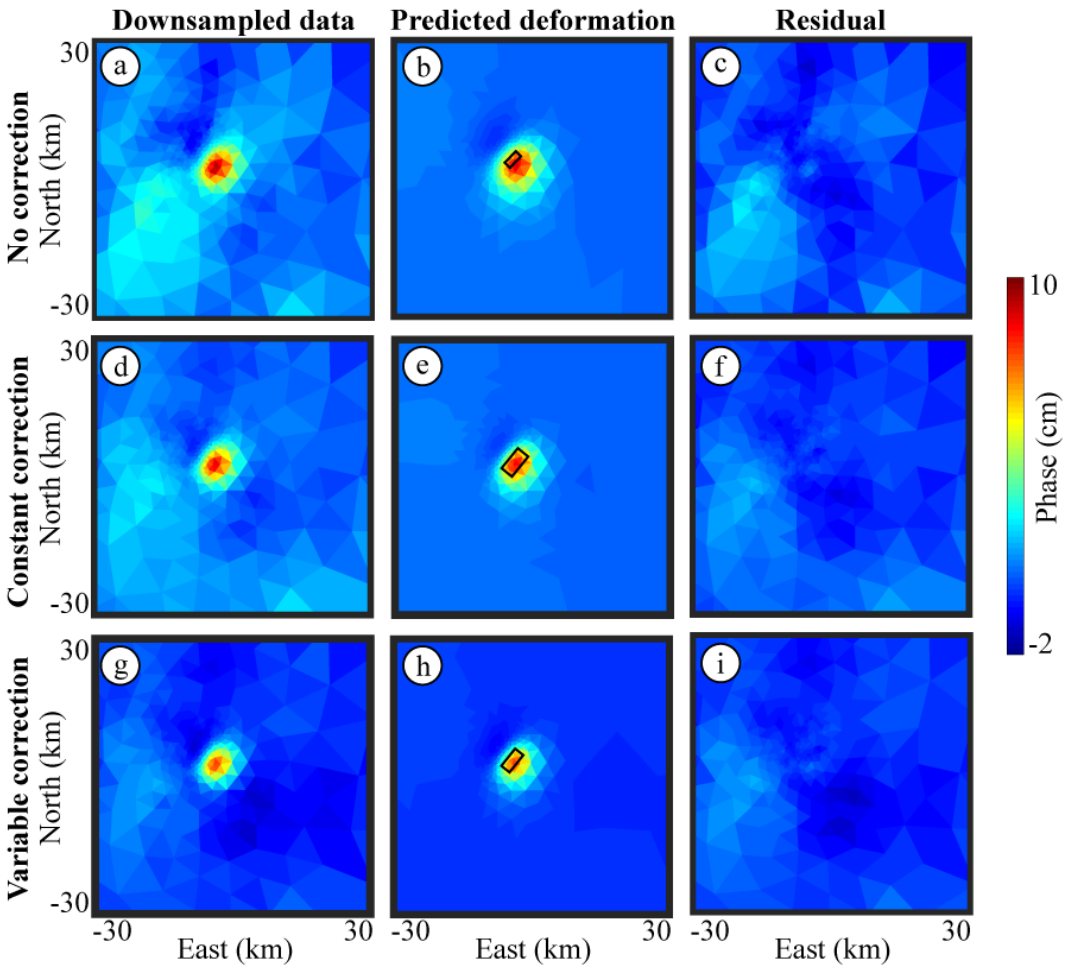

Figure 2.8: Results of the earthquake source inversion of synthetic data after applying the three atmospheric correction approaches. The first column shows the downsampled data with a coseismic signal produced by 60^o dipping normal fault and the same realization of atmospheric turbulence for each row applying (a) no atmospheric correction, (d) a correction for constant atmospheric properties, (g) and a correction for variable atmospheric properties. The second column shows the predicted surface deformation of the best-fit fault model inferred from the first column. The third column shows the residual signal.

and both of the corrected interferograms. We place error bounds on each of the three sets of retrieved fault parameters by inverting for the earthquake source parameters from 300 synthetic datasets that contain the signal from the optimized focal mechanism and atmospheric noise as outlined Sections 3.1-3.4.

2.6 Results

2.6.1 Synthetic data

As expected, the correction accounting for constant atmospheric properties (Figure 2.6a) predicts an atmospheric contribution that is smaller in magnitude than the input atmospheric signal and results in a long wavelength, several centimeter amplitude residual in the corrected interferogram (Figure 2.6b). The correction for spatially heterogeneous atmospheric properties removes the majority of the atmospheric signal (Figure 2.6c), leaving a residual signal that is less than 5 mm in amplitude (Figure 2.6d). Across the topographic relief surrounding the Dixie Valley, the spatially constant and variable corrections leave a $\sim$1 cm and $\sim$0.2 cm residual, respectively, in the particular example shown in Figure 2.7.

To characterize the impact of the atmospheric noise on the inferred earthquake source parameters, we explore multiple source mechanisms that produce surface deformation fields with different relationships to topography (Figures 2.8 and 2.9). The uncertainty in the earthquake magnitude and depth for the 30^o dipping fault decreases after applying either of the two atmospheric corrections. Correcting for the spatially variable atmospheric noise in interferograms associated with the two steeper fault geometries results in a significant decrease in the uncertainty and bias of the earthquake magnitude, depth, and dip constraints,

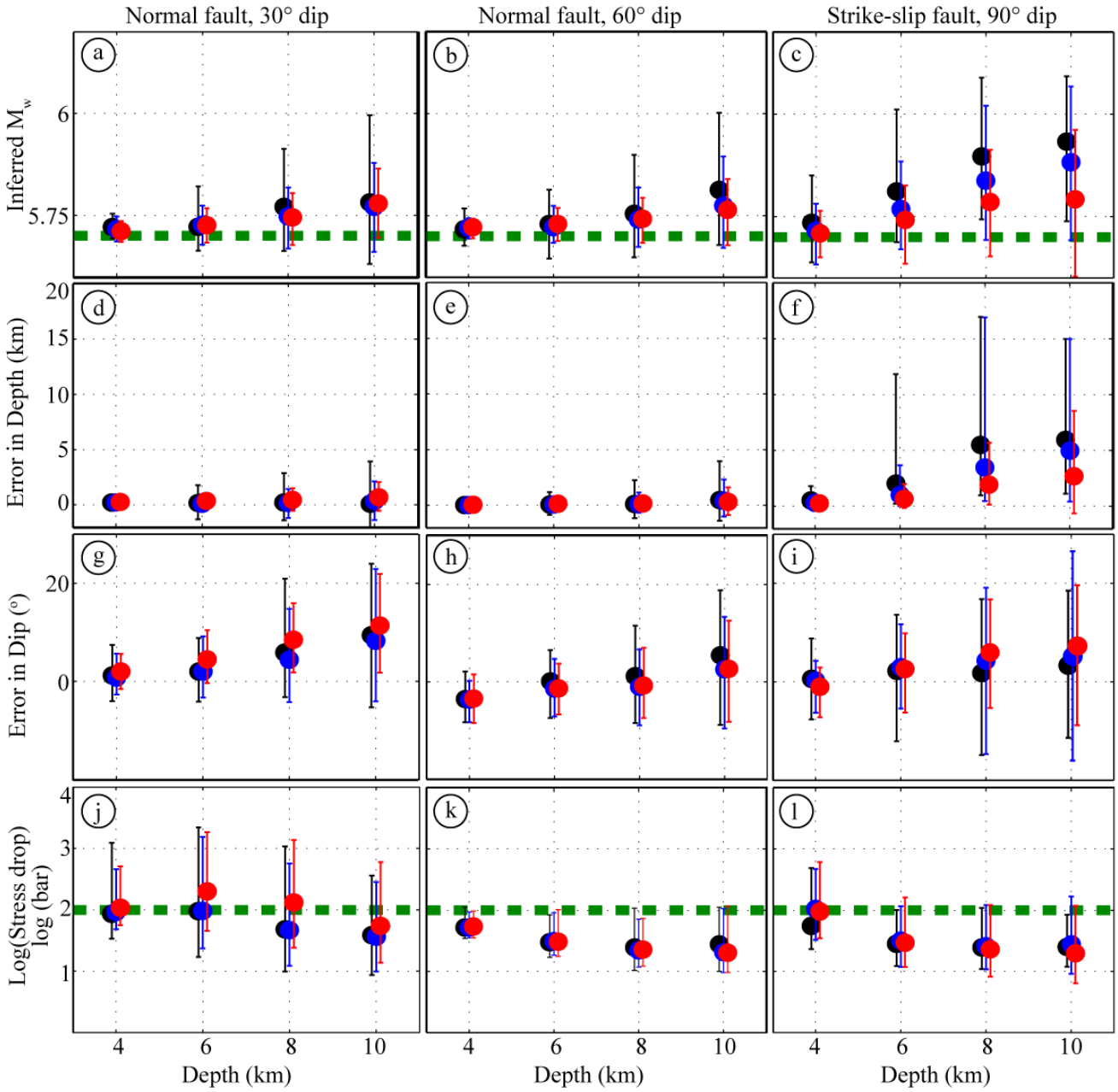

Figure 2.9: Results of 300 earthquake simulations for each correction approach, fault geometry, and depth. Constraints on earthquake magnitude, depth, dip, and stress drop for a 30^o dipping normal fault (first column), 60^o dipping normal fault (second column), and a vertical strike-slip fault (third column) from applying no atmospheric correction (black), a correction for constant atmospheric properties (blue), and a correction for variable atmospheric properties (red). The black, blue, and red dots show the inferred median parameter value, and the error bars show the 16th to 84th percentiles (i.e., 1σ) of the resulting ensemble. The green lines show the input value of each respective parameter.

presumably because the deformation fields themselves are more correlated with topography. For the deeper sources, the uncertainty on each parameter increases, as expected, but the spatially variable correction still offers improvements over the spatially constant correction or no correction. The uncertainty in stress drop for all tested fault geometries is minimally affected by the atmospheric correction approaches.

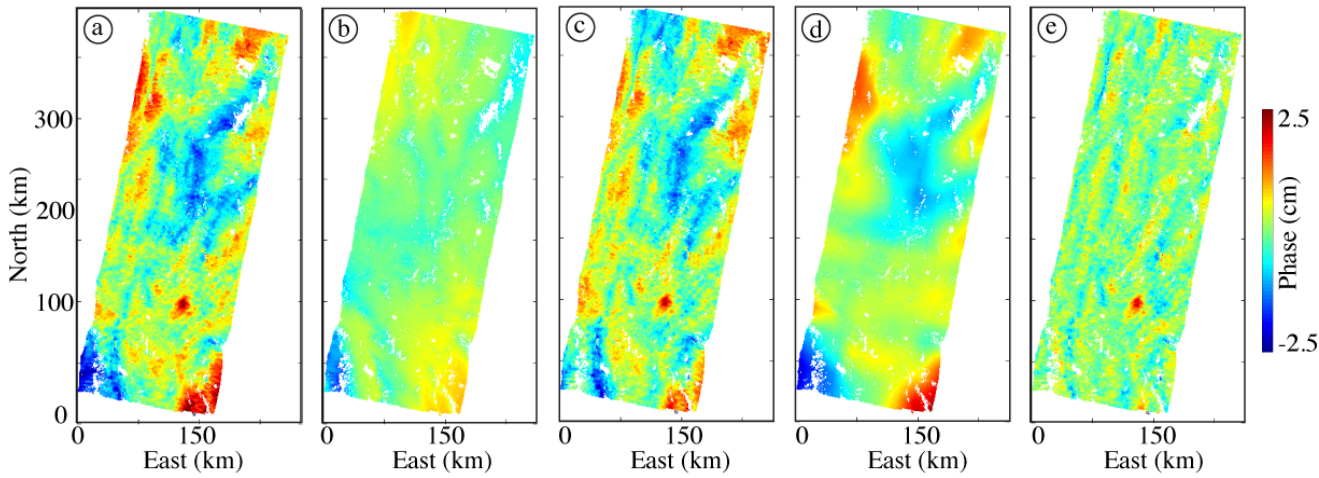

Figure 2.10: Little Skull Mountain earthquake. (a) Interferogram, (b and d) corrections, and (c and e) residual, for the approach with constant (b and c) and variable (d and e) atmospheric properties.

2.6.2 Little Skull Mountain earthquake

Similar to what we observed in the synthetic data cases, the correction for constant atmospheric properties (Figure 2.10b) removes several centimeters of noise from the coseismic interferogram. The spatially variable correction (Figure 2.10d) removes a larger atmospheric contribution and leaves the coseismic signal as the largest residual feature (Figure 2.10e). The fact that the residual atmospheric noise is not strictly turbulence illustrates that atmospheric corrections may not remove the full contribution from the stratified component of the

atmosphere. The inversion for the earthquake source parameters results in oblique motion (near-normal) on a northeast striking fault plane (Figure 2.11). Applying the atmospheric corrections decreases the error in the inferred earthquake magnitude and depth (Figures 2.12a- 2.12d), although the spatially variable atmospheric correction offers no significant improvement over the spatially constant correction. Further, both corrections accentuate an already present bias in the inferred strike (Figures 2.12e- 2.12g) likely related to the topographically correlated atmospheric noise. When we instead focus on the inferred slip vector, the lack of bias and the increased concentration following the atmospheric corrections suggest that the slip orientation and therefore fault kinematics are more robustly measured than the fault orientation.

2.7 Discussion

For the synthetic scenarios explored here, we find lower uncertainty and bias in earthquake magnitude, depth, and dip relative to the input set of parameters after applying the correction accounting for spatially heterogeneous atmospheric characteristics relative to the two other correction approaches. The stronger constraints on fault parameters likely reflect the diminished impact of the longer wavelength and topographically correlated atmospheric signal. The large decrease in uncertainty associated with the fault planes dipping 60^o and 90^o is indicative of the high degree of spatial correlation between elevation and coseismic deformation for these particular earthquake mechanisms at the location chosen in this study. The large errors in both magnitude and depth associated with the vertical strike-slip fault at depths of 8 km and 10 km are likely due to residual noise from the stratified atmosphere and the relatively small, spatially broad, pattern of line-of-sight displacements associated with these fault sources. The fact that the errors for the 30^o dipping fault are largely iden-

tical after applying either atmospheric correction indicates that most of the sensitivity to the stratified component of the atmosphere is removed with the simpler correction and that turbulence likely dominates the residual uncertainty. When the deformation signal and the turbulent noise are of a similar spatial scale or magnitude, they are challenging to distinguish from one another. The large error in stress drop reflects the known trade-offs between source dimensions and slip magnitude that worsen with depth as the source becomes more and more indistinguishable from a point source.

The smaller changes to constraints on the Little Skull Mountain earthquake parameters following both corrections indicate that the impact of noise from the stratified component of the atmosphere is largely mitigated with the spatially constant correction. This result likely reflects the degree of correlation between topography and deformation– the Little Skull Mountain earthquake occurred in a region with less relief than exists in our Dixie Valley example. We find that the error bounds on this earthquake estimated by Lohman et al. [2002] are overly confident, likely because the error bounds from this earlier work do not fully account for the complex and variable character of atmosphere.

Expanding the functionality of the presented workflow beyond North America will require the usage of GAMs such as the ERA-Interim produced by the European Centre for Medium-Range Weather Forecasts [Dee et al., 2011]. The ERA-Interim operates at a grid spacing of $\sim$75 km and therefore may be insensitive to some of the shorter spatial scale variability of the atmospheric characteristics captured by NARR. Still, Jolivet et al. [2014] show that the delay predicted by GAMs along the coarser grid is consistent with the long wavelength signal observed in InSAR data. The effect of atmospheric turbulence, which dominates at spatial scales of $\sim$20 km [e.g., Lohman and Simons, 2005] and is poorly characterized with any GAM, is still best estimated from InSAR data itself as described in Section 2.4.2.

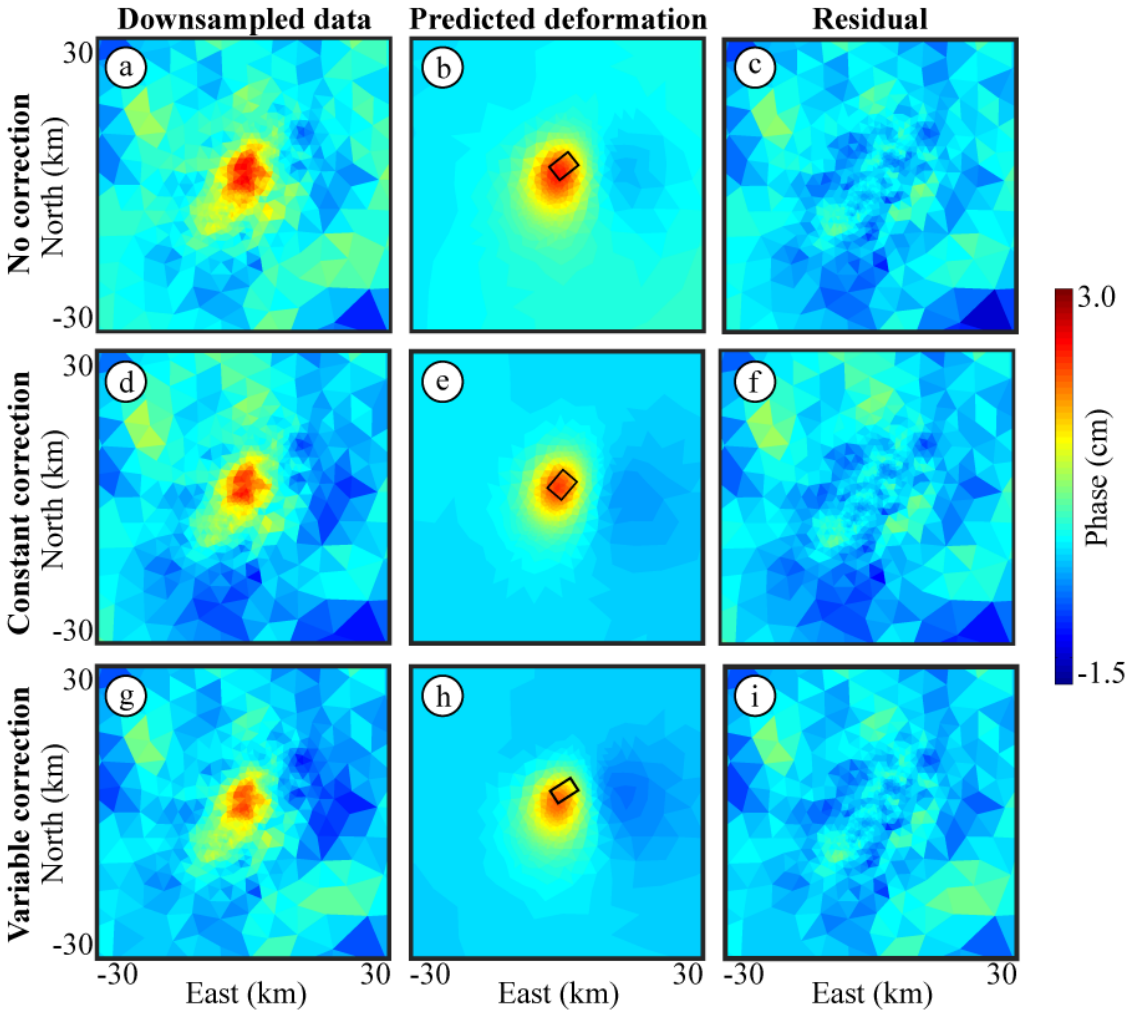

Figure 2.11: Little Skull Mountain earthquake source inversion results. The first column shows the downsampled data after applying (a) no atmospheric correction, (d) a correction for constant atmospheric properties, (g) and a correction for variable atmospheric properties. The second column shows the predicted surface deformation of the best-fit fault model inferred from the first column. The third column shows the residual signal.

Additionally, a similar workflow could be applied to assess the uncertainty in large subduction zone earthquake or interseismic strain accumulation source parameters. Commonly, researchers distinguish broad deformation signals at the wavelength of interest from atmospheric noise by applying a band-pass [e.g., Lin et al., 2010; Bekaert et al., 2015a] or a wavelet filter [e.g., Hetland et al., 2012]. However, these filtering approaches convolve real atmospheric features that have the same spatial scales as the tectonic signal. Our workflow could illustrate the trade-offs between the spatial scale of the filter and along-strike or depth-dependent variations in fault slip or interseismic coupling.

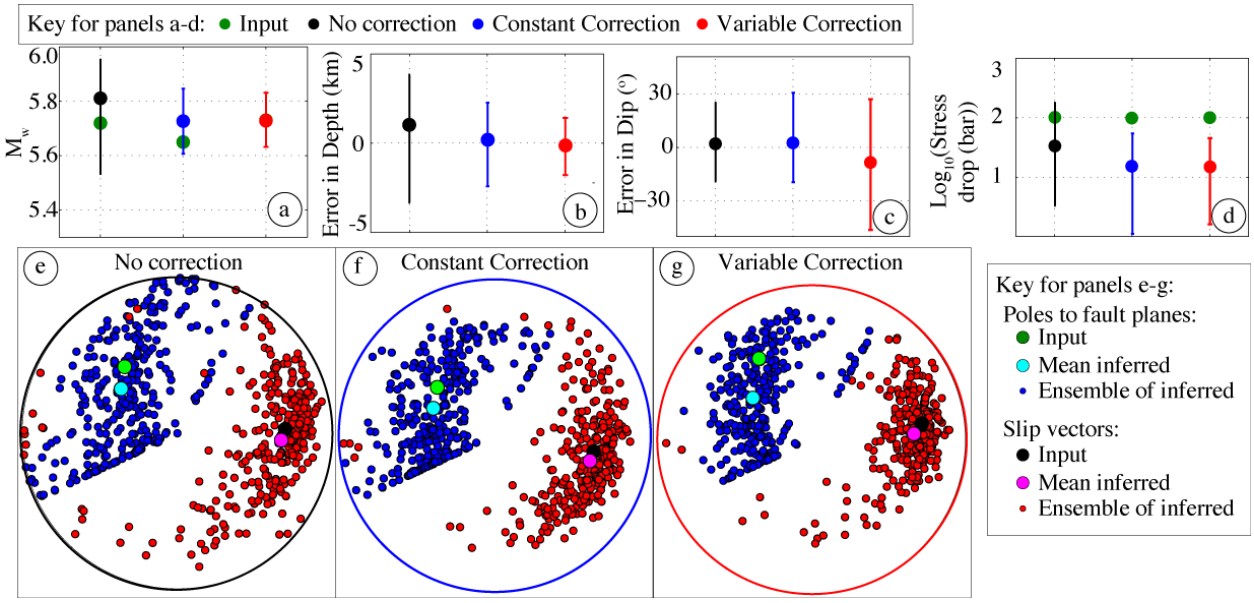

Figure 2.12: Little Skull Mountain earthquake source parameters and error bounds based on 300 synthetic datasets. (a-d) The inferred median magnitude, depth, dip, and stress drop and the 1σ error bars on the resulting ensemble. (e-g) Lower-hemisphere, equal area stereographic projections showing the inferred mean and ensemble fault plane poles and slip vectors. Statistical approaches are outlined in Fisher et al. [1987], and stereonets are plotted using routines from Allmendinger et al. [2012].

2.8 Conclusions

We present an approach for characterizing the effects of atmospheric noise and elevation-dependent empirical corrections on earthquake source parameters retrieved from InSAR data. While empirical correction approaches mitigate the impact of noise from the vertically stratified troposphere, their efficiency is known to suffer in the presence of non-stationary atmospheric characteristics. We show that accounting for this variability generally results in improved constraints on earthquake source parameters, although the decrease in uncertainty and bias depends on the local topographic relief and the fault geometry. Our work directly illustrates the impact of atmospheric noise on inferred subsurface earthquake processes and outlines an approach for assessing the potential benefits of and biases from applying empirical atmospheric corrections with a range of complexity.

2.9 Acknowledgements

We acknowledge the use of ERS SAR imagery made available through the NSF-supported EarthScope facility as part of the GeoEarthScope archive: https://www.unavco.org/data /imaging/sar/sar.html. The Physical Sciences Division of NOAA/ESR made the NARR model available at http://nomads.ncdc.noaa.gov/data/narr. Some figures were made using the Generic Mapping Tools [Wessel et al., 2013]. We thank Paul Tregoning, Thorsten Becker, and three anonymous reviewers for their constructive comments that improved this manuscript. C. Scott was supported by NSF grant 1358573, SCEC award 15167, and the McMullen Fellowship from Cornell University, New York.

2.10 References

Abbott, R. E., J. N. Louie, S. J. Caskey, and S. Pullammanappallil (2001), Geophysical confirmation of low-angle normal slip on the historically active Dixie Valley fault, Nevada, J. Geophys. Res., 106, 4169-4181, doi:10.1029/2000JB900385.

Allmendinger, R. W., N. Cardozo, and D. Fisher (2012), Structural Geology Algorithms, Cambridge Univ. Press, New York.

Amelung, F., and J. Bell (2003), Interferometric synthetic aperture radar observations of the 1994 Double Spring Flat, Nevada, earthquake (M 5.9): Main shock accompanied by triggered slip on a conjugate fault, J. Geophys. Res., 108(B9), 2433, doi:10.1029/2002JB001953.

Amelung, F., D. L. Galloway, J. W. Bell, H. A. Zebker, and R. J. Laczniak (1999), Sensing the ups and downs of Las Vegas: InSAR reveals structural control of land subsidence and aquifer-system deformation, Geology, 27(6), 483, doi:10.1130/0091-7613(1999)027<0483:STUADO>2.3.CO;2.

Argus, D. F., Y. Fu, and F. W. Landerer (2014), Seasonal variation in total water storage in California inferred from GPS observations of vertical land motion: Argus et al.: California Water from GPS, Geophys. Res. Lett., 41, 1971-1980, doi:10.1002/2014GL059570.

Aster, R., B. Borchers, and C. Thurber (2013), Parameter Estimation and Inverse Problems, 2nd ed., Academic Press, Amsterdam.

Barnhart, W. D., and R. B. Lohman (2010), Automated fault model discretization for inversions for coseismic slip distributions, J. Geophys. Res., 115, B10419, doi:10.1029/2010JB007545.

Barnhart, W. D., and R. B. Lohman (2013), Characterizing and estimating noise in InSAR and InSAR time series with MODIS, Geochem. Geophys. Geosyst., 14, 4121-4132, doi:10.1002/ggge.20258.

Becker, T. W., J. L. Hardebeck, and G. Anderson (2005), Constraints on fault slip rates of the southern California plate boundary from GPS velocity and stress inversions, Geophys. J. Int., 160(2), 634-650, doi:10.1111/j.1365-246X.2004.02528.x.

Béjar-Pizarro, M., A. Socquet, R. Armijo, D. Carrizo, J. Genrich, and M. Simons (2013), Andean structural control on interseismic coupling in the North Chile subduction zone, Nat. Geosci., 6(6), 462-467, doi:10.1038/ngeo1802.

Bekaert, D. P. S., A. Hooper, and T. J. Wright (2015a), A spatially variable power law tropospheric correction technique for InSAR data, J. Geophys. Res. Solid Earth, 120, 1345-1356, doi:10.1002/2014JB011558.

Bekaert, D. P. S., R. J. Walters, T. J. Wright, A. J. Hooper, and D. J. Parker (2015b), Statistical comparison of InSAR tropospheric correction techniques, Remote Sens. Environ., 170, 40-47, doi:10.1016/j.rse.2015.08.035.

Bell, J. W., F. Amelung, A. Ferretti, M. Bianchi, and F. Novali (2008), Permanent scatterer InSAR reveals seasonal and long-term aquifer-system response to groundwater pumping and artificial recharge, Water Resour. Res., 44, W02407, doi:10.1029/2007WR006152.

Bell, J. W., and T. Katzer (1990), Timing of late Quaternary faulting in the 1954 Dixie Valley earthquake area, central Nevada, Geology, 18(7), 622, doi:10.1130/ 0091-7613(1990)018 <0622:TOLQFI>2.3.CO;2.

Berrada Baby, H., P. Golé, and J. Lavergnat (1988), A model for the tropospheric excess path length of radio waves from surface meteorological measurements, Radio Sci., 23(6), 1023-1038, doi:10.1029/RS023i006p01023.

Borsa, A. A., D. C. Agnew, and D. R. Cayan (2014), Ongoing drought-induced uplift in the western United States, Science, 345(6204), 1587-1590, doi:10.1126/science.1260279.

Bürgmann, R., P. A. Rosen, and E. J. Fielding (2000), Synthetic aperture radar interferometry to measure Earth's surface topography and its deformation, Annu. Rev. Earth Planet. Sci., 28(1), 169-209, doi:10.1146/annurev.earth.28.1.169.

Caskey, S. J., R. S. Stein, and G. Marshall (1996), Surface faulting of the 1954 Fairview Peak (Ms = 7.2) and Dixie Valley (Ms = 6.9) earthquakes, central Nevada, Bull. Seismol. Soc. Am., 86, 761-787.

Cavalié, O., M.-P. Doin, C. Lasserre, and P. Briole (2007), Ground motion measurement in the Lake Mead area, Nevada, by differential synthetic aperture radar interferometry time series analysis: Probing the lithosphere rheological structure, J. Geophys. Res., 112, B03403, doi:10.1029/2006JB004344.

Dee, D. P., et al. (2011), The ERA-Interim reanalysis: Configuration and performance of the data assimilation system, Q. J. R. Meteorol. Soc., 137(656), 553-597, doi:10.1002/qj.828.

Doin, M.-P., C. Lasserre, G. Peltzer, O. Cavalié, and C. Doubre (2009), Corrections of stratified tropospheric delays in SAR interferometry: Validation with global atmospheric models, J. Appl. Geophys., 69(1), 35-50, doi:10.1016/j.jappgeo.2009.03.010.

Doser, D. I. (1986), Earthquake processes in the Rainbow Mountain-Fairview Peak-Dixie Valley, Nevada, region 1954-1959, J. Geophys. Res., 91, 12,572-12,586, doi:10.1029 /JB091iB12p12572.

Elliott, J. R., J. Biggs, B. Parsons, and T. J. Wright (2008), InSAR slip rate determination

on the Altyn Tagh Fault, northern Tibet, in the presence of topographically correlated atmospheric delays, Geophys. Res. Lett., 35, L12309, doi:10.1029/2008GL033659.

Emardson, T. R. (2003), Neutral atmospheric delay in interferometric synthetic aperture radar applications: Statistical description and mitigation, J. Geophys. Res., 108(B5), 2231, doi:10.1029/2002JB001781.

Farr, T. G., et al. (2007), The Shuttle Radar Topography Mission, Rev. Geophys., 45, RG2004, doi:10.1029/2005RG000183.

Fattahi, H., and F. Amelung (2014), InSAR uncertainty due to orbital errors, Geophys. J. Int., 199(1), 549-560, doi:10.1093/gji/ggu276.

Fialko, Y., and M. Simons (2000), Deformation and seismicity in the Coso geothermal area, Inyo County, California: Observations and modeling using satellite radar interferometry, J. Geophys. Res., 105, 21,781-21,793, doi:10.1029/2000JB900169.

Fisher, N. I., T. Lewis, and B. J. J. Embleton (1987), Statistical Analysis of Spherical Data, Cambridge Univ. Press, Cambridge.

Fournier, T., M. E. Pritchard, and N. Finnegan (2011), Accounting for atmospheric delays in InSAR data in a search for long-wavelength deformation in South America, IEEE Trans. Geosci. Remote Sens., 49(10), 3856-3867, doi:10.1109/TGRS.2011.2139217.

Gourmelen, N., and F. Amelung (2005), Postseismic mantle relaxation in the central Nevada seismic belt, Science, 310(5753), 1473-1476, doi:10.1126/science.1119798.

Hanssen, R. (2001), Radar Interferometry: Data Interpretation and Error Analysis, Kluwer Academic Press, Dordrecht.

Harmsen, S. (1994), The Little Skull Mountain, Nevada, earthquake of 29 June 1992: Aftershock focal mechanisms and tectonic stress field implications, Bull. Seismol. Soc. Am., 84, 1484-1505.

Harris, R. A., and P. Segall (1987), Detection of a locked zone at depth on the Parkfield, California, segment of the San Andreas Fault, J. Geophys. Res., 92, 7945-7962, doi:10.1029/JB092iB08p07945.

Hetland, E. A., P. Musé, M. Simons, Y. N. Lin, P. S. Agram, and C. J. DiCaprio (2012), Multiscale InSAR Time Series (MInTS) analysis of surface deformation, J. Geophys. Res., 117, B02404, doi:10.1029/2011JB008731.

Hodgkinson, K. M., R. S. Stein, and G. Marshall (1996), Geometry of the 1954 Fairview Peak-Dixie Valley earthquake sequence from a joint inversion of leveling and triangulation

data, J. Geophys. Res., 101, 25,437-25,457, doi:10.1029/96JB01643.

Holt, W. E., and G. Shcherbenko (2013), Toward a continuous monitoring of the horizontal displacement gradient tensor field in Southern California using cGPS observations from Plate Boundary Observatory (PBO), Seismol. Res. Lett., 84(3), 455-467, doi:10.1785/0220130004.

Jolivet, R., P. S. Agram, N. Y. Lin, M. Simons, M.-P. Doin, G. Peltzer, and Z. Li (2014), Improving InSAR geodesy using slobal atmospheric models, J. Geophys. Res Solid Earth, 119, 2324-2341, doi:10.1002/2013JB010588.

Jolivet, R., R. Grandin, C. Lasserre, M.-P. Doin, and G. Peltzer (2011), Systematic InSAR tropospheric phase delay corrections from global meteorological reanalysis data, Geophys. Res. Lett., 38, L17311, doi:10.1029/2011GL048757.

Lin, Y. N., M. Simons, E. A. Hetland, P. Muse, and C. DiCaprio (2010), A multiscale approach to estimating topographically correlated propagation delays in radar interferograms, Geochem. Geophys. Geosyst., 11, Q09002, doi:10.1029/2010GC003228.

Liu, Z., D. Dong, and P. Lundgren (2011), Constraints on time-dependent volcanic source models at Long Valley Caldera from 1996 to 2009 using InSAR and geodetic measurements: Time-dependent volcanic source models, Geophys. J. Int., 187(3), 1283-1300, doi:10.1111/j.1365-246X.2011.05214.x.

Li, Z., E. J. Fielding, P. Cross, and J.-P.Muller (2006), Interferometric synthetic aperture radar atmospheric correction: GPS topography-dependent turbulence model, J. Geophys. Res., 111, B02404, doi:10.1029/2005JB003711.

Li, Z., E. J. Fielding, P. Cross, and R. Preusker (2009), Advanced InSAR atmospheric correction: MERIS/MODIS combination and stacked water vapour models, Int. J. Remote Sens., 30(13), 3343-3363, doi:10.1080/01431160802562172.

Li, Z., J.-P. Muller, and P. Cross (2003), Comparison of precipitable water vapor derived from radiosonde, GPS, and Moderate-Resolution Imaging Spectroradiometer measurements, J. Geophys. Res., 108(D20), 4651, doi:10.1029/2003JD003372.

Li, Z., J.-P. Muller, and P. Cross (2005), Interferometric synthetic aperture radar (InSAR) atmospheric correction: GPS, Moderate Resolution Imaging Spectroradiometer (MODIS), and InSAR integration, J. Geophys. Res., 110, B03410, doi:10.1029/2004JB003446.

Lohman, R. (2004), The inversion of geodetic data for earthquake parameters, Ph.D Thesis, California Institute of Technology.

Lohman, R. B., and J. J. McGuire (2007), Earthquake swarms driven by aseismic creep in the Salton Trough, California, J. Geophys. Res., 112, B04405, doi:10.1029/2006JB004596.

Lohman, R. B., and M. Simons (2005), Some thoughts on the use of InSAR data to constrain models of surface deformation: Noise structure and data downsampling, Geochem. Geophys. Geosyst., 6, Q01007, doi:10.1029/2004GC000841.

Lohman, R. B., M. Simons, and B. Savage (2002), Location and mechanism of the Little Skull Mountain earthquake as constrained by satellite radar interferometry and seismic waveform modeling, J. Geophys. Res., 107(B6), 2118, doi:10.1029/2001JB000627.

Massonnet, D., and K. L. Feigl (1998), Radar interferometry and its application to changes in the Earth's surface, Rev. Geophys., 36, 441-500, doi:10.1029/97RG03139.

Massonnet, D., K. Feigl, M. Rossi, and F. Adragna (1994), Radar interferometric mapping of deformation in the year after the Landers earthquake, Nature, 369(6477), 227-230, doi:10.1038/369227a0.

McGuire, J. J., R. B. Lohman, R. D. Catchings, M. J. Rymer, and M. R. Goldman (2015), Relationships among seismic velocity, metamorphism,and seismic and aseismic fault slip in the Salton Sea Geothermal Field region: Salton Sea Geothermal Field, J. Geophys. Res. Solid Earth, 120,2600-2615, doi:10.1002/2014JB011579.

Meade, B. J., and B. Hager (2005), Block models of crustal motion in southern California constrained by GPS measurements, J. Geophys. Res.,110, B03403, doi:10.1029/2004JB003209.

Menke, W. (1989), Geophysical Data Analysis: Discrete Inverse Theory, Int. Geophys. Ser., vol. 45, Academic Press, New York.

Meremonte, M., J. Gomberg, and E. Cranswick (1995), Constraints on the 29 June 1992 Little Skull Mountain, Nevada, earthquake sequenceprovided by robust hypocenter estimates, Bull. Seismol. Soc. Am., 85, 1039-1049.

Mesinger, F., et al. (2006), North American Regional Reanalysis, Bull. Am. Meteorol. Soc., 87(3), 343-360, doi:10.1175/BAMS-87-3-343.

Okada, Y. (1985), Surface deformation due to shear and tensile faults in a half space, Bull. Seismol. Soc. Am., 74, 1135-1154.

Onn, F., and H. A. Zebker (2006), Correction for interferometric synthetic aperture radar atmospheric phase artifacts using time series of zenith wet delay observations from a GPS network, J. Geophys. Res., 111, B09102, doi:10.1029/2005JB004012.

Parker, A. L., J. Biggs, R. J. Walters, S. K. Ebmeier, T. J. Wright, N. A. Teanby, and Z. Lu (2015), Systematic assessment of atmospheric uncertainties for InSAR data at volcanic arcs using large-scale atmospheric models: Application to the Cascade volcanoes, United States, Remote Sens. Environ., 170, 102-114, doi:10.1016/j.rse.2015.09.003.

Pollitz, F. F., C. Wicks, and W. Thatcher (2001), Mantle flow beneath a continental strike-slip fault: Postseismic deformation after the 1999 Hector Mine earthquake, Science, 293(5536), 1814-1818, doi:10.1126/science.1061361.

Sambridge, M. (1999), Geophysical inversion with a neighbourhood algorithm-I. Searching a parameter space, Geophys. J. Int., 138(2), 479-494, doi:10.1046/j.1365-246X.1999.00876.x.

Scott, C., R. Lohman, M. Pritchard, P. Alvarado, and G. Sánchez (2014), Andean earthquakes triggered by the 2010 Maule, Chile (M_w 8.8) earthquake: Comparisons of geodetic, seismic and geologic constraints, J. South Am. Earth Sci., 50, 27-39, doi:10.1016/j.jsames.2013.12.001.

Simons, M., Y. Fialko, and L. Rivera (2002), Coseismic deformation from the 1999 M_w 7.1 Hector Mine, California, earthquake as inferred from InSAR and GPS observations, Bull. Seismol. Soc. Am., 92(4), 1390-1402, doi:10.1785/0120000933.

Slemmons, B. (1957), Geological effects of the Dixie Valley-Fairview Peak, Nevada, earthquakes of December 16, 1954, Bull. Seismol. Soc. Am., 47, 353-375.

Smith, K. D., J. N. Brune, D. dePolo, M. K. Savage, R. Anooschehpoor, and A. Sheehan (2001), The 1992 Little Skull Mountain earthquake sequence, Southern Nevada test site, Bull. Seismol. Soc. Am., 91(6), 1595-1606, doi:10.1785/0120000089.

Stein, S., and M. Wysession (2003), An Introduction to Seismology, Earthquakes, and Earth Structure, Blackwell Publ, Malden, MA.

Tymofyeyeva, E., and Y. Fialko (2015), Mitigation of atmospheric phase delays in InSAR data, with application to the eastern California shear zone, J. Geophys. Res. Solid Earth, 120, 5952-5963, doi:10.1002/2015JB011886.

Walter, W. R. (1993), Source parameters of the June 29, 1992 Little Skull Mountain earthquake from complete regional waveforms at a single station, Geophys. Res. Lett., 20, 403-406, doi:10.1029/92GL03031.

Walters, R. J., J. R. Elliott, Z. Li, and B. Parsons (2013), Rapid strain accumulation on the Ashkabad fault (Turkmenistan) fromatmosphere-corrected InSAR, J. Geophys. Res. Solid Earth, 118, 3674-3690, doi:10.1002/jgrb.50236.

Wessel, P., W. H. F. Smith, R. Scharroo, J. Luis, and F. Wobbe (2013), Generic Mapping Tools: Improved version released, Eos Trans. AGU, 94(45), 409-410, doi:10.1002/2013EO450001.

Wicks, C. W., D. Dzurisin, S. Ingebritsen, W. Thatcher, Z. Lu, and J. Iverson (2002), Magmatic activity beneath the quiescent Three Sisters volcanic center, central Oregon Cascade Range, USA, Geophys. Res. Lett., 29(7), 1122, doi:10.1029/2001GL014205.

Wicks, C. W., W. Thatcher, F. C. Monastero, and M. A. Hasting (2001), Steady state deformation of the Coso Range, east central California, inferred from satellite radar interferometry, J. Geophys. Res., 106, 13,769-13,780, doi:10.1029/2001JB000298.

Wicks, C., W. Thelen, C. Weaver, J. Gomberg, A. Rohay, and P. Bodin (2011), InSAR observations of aseismic slip associated with an earthquake swarm in the Columbia River flood basalts, J. Geophys. Res., 116, B12304, doi:10.1029/2011JB008433.

Zebker, H. A., and J. Villasenor (1992), Decorrelation in Interferometric Radar Echoes, IEEE Transactions on Geoscience and Remote Sensing, 30, 950-959.

CHAPTER 3

ANDEAN EARTHQUAKES TRIGGERED BY THE 2010 MAULE, CHILE (M_W 8.8) EARTHQUAKE: COMPARISONS OF GEODETIC, SEISMIC AND GEOLOGIC CONSTRAINTS

3.1 Abstract

The Maule, Chile, (M_w 8.8) earthquake on 27 February 2010 triggered deformation events over a broad area, allowing investigation of stress redistribution within the upper crust following a mega-thrust subduction event. We explore the role that the Maule earthquake may have played in triggering shallow earthquakes in northwestern Argentina and Chile. We investigate observed ground deformation associated with the M_w 6.2 (GCMT) Salta (1450 km from the Maule hypocenter, nine hours after the Maule earthquake), M_w 5.8 Catamarca (1400 km; nine days), M_w 5.1 Mendoza (350 km; between one to five days) earthquakes, as well as eight additional earthquakes without an observed geodetic signal. We use seismic and Interferometric Synthetic Aperture Radar (InSAR) observations to characterize earthquake location, magnitude and focal mechanism, and characterize how the non-stationary, spatially correlated noise present in the geodetic imagery affects the accuracy of our parameter estimates. The focal mechanisms for the far-field Salta and Catamarca earthquakes are broadly consistent with regional late Cenozoic fault kinematics. We infer that dynamic stresses due to the passage of seismic waves associated with the Maule earthquake likely brought the Salta and Catamarca regions closer to failure. Possibly, the activated faults were approaching a more advanced stage of their seismic cycle relative to faults that were not activated following the Maule earthquake. The near-field Mendoza earthquake geometry is consistent with triggering related to positive static Coulomb stress changes due to the Maule earth-

quake but is also aligned with the South America-Nazca shortening direction. None of the earthquakes considered in this study require that the Maule earthquake reactivated faults in a sense that is inconsistent with their long-term behavior.

3.2 Introduction

Stress within the lithosphere controls the distribution of deformation (seismic and aseismic), making constraints on the stress field an attractive target for geophysical research. However, there are relatively few direct measurements of the characteristics of the crustal stress field (e.g., Zoback et al., 1992). Because earthquakes occur when deviatoric stresses exceed the frictional resistance along pre-existing faults or the rock strength, the style of earthquake deformation is often used as a proxy for changes in the orientation and magnitude of the stress field (e.g., Hicks et al., 2000; Hardebeck, 2010). Aftershocks, which generally occur within one to two fault lengths of a mainshock or in the near-field, offer the opportunity to investigate the short-term evolution of stress within a seismogenic zone (e.g., Stein and Lisowski, 1983; Hardebeck, 2012). Regions of high aftershock density often correlate with locations of estimated increases in static Coulomb stress (SCS) (e.g., King et al., 1994; Kundu et al., 2012; Sevilgen et al., 2012; Toda et al., 2012). In contrast, dynamically triggered far-field events frequently occur greater than one to two fault lengths from the mainshock where the SCS changes are negligible, but where transient stress changes due to the passage of seismic waves may be significant (e.g., Hill et al., 1993; Prejean et al., 2004; Velasco et al., 2004; Pollitz et al., 2012). These changes in transient stresses can trigger immediate seismicity or promote delayed earthquakes by processes that may involve evolution of rate- and state- friction parameters along the target fault planes (e.g., Gomberg et al., 1997) or elevated pore pressure (e.g., Roeloffs et al., 2003).

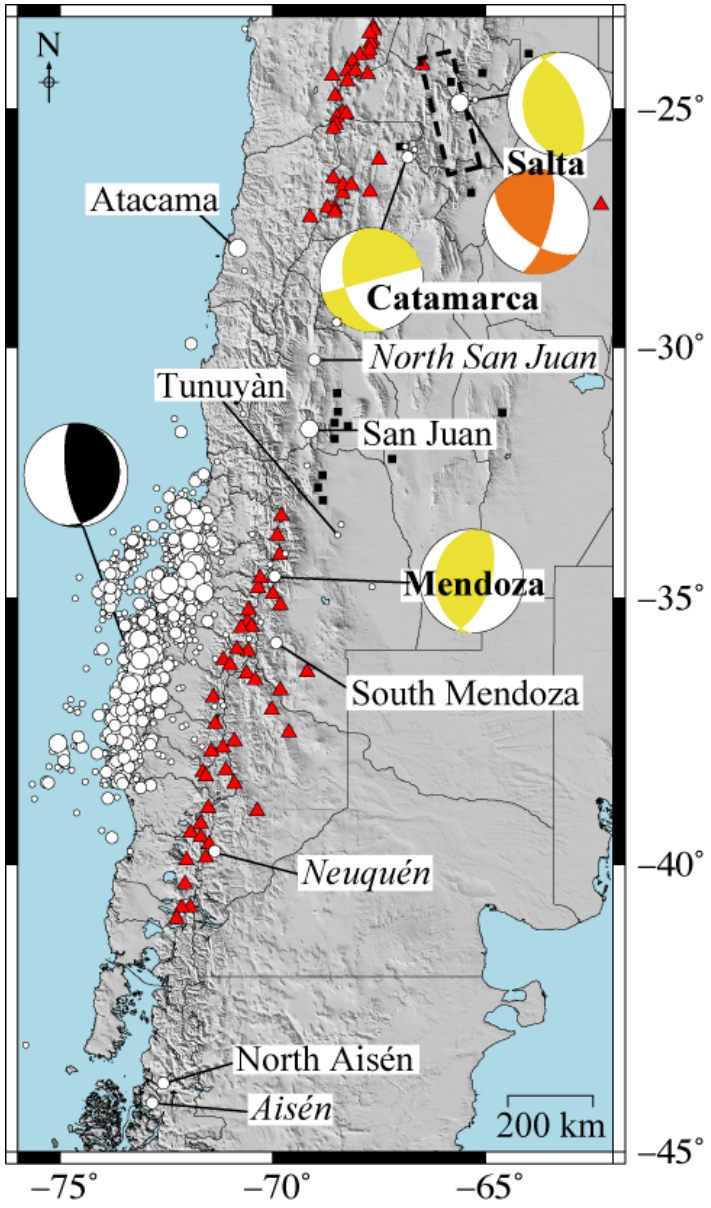

Figure 3.1: Location of earthquakes in this study. Circles indicate shallow earthquakes (depth $\leq$ 50 km), between 27 February, 2010- 27 March, 2010- large: $M_w \geq 6$, medium: $5 \leq M_w \leq 6$, small: $M_w \leq 5$. Locations of labeled crustal earthquakes are from our InSAR work, the INPRES seismic network and the PDE and GCMT catalogs. Non-labeled earthquakes are from the PDE catalog. Font denotes level of InSAR analysis performed- bold: full inversion, regular: estimate minimum depth, italic: interferograms poor quality. Dashed black rectangle outlines the Salta path 97 interferogram area in Figure 3.2. Focal mechanisms are from our InSAR analysis (yellow), our seismic analysis (orange), and the GCMT catalog (black). Black squares are stations from the INPRES seismic network. Red triangles are volcanoes listed in the Smithsonian Institution's Global Volcanism Program.

The 2010 Maule, Chile (M_w 8.8) earthquake, which ruptured over 500 km of the South America- Nazca subduction zone (e.g., Lorito et al., 2011), is associated with many observations of deformation covering a wide range of temporal scales at varying distances from the main event. The Pichilemu seismic sequence, which occurred in the forearc upper crust suggests that the Maule earthquake reactivated extensional structures active during large Quaternary subduction events (Farías et al., 2011; Aron et al., 2013). The subsidence of five calderas in the Andean Southern Volcanic Zone following the Maule earthquake is potentially related to the coseismic release of fluids at hydrothermal systems (Pritchard et al., 2013). The passage of surface waves from the Maule earthquake is associated with two days of increased seismicity at the Uturuncu volcano in southern Bolivia (Jay et al., 2012), as well as microearthquakes near the Coso Geothermal Field, California (Peng et al., 2010). Month-long increases in seismic tremor and modulation of ongoing slow slip events along the Guerrero, Mexico subduction zone suggests long-lived effects from the Maule earthquake (Zigone et al., 2012).

In this paper, we investigate the seismic and geodetic data associated with several continental earthquakes of M_w 5.0 or greater in northwestern Argentina and Chile (Figure 3.1) that were likely triggered by the Maule interplate earthquake. We characterize the fault geometry for three events using seismic and Interferometric Synthetic Aperture Radar (InSAR) observations. In cases where no observable deformation is present (five earthquakes), despite the presence of good-quality InSAR imagery, we estimate the minimum centroid depths that would result in the predicted deformation signal to be smaller than the noise. The remaining three events are only spanned by low-quality interferograms that do not warrant further investigation.

InSAR data, which can be used to precisely locate earthquakes in space (e.g., Lohman and Simons, 2005a), may have a temporal uncertainty of weeks to years based on the finite

time span of the available interferograms. InSAR is complementary to seismic data which provides highly accurate constraints on earthquake timing but may have a 10-50 km error in epicenter location, particularly from regional or global networks in sparsely instrumented areas (e.g., Lohman and Simons, 2005a; Weston et al., 2011; Devlin et al., 2012). For the three events observable with InSAR, we estimate the uncertainty associated with our inferred solutions due to atmospheric and ionospheric noise using both standard Monte Carlo approaches and a visual assessment. We find that the visual assessment, while less rigorous, avoids problems involving the difficulty in characterizing the statistical behavior of the highly spatially variable noise present in interferograms. We apply two types of comparisons to understand the potential impact of the 2010 M_w 8.8 Maule earthquake on the potentially- triggered earthquakes of focus. We calculate the SCS changes on the event in the near-field due to the Maule earthquake. For all events, we evaluate the consistency between our inferred focal mechanisms, strain indicators determined from mapped faults, and the plate-scale convergence direction. We infer that the location and geometry of the triggered events do not require that the Maule earthquake is associated with stress changes that overwhelmed the style of long-term stress in each region.

3.3 Characterizing noise in interferograms

The reported results of geophysical inversions typically take the form of best-fit models that produce the closest fit to the dataset in a least squares sense. The associated uncertainty ideally includes the effects of noise present in the data and errors in the type of model used to simulate the behavior of earth materials. In cases where the statistical behavior of the noise can be well characterized and the inversion is linear, error bounds on fault parameters can easily be determined by propagating the data covariance matrix through the inversion

to form a model covariance matrix. For non-linear problems, linearized inversions or Monte Carlo sensitivity tests can provide error bounds on model parameters. In a Monte Carlo error analysis, many independent realizations of the noise are added to either the data (e.g., Wright et al., 2003) or the synthetic displacement field produced by slip on the optimal fault plane (e.g., Lohman and Simons, 2005b; Barnhart and Lohman 2010a). An inversion is performed on each predicted dataset, and error bounds are derived from the full set of models. If the characteristics of the noise are estimated poorly, the error bounds will be inaccurate.

A significant source of noise in InSAR originates from interferometric phase delays due to the variability in atmospheric water vapor and ionosphere characteristics. Atmospheric and ionospheric artifacts, which are spatially coherent over length scales of tens to hundreds of kilometers (e.g., Emardson, 2003; Lohman and Simons, 2005b), are difficult to characterize because their statistical behavior may vary significantly within the area of an interferogram (e.g., Barnhart and Lohman, 2013a). Tropospheric water vapor variations are also frequently spatially correlated with topography (e.g., Fujiwara et al., 1998) exacerbating the problem of spatially non-stationary noise.

The effect of noise can be mitigated by excluding interferograms with significant atmospheric signatures (e.g., Massonnet et al., 1994), stacking many interferograms to average out the atmospheric component (e.g., Zebker et al., 1997), correcting for the atmospheric signal using independent data from satellites or weather models (e.g., Li et al., 2005; Elliott et al., 2008), or penalizing topographically correlated signals with a wavelet filter (e.g., Hetland et al., 2012). However, tropospheric and ionospheric effects always still persist at some level, and must be assessed if we are to place meaningful bounds on inversion results.

3.4 Data

We use seismic data from the permanent seismic network of the Argentine Instituto Nacional de Prevención Sísmica (INPRES) to study the Salta, Catamarca, Mendoza, San Juan and Tunuyán earthquakes (Figure 3.1). For the Salta, Catamarca and Atacama earthquakes, we also use the Global Centroid Moment Tensor (GCMT) catalogs (Dziewonski et al., 1981; Ekström et al., 2012). For all events, we also refer to the Preliminary Determination of Epicenters (PDE) solution from the National Earthquake Information Center (NEIC).

We produced interferograms using L-band (23.6 cm) SAR imagery from the PALSAR instrument on the Japanese Aerospace Exploration Agency's (JAXA) Advanced Land Observing Satellite (ALOS), made available at the Alaska Satellite Facility through an agreement between NASA and JAXA. The available interferograms are all from ascending tracks with perpendicular baselines less than 1080 m. The signal for each earthquake where deformation is observed is covered by two independent, overlapping tracks. The two viewing geometries provide stronger constraints on earthquake fault geometry than would be possible with data with a single satellite line-of-sight (LOS) direction (e.g., Lohman et al., 2002). Unfortunately, no data from ALOS descending tracks spanning the earthquakes with significant deformation were acquired, and data acquired from the C-band (5.6 cm) European Space Agency's Environmental Satellite (ENVISAT) have poor coherence due to the non-optimal temporal spacing of the available data and the faster decorrelation timescale of the shorter wavelength C-band interferograms. We processed all interferograms using the Repeat Orbit Interferometry PACkage (ROI- PAC) from Rosen et al. (2004). We removed topographic effects with a 90 m digital elevation model (DEM) produced by NASA's Shuttle Radar Topography Mission (SRTM, Farr et al., 2007).

3.5 Methods

3.5.1 Seismicity

In addition to the PDE and GCMT location for the earthquakes, we use observations from local and regional INPRES stations, when available. For instance, for the largest, best-recorded Salta earthquake, we estimate the hypocenter location from 18 arrival times, including five S-wave phases from local and regional INPRES stations (Figure 3.1) using the program Hypocenter (Lienert, 1994). We assume a seismic velocity structure consistent with a crustal thickness of 60 km based on Cahill et al. (1992). We estimate the focal mechanism using 24 P-wave polarities and 16 SV/P, SH/P and SV/SH amplitude ratios allowing for a maximum of four misfit polarities using FOCMEC (Smoke, 2003).

3.5.2 InSAR

Individual interferograms (Figure 3.2) contain several million data points, making their use at full resolution during fault parameter inversions computationally unfeasible. We downsample the interferograms according to the fault resolution-based algorithm developed by Lohman and Simons (2005b), which substantially decreases the number of data points with minimal loss of relevant information (Figure 3.3). The variance of each resampled point is a function of the number of data points used in each average and their spatial covariance, estimated from the interferogram itself.

As an initial constraint on fault parameters, we model the earthquake as a single rectangular dislocation in an elastic half-space (Okada, 1985). We search for the best-fit location and

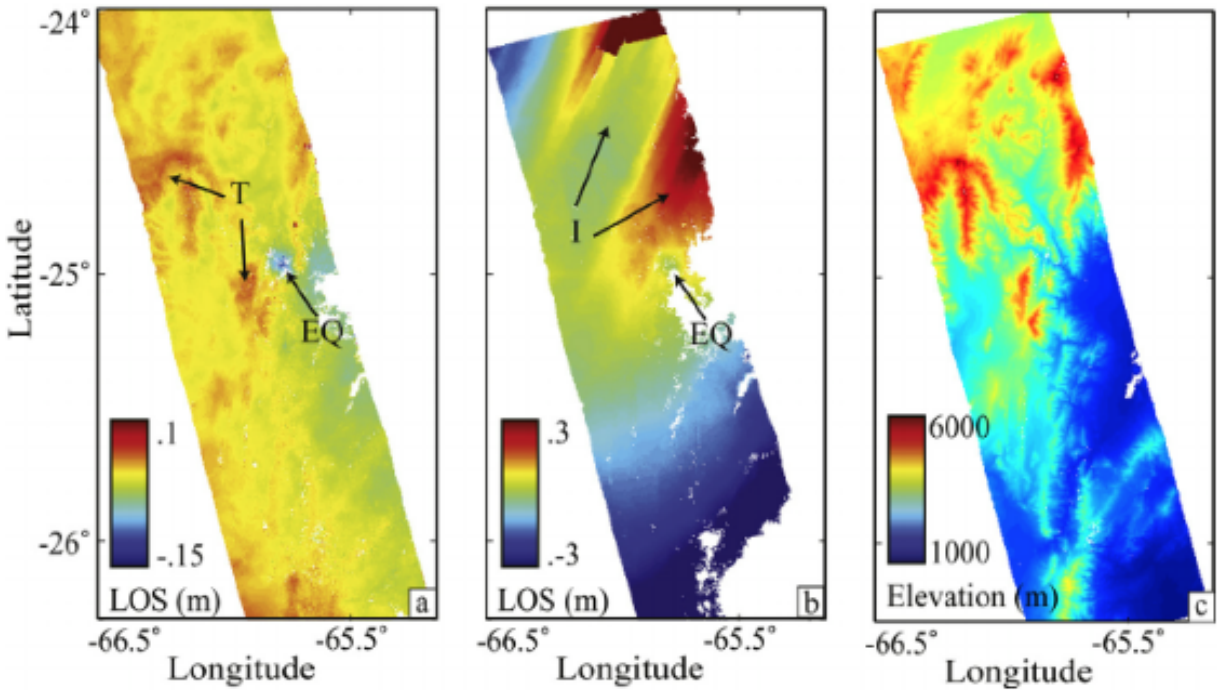

Figure 3.2: Spatially correlated noise in unwrapped interferograms from Path 97 spanning the Salta earthquake. (a) Interferogram spanning 5 April, 2008- 27 May, 2010 with large magnitude of topographically correlated noise (T), likely due to variations in atmospheric water vapor content. Note that the signal due to the earthquake (EQ) is of similar size and magnitude to features in the noise. (b) Spatially correlated ionospheric banding (I) with magnitude that exceeds that of the earthquake (EQ) in interferogram spanning 4 October, 2007- 11 April, 2010 (c) Topography from NASA's STRM DEM (Farr et al., 2007), for comparison.

geometry using the Neighborhood algorithm (Sambridge, 1999), an iterative global search method that progressively focuses in on regions of the parameter space with better fits to the data. After finding the best-fit location and focal mechanism, we invert for spatially variable slip across a fault plane with the same centroid location and geometry but a larger area (Figure 3.4), discretized with triangular dislocations chosen to optimize the spatial resolution of slip on the fault plane given the available data (Barnhart and Lohman, 2010b).

To estimate error bounds on our inferred source parameters we perform Monte Carlo sensitivity tests with 1000 realizations of the noise (Lohman and Simons, 2005b; Barnhart

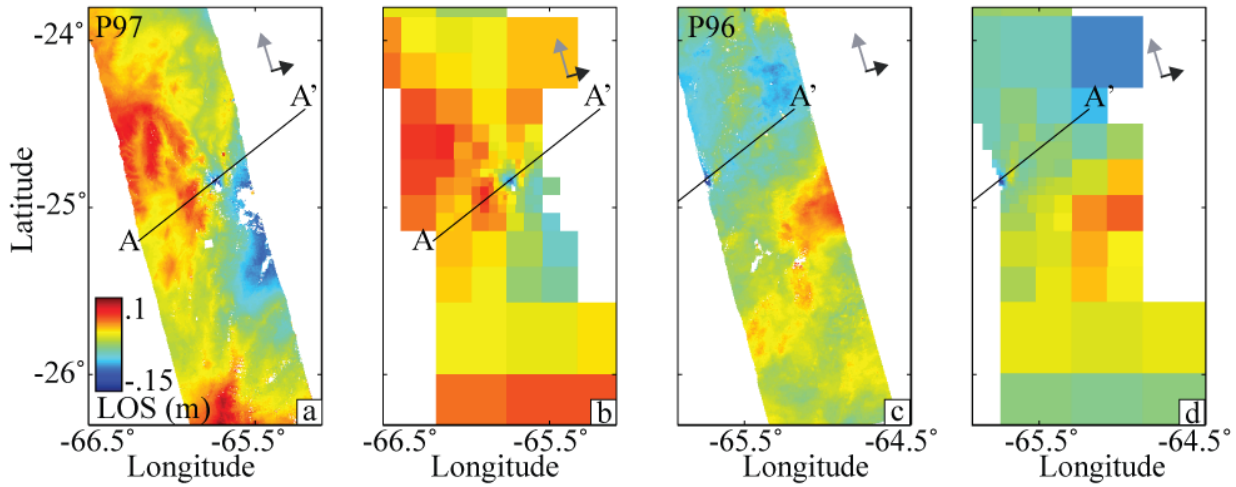

Figure 3.3: Full-length interferograms showing the Salta earthquake spanning 5 April, 2008-27 August, 2010 in (a) and (b), and 7 February, 2010- 25 March, 2010 in (c) and (d). The downsampled inteferograms in (b) and (d) are used in the earthquake parameter inversions. A negative signal is ground motion towards the satellite. Arrows show look direction and satellite azimuth. The A-A' line indicates the location of transect in Figure 3.9. Pixel size is 100 m.

and Lohman, 2010b). We use the best model based on our visual method (described below) as a starting point, although the error bounds are not heavily dependent on the exact choice of model. The error bounds derived from the resulting family of fault location and slip models reflect only the uncertainty given the noise characteristics estimated directly from the data, assuming that the noise is spatially stationary across each interferogram (e.g., Lohman and Simons, 2005b). True error bounds that reflect our incomplete knowledge of crustal elastic structure, complex fault geometry, non-seismic deformation sources, and non-stationary noise would likely be larger.

Several of the interferograms are marked by obvious ionospheric or atmospheric artifacts, resulting in banding across a portion of the image or signals that clearly correlate with topography (Figure 3.2). This is a clear example of the types of spatially non-stationary noise that can be difficult to characterize statistically. To assess how our characterization of

Earthquake	**Time/ Date**	**Strike** (^{o})	**Dip** (^{o})	**Rake** (^{o})	**Lat.** (^{o})	**Long** (^{o})	**Depth (km)**	**M_w**
Salta (InSAR)	07/02/10-25/03/10	180*	30*	111	-24.85	-65.76	7.1	6.1
Salta (InSAR)	07/02/10-26/03/10	150*	30*	093	-24.86	-65.76	7.0	6.1
Salta (INPRES)	15:45:36/ 27/02/10	127	58	033	-24.842	-65.685	8.1±1.5	6.3
Salta (GCMT)	15:45:43/ 27/02/10	162 /342	25/ 66	097 /087	-24.91	-65.59	27	6.2
Catamarca (InSAR)	24/03/08-15/08/10	165*	45*	000	-25.85	-67.00	7.9	5.8
Catamarca (INPRES)	17:03/ 08/03/10	–	–	–	-25.71	-66.62	10	5.8
Catamarca (GCMT)	17:03:22/ 08/03/10	149/ 058	75 /84	006 /165	-25.94	-66.84	15.1	5.8
Catamarca (GCMT)	13:02:27 05/05/10	136/228	46/88	-003/ -136	-25.90	-67.06	17.1	5.1
Mendoza (InSAR)	15/02/10-03/04/10	180*	30*	075	-34.60	-69.99	0.9	5.2
Mendoza (INPRES)	05:15 28/02/10	–	–	–	-33.85	-68.68	15	4.9†

Table 3.1: Earthquake fault parameters: Dates from the InSAR models indicate the satellite acquisitions. * denotes value was fixed in the inversion.† denotes local magnitude. Refer to Figures 5, 11, and 13 for error estimates. Rake values are in the Aki and Richards (1980) convention.

errors on the solution may be impacted by the existence of spatially non-stationary noise in our interferograms, we explore a visually based qualitative approach as well. We generate 144 models that represent a coarse grid search over all possible combinations of strike and dip values (Figure 3.5). The fault location and remaining slip parameters for each fault orientation are optimized using the Neighborhood algorithm inversion method described above. This non-linear search within a global search approach selects the optimal model for each fixed fault orientation and provides a different view of the parameter space than when all parameters are optimized simultaneously.

We use two metrics to evaluate each fault orientation model. The first (quantitative) metric is the weighted root-mean-square (RMS) of the residual deformation signal remaining after the predicted deformation is removed from the data (contour in Figure 3.5c). The standard best-fit model minimizes the RMS residual. The second (qualitative) metric is based on a visual inspection of each slip model and residual, and an assessment of whether the predicted deformation satisfactorily represents key features present in the data (symbols in Figure 3.5c, InSAR solutions in Table 3.1, fault slip distributions in Supplementary Materials). We distinguish between cases where the residual deformation signal is dominated by features that are likely associated with the coseismic signal (Figure 3.6), and those where the residual signal is correlated with topographic features and note when the residual deformation signal is similar between independent interferograms. Throughout, we show the data and prediction on the same color scale, and the data residual on a different color scale to highlight smaller features. The visual inspection method is subjective, but the resulting set of acceptable fault orientations may better reflect the true fault parameter uncertainty than approaches that require accurate estimates of the noise characteristics.

3.5.3 Consistency between InSAR and seismic data

We assess the difference between the earthquake locations inferred using seismic data and the InSAR results. In addition to inverting the InSAR data in the non-linear search approach, we also perform inversions where we fix the strike, dip, and rake to each of the seismic solutions and leave the hypocenter and fault dimensions as free parameters. Effectively, this generates an additional data point for each seismic model in the nonlinear search within a

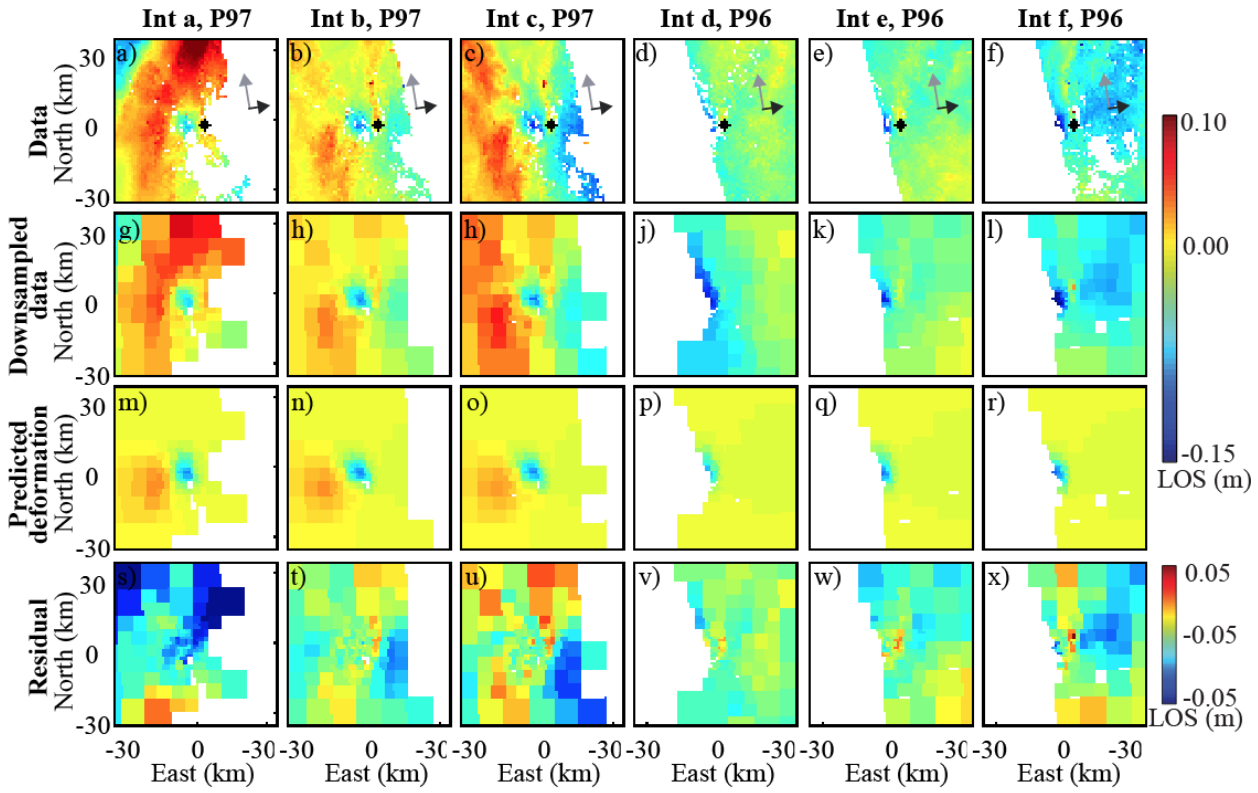

Figure 3.4: Results for the 2010 Salta earthquake. (a)-(f): full-resolution interferograms, (g)-(i): downsampled interferograms, (m)-(r): predicted deformation for fault plane striking 180^o and dipping 30^o to the west (other parameters in Table 3.1), (s)-(x): residual interferogram. Black dot in (a)-(f) is the Salta epicenter determined from the INPRES seismic network. The dates spanned by each interferogram are in Table 3.3.

global search described above (hexagons in Figure 3.5 and later figures).

3.5.4 Consistency between InSAR and geologic data

To relate the events in this study to permanent deformation trends, we use late Cenozoic fault orientations in the Quebrada del Toro region of northwestern Argentina. The fault kinematics are characterized by a change in the horizontal shortening direction from NW-SE to NE-SW that occurred 4.17-0.98 Ma, which may represent an absolute change in

South American plate motion (Marrett et al., 1994; Marrett and Strecker, 2000). The most recent deformation sequence appears to be aligned with the modern South America- Nazca shortening direction (DeMets et al., 1994) and still active today based on kinematics inferred from faults that cut young deposits (Marrett et al., 1994; Marrett and Strecker, 2000) and seismicity in the Jujuy province of northwestern Argentina (Cahill et al., 1992). For the Salta earthquake, we use the Sola and La Poma valley faults located approximately 25 and 40 km, respectively, from the Salta earthquake (Marrett et al., 1994). The Sola fault (Figure 3.7) strikes NW-SE and has accommodated Cenozoic through Quaternary dip-slip motion characterized by WSW-ENE shortening and subvertical extension (Marrett et al., 1994). The La Poma valley faults express moderately SSW-plunging to subhorizontal ENE-WSW shortening and NW-plunging to subvertical extension. Geologic mapping of Quaternary structures has highlighted dominantly NS striking and east dipping faults surrounding the Salta epicenter (Fuertes et al., 1997; García et al., 2013). Although the Quebrada del Toro region is structurally complex, these faults may approximate the modern structural style at the Salta epicenter, because the distance between the faults and the Salta epicenter is less than the crustal thickness of 45-50 km (Lloyd et al., 2010) and the fault kinematics are consistent with plate-scale motion. For the Catamarca earthquake, we rely on the average shortening direction from field sites in the Puna plateau and Argentine foreland (Marrett et al., 1994), which we term the regional shortening direction. The broad consistency between the shortening directions inferred in several studies (Grier et al., 1991; Marrett et al., 1994; Coutand et al., 2001), and the most recent sequence with the modern plate convergence direction suggests that this averaging may be appropriate.

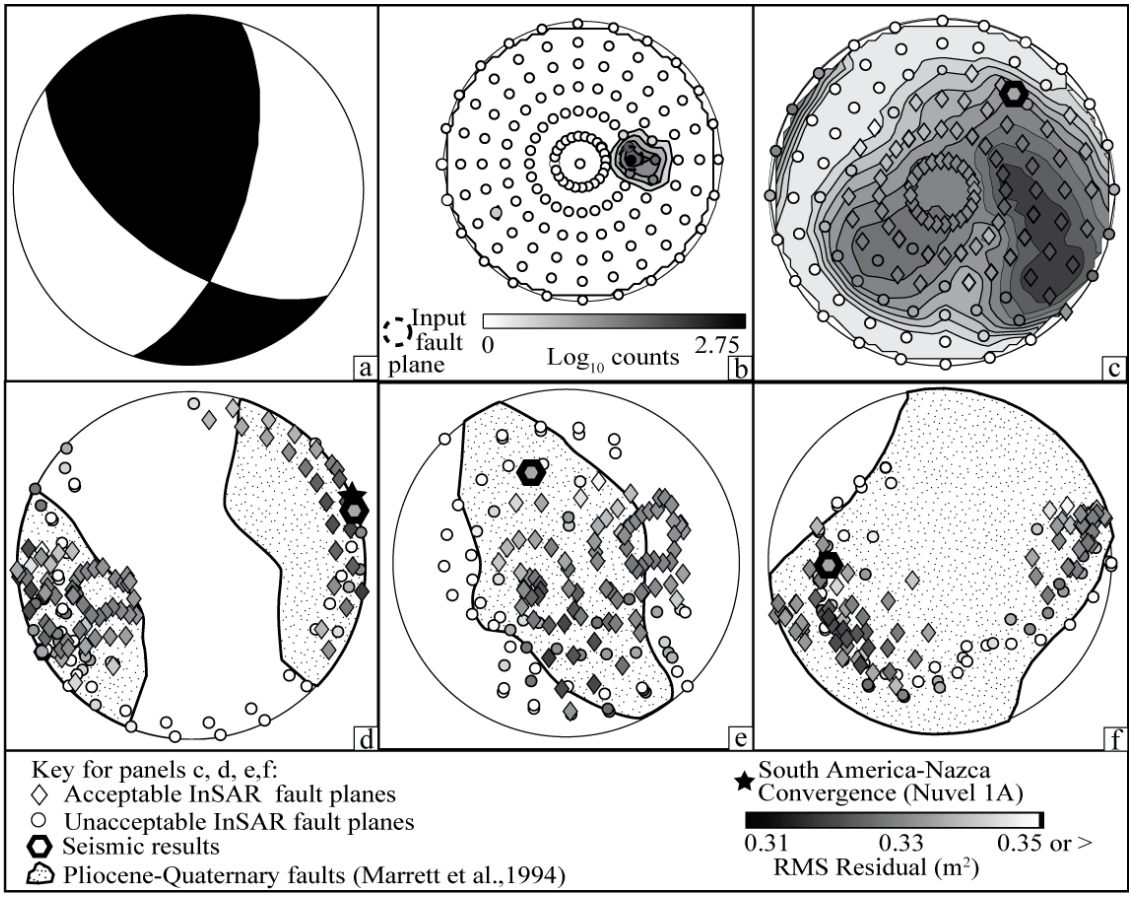

Figure 3.5: Results for the Salta earthquake: Plots are lower-hemisphere stereographic projections showing: (a) Seismic focal mechanism using INPRES data from Sanchez (2012). (b) Monte Carlo sensitivity test from 1000 simulations highlighting preferred fault orientations. (c) Summary of fault parameter inversion: Grid search results are contoured by RMS residual, and the visual assessment results are shown by the diamond and circle symbols. Results from InSAR and seismic models (hexagon) are shown with the same color scheme. (d), (e), (f) Comparison of kinematic indicators (shortening, extension, and slip or striae direction) highlighting the similarity between the geometry of the Salta earthquake, local late Cenozoic faults (Marrett et al., 1994) and the plate-scale shortening direction (DeMets et al., 1994). All stereonets plotted using routines from Allmendinger et al. (2012).

3.5.5 Static Coulomb stress changes

We use the Maule earthquake coseismic slip distribution produced by Lorito et al. (2011) to evaluate if SCS changes promoted the earthquakes in this study. Lorito et al. (2011) incorporated GPS, InSAR and tsunami height observations to invert for the slip along 200 25x25 km^2 patches covering a 625 km long and 200 km wide fault plane. We predict the SCS change in an elastic half-space (Meade, 2007) at each target fault in our grid search using friction coefficients of μ= 0, .2, .4, .6, .8, and 1. We use an elastic half-space, so our analysis does not include any contributions from the 3D heterogeneity in elastic parameters that are likely present near the Mendoza signal, as it is associated with a recently-active caldera.

3.5.6 Depth sensitivity

Of the 11 seismically reported events of M_w 5 or greater that occurred outside the interplate aftershock cluster and within three fault lengths of the Maule epicenter, five additional events (Figure 3.1, Table 3.2) were spanned by good quality interferograms, but lacked a detectable geodetic signal. We evaluated forward earthquake models (Okada, 1985) using the magnitude estimated from seismic data, stress drops of 100 bars, and a range of focal mechanisms. The minimum depth permissible by the InSAR dataset (Table 3.2) is defined as the shallowest fault plane producing a deformation signal that would likely be hidden by the noise in the available interferograms. The North San Juan, Neuquén, and Aisén earthquakes are covered by low quality interferograms that do not merit investigation (Table 3.2).

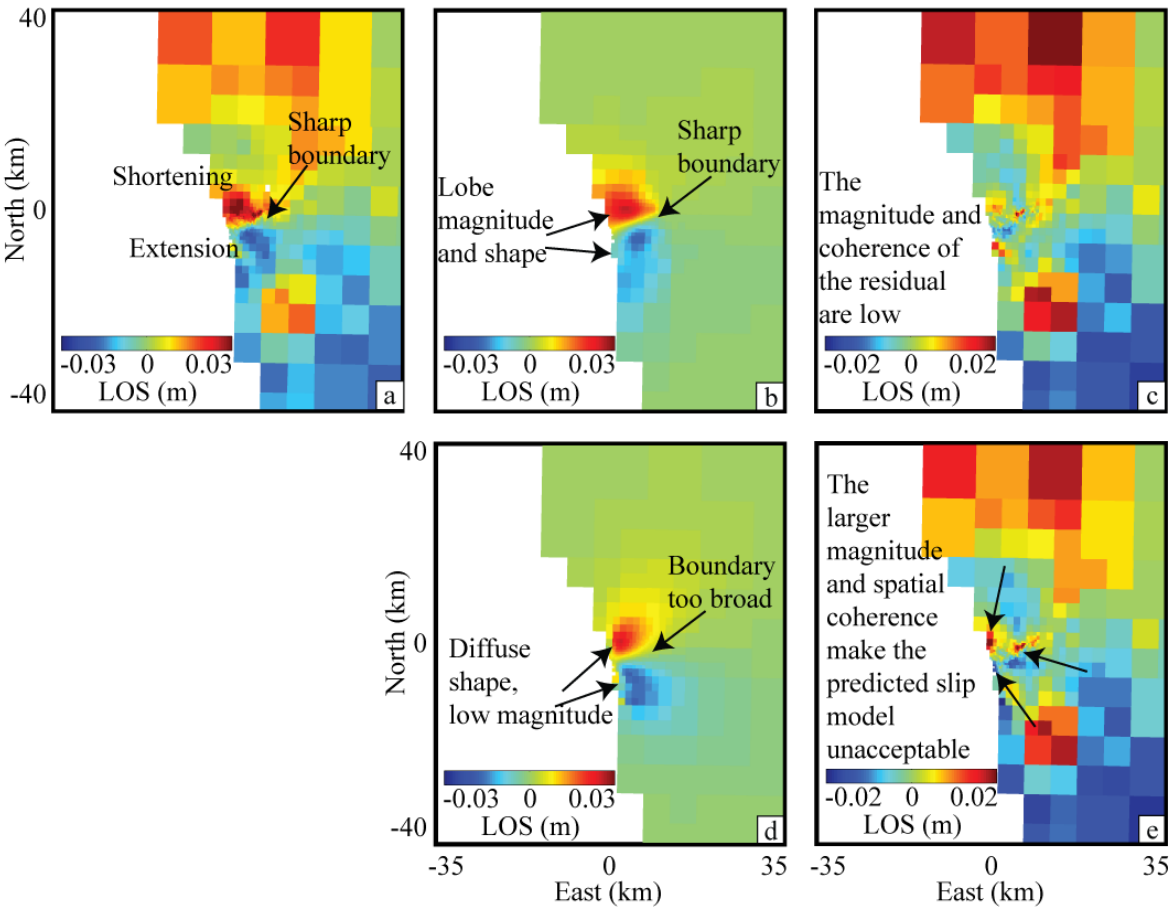

Figure 3.6: Examples of acceptable and unacceptable predicted deformation fields for the 2010 Mw 5.8 Catamarca earthquake. (a) Downsampled Path 99 interferogram spanning 24 March 2008-15 February 2011. (b) and (d) Predicted surface displacement using the acceptable 165/45 and the unacceptable 345/75 fault models, respectively. (c) and (e) data residuals. Arrows highlight key features used to discriminate between acceptable and unacceptable slip models.

3.6 Results

3.6.1 The Salta earthquake

The Salta earthquake, which occurred 9 hours after and 1450 km from the Maule earthquake hypocenter, is the earthquake furthest from the Maule epicenter examined in this

study. The earthquake is associated with two deaths, multiple injuries and infrastructure damage the near the epicenter, and Modified Mercalli seismic intensity values of VII within the city of Salta. Historically, other damaging events such as Talavera del Esteco earthquake in 1692, with an intensity value of VIII and subsequent events in 1844, 1971, 1874, 1908, 1930, 1948, 1973 and 1974 (INPRES, 2005) were felt in the province of Salta. The 2010 Salta earthquake represents a significant peak in the moment release only hours after the Maule earthquake relative to the preceding 36 years, since the advent of the PDE catalog (Figure 3.8). The large increase in seismicity in Salta shortly following the Maule earthquake suggests an association between the two events, where the Salta event may be a result of delayed dynamic triggering due to the passage of the seismic waves (e.g., Hill et al., 1993; Prejean et al., 2004; Velasco et al., 2004; Pollitz et al., 2012).

Using the INPRES seismic network, we estimate the location to be 24.842^{o}S, 65.685^{o}W and the depth to be 8 km, with uncertainties of 2 km and 1.5 km, respectively (Sánchez, 2012). The focal mechanism indicates a left lateral reverse strike-slip solution along a fault with a strike of 127^o, a dip of 58^o to 59^o to the southwest and a rake of 33^o to 34^o.

The Salta earthquake InSAR deformation signal is centered at the southern end of a NNW trending valley, although the entire signal covers several valleys and ridges with 2300 m of topographic relief. The signal (Figures 3.3 and 3.4) includes a lobe of LOS shortening to the east of a lobe of LOS extension that is partially correlated with topography, which together represent a maximum of 9-18 cm of LOS displacement. While increased displacement within coseismic interferograms correlates with the length of the post-seismic timespan (Table 3.3), individual interferograms covering only the postseismic period do not show deformation that exceeds the noise level. For the distributed slip inversion, we divide the interferograms into short and long groups based on the length of the post-seismic timespan (Table 3.3). Our results show no appreciable difference between the two groups.

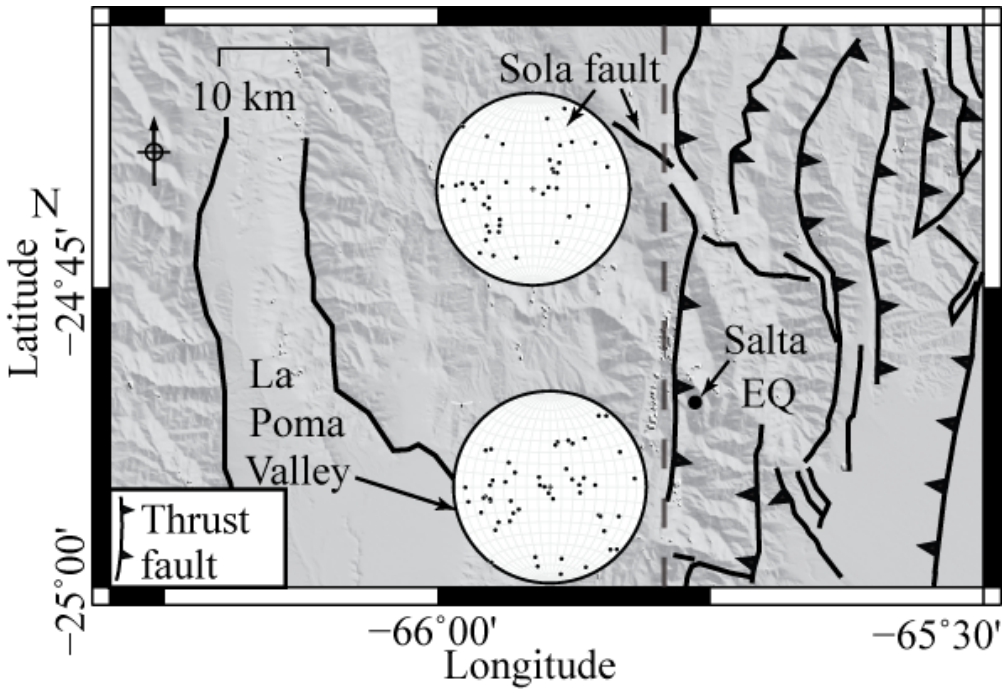

Figure 3.7: Shaded relief map near Salta, NW Argentina showing mapped faults (modified from Fuertes et al., 1997.; García et al., 2013) and poles to the Plio-Quaternary Sola and La Poma valley faults (Marrett et al., 1994).

The weighted RMS residuals for the fixed orientation grid search vary smoothly with fault orientation. NS to NE-SW striking and W to NW dipping faults produce the lowest residuals (Figure 3.5). The 180/30 fault plane model (Figure 3.4, Table 3.1), deemed acceptable by our visual inspection and which we define as the best model for this earthquake, captures the overall shape and magnitude of the deformation signal, and results in small residual deformation features that are not consistent between interferograms.

The large atmospheric features in the data, which are comparable in magnitude and shape to the nearly radially symmetric coseismic signal, allow a wide range of fault orientations to be consistent with the data. Fault orientations associated with low RMS residual values for the Salta earthquake essentially differ only in the degree to which the predicted uplift correlates with topography (Figure 3.9). The 30^o difference in strike between the best-fit

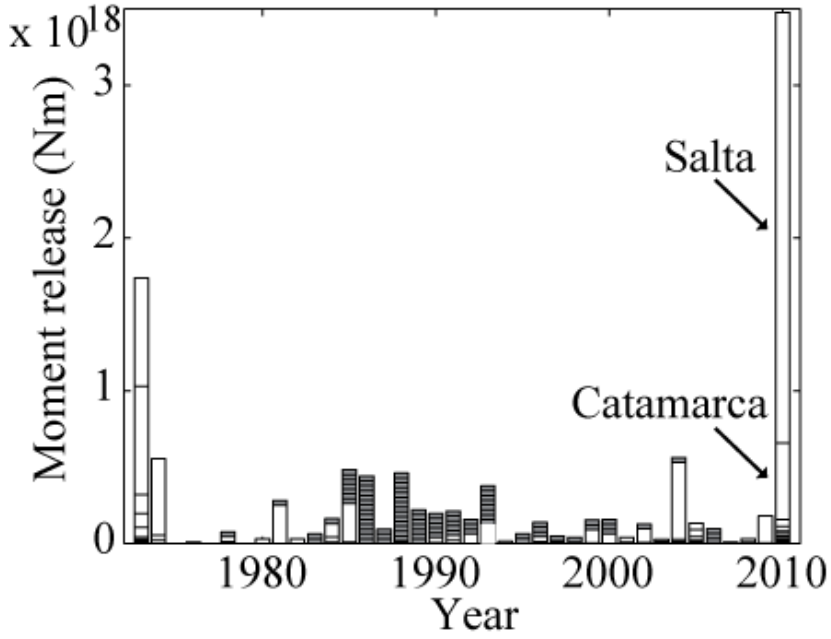

Figure 3.8: Annual seismic moment release during 1973-2010 for shallow events (depth $<$ 50 km) in a 300 km radius about the Salta epicenter contained the PDE catalog. White bars represent the moment release of individual events, and grey bars are sized to M_w 5.0 as an upper bound magnitude estimate for earthquakes without a cited magnitude. Note the increase in seismicity in 2010.

180/30 and the also acceptable 150/30 fault models exceeds the Monte Carlo derived bounds on strike of $\pm 15^o$, suggesting that Monte Carlo sensitivity tests may inadequately capture the permissible parameter range in the presence of spatially non-stationary noise of this magnitude.

The fault location, depth and orientation constrained from seismic data are consistent with the distribution of fault solutions from our InSAR modeling (Figure 5c). The shortening, extension, and slip direction of acceptable models for the Salta earthquake are consistent with the broad distribution of Plio-Quaternary fault kinematics (Figure 3.5d-f, Figure 3.7) and with the South America-Nazca shortening direction (Figure 3.5d). Because the Salta earthquake represents a significant increase in local seismic activity closely linked in time

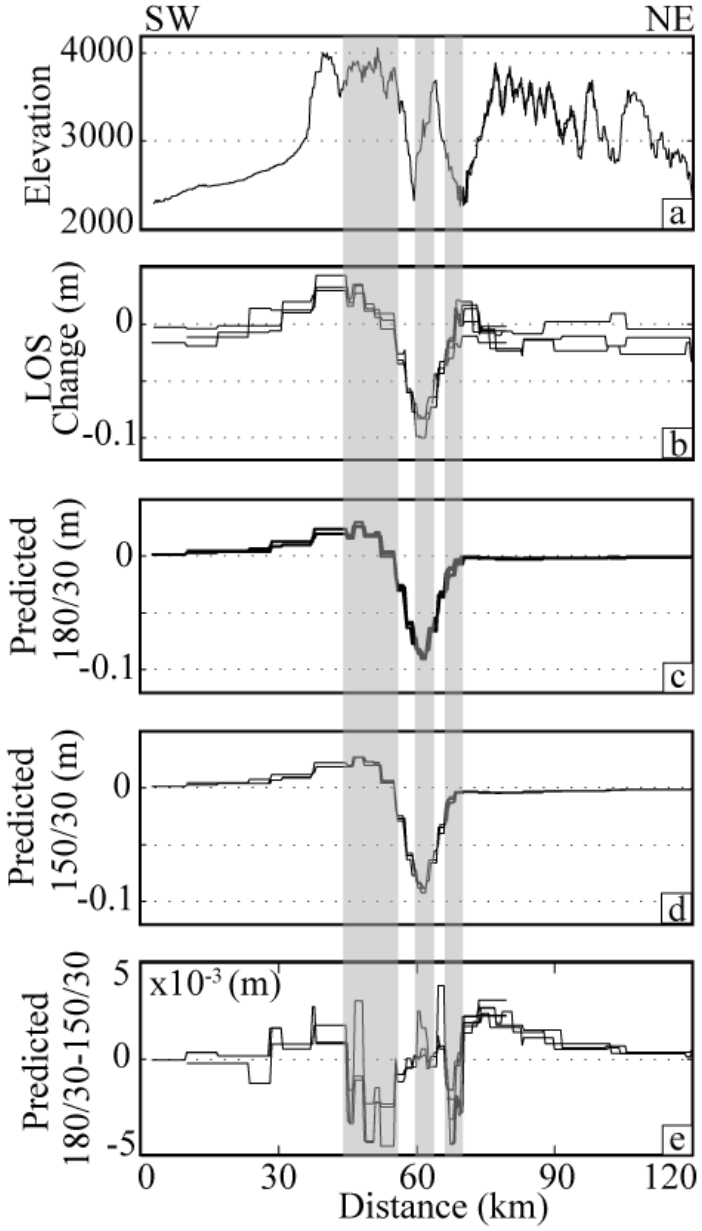

Figure 3.9: SW-NE transect (See Figure 3.3 for location) across the Salta earthquake region showing (a) topography, (b) LOS displacement, (c) predicted deformation for the 180/30 model, (d) predicted deformation for the 150/30 model, and (e) difference between (c) and (d). Grey bars highlight differences between predicted deformation fields, which roughly correlate with topography.

to the Maule earthquake and the inferred fault orientation is consistent with longer-term kinematic indicators, we propose that the Maule earthquake advanced the earthquake cycle along a fault that was already near failure.

3.6.2 The Catamarca earthquakes

On March 8, 2010 and May 3, 2010, earthquakes of M_w 5.8 and M_w 5.1 respectively, occurred along the Salta and Catamarca province border (Figure 3.1). The seismic epicenters in the GCMT catalog are, respectively, 25 and 40 km from the center of a pronounced deformation signal present in five interferograms (Figure 3.10). The signal contains a lobe of 1-2 cm of LOS extension south of a lobe of 2-3 cm of LOS shortening in a region with 500 m of topographic relief. The timing of the interferograms and the fact that there is only a single deformation signal imply that we cannot determine which of the two earthquakes is responsible for the InSAR deformation signal. The magnitude inferred from InSAR is consistent with the larger event (Table 3.1), but we cannot rule out the possibility that the smaller event occurred in the same location and contributed to the observed deformation.

The fault orientation grid search (Figure 3.11b) highlights three regions of low RMS residual fault orientations. The results of the Monte Carlo sensitivity test closely mimic this pattern. Our qualitative approach results in a single fault plane from each of these three regions that is deemed acceptable. The acceptable models capture the sharpness of the transition separating the two deformation lobes and their approximate shape. The E to SE shortening direction deviates from the South America-Nazca convergence direction, but is more consistent with the WNW-ESE regional Mio-Pliocene shortening direction (Marrett et al., 1994).

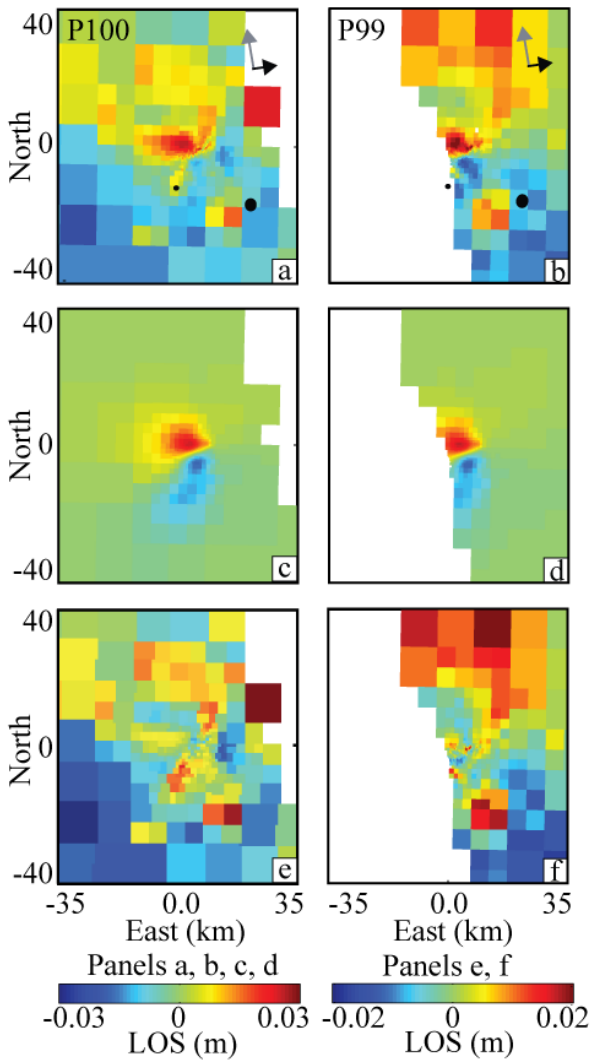

Figure 3.10: Catamarca earthquake: Downsampled interferograms from (a) 24 February, 2008- 17 October 2010 and (b) 24 March 2008-15 February 2011. The large and small dots are, respectively, the M_w 5.8, 8 March 2010 and the M_w 5.1, 8 May 2010 centroid locations from the GCMT catalog. (c) and (d) are predicted interferograms constructed from the preferred visual slip model (fault plane striking 165^o dipping 45^o; Table 3.1). (e) and (f) are residual interferograms. A negative signal is ground motion towards the satellite. Arrows show look direction and satellite azimuth.

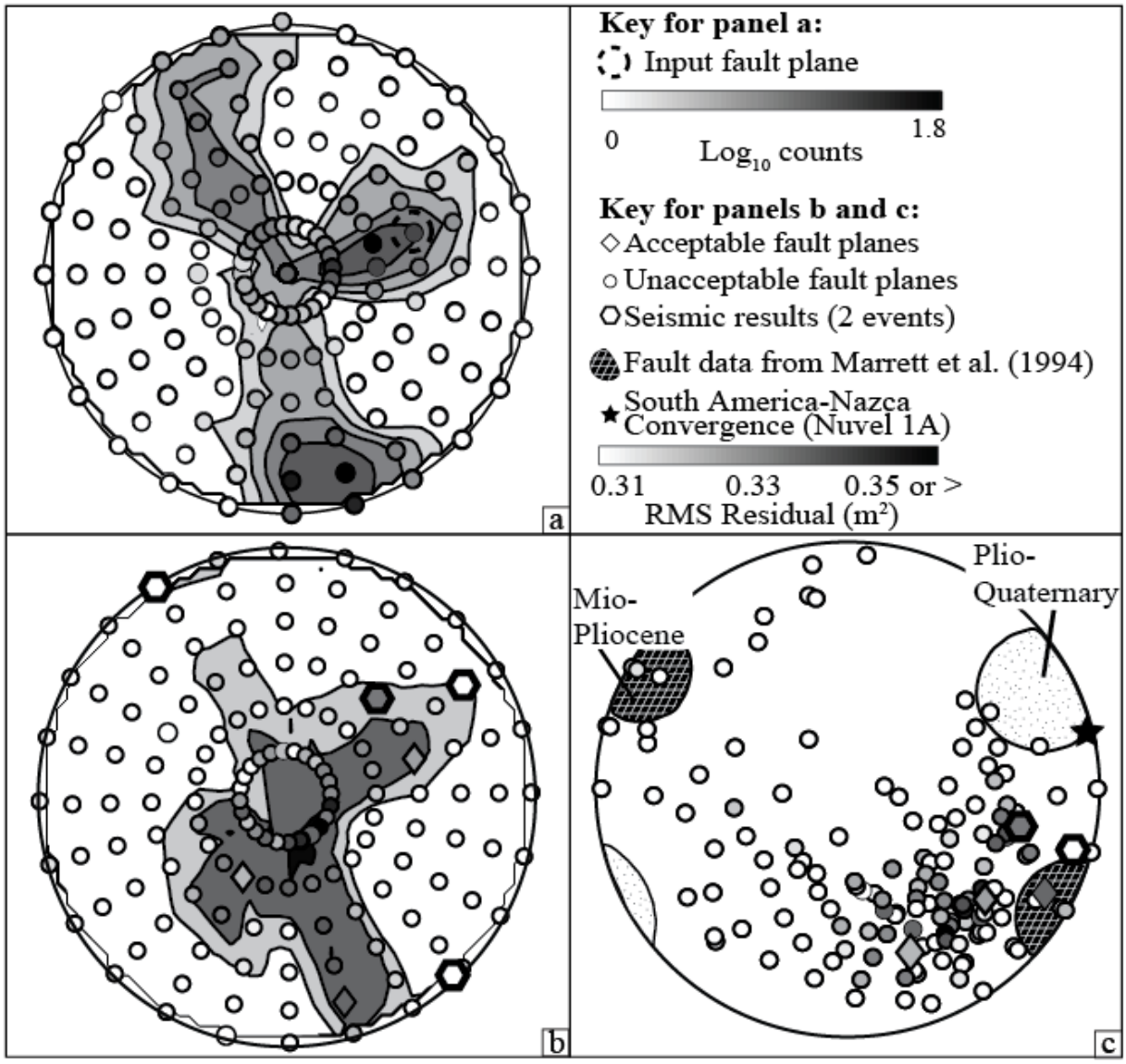

Figure 3.11: Results for the Catamarca earthquake: (a) Monte Carlo sensitivity test from 1000 simulations. (b) Summary of fault parameter inversions. (c) Comparison of shortening directions from our InSAR modeling, Mio- Pliocene faults in the Puna Plateau and foreland (Marrett et al., 1994), and South America-Nazca plate motion (Marrett et al., 1994). Symbols as in Figure 3.5.

We propose two possibilities that place our mechanisms for the Catamarca earthquakes in the context of regional structures and the close temporal relationship to the Maule earthquake, although we cannot completely rule out the possibility that the Maule and Catamarca earthquakes are entirely unrelated. (1) The Catamarca earthquake reactivated a Mio-Pliocene crustal weakness that, while not optimal, is still favorably oriented for rupture. (2) The observed fault orientation is a response to a time-delayed change in stress field orientation triggered by passing waves from the Maule earthquake. A transient change in the stress field after the passage of the Maule earthquake seismic waves that was large enough to overcome the background stress magnitude may explain rupture along unusually oriented faults. Kundu et al., (2012) observe a change in focal mechanism during a six-day swarm 31 days after the M_w 9.2 Sumatra-Andaman earthquake, which may be due a time-delayed increase in pore pressure.

3.6.3 The Mendoza earthquakes

The observed InSAR deformation signal for the Mendoza region is a NE-elongated ellipse with a maximum of 45 cm of LOS shortening within a NS striking structure with 150 m of topographic relief that may be a caldera active since the Holocene (Gonzalez-Ferran, 1995). The deformation signal present in the Mendoza region could also be associated with one or more earthquakes. The PDE catalog contains four shallow M_w 4.1-4.9 earthquakes that occurred during the timespan of the interferograms and that are located within 200 km of the InSAR deformation signal. The INPRES network locates one of these events at a depth of 15 km (Table 3.1), too deep to be detected with InSAR given the present noise level.

The lowest RMS InSAR residual model and the visually acceptable models suggest thrust motion along approximately NS-striking and moderately westward dipping fault planes.

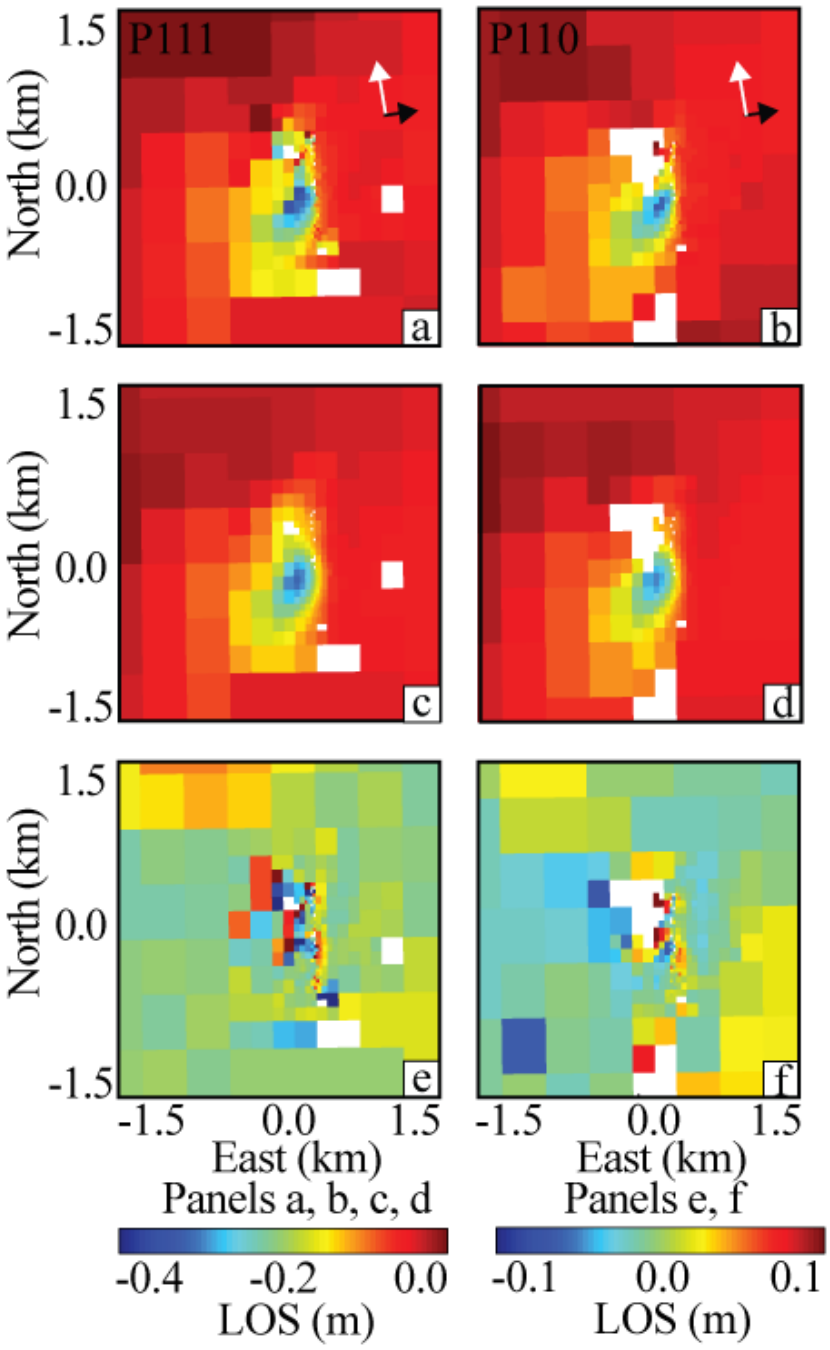

Figure 3.12: Mendoza earthquake: downsampled interferograms spanning (a) 27 February 2008-4 March 2010 and (b) 15 February 2010- 2 April 2010. (c) and (d): predicted deformation for fault plane striking 180^o and dipping 45^o (see Table 3.1 for parameter values), (e) and (f): residual interferograms. A negative signal is ground motion towards the satellite. Arrows show look direction and satellite azimuth.

These models (Figure 3.12) capture the deformation signal's shape, while unacceptable models predict a broader but lower magnitude signal. The similarity between the results of the visual inspection and the Monte Carlo sensitivity tests suggests, that in this case, the Monte Carlo sensitivity tests characterize the range of likely fault parameters well. For acceptable fault planes, we predict an E-ESE shortening (Figure 3.13c), somewhat aligned with the South America-Nazca convergence direction. The SCS increase due to the Maule earthquake is 1-3 bars for the range of frictional parameters explored (Figure 3.13d), which may be sufficient to promote seismicity (Lin and Stein, 2004).

The significant difference in location (>100km), magnitude and depth (Table 3.1) between the INPRES network location and the InSAR results suggests that the two data types are associated with different subsets of the four potential earthquakes present in the PDE catalog. The inferred location and depth from seismic data in the INPRES network suggests that at least one of the Mendoza earthquakes may be related to structures within the Cuyana Basin (Figure 3.14). The observed geometry is consistent with the reactivation of Triassic normal faults (Ramos and Kay, 1991), which resulted in the uplift of anticlinal structures active in regional earthquakes in 1861 and 1929 (Alvarado and Araujo, 2011), or faulting on a deeper fault plane such as the one activated in the M_w 5.9 1985 Mendoza earthquake (e.g., Brooks et al., 2000; Chiaramonte et al., 2000). The InSAR data suggests that at least one of the earthquakes occurred in the Caldera del Atuel which is the northernmost of five calderas in the Andean Southern Volcanic Zone that exhibited NS trending subsidence following the Maule earthquake (Pritchard et al., 2013). Pritchard et al., (2013) propose that the Maule earthquake perturbed a system of regional NS striking faults controlling a hydrothermal or magmatic system, resulting in a change in fluid storage that is associated with the observed subsidence. The Mendoza earthquake may have occurred on one such NS striking fault. The fault plane was suitably oriented for slip due to the increased SCS following the Maule

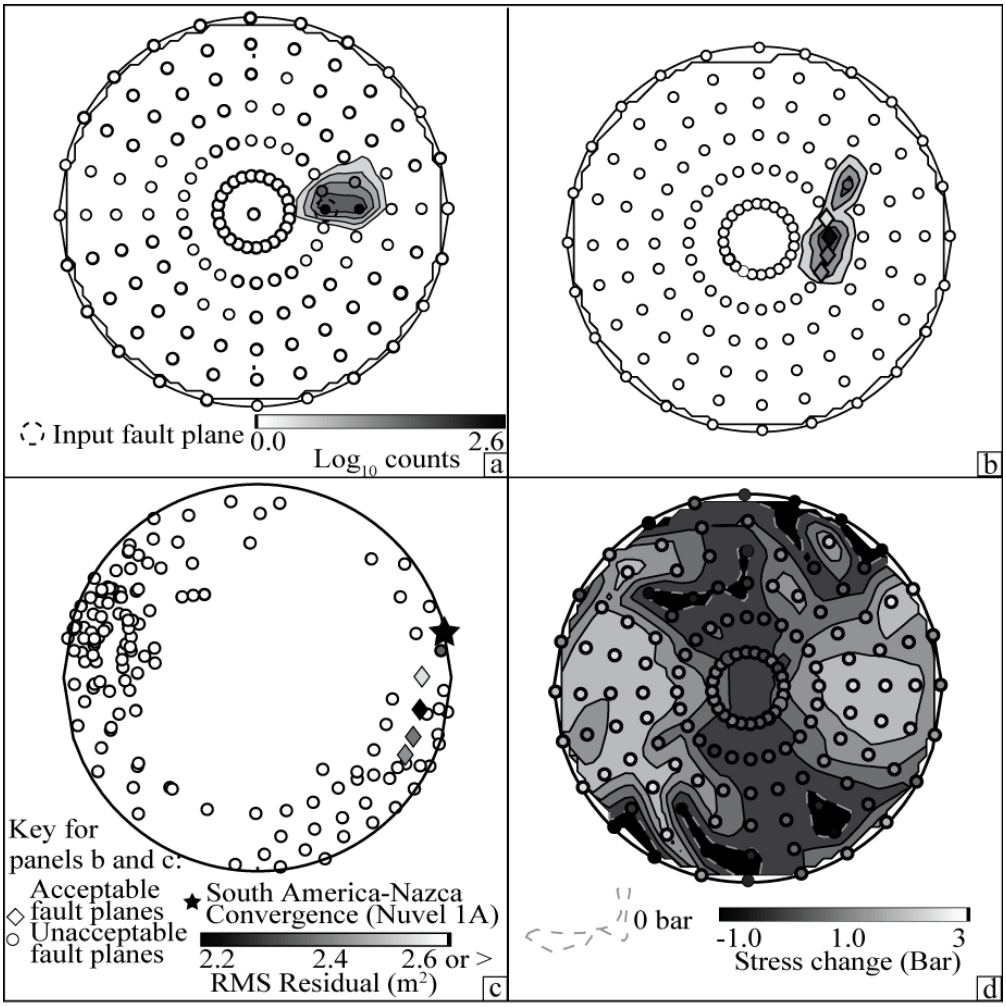

Figure 3.13: Results for the Mendoza earthquake: (a) Monte Carlo sensitivity test from 1000 simulations. (b) Summary of fault parameter inversions. (c) Comparison of Mendoza earthquake and South America-Nazca shortening directions (Marrett et al., 1994). (d) SCS changes due to the Maule earthquake with μ=0.4. Symbols as in Figure 3.5.

earthquake, and the release of hydrothermal fluids may have increased pore fluid pressure to weaken the rock and further promote slip.

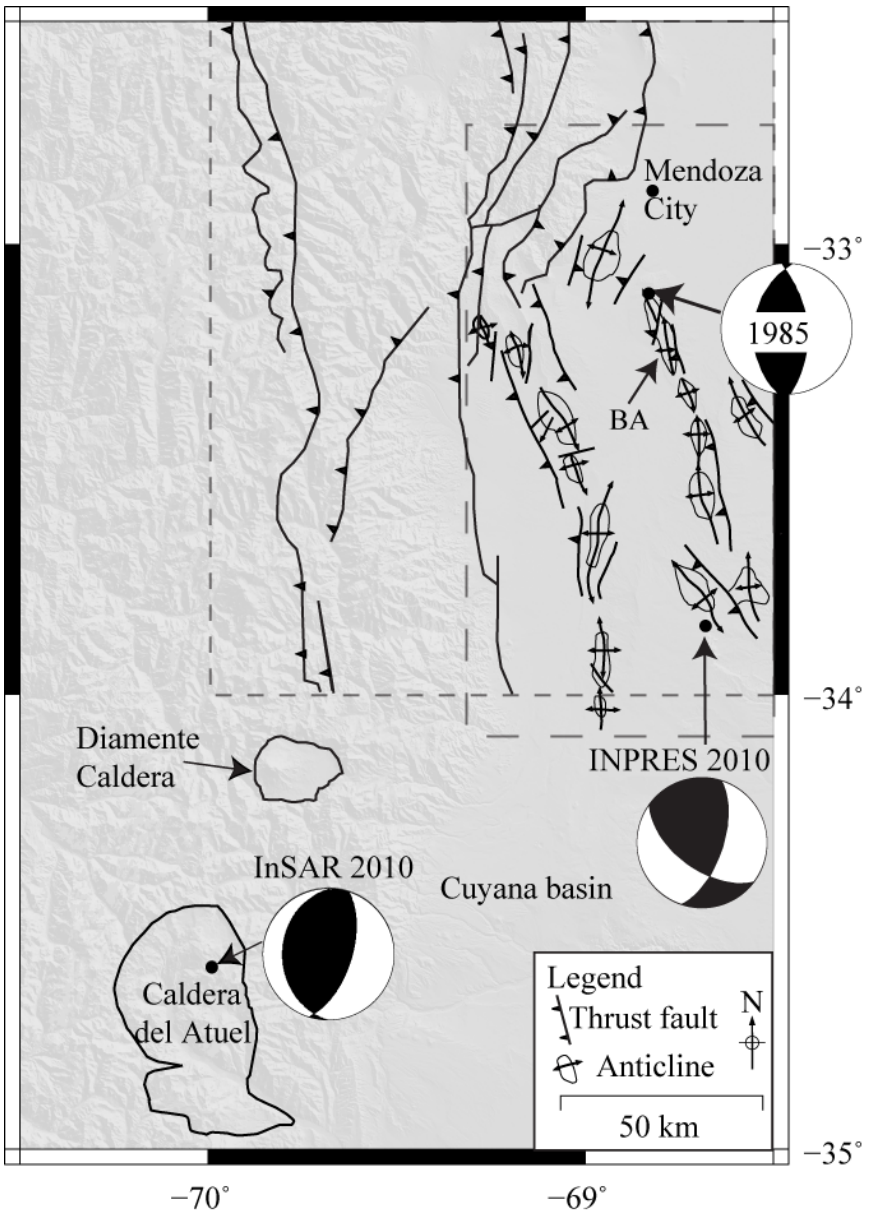

Figure 3.14: Shaded relief map highlighting the Mendoza earthquake locations and focal mechanisms from the InSAR analysis and the INPRES network. The 1985 M_w 5.9 earthquake occurred near the city of Mendoza, likely on neotectonic basement faults and not within the Barrancas anticline (BA) (Chiaramonte et al., 2000). Mapped geologic structures within the coarsely and finely dashed boxes, respectively, are modified from Dellapé and Hegedus (1993) and Sarewitz (1988), and the outline of the Caldera del Atuel is modified from Gonzalez-Ferran (1995).

3.6.4 Other earthquakes

The deformation signal associated with the Atacama, San Juan, Tunuyán, South Mendoza, and North Aisén earthquakes (Figure 3.13) is not visible within the InSAR dataset, despite the presence of high-quality interferograms. The estimated minimum depths for these events constrained by the noise level in the interferograms (bar in Figure 3.15; Table 3.2) does not exceed the depths predicted by seismology. The Atacama earthquake occurred near the coastline, with the GCMT location 10 km offshore. If the event occurred under water at shallow depths, we would not expect any observable deformation and the constraints on depth would not be applicable.

3.7 Discussion

The existence of completely independent InSAR and seismic data sets improves our ability to assess uncertainties on the inferred earthquake parameters. Particularly in regions with low instrument density where seismic results from regional and global catalogs may be associated with a location uncertainty of 50 km (e.g., Weston et al., 2011; Devlin et al., 2012), definitively associating an observed InSAR signal with a particular earthquake may be impossible. The higher local station density used to generate the INPRES catalog is reflected in the smaller differences in the estimated locations between the InSAR results and the INPRES catalog relative to the PDE and GCMT catalogs. Still, differences in the

Earthquake	**Time/ Date**	**Lat. (^{o})**	**Long (^{o})**	**Depth (km)**	**M_w**	**Minimum depth (km)**
Atacama (*) (GCMT)	14:52:11/ 26/03/10	-28.11	-71.31	41	6.1	17.5±2.5
Atacama (*) (PDE)	14:52:07/ 26/03/10	-27.95	-70.82	42	6.3	17.5±2.5
San Juan (INPRES)	06:51:17/ 27/02/10	-31.66	-69.14	24	6.0	10±1
Tunuyán (INPRES)	08:15:17/ 28/02/10	-33.84	-68.68	15	4.9	1.5±.5
S Mendoza (PDE)	10:53:53/ 04/03/10	-35.87	-69.919	35	5.0	1
North Aisen (PDE)	17:38:33/ 03/03/10	-43.84	-72.56	10	5.4	1.5±.5
North San Juan (PDE)	21:56:43 02/03/10	-30.25	-69.02	36	5.1	N/A
Neuquen (PDE)	02:09:35 02/03/10	-39.76	-71.37	25	5.1	N/A
Aisen (PDE)	09:32:21 18/03/10	-44.18	-72.83	4	5.2	N/A

Table 3.2: Earthquakes with no observed deformation: The first six columns are results from seismicity, and the minimum depth is based on the noise level in the InSAR dataset. N/A indicates earthquakes where the InSAR quality was poor. (*) indicates that earthquakes that were near the coastline.

predicted locations, depths and magnitudes for the Mendoza signal (Figure 15, Table 3.1) could indicate that the InSAR and seismic data were affected by different events, such as the possible scenario that the InSAR signal was associated with groundwater or aseismic motion (e.g., Barnhart and Lohman, 2013b) instead of coseismic shaking. The InSAR inversions consistently predict a shallower depth than is predicted from seismic data (Figure 3.15), a result that has been found for other earthquakes (Weston et al., 2011).

When the noise statistics of a dataset are poorly characterized, Monte Carlo tests seem to perform poorly at quantifying the appropriate error bounds. Our visual grid search approach provides an alternative approach that may be useful as an initial step while characterizing

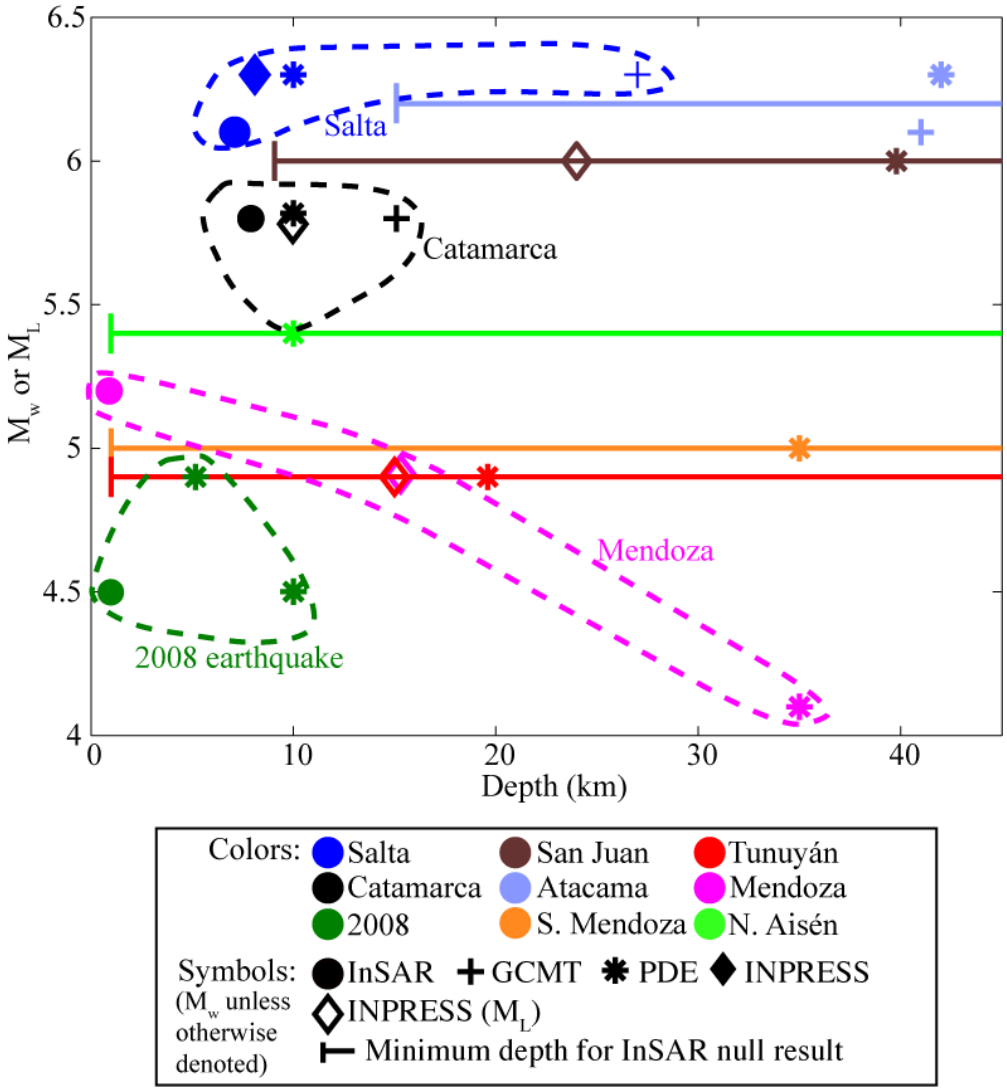

Figure 3.15: The role of depth in InSAR event detection: comparison of event magnitude and depth for events associated with quality interferograms. Dashed circles show events detectable with InSAR. The Mendoza InSAR signal may represent one of three seismic recordings in the PDE catalog: here we plot the event closest to the InSAR signal. Note the difference in inferred depth and magnitude between the InSAR and seismic solutions, particularly for the Mendoza earthquakes where the InSAR and seismic records may be associated with different events. The 2008 earthquake, included as a reference for low magnitude detectability, occurred in San Juan, Argentina. The InSAR signal spans two events in the PDE catalog located within 15 km of the InSAR epicenter.

Interferogram dates	**Path**	**Days since Maule**	**Max. LOS disp. (cm)**	**Group**	**Fig. 3.4**
4 Oct 2007- 11 April 2010	97	43	13	Short	a
5 April 2008- 27 May 2010	97	89	16	Long	b
5 April 2008- 27 August 2010	97	181	18	Long	c
7 Feb 2010- 25 March 2010	96	26	9	Short	d
23 Dec 2009- 25 March 2010	96	26	12	Short	e
2 Feb 2008- 25 June 2010	96	118	14	Long	f

Table 3.3: Salta earthquake interferograms: Group refers to the interferogram division into the short and long groups due to post-seismic deformation. Lettering in last column is as in Fig. 3.4

an earthquake. When a signal lacks a distinctive component (e.g. sharp gradient due to strike-slip motion), the signal may be easily modulated by noise, and the stereonet plot may illuminate the broad range of parameters that provide reasonable fits to the data. This technique for selecting preferred slip models is undoubtedly highly subjective, but highlights the importance of accurate noise estimation and can act as a check against more automated approaches for characterizing a best-fit solution and the associated uncertainties. This work may serve as an initial step towards a more rigorous method for accounting for the non-stationary nature of noise in geodetic datasets.

The InSAR results suggest that the earthquakes that were likely triggered by the Maule earthquake occurred at relatively shallow depths. The triggered earthquakes may suggest that the seismic waves generated by the Maule earthquake weakened portions of the shallow crust. The weakening of fault zones associated with dynamic stresses has been studied in California. Vidale and Li (2003) show that the 1992 M_w 7.3 Landers and the 1999 M_w 7.1 Hector Mine earthquakes decreased the seismic velocity of the upper crust surrounding a

neighboring fault. They propose that the coseismic shaking associated with these two events further weakened the already compliant fault zone rocks. Li et al. (2007) show that variations in seismic velocity in the Parkfield segment of the San Andreas fault zone extend to depths of $\sim$ 6 km. Understanding the potential of the Maule earthquake to have weakened fault zones in the far-field requires additional knowledge about the magnitude of stress required to significantly alter the mechanical properties of fault rocks.

3.8 Conclusion

We use seismic and InSAR data to constrain the location and geometry of coastal, volcanic-arc and back-arc seismic events in Argentina and Chile associated with the Maule earthquake. We focus on how noise from ionospheric features and topographically correlated water vapor affects fault parameter accuracy, and find that the range of fault parameters consistent with the data depends on how distinct the shapes of the deformation signals are from the atmospheric and ionospheric artifacts. The events in this study suggest that the Maule earthquake triggered seismic activity along structures that were favorably oriented with the plate convergence direction and late Cenozoic deformation trends. The observed events do not require, for instance, low background stresses that could easily be overwhelmed by static or dynamic stress changes due the Maule event. Additional earthquake observations from higher-quality seismic data from local dense temporary networks and geodetic measurements would strengthen constraints on stress field evolution after a mega-thrust event, and will improve our understanding of how the redistribution of crustal stress following a large earthquake impacts future seismicity, our knowledge of stress evolution throughout the seismic cycle and hazard assessment.

3.9 Acknowledgements

We would like to thank R. Allmendinger for useful discussions on the structural geology near Salta, Argentina and for providing a bounty of structural data. We also thank two anonymous reviewers for constructive reviews. C. Scott was supported by National Science Foundation grant EAR-0911464 and by a grant from the American Chemical Society Petroleum Research Fund.

3.10 References

Allmendinger, R.W., Cardozo, N., Fisher, D.M., 2012. Structural Geology Algorithms. Cambridge University Press.

Alvarado, P., Araujo, M., 2011. La importancia de las redes sísmicas locales en la caracterización de la sismicidad cortical más peligrosa de la Argentina, in: Conferencia Internacional En Homenaje Al Ing. Alberto Giesecke M., Lima, Perú. 57-72.

Aki, K., Richards, P.J., 1980. Quantitative seismology. Freeeman, San Francisco.

Aron, F., Allmendinger, R.W., Cembrano, J., González, G., Yáñez, G., 2013. Permanent fore-arc extension and seismic segmentation: Insights from the 2010 Maule earthquake, Chile. Journal of Geophysical Research: Solid Earth 118, 724-739.

Barnhart, W.D., Lohman, R.B., 2010a. Evaluation of earthquake triggering during the 2005-2008 earthquake sequence on Qeshm Island, Iran. Journal of Geophysical Research 115.

Barnhart, W.D., Lohman, R.B., 2010b. Automated fault model discretization for inversions for coseismic slip distributions. Journal of Geophysical Research 115.

Barnhart, W.D., Lohman, R.B., 2013a. Characterizing and estimating noise in InSAR and InSAR time series with MODIS. Geochemistry, Geophysics, Geosystems 13.

Barnhart, W.D., Lohman, R.B., 2013b. Phantom earthquakes and triggered aseismic creep: Vertical partitioning of strain during earthquake sequences in Iran. Geophysical Research Letters 40, 819-823.

Brooks, B. A., E. Sandvol, and A. Ross, 2000. Fold style inversion: Placing probabilistic constraints on the predicted shape of blind thrust faults, Journal of Geophysical Research, 105(B6), 13281.

Cahill, T., Isacks, B.L., Whitman, D., Chatelain, J.-L., Perez, A., Chiu, J.M., 1992. Seismicity and tectonics in Jujuy Province, northwestern Argentina. Tectonics 11, 944-959.

Chiaramonte, L., Ramos, V.A., Araujo, M., 2000. Estructura y sismotectónica del anticlinal Barrancas, cuenca Cuyana, provincia de Mendoza. Revista de la Asociasión Geológica Argentina 55, 309-336.

Coutand, I., Cobbold, P.R., de Urreiztieta, M., Gautier, P., Chauvin, A., Gapais, D., Rossello, E.A., López-Gamundí, O., 2001. Style and history of Andean deformation, Puna plateau, northwestern Argentina. Tectonics 20, 210-234.

Dellapé, D.A., Hegedus, A.G., 1993. Inversión estructural de la Cuenca Cuyana y su relación con las acumulaciones de hidrocarburos. Actas del 12^o Congresso Geológico Argentino y 2^o Congresso de Exploración de Hidrocarburos 3, 211-218.

DeMets, C., Gordon, R.G., Argus, D.F., Stein, S., 1994. Effect of recent revisions to the geomagnetic reversal time scale on estimates of current plate motions. Geophysical Research Letters 21, 2191-2194.

Devlin, S., Isacks, B.L., Pritchard, M.E., Barnhart, W.D., Lohman, R.B., 2012. Depths and focal mechanisms of crustal earthquakes in the central Andes determined from teleseismic waveform analysis and InSAR. Tectonics 31.

Dziewonski, A.M., Chou, T.-A., Woodhouse, J.H., 1981. Determination of earthquake source parameters from waveform data for studies of global and regional seismicity. Journal of Geophysical Research 86, 2825.

Ekström, G., Nettles, M., Dziewoński, A.M., 2012. The global CMT project 2004-2010: Centroid-moment tensors for 13,017 earthquakes. Physics of the Earth and Planetary Interiors 200-201, 1-9.

Elliott, J.R., Biggs, J., Parsons, B., Wright, T.J., 2008. InSAR slip rate determination on the Altyn Tagh Fault, northern Tibet, in the presence of topographically correlated atmospheric delays. Geophysical Research Letters 35.

Emardson, T.R., 2003. Neutral atmospheric delay in interferometric synthetic aperture radar applications: Statistical description and mitigation. Journal of Geophysical Research 108.

Farías, M., Comte, D., Roecker, S., Carrizo, D., Pardo, M., 2011. Crustal extensional

faulting triggered by the 2010 Chilean earthquake: The Pichilemu Seismic Sequence. Tectonics 30.

Farr, T.G., Rosen, P.A., Caro, E., Crippen, R., Duren, R., Hensley, S., Kobrick, M., Paller, M., Rodriguez, E., Roth, L., Seal, D., Shaffer, S., Shimada, J., Umland, J., Werner, M., Oskin, M., Burbank, D., Alsdorf, D., 2007. The Shuttle Radar Topography Mission. Reviews of Geophysics 45.

Fuertes, A., García, R.F., Moya Ruíz, F., Rocha, V., Abraham, C., Dib Ashur, P., 1997. Hoja hidrogeológica Salta. Mapa geológico 1:250.000. Universidad Nacional de Salta, Consejo de Investigación.

Fujiwara, S., Rosen, P.A., Tobita, M., Murakami, M., 1998. Crustal deformation measurements using repeat-pass JERS 1 synthetic aperture radar interferometry near the Izu Peninsula, Japan. Journal of Geophysical Research 103, 2411.

García, V.H., Hongn, F., Cristallini, E.O., 2013. Late Miocene to recent morphotectonic evolution and potential seismic hazard of the northern Lerma valley: Clues from Lomas de Medeiros, Cordillera Oriental, NW Argentina. Tectonophysics.

Gomberg, J., Blanpied, M.L., Beeler, N.M., 1997. Transient triggering of tear and distant earthquakes. Bulletin of the Seismological Society of America 87, 294-309.

Gonzalez-Ferran, O., 1995. Volcanes de Chile. Instituto Geografico Militar.

Grier, M.E., Salfity, J.A., Allmendinger, R.W., 1991. Andean reactivation of the Cretaceous Salta rift, northwestern Argentina. Journal of South American Earth Sciences 4, 351-372.

Hardebeck, J., 2010. Aftershocks are well aligned with the background stress field, contradicting the hypothesis of highly heterogeneous crustal stress. Journal of Geophysical Research 115.

Hardebeck, J.L., 2012. Coseismic and postseismic stress rotations due to great subduction zone earthquakes. Geophysical Research Letters 39.

Hicks, E.C., Bungum, H., Lindholm, C.D., 2000. Stress inversion of earthquake focal mechanism solutions from onshore and offshore Norway. Norsk Geologisk Tidsskrift 80, 235-250.

Hetland, E. A., Muse, P., Simons, M., Lin, Y. N., Agram, P. S., DiCaprio, C. J., 2012. Multiscale InSAR time series (MInTS) analysis of surface deformation. Journal of Geophysical Research 117.

Hill, D.P., Reasenberg, P.A., Michael, A., Arabaz, W.J., Beroza, G., Brumbaugh, D., Brune, J.N., Castro, R., Davis, S., dePolo, D., Ellsworth, W.L., Gomberg, J., Harmsen, S., House, L., Jackson, S.M., Johnston, M.J.S., Jones, L., Keller, R., Malone, S., Munguia, L., Nava, S., Pechmann, J.C., Sanford, A., Simpson, R.W., Smith, R.B., Stark, M., Stickney, M., Vidal, A., Walter, S., Wong, V., Zollweg, J., 1993. Seismicity remotely triggered by the magnitude 7.3 Landers, California, earthquake. Science 260, 1617-1623.

INPRES, 2005. Manual de Prevención Sísmica.

Jay, J.A., Pritchard, M.E., West, M.E., Christensen, D., Haney, M., Minaya, E., Sunagua, M., McNutt, S.R., Zabala, M., 2012. Shallow seismicity, triggered seismicity, and ambient noise tomography at the long-dormant Uturuncu Volcano, Bolivia. Bulletin of Volcanology 74, 817-837.

King, G.C.P., Stein, R.S., Lin, J., 1994. Static stress changes and the triggering of earthquakes. Bulletin of the Seismological Society of America 84, 935-953.

Kundu, B., Legrand, D., Gahalaut, K., Gahalaut, V.K., Mahesh, P., Kamesh Raju, K.A., Catherine, J.K., Ambikapthy, A., Chadha, R.K., 2012. The 2005 volcano-tectonic earthquake swarm in the Andaman Sea: Triggered by the 2004 great Sumatra-Andaman earthquake. Tectonics 31.

Li, Z., Muller, J.-P., Cross, P., 2005. Interferometric synthetic aperture radar (InSAR) atmospheric correction: GPS, Moderate Resolution Imaging Spectroradiometer (MODIS), and InSAR integration. Journal of Geophysical Research 110.

Li, Y.-G., P. Chen, E. S. Cochran, and J. E. Vidale, 2007. Seismic velocity variations on the San Andreas fault caused by the 2004 M6 Parkfield Earthquake and their implications. Earth, Planets and Space, 59(1), 21Ð31.

Lienert, B.R.E., 1994. A computer program for locating earthquakes locally, regionally and globally. Hawaii Institute of Geophysics and Planetology. Lin, J., Stein, R.S., 2004. Stress triggering in thrust and subduction earthquakes and stress interaction between the southern San Andreas and nearby thrust and strike-slip faults. Journal of Geophysical Research 109.

Lloyd, S., van der Lee, S., Franca, G.S., Assumpão, M., Feng, M., 2010. Moho map of South America from receiver functions and surface waves. Journal of Geophysical Research 115.

Lohman, R.B., Simons, M., Savage, B., 2002. Location and mechanism of the Little Skull Mountain earthquake as constrained by satellite radar interferometry and seismic waveform modeling. Journal of Geophysical Research 107.

Lohman, R. B., Simons, M., 2005a. Locations of selected small earthquakes in the Zagros mountains. Geochemistry, Geophysics, Geosystems, 6(3), doi:10.1029/2004GC000849.

Lohman, R.B., Simons, M., 2005b. Some thoughts on the use of InSAR data to constrain models of surface deformation: Noise structure and data downsampling. Geochemistry, Geophysics, Geosystems, 6(1), doi:10.1029/2004GC000841.

Lorito, S., Romano, F., Atzori, S., Tong, X., Avallone, A., McCloskey, J., Cocco, M., Boschi, E., Piatanesi, A., 2011. Limited overlap between the seismic gap and coseismic slip of the great 2010 Chile earthquake. Nature Geoscience 4, 173-177.

Marrett, R.A., Allmendinger, R.W., Alonso, R.N., Drake, R.E., 1994. Late Cenozoic tectonic evolution of the Puna Plateau and adjacent foreland, northwestern Argentine Andes. Journal of South American Earth Sciences 7, 179-207.

Marrett, R., Strecker, M.R., 2000. Response of intracontinental deformation in the central Andes to late Cenozoic reorganization of South American Plate motions. Tectonics 19, 452-467.

Massonnet, D., Feigl, K., Rossi, M., Adragna, F., 1994. Radar interferometric mapping of deformation in the year after the Landers earthquake. Nature 369, 227-230.

Meade, B.J., 2007. Algorithms for the calculation of exact displacements, strains, and stresses for triangular dislocation elements in a uniform elastic half space. Computers & Geosciences 33, 1064-1075.

Okada, Y., 1985. Surface deformation due to shear and tensile faults in a half-space. Bulletin of the Seismological Society of America 75, 1135-1154.

Peng, Z., Hill, D.P., Shelly, D.R., Aiken, C., 2010. Remotely triggered microearthquakes and tremor in central California following the 2010 M_w 8.8 Chile earthquake. Geophysical Research Letters 37.

Pollitz, F.F., Stein, R.S., Sevilgen, V., Bürgmann, R., 2012. The 11 April 2012 east Indian Ocean earthquake triggered large aftershocks worldwide. Nature 490, 250-253.

Prejean, S.G., Hill, D.P., Brodsky, S.E., Hough, S.E., Johnston, M.J.S., Malone, S.D., Oppenheimer, D.H., Pitt, A.M., Richards- Dinger, K.B., 2004. Remotely triggered seismicity on the United States West Coast following the M_w 7.9 Denali Fault Earthquake. Bulletin of the Seismological Society of America 94, S348-S359.

Pritchard, M.E., Jay, J.A., Aron, F., Henderson, S.T., Lara, L.E., 2013. Subsidence at southern Andes volcanoes induced by the 2010 Maule, Chile earthquake. Nature Geoscience 6, 632-636.

Ramos, V.A., Kay, S.M., 1991. Triassic rifting and associated basalts in the Cuyo basin, central Argentina. Geological Society of America Special Papers 265, 79-92.

Roeloffs, E., Sneed, M., Galloway, D.L., Sorey, M.L., Farrar, C.D., Howle, J.F., Hughes, J., 2003. Water-level changes induced by local and distant earthquakes at Long Valley caldera, California. Journal of Volcanology and Geothermal Research 127, 269-303.

Rosen, P.A., Hensley, S., Peltzer, G., Simons, M., 2004. Updated repeat orbit interferometry package released. Eos, Transactions American Geophysical Union 85, 47.

Sambridge, M., 1999. Geophysical inversion with a neighbourhood algorithm-I. Searching a parameter space. Geophysical Journal International 138, 479-494.

Sánchez, G., 2012. Estudio de la fuente sísmica del terremoto de Salta del 27 de Febrero de 2010 (Final thesis work). Faculty of Exact, Physical and Natural Sciences, National University of San Juan.

Sarewitz, D., 1988. High rates of late Cenozoic crustal shortening in the Andean foreland, Mendoza Province, Argentina. Geology 16, 1138-1142.

Sevilgen, V., Stein, R.S., Pollitz, F.F., 2012. Stress imparted by the great 2004 Sumatra earthquake shut down transforms and activated rifts up to 400 km away in the Andaman Sea. Proceedings of the National Academy of Sciences 109, 15152-15156.

Smoke, J.A., 2003. FOCMEC: FOcal MEChanism determinations. International Handbook of Earthquake and Engineering Seismology, ed. Lee, W. H. K., Kanamori, H., Jennings, P.C., and Kisslinger, C., International geophysics series. San Diego: Academic Press, Amsterdam; Boston.

Stein, R.S., Lisowski, M., 1983. The 1979 Homestead Valley Earthquake Sequence, California: Control of aftershocks and postseismic deformation. Journal of Geophysical Research 88, 6477.

Toda, S., Stein, R.S., Beroza, G.C., Marsan, D., 2012. Aftershocks halted by static stress shadows. Nature Geoscience 5, 410-413.

Velasco, A.A., Ammon, C.J., Farrell, J., Pankow, K., 2004. Rupture directivity of the 3 November 2002 Denali Fault earthquake determined from surface waves. Bulletin of the Seismological Society of America 94, S293-S299.

Vidale, J. E., and Y.-G. Li, 2003. Damage to the shallow Landers fault from the nearby Hector Mine earthquake, Nature, 421(6922), 524Đ526.

Weston, J., Ferreira, A.M.G., Funning, G.J., 2011. Global compilation of interferometric

synthetic aperture radar earthquake source models: 1. Comparisons with seismic catalogs. Journal of Geophysical Research 116.

Wright, T.J., Lu, Z., Wicks, C., 2003. Source model for the Mw 6.7, 23 October 2002, Nenana Mountain Earthquake (Alaska) from InSAR. Geophysical Research Letters 30.

Zebker, H.A., Rosen, P.A., Hensley, S., 1997. Atmospheric effects in interferometric synthetic aperture radar surface deformation and topographic maps. Journal of Geophysical Research 102, 7547.

Zigone, D., Rivet, D., Radiguet, M., Campillo, M., Voisin, C., Cotte, N., Walpersdorf, A., Shapiro, N.M., Cougoulat, G., Roux, P., Kostoglodov, V., Husker, A., Payero, J.S., 2012. Triggering of tremors and slow slip event in Guerrero, Mexico, by the 2010 Mw 8.8 Maule, Chile, earthquake. Journal of Geophysical Research 117.

Zoback, M. L., 1992. First- and second-order patterns of stress in the lithosphere: The World Stress Map Project, Journal of Geophysical Research, 97(B8), 11703.

CHAPTER 4

COSEISMIC EXTENSION FROM SURFACE CRACKS REOPENED BY THE 2014 PISAGUA, NORTHERN CHILE, EARTHQUAKE SEQUENCE

4.1 Abstract

The A.D. 2014 Pisagua earthquake sequence reactivated ancient surface cracks along the entire rupture length in the northern Chilean forearc. These subtle brittle strain features that are 50 km above the subduction zone interface in the hyperarid Atacama Desert record deformation from the single earthquake sequence. In this study we document how ancient cracks, formed during thousands of plate boundary earthquake cycles, were reopened during the 2014 earthquake sequence. We show that crack orientations along the rupture length reflect deformation from the M_w 8.1 mainshock and from a M_w 7.7 aftershock 100 km to the south, as documented by displacements calculated from continuous geodetic observations. We suggest that cracks form during the passage of surface waves, and repeated opening and closing enhance crack aperture. The orientation and opening of the oldest cracks in the forearc are indicative of the modal or most common rupture area of major megathrust earthquakes in the region. While the long-term preservation of cracks may be limited to northern Chile, similar features likely form during strong earthquakes at other subduction zones and represent permanent forearc deformation.

4.2 Introduction

Upper plate strain resulting from coseismic slip along a subduction zone interface indicates the transfer of stress from the main thrust to the overlying forearc. Strain markers from

recent subduction earthquakes are commonly elusive because a majority of the deformation occurs offshore or is rapidly obliterated onshore by surface processes (e.g., Arriagada et al., 2011). The Atacama Desert of northern Chile overlies a segment of the Nazca-South America plate boundary, and creates a unique environment for the long-term preservation of subtle strain features. In particular, prior work suggested that ancient cracks record permanent forearc extension over thousands of earthquake cycles and are likely indicative of the rupture extent and magnitude of the modal or most common earthquake (Loveless et al., 2005, 2009; González et al., 2008; Allmendinger and González, 2010; Baker et al., 2013). Here we show that ancient cracks were reopened during or shortly after the 2014 Pisagua earthquake sequence. We propose that the static and dynamic stresses generated by the three largest earthquakes in the sequence reopened suitably oriented ancient cracks. Crack orientations vary systematically along the earthquake sequence rupture area in a manner consistent with principal strain axes derived from coseismic geodetic displacement fields. Our field observations and strain modeling provide constraints on conditions favorable for crack reactivation that are crucial for interpreting the long-term plate boundary behavior from coseismic cracks. We propose that while the preservation of cracks over many earthquake cycles may be limited to northern Chile due to the climatic conditions, our conclusions about earthquake mechanics and distribution of brittle surface strain are probably applicable to other subduction zones.

4.3 Background

The soils of the hyperarid Atacama Desert surrounding the Pisagua rupture are indurated with gypsum, salt, or nitrate (Rech et al., 2003), making them relatively brittle and able to preserve cracks and other features exceptionally well. Satellite-based observation, both in

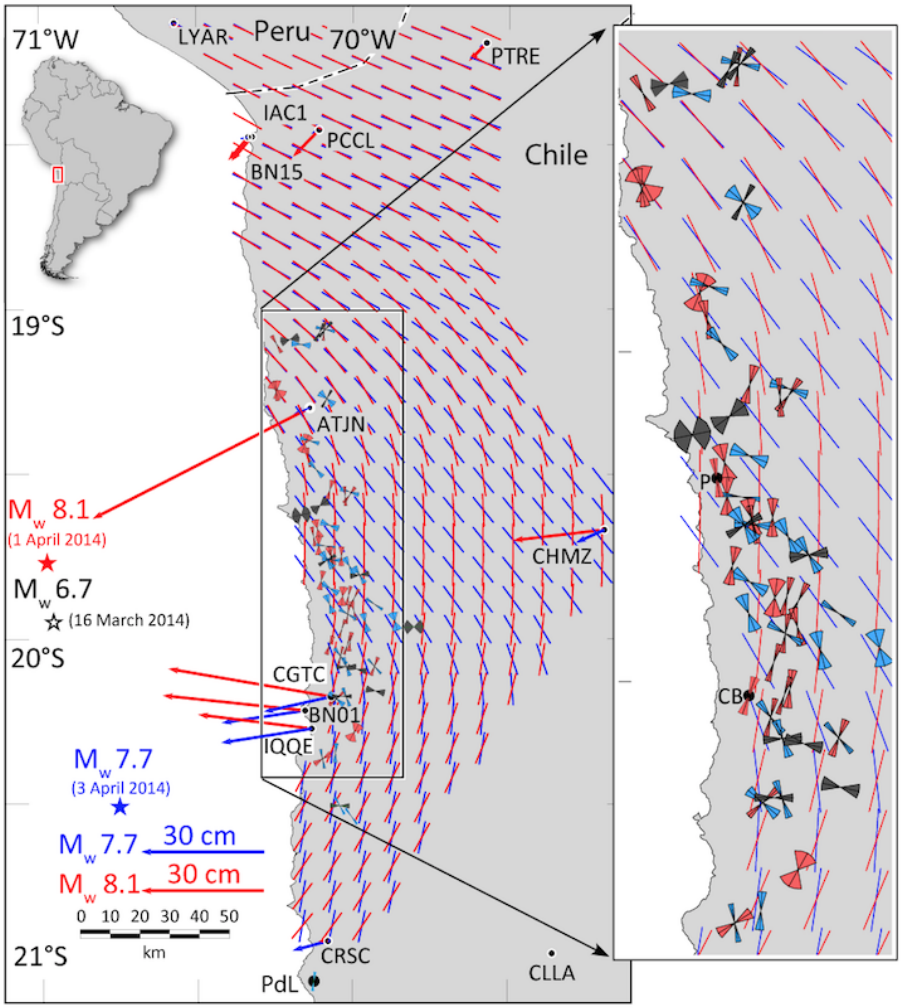

Figure 4.1: Location map of northern Chile. Stars represent Global Centroid Moment Tensor (GCMT) locations for the three largest earthquakes in the A.D. 2014 sequence. Blue and red arrows indicate GPS displacements extracted from the California Institute of Technology (Pasadena, California, USA) stations (Simons et al., 2010) and Chilean government stations as processed by Blewitt (2015) for the M_w 8.1 and M_w 7.7 earthquakes, respectively. The colored tick marks show the principal horizontal shortening axes plotted at a 10 km spacing obtained by inverting the GPS data using a 50 km distance weighting factor. Bowtie symbols are the average and 2σ spread of reopened crack orientations at the 72 sites: red and blue bowties represent cracks most closely aligned with the M_w 8.1 and M_w 7.7 strain fields, respectively; gray bowties show cracks whose orientation deviates from the GPS strain axes by more than 50^o. Transects: P-Pisagua; CB-Caleta Buena; PdL-Punta de Lobos.

visible and radar bands, is particularly effective at imaging surface features and displacement with extremely high coherence (Pritchard et al., 2002; Loveless et al., 2005).

The late Cenozoic structures of the coastal Cordillera include north-south striking normal faults (e.g., Armijo and Thiele, 1990) and east-west to east-northeast striking, margin-perpendicular reverse faults. The east-west to east- northeast striking faults, which became active during the late Miocene and are still active (González et al., 2015), produce well-developed scarps that span the rupture length of the 2014 earthquake sequence (Allmendinger et al., 2005; Allmendinger and González, 2010). The scarps locally influence coseismic shaking and crack orientation (González et al., 2008).

Most segments of the Nazca- South America plate boundary have recorded a great earthquake ($M_w > 8.0$) during the past 100 yr. A notable exception was the Iquique Gap, a region in southernmost Peru and northern Chile that overlies a zone of interplate coupling. Until 2014, this area had not undergone a great earthquake since the 1868 earthquake in southern Peru and the 1877 earthquake centered on Iquique, Chile (station IQQE; Figure 4.1). Both of these events probably had magnitudes significantly greater than 8.5 (Comte and Pardo, 1991). The 2014 Pisagua earthquake sequence (Figure 4.1), which filled one-third of the accumulated seismic gap, was initiated by an M_w 6.7 foreshock on 16 March 2014 located 35 km to the south of the M_w 8.1 mainshock on 1 April 2014 (Schurr et al., 2014; González et al., 2015). The aftershocks migrated rapidly southward by 100 km, culminating 2 days later in an M_w 7.7 aftershock.

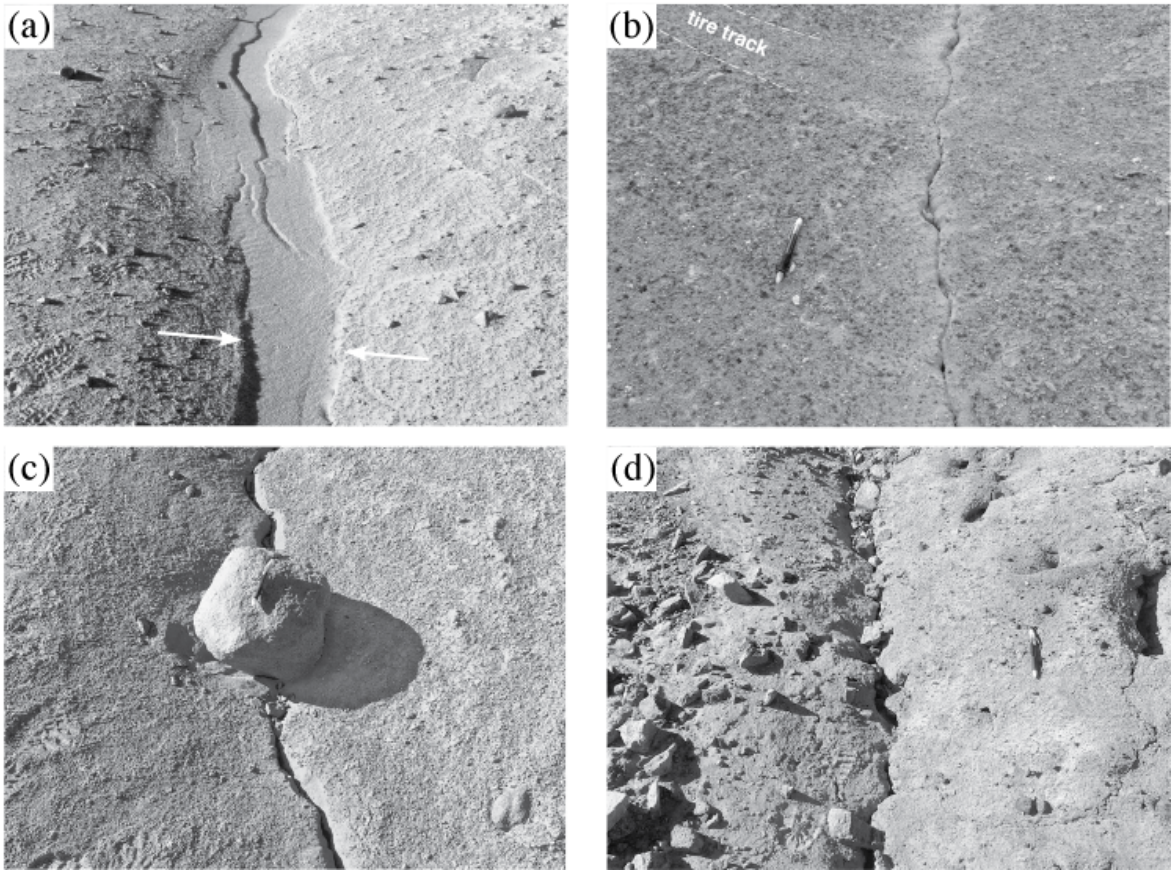

Figure 4.2: Photographs of fresh coseismic cracks. A: Newly opened cracks in unconsolidated eolian sand filling an older crack indicated by white arrows (40 cm between arrows; see also footprints in lower left for scale). B: Crack displaying fine light colored dust, which we interpret to have been ejected as the crack opened and closed during the seismic wave propagation (pen is 15 cm long). C: Small boulder on a fresh coseismic crack. Divots at the base suggest that the boulder rocked back and forth (pen on top of boulder is 15 cm long). D: Small clasts that have fallen into a fresh crack (pen is 15 cm long). Color version is shown in Figure C.3. Photos by Richard Allmendinger.

4.4 Field methods

We conducted three field excursions within 1 week, 6 weeks, and 3 months of the 1 April 2014 event. We measured the orientations of more than 3700 newly opened coseismic cracks at 72 sites spanning 200 km of coast length (Figure 4.1), completely covering the rupture region as identified by foreshocks and aftershocks. We measured crack

strikes in the field with iPhones © using the program Fieldmove Clino Pro by Midland Valley (www.mve.com/digital-mapping/) and compared periodically using traditional Brunton compasses. Differences between the iPhone app and the traditional compass were nearly always $<<10^o$, and commonly $<5^o$. The phone is one to two orders of magnitude faster in measurement and recording than traditional methods, enabling data redundancy unattainable with other methods. We collected 20-200 measurements of coseismic crack strikes at each site (on average each site had $>$ 50 measurements), constructed rose diagrams, and calculated the mean and standard deviation of the crack orientations (Figure 4.1). Approximately 25% of the sites displayed a bimodal distribution of crack orientations; in those cases, each population was analyzed separately. We measured the opening and orientation of cracks along 5 transects (Table C.1; Figure C.1 and C.2) ranging in length from 500 to 1000 m with a tape measure or GPS phone receiver and tablet mapping system (GIS Pro software on iPad Air ©). The transects are in areas with low topographic relief and, at the time of measurement, showed little eolian activity that would have obviously obscured the opening measurements.

4.5 Field description

Although we were not in the field during the earthquakes and did not observe cracks opening, the cracks formed in 2014 were easy to identify in the weeks and months following the earthquakes. Fresh coseismic cracks have vertical walls in virtually unconsolidated eolian sand that commonly exhibits ripple structures (Figure 4.2A), and cut across tire tracks and other human modifications of the surface (Figure 4.2B). Our observations following the 2007 M_w 7.7 Tocopilla earthquake and the 2014 sequence suggest that evidence of recent cracking is ephemeral. The characteristic vertical walls may still be visible six to eight

months after the earthquake, but degrade quickly, especially where eolian processes are prevalent. More than 95% of the evidence for recent cracking observed shortly after the 2007 Tocopilla earthquake was completely obscured by 2012 when the scan lines were reoccupied. Nearly all observed fresh coseismic cracks are located within and along the trace of larger preexisting cracks (Figure 4.2A). The fresh cracks observed in 2014 cut only the brittle soils but, where exposures are adequate, ancient cracks extend more than 10 m into the Mesozoic and Paleozoic basement rocks. Not all preexisting cracks were reactivated: for example, of the old north-northeast and northwest-striking crack populations at the Caleta Buena site (Figure C.1), only the north-northeast set reopened. We use the term coseismic crack, but cannot rule out the possibility that some cracks actually formed during the post-seismic period.

Horizontal apertures of fresh cracks range from millimeters to 2 cm. While some cracks show evidence of oblique opening, unambiguous markers of the actual opening vector are very sparse (Figure 4.2B). We infer that many cracks opened at a high angle, but not necessarily perpendicular to the maximum horizontal coseismic strain axis. Of the >3700 cracks sampled, a single crack showed clear evidence of thrust faulting. We infer that, if localized shortening occurred during or immediately following the earthquake sequence, it did not compensate for the documented extension.

Field observations show evidence for high dynamic stresses. The light colored dust surrounding cracks was probably ejected during the seismic wave propagation (Figure 4.2B). Seismic shaking likely rocked smaller boulders and encouraged clasts to drop into cracks (Figures 4.2C and 4.2D). Coseismic cracks opened on steep slopes, ridges, and valleys (e.g., east-west to east-northeast trending scarps) with orientations that suggest opening subparallel to the direction of maximum relief.

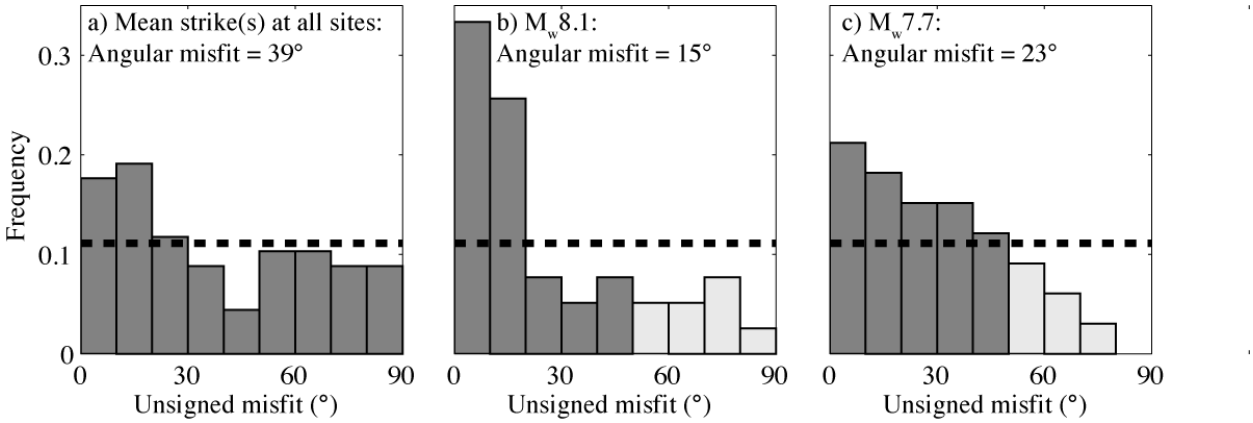

Figure 4.3: Histogram showing the angular misfit between the GPS shortening axes and the average crack orientations. A: At all sites. B: Those that more consistent with the M_w 8.1 rather than the M_w 7.7 earthquake. C: Those that more consistent with the M_w 7.7 earthquake. The light gray bars represent crack orientations that deviate by more than 50ř from the strain axes for both earthquakes and are omitted from the misfit calculation. The dashed line shows the expected frequency for a uniform distribution with a mean misfit of 45^o.

4.6 Crack orientations

We observe a crude but systematic change in crack strike over the rupture length, from dominantly north-northwest striking north of 19.9^oS to north-northeast striking south of this latitude (Figure 4.1). The most extreme deviations to this rupture-scale trend occur along the prominent east-northeast to east-west trending topographic scarps (Figures C.4 and C.5). Between the latitudes of the M_w 8.1 and M_w 7.7 earthquake centroids, single sites show both northeast- and northwest-oriented openings.

4.7 Transects for strain evaluation

At the Caleta Buena and Pisagua transects (e.g., Figures 4.1 and C.1), both located within 35 km along strike of the M_w 8.1 centroid, the summed crack openings suggest apparent strain

magnitudes of 5.48 x 10^{-4} and 1.15 x10^{-4}, respectively. The Punta de Lobos transects, located 155 km south of the M_w 8.1 centroid, suggest a lower apparent strain magnitude of 6.42 x 10^{-5}. We compare crack openings at Punta de Lobos that accumulated over nearly 1 m.y. (Baker et al., 2013), measured prior to 2014, to the Pisagua cracking. Those transects yielded a total opening strain of 7 x 10^{-3} to 4 10^{-2} that accumulated over 800 k.y., suggestive of a long- term strain rate of 0.3 x 10^{-15} s^{-1} to 2 x 10^{-15} s^{-1}. If, for the long-term transects, we assume a great earthquake recurrence interval of 150-300 yr, that strain rate would translate to a per event strain of 4 x 10^{-6} to 9 x 10^{-6} . The long-term strain is one to two orders of magnitude smaller than the crack opening produced by the 2014 earthquake sequence at Punta de Lobos.

4.8 Geodetic measures of surface strain

As an independent means of evaluating regional-scale coseismic deformation due to the Pisagua earthquake sequence, we examine spatial gradients in horizontal GPS displacements (e.g., Duputel et al., 2015) across a network of 11 continuous GPS stations (Figure 4.1). The GPS data set captures rupture-scale strain patterns but cannot resolve strain anomalies that might conceivably exist over a field site. We complement the GPS data with 30-m-resolution Interferometric Synthetic Aperture Radar (InSAR) displacement data. The InSAR line-of-sight displacements, which have a combined sensitivity to vertical and horizontal deformation, result in strong constraints on strain gradients over the spatial scale of a single field site (Figures C.6 and C.7).

To compare crack orientations to patterns of geodetically derived strain, we independently invert GPS displacements for the principal horizontal strain axes and magnitudes for

the entire sequence, the M_w 8.1 event and the M_w 7.7 event (Allmendinger et al., 2009; Cardozo and Allmendinger, 2009). Pure opening mode cracks parallel the principal horizontal shortening axes: the change in direction of the inferred strain axes (Figure 4.1), from north-northwest to north-northeast over the rupture zone, is coincident with a similar change in crack orientation. In more detail, the majority of crack sites are consistent with the calculated coseismic strain patterns for either the M_w 8.1 or M_w 7.7 earthquake. Although the details in the spatial pattern of the calculated strain axes depend on the distance weighting factor used in the inversion, the mean angular mismatch between the mean crack strikes at each field site and the shortening axes calculated from GPS data over the entire sequence is 38^o (Figure 4.3). We divide the mean crack orientations into three groups: (1) orientations most consistent with the M_w 8.1 event (Figure 4.1, blue bowties), (2) orientations most consistent with the M_w 7.7 event (Figure 4.1, red bowties), and (3) orientations that deviate from both events by more than 50^o (Figure 4.1, gray bowties). When cracks are assigned to either the M_w 8.1 or M_w 7.7 earthquakes, the angular mismatch decreases to 15^o and 23^o, respectively (Figure 4.3). Approximately 75% of the cracks in the third group are subparallel to nearby topographic scarps, commonly trending east-northeast. North of the ATJN station, M_w 8.1 and M_w 7.7 event strain axes become increasingly aligned and produce comparable fits to the crack strikes.

At the Pisagua and Caleta Buena transects, the apparent strain inferred from crack apertures is almost two orders of magnitude larger than the coseismic strain inferred from GPS (Table C.2). This strain, however, is calculated and smoothed from sparse data points and thus it is possible that the transects record anomalously large coseismic strain. To test that possibility, we analyzed the InSAR data set over the Pisagua transect, and found no high strain anomalies (Figure C.7).

4.9 Discussion

We propose that both the coseismic dynamic and static stresses control the opening of fresh cracks along the traces of suitably oriented pre-existing cracks. The fact that cracks located along ridges are commonly reactivated even when their orientation is poorly aligned for mode I opening relative to the static strain field suggests that dynamic stresses are often critical for crack opening. The shaking is likely enhanced as seismic waves are focused by material contrasts across the underlying faults, and opening may be further influenced by local gravitational instabilities. We further propose that the unconsolidated sand and clasts that fall into the cracks during or shortly after the passage of the seismic waves partially fill the crack volume that remains open following the earthquake.

The similarity between the crude fanning crack-strike pattern and the geodetic strain axes suggests a first-order control of the static stress field on crack opening. The M_w 8.1 and M_w 7.7 earthquakes, and perhaps the M_w 6.7 foreshock, probably opened cracks with spatially overlapping distributions, although we cannot unequivocally relate any particular crack to a specific earthquake. The strain fields for the M_w 8.1 and 7.7 earthquakes are most discordant within the region between stations ATJN and IQQE (Figure 4.1). In this region, cracks at neighboring sites with unimodal or bimodal crack populations are closely consistent with the strain field from one earthquake or the other. The M_w 6.7 foreshock, which occurred along an east-west striking thrust fault in the upper plate (González et al., 2015), may have activated cracks along the east-west scarps immediately to the east of the M_w 6.7 earthquake centroid.

Crack apertures along the measured transects overlying the rupture area of the earthquake sequence appear to overestimate the geodetically estimated coseismic strain by nearly two orders of magnitude (Table C.2). We found no evidence in the field or geodetic data

of compensating shortening of the magnitude needed to offset the large crack opening. We suggest that the apparent excessive widening of the cracks is in part a dynamic effect, probably largely due to crack wall damage during repeated opening and closing during seismic wave propagation. The cracks may continue to degrade after the earthquake as loose sand falls into the cracks. The highest apparent strain at the Caleta Buena site likely reflects the presence of poorly consolidated and/or cemented sandy soil.

It is significant that the apparent strains from cracks opened in 2014 earthquakes are also 1-2 orders of magnitude larger than those suggested by the 1 m.y. opening record at Punta de Lobos fan locality (Table C.2; Baker et al., 2013). Baker et al. (2013) excavated coseismic cracks in unconsolidated sand and found that the near surface walls are commonly formed by steep normal faults forming a symmetric graben over the hairline crack at depth in more coherent material (Figure C.8). Thus, it appears that the large surficial openings of the ancient cracks are a superficial feature enhanced by the degradation of the delicate crack walls following the passage of the seismic waves and eolian processes occurring within days of the earthquake, and are not indicative of the actual aperture below the surface (Figure C.9).

4.10 Conclusions

How do cracks from a single event like the Pisagua sequence sum over repeated earthquake cycles to give the million-year record such as that documented at Punta de Lobos (Baker et al., 2013) and elsewhere (Loveless et al., 2009)? We illustrate that the static and dynamic stresses associated with a single subduction earthquake drive the reopening of ancient surface cracks. The widest and longest cracks have been activated the greatest number of times, and

their orientations reflect the rupture area of a modal earthquake for the region. While the hyperarid Atacama environment responsible for the long- term crack preservation is unique, it is likely that similar brittle strain features develop at other subduction zones with a spatial pattern that provides diagnostic information about earthquake rupture area.

4.11 Acknowledgements

We are grateful to the U.S. National Science Foundation (grant EAR-1443410) for RAPID (Rapid Response Research) and the Centro Nacional de Investigación para la Gestión Integrada de Desastres Naturales [CIGIDEN; Grant CONICYT/ FONDAP 15110017] of Chile for funding this research. Scott was supported by the McMullen Fellowship from Cornell University, New York. We thank the German Aerospace Center (DLR) for providing SAR data under grant GEO2441, courtesy of Matthew Pritchard, and Rowena Lohman for stimulating discussions about the InSAR data. Constructive and thoughtful reviews from Graham Yielding, Romain Jolivet, and Christoph Grützner greatly improved the manuscript. Without the expert driving skills of Antonio Tapia Díaz, we would not have made it to even half as many sites.

4.12 References

Allmendinger, R.W., and González, G., 2010, Invited review paper: Neogene to Quaternary tectonics of the coastal Cordillera, northern Chile: Tectonophysics, v. 495, p. 93-110, doi:10.1016/j.tecto.2009.04.019.

Allmendinger, R.W., González, G., Yu, J., Hoke, G., and Isacks, B., 2005, Trench- parallel shortening in the northern Chilean forearc: Tectonic and climatic implications: Geological Society of America Bulletin, v. 117, p. 89-104, doi:10.1130/B25505.1.

Allmendinger, R.W., Loveless, J.P., Pritchard, M.E., and Meade, B., 2009, From decades to epochs: Spanning the gap between geodesy and structural geology of active mountain belts: Journal of Structural Geology, v. 31, p. 1409-1422, doi:10.1016/j.jsg.2009.08.008.

Armijo, R., and Thiele, R., 1990, Active faulting in northern Chile: Ramp stacking and lateral decoupling along a subduction plate boundary?: Earth and Planetary Science Letters, v. 98, p. 40-61, doi:10.1016/0012-821X(90)90087-E.

Arriagada, C., et al., 2011, Nature and tectonic significance of co-seismic structures associated with the M_w 8.8 Maule earthquake, central-southern Chile forearc: Journal of Structural Geology, v. 33, p. 891-897, doi:10.1016/j.jsg.2011.03.004.

Baker, A., Allmendinger, R.W., Owen, L.A., and Rech, J.A., 2013, Permanent deformation caused by subduction earthquakes in northern Chile: Nature Geoscience, v. 6, p. 492-496, doi:10.1038/ngeo1789.

Blewitt, G., 2015, GPS Networks Map from the Nevada Geodetic Laboratory: Nevada Geodetic Laboratory, http://geodesy.unr.edu/billhammond/gpsnetmap/GPSNetMap.html.

Cardozo, N., and Allmendinger, R.W., 2009, SSPX: A program to compute strain from displacement/velocity data: Computers & Geosciences, v. 35, p. 1343-1357, doi:10.1016/j.cageo.2008.05.008.

Comte, D., and Pardo, M., 1991, Reappraisal of great historical earthquakes in the northern Chile and southern Peru seismic gaps: Natural Hazards, v. 4, p. 23-44, doi:10.1007/BF00126557.

Duputel, Z., et al., 2015, The Iquique earthquake sequence of April 2014: Bayesian modeling accounting for prediction uncertainty: The 2014 Iquique earthquake: Geophysical Research Letters, v. 42, p. 7949-7957, doi:10.1002/2015GL065402.

González, G., Gerbault, M., Martinod, J., Cembrano, J., Carrizo, D., Allmendinger, R., and Espina, J., 2008, Crack formation on top of propagating reverse faults of the Chuculay fault system, northern Chile: Insights from field data and numerical modelling: Journal of Structural Geology, v. 30, p. 791-808, doi:10.1016/j.jsg.2008.02.008.

González, G., Salazar, P., Loveless, J.P., Allmendinger, R.W., Aron, F., and Shrivastava, M., 2015, Upper plate reverse fault reactivation and the unclamping of the megathrust during the 2014 northern Chile earthquake sequence: Geology, v. 43, p. 671-674, doi:10.1130/G36703.1.

Loveless, J.P., Hoke, G.D., Allmendinger, R.W., González, G., Isacks, B.L., and Carrizo, D.A., 2005, Pervasive cracking of the northern Chilean Coastal Cordillera: New evidence for forearc extension: Geology, v. 33, p. 973-976, doi:10.1130/G22004.1.

Loveless, J.P., Allmendinger, R.W., Pritchard, M.E., Garroway, J.L., and Gonzalez, G., 2009, Surface cracks record long-term seismic segmentation of the Andean margin: Geology, v. 37, p. 23-26, doi:10.1130/G25170A.1.

Pritchard, M.E., Simons, M., Rosen, P.A., Hensley, S., and Webb, F.H., 2002, Co- seismic slip from the 1995 July 30 M_w = 8.1 Antofagasta, Chile, earthquake as constrained by InSAR and GPS observations: Geophysical Journal International, v. 150, p. 362-376, doi:10.1046/j.1365-246X.2002.01661.x.

Rech, J.A., Quade, J., and Hart, W.S., 2003, Isotopic evidence for the source of Ca and S in soil gypsum, anhydrite and calcite in the Atacama Desert, Chile: Geochimica et Cosmochimica Acta, v. 67, p. 575-586, doi:10.1016/S0016-7037(02)01175-4.

Schurr, B., et al., 2014, Gradual unlocking of plate boundary controlled initiation of the 2014 Iquique earthquake: Nature, v. 512, p. 299-302, doi:10.1038/nature13681.

Simons, M., Galetzka, J., Genrich, J., Ortega, F., Comte, D., Glass, B., González, G., and Norabuena, E., 2010, Central Andean Tectonic Observatory Geodetic Array: GPS data set citation summary (aggregation of multiple data sets): Boulder, Colorado, UNAVCO, doi:10.7283/T50P0X37.

APPENDIX A

SUPPLEMENTAL MATERIAL: SENSITIVITY OF EARTHQUAKE SOURCE INVERSIONS TO ATMOSPHERIC NOISE AND CORRECTIONS OF INSAR DATA

A.1 Atmospheric turbulence, interferogram downsampling, and parameter convergence

To assess the seasonal variability of the turbulent noise, we calculate the amplitude of the turbulent contribution at individual dates with our interferogram time series. Because the Envisat data used in this calculation are acquired at dates separated by many weeks to months, we can safely assume that the turbulent contributions (which change on timescales of minutes to hours [Onn and Zebker, 2006]) at the individual acquisitions are uncorrelated [Emardson, 2003]. The spatially averaged variance of the turbulence in an interferogram (σ^2_{int}) is:

$$\sigma^2_{int} = \sigma^2_{date1} + \sigma^2_{date2} \tag{A.1}$$

where σ^2_{date1} and σ^2_{date2} are the variance of the contribution from the first and second acquisitions, respectively. Therefore, while inversions for the phase at individual pixels at each date within an interferometric time series is non-unique, we can uniquely invert for the spatially averaged variance at each of the 17 acquisitions from our set of 22 interferograms (Figure 3d).

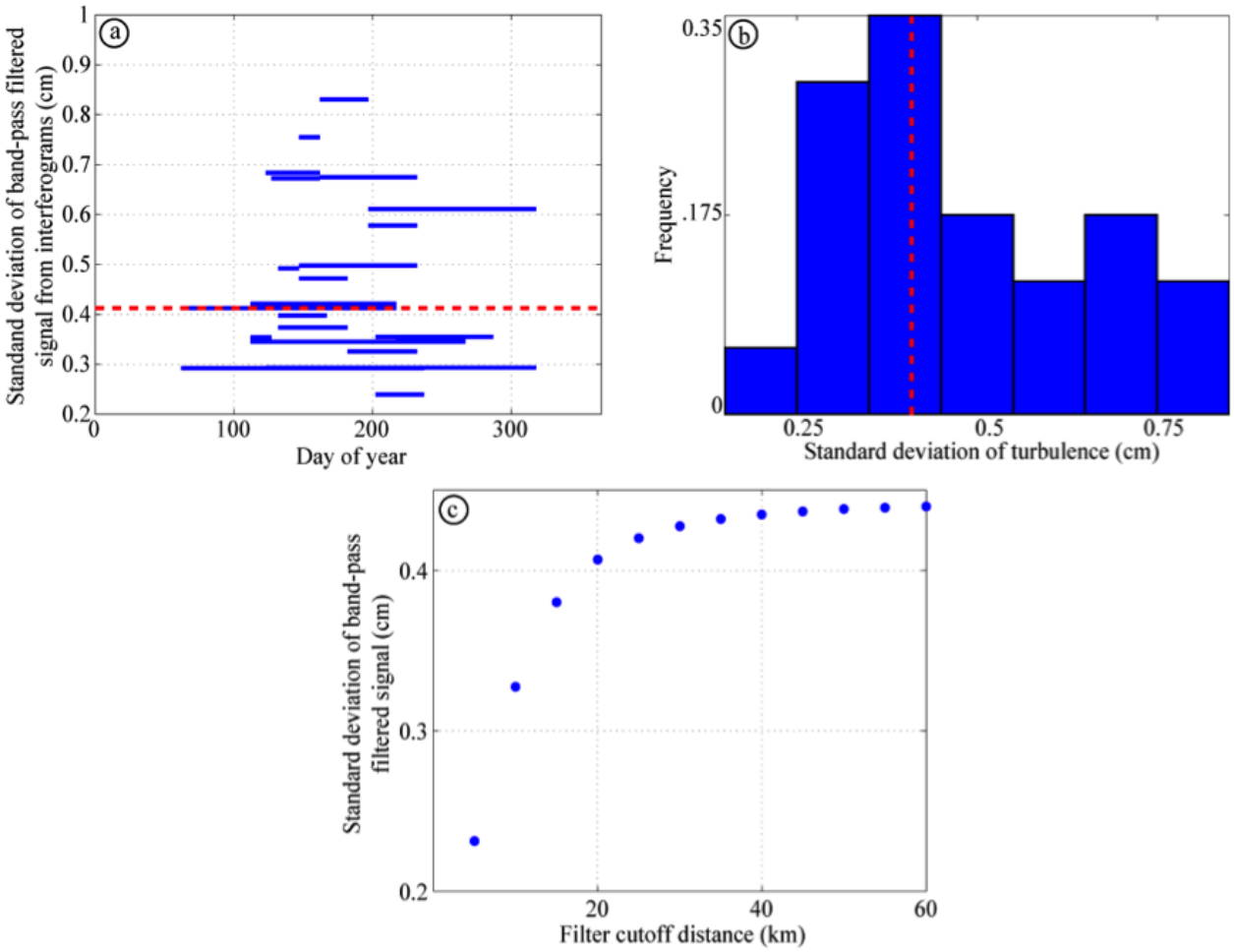

Figure A.1: Amplitude of turbulence from Envisat Track 213, Frame 2817. (a) Standard deviation of the turbulence in individual interferograms calculated from the residual after removing a bilinear ramp and a linear elevation- phase relationship, and a applying a band-pass filter to retain signals at wavelengths of 1-20 km. Each blue line spans the two acquisition dates of individual interferograms, regardless of year. The dashed red line is the mean amplitude of the turbulence in the interferograms. (b) Frequency versus standard deviation of the results in (a). (c) Standard deviation of the mean residual of the set of interferograms after applying a set of Gaussian filters designed to retain signals from 1 km up to the indicated filter cutoff distance.

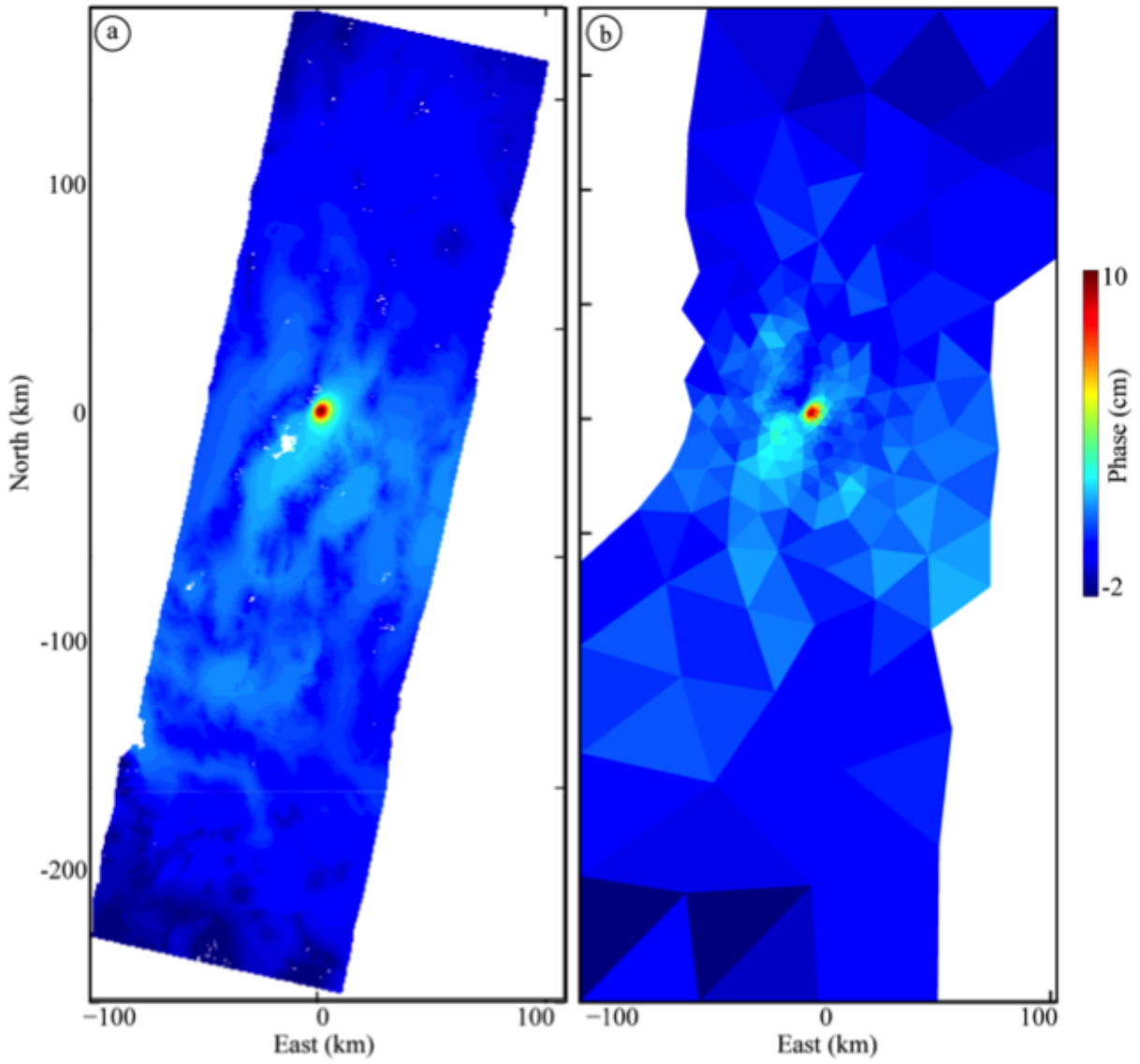

Figure A.2: Interferogram downsampling. (a) Interferogram at full-resolution containing the stratified atmospheric noise and the coseismic contribution. (b) Downsampled interferogram using the algorithm developed by Lohman and Simons [2005] and modified by McGuire et al. [2015].

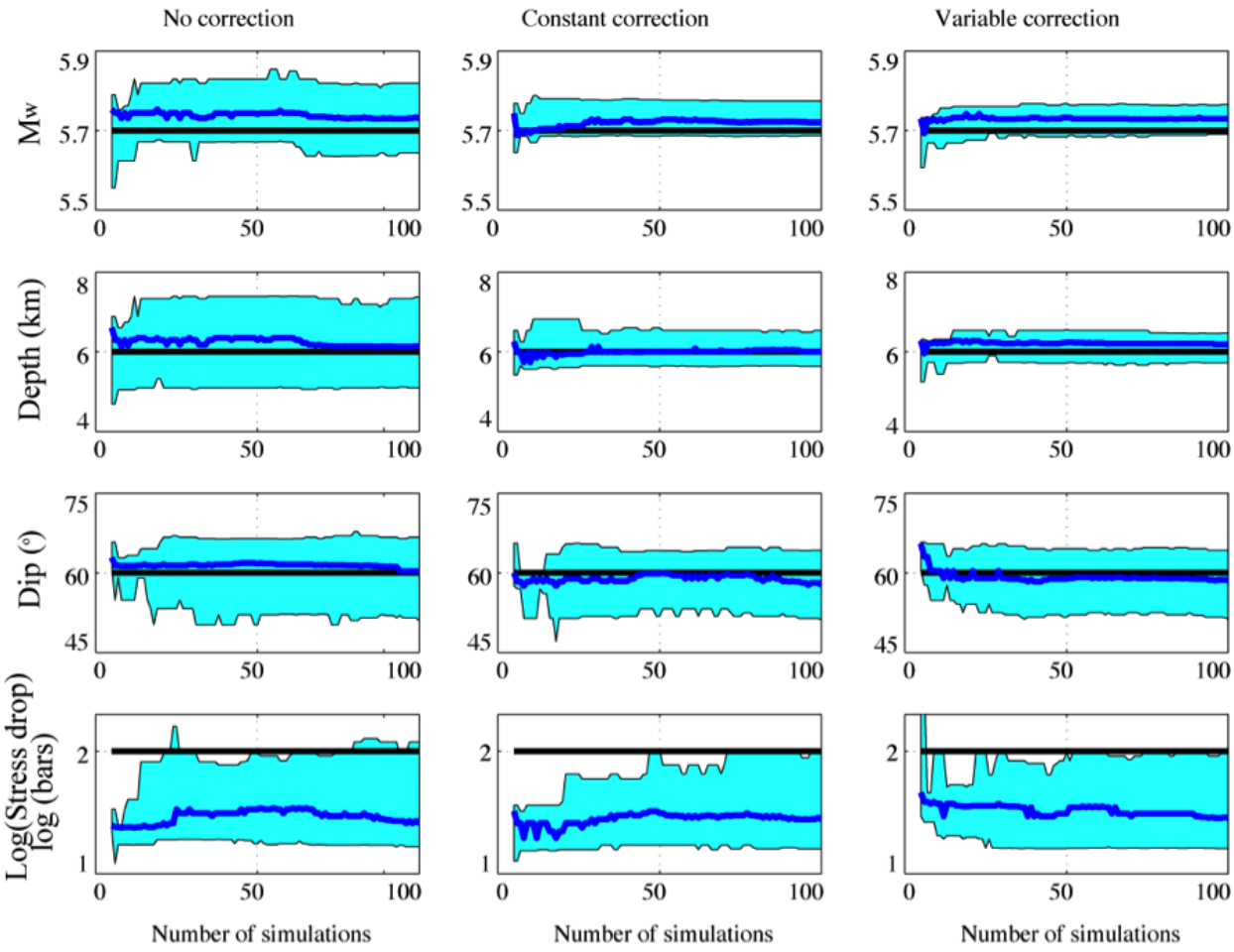

Figure A.3: Convergence of the inferred earthquake source parameters versus number of simulations for the 60° dipping normal fault at a 6 km depth. The black lines show the value of the input fault parameter. The blue lines show the median value of the each fault parameter versus number of simulations. The light blue clouds show the 16th to 84th percentile (i.e., 1σ) of the resulting ensemble.

A.2 References

Emardson, T. R. (2003), Neutral atmospheric delay in interferometric synthetic aperture radar applications: Statistical description and mitigation, Journal of Geophysical Research, 108(B5), doi:10.1029/2002JB001781.

Lohman, R. B., and M. Simons (2005), Some thoughts on the use of InSAR data to constrain models of surface deformation: Noise structure and data downsampling, Geochemistry, Geophysics, Geosystems, 6(1), doi:10.1029/2004GC000841.

McGuire, J. J., R. B. Lohman, R. D. Catchings, M. J. Rymer, and M. R. Goldman (2015), Relationships among seismic velocity, metamorphism, and seismic and aseismic fault slip in the Salton Sea Geothermal Field region: Salton Sea Geothermal Field, Journal of Geophysical Research: Solid Earth, 120(4), 2600-2615, doi:10.1002/2014JB011579.

Onn, F., and H. A. Zebker (2006), Correction for interferometric synthetic aperture radar atmospheric phase artifacts using time series of zenith wet delay observations from a GPS network, Journal of Geophysical Research, 111(B9), doi:10.1029/2005JB004012.

APPENDIX B

DERIVING EMPIRICAL ATMOSPHERIC CORRECTIONS OF INSAR DATA

B.1 Introduction

Empirical atmospheric corrections aid in the mitigation of the impact of atmospheric noise on ground displacements inferred from InSAR observations [e.g., Cavalié et al., 2007; Elliott et al., 2008; Tymofyeyeva and Fialko, 2015]. Before applying an empirical atmospheric correction, the researcher must impose a functional form to the relationship between elevation and phase. Here, I describe the methods in Chapter 2 that are used to select the optimal spatial scale of the variations in the inferred empirical elevation- phase relationship over the length of the interferogram. This relationship is used to account for the spatial variability in the character of the stratified component of the atmosphere.

As discussed in Chapter 2, the relationship between phase and topography can be approximated as [e.g., Bekaert et al., 2015],

$$\Delta\phi_i = K'_{\Delta\phi}(h_0 - h_i)^{\alpha}, \tag{B.1}$$

where $\Delta\phi_i$ is the phase delay at the ith pixel, $K'_{\Delta\phi}$ relates the local topographic relief to phase, h_0 is an upper tropospheric altitude above which the atmospheric properties are approximated as constant in time, h_i is the elevation at the ith pixel, and α is the power law coefficient.

Empirical corrections require an extraction of the phase vs. elevation relationship (i.e., $K'_{\Delta\phi}$) directly from the InSAR data itself. However, an estimation of $K'_{\Delta\phi}$ over the area of

earthquake deformation would significantly bias the inferred atmospheric correction. Therefore, we estimate $K'_{\Delta\phi}$ outside of the region of earthquake deformation and interpolate the inferred atmospheric characteristics into this area. Accurate inferences of atmospheric characteristics support a correction that does not introduce artifacts in the area of earthquake deformation. The interpolation step, if done incorrectly, can introduce elevation-dependent artifacts in the area that was masked out during assessment of the atmospheric characteristics. Ultimately, the inferred earthquake source parameters will suffer if the inferred values of $K'_{\Delta\phi}$ are incorrect. Below, I outline the procedure used to select the optimal smoothing parameter and use a coseismic interferogram in Nevada to illustrate the potential consequences to data quality if an incorrect parameter value is used.

B.2 Second- order Tikhonov regularization

Smoothing constraints are applied by augmenting the traditional least squares problem to [e.g., Menke, 1989; Aster et al., 2013],

$$min(||\mathbf{G}m - d||_2^2 + \xi^2||\mathbf{L}_2 m||_2^2), \tag{B.2}$$

where $\mathbf{G}$ is the matrix of Green's functions that relate the atmospheric model parameters (m) to the interferometric phase (d) following Equation B.1. The amount of smoothing is controlled by ξ, the regularization parameter. $\mathbf{L}_2 m$ is the finite difference approximation to the second derivative: this term scales with the smoothness of the model parameters. Equation B.2 is rewritten as a standard least squares problem as,

$$min||[\mathbf{G}; \xi\mathbf{L}] * m - [d; 0]||_2^2. \tag{B.3}$$

When solved by method of normal equations,

$$(\mathbf{G}^T\mathbf{G} + \xi^2\mathbf{L}_2^T L_2)m = \mathbf{G}^T d, \tag{B.4}$$

and,

$$m = (\mathbf{G}^T\mathbf{G} + \xi^2\mathbf{L}_2^T\mathbf{L}_2)^{-1}\mathbf{G}^T d. \tag{B.5}$$

When the Green's functions and data are weighted by the inverse of the Cholesky factorization of the data covariance matrix ($\mathbf{C}_d$), the inferred correlations between topography and phase are not penalized for failing to account for features that statistically mimic noise characteristics [e.g., Harris and Segall, 1987]. In this case, the weighted $\mathbf{G}$ and d become, $G_w = \mathbf{C}_d G$, $d_w = \mathbf{C}_d d$, and inferred model (Equation B.5) is re-expressed as,

$$m = (\mathbf{G}_w^T\mathbf{G}_w + \xi^2\mathbf{L}_2^T\mathbf{L}_2)^{-1}\mathbf{G}_w^T d_w. \tag{B.6}$$

Equation B.6 can be re-expressed as,

$$m = \mathbf{G}_w^{g*} d_w, \tag{B.7}$$

where $\mathbf{G}_w^{g*} = (\mathbf{G}_w^T\mathbf{G}_w + \xi^2\mathbf{L}_2^T\mathbf{L}_2)^{-1}\mathbf{G}_w$, and is known as the generalized inverse of the weighted regularized inversion.

B.3 ${}_jR_i$: Optimize ξ

We use the ${}_jR_i$ method to select the optimal value of ξ [Lohman, 2004; Lohman and Simons, 2005; Barnhart and Lohman, 2010]. This approach seeks a compromise between over-smoothing the signal from the stratified component of the troposphere (regularization error) and mapping atmospheric turbulence into the topographically correlated contribution (perturbation error). The text below refers to the application of the ${}_jR_i$ technique to atmospheric noise corrections, although the same approach could be applied to other problems (e.g., distributed slip inversion). I first describe the general set-up of the ${}_jR_i$ technique and then apply the technique to real InSAR data.

The interferometric phase ($d_i(\Phi)$) is expressed as the sum of the signal from the topographically correlated contribution from the stratified component of the atmosphere ($d_0(\Phi)$) and the noise resulting from atmospheric turbulence ($n_i(\Phi)$),

$$d_i(\Phi) = d_0(\Phi) + n_i(\Phi). \tag{B.8}$$

Note that the $n_i(\Phi)$ term is also likely to have contributions from DEM errors, unwrapping errors, orbital errors, and non- coseismic sources of ground deformation. The smoothed signal from the stratified atmosphere (d_0^*) is expressed as,

$$d_0^* = \mathbf{N}d_0, \tag{B.9}$$

where

$$\mathbf{N} = \mathbf{G}\mathbf{G}_w^{g*}. \tag{B.10}$$

$\mathbf{G}$ is the matrix of Green's functions that relate the inferred $K'_{\Delta\phi}$ values to interferometric phase delay, and $\mathbf{N}$ is the data resolution matrix (e.g., Hanssen, 1998). The regularization error ($_0r_0$) is the difference between the noise-free data and the smoothed version of that data, and is expressed as,

$$_0r_0 = d_0 - d_0^* = [\mathbf{I} - \mathbf{N}]d_0, \tag{B.11}$$

The perturbation error ($_jr_i^n$) quantifies the extent to which the turbulence is mapped into the $K'_{\Delta\phi}$ values and the predicted topographic contribution. This form of error is calculated as the difference between one realization of noise and a smoothed realization of an independent set of noise:

$$_jr_i^n = n_j - n_i^*. \tag{B.12}$$

$_jr_i^n$ will increase as ξ decreases, as an inversion that fits one set of noise well is unlikely to fit another noise set well. $_jr_i$ is the sum of the regularization and perturbation errors,

$$_jr_i =_0 r_0 +_j r_i^n. \tag{B.13}$$

$\mathbf{M} = [\mathbf{I} - \mathbf{N}]$ can be used to conveniently express the residual quantities,

$$ {}_{o}r_{o} = \mathbf{M}[d_o \quad d_o]^T, \tag{B.14a} $$

$$ {}_{j}r_{i}^{n} = \mathbf{M}[n_i \quad n_j]^T, \tag{B.14b} $$

$$ {}_{j}r_{i} = \mathbf{M}[d_i \quad d_j]^T. \tag{B.14c} $$

B.4 ${}_{j}R_{i}$: Synthetic data

I outline how the above solution is applied to atmospheric corrections of synthetic datasets where the underlying topographically- correlated phase contribution and data covariances are known for many realizations of atmospheric noise.

Over an entire interferogram, ${}_{j}R_{i}$ is the sum of contributions from $({}_{j}r_{i})$ at each of the k pixels,

$$ {}_{j}R_{i} = \frac{1}{k}\sum_{x}({}_{j}r_{i})^2. \tag{B.15} $$

By expansion using Equation B.13,

$$ {}_{j}R_{i} = \frac{1}{k}\sum_{x}[({}_{0}r_{0})^2 + 2({}_{0}r_{0})({}_{j}r_{i}^{n}) + ({}_{j}r_{i}^{n})^2]. \tag{B.16} $$

Because ${}_{j}r_{i}^{n}$ is a random variable with mean 0, the middle term cancels out, leaving:

$$ {}_{j}R_{i} = \frac{1}{k}\sum_{x}[({}_{0}r_{0})^2 + ({}_{j}r_{i}^{n})^2]. \tag{B.17} $$

Because ${}_{0}r_{0}$ is unknown for real data, the substitution, ${}_{0}r_{0} =_{i} r_{i} -_{i} r_{i}^{n}$, is made:

$$ \frac{1}{k}\sum_{x}({}_{0}r_{0})^2 = \frac{1}{k}\sum_{x}({}_{i}r_{i} -_{i} r_{i}^{n})^2 = \frac{1}{k}\sum_{x}({}_{i}r_{i})^2 - 2({}_{i}r_{i})({}_{i}r_{i}^{n}) + ({}_{i}r_{i}^{n})^2. \tag{B.18} $$

${}_{i}r_{i}^{n}$ is also a random variable with expectation 0, so the term $2({}_{i}r_{i})({}_{i}r_{i}^{n})$ cancels out. Then,

$$ {}_{j}R_{i} = \frac{1}{k}\sum_{x}[({}_{i}r_{i})^2 - ({}_{i}r_{i}^{n})^2 + ({}_{j}r_{i}^{n})^2]. \tag{B.19} $$

Because the mean value of ${}_jr_i^n$ is 0, the expected value of $\frac{1}{k}\sum_x({}_jr_i^n)^2$ is the sum of the variances at each data point. By the law of covariance propagation, the covariance of ${}_jr_i^n$ is,

$$C_r = \mathbf{M}\mathbf{C}_d\mathbf{M}^T. \tag{B.20}$$

When $\mathbf{G}$ and d have been pre-weighted by $\mathbf{C}_d$,

$$C_r = \mathbf{M}\mathbf{M}^T. \tag{B.21}$$

Similarly the covariance of the matrix of ${}_ir_i^n$ for pre-weighted G and d is,

$$C_2 = \mathbf{M}\mathbf{I}_2\mathbf{M}^T. \tag{B.22}$$

Where $\mathbf{I}_2$ is a matrix of block identity matrices. So ${}_jR_i$ becomes,

$${}_jR_i = \frac{1}{k}\sum_x({}_ir_i)^2 - \frac{1}{k}\sum diag(C_2) + \frac{1}{k}\sum diag(\mathbf{C}_r) \tag{B.23}$$

B.5 Atmospheric corrections of InSAR data

In this section, I explore how the smoothing of the topographically correlated delay impacts the resulting atmospheric corrections and the shape of the coseismic signal in the corrected interferogram. I focus on the 1992 M5.6 Little Skull Mountain earthquake of southern Nevada as described in Chapter 2 and explicitly examine cases where the wrong quantity of spatial smoothing is applied between neighboring values of the inferred relationship between topography and phase.

Figure B.1a shows the uncorrected InSAR interferogram and highlights the location of the Little Skull Mountain earthquake, which produced ∼2 cm of displacement in the SAR line-of-sight. The earthquake occurred to the northeast of Death Valley in an area with moderate

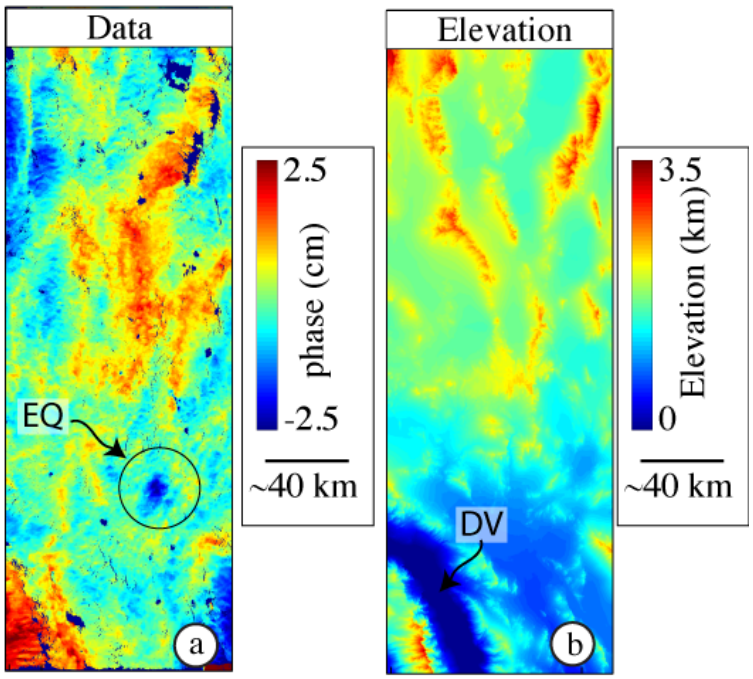

Figure B.1: InSAR data: (a) ERS interferogram that contains the 1992 M_w 5.6 Little Skull Mountain earthquake and spans 1992/04/24-1996/06/18 (Track 399, Frames 2835-2871). The darkest blue represent areas lacking data. (b) Digital elevation model (DEM) highlighting the location of Death Valley (DV).

topographic relief (Figure B.1b). A comparison between phase and topography illustrates that while many of the atmospheric features in the data correlate with topography, many do not. For example, the ∼1200 m of relief on the northeast rim of Death Valley produces a only minor phase contribution in this particular interferogram.

When too little smoothing is applied, the correction looks similar to the original data except near the coseismic signal (Figure B.2a). Turbulent features to the east and west of the coseismic signal in the original data (Figure B.1a) increase in amplitude (Figure B.2b). When the correct smoothing parameter is used, the longer wavelength features are corrected (Figure B.2c). The residual atmospheric contribution (Figure B.2d) clearly contains more than turbulence, which suggests that not all of the topographically correlated noise is removed even with the optimal smoothing parameter. When too little smoothing is applied, the noise

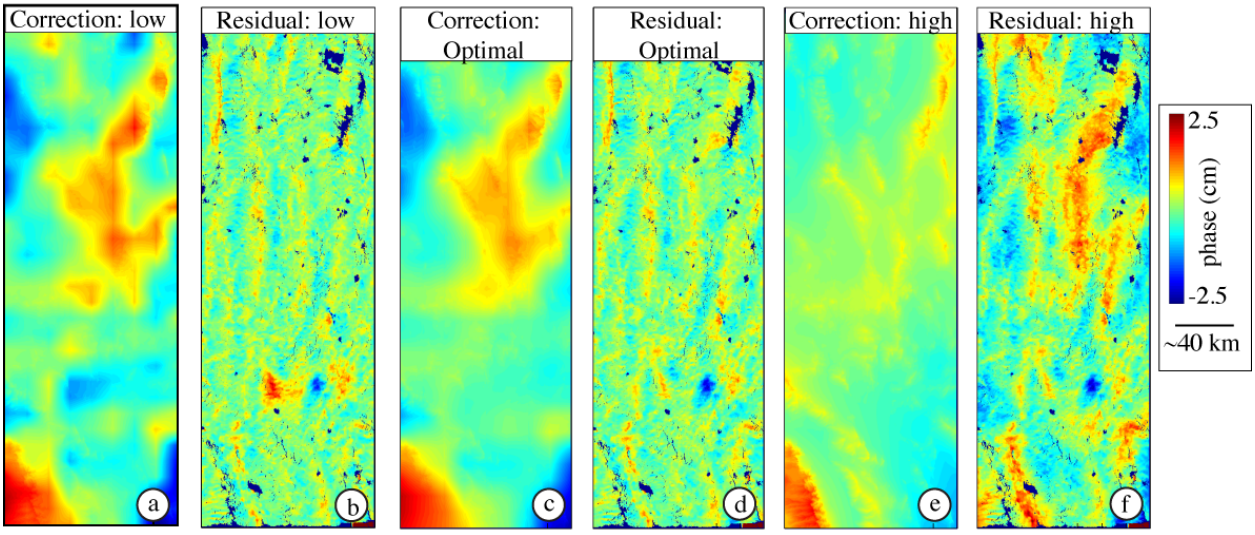

Figure B.2: Atmospheric noise corrections associated with different amounts of smoothing. The smoothing regularization parameters are varied to produce results where the inferred variation in the relationship between topography and phase is under-smoothed (a and b), optimally smoothed (c and d), and over-smoothed (e and f). (a), (c), and (e) are the atmospheric corrections, and (b), (d), and (f) are the residuals after the corrections are removed from the data in Figure B.1a.

associated with Death Valley is accentuated and most of the remaining atmospheric noise persists (Figure B.2d).

As expected, spatial variations in the inferred values of $K'_{\Delta\phi}$ depend on the imposed smoothing parameter. When too little smoothing is applied (Figure B.3a), neighboring values of $K'_{\Delta\phi}$ vary significantly. This results in a correction that accounts for turbulent features as part of the topographically correlated contribution and predicts spatial variations in $K'_{\Delta\phi}$ that are unsupported by the data. When the correct smoothing parameter is used (Figure B.3b), $K'_{\Delta\phi}$ varies smoothly over multiple model points. The spatial variation in $K'_{\Delta\phi}$ appears damped when the solution is over-smoothed (Figure B.3c).

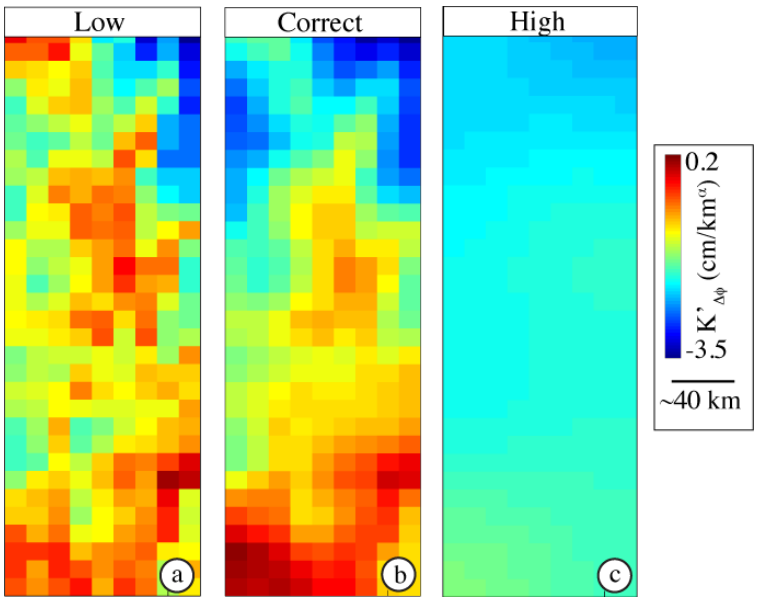

Figure B.3: Spatial variability of $K'_{\Delta\phi}$ over the study area. The amount of applied smoothing is varied: too little smoothing (a: $\xi = 0.7$), the correct amount of smoothing (b: $\xi = 1.4$), and too much smoothing (c: $\xi = 3$).

B.6 References

Barnhart, W. D., and R. B. Lohman (2010), Automated fault model discretization for inversions for coseismic slip distributions, Journal of Geophysical Research, 115(B10), doi:10.1029/2010JB007545.

Bekaert, D. P. S., A. Hooper, and T. J. Wright (2015), A spatially variable power law tropospheric correction technique for InSAR data, Journal of Geophysical Research: Solid Earth, doi:10.1002/2014JB011558.

Cavalié, O., M.-P. Doin, C. Lasserre, and P. Briole (2007), Ground motion measurement in the Lake Mead area, Nevada, by differential synthetic aperture radar interferometry time series analysis: Probing the lithosphere rheological structure, Journal of Geophysical Research, 112(B3), doi:10.1029/2006JB004344.

Elliott, J. R., J. Biggs, B. Parsons, and T. J. Wright (2008), InSAR slip rate determination on the Altyn Tagh Fault, northern Tibet, in the presence of topographically correlated atmospheric delays, Geophysical Research Letters, 35(12), doi:10.1029/2008GL033659.

Hanssen, P.C. (1998), Rank-Deficient and Discrete Ill-Posed Problems: Numerical Aspects of Linear Inversion, Society for Industrial and Applied Mathematics, Philadelphia, doi:/10.1137/1.9780898719697.

Harris, R. A., and P. Segall (1987), Detection of a locked zone at depth on the Parkfield, California, segment of the San Andreas Fault, Journal of Geophysical Research, 92(B8), 7945, doi:10.1029/JB092iB08p07945.

Lohman, R. (2004), The inversion of geodetic data for earthquake parameters, Ph.D Thesis, California Institute of Technology.

Lohman, R. B., and M. Simons (2005), Some thoughts on the use of InSAR data to constrain models of surface deformation: Noise structure and data downsampling: Geochemistry, Geophysics, Geosystems, 6(1), doi:10.1029/2004GC000841.

Menke, W. (1989), Geophysical Data Analysis: Discrete Inverse Theory, International Geophysics Series, vol. 45., Academic Press, New York.

Tymofyeyeva, E., and Y. Fialko (2015), Mitigation of atmospheric phase delays in InSAR data, with application to the eastern California shear zone, Journal of Geophysical Research: Solid Earth, 120(8), 5952-5963, doi:10.1002/2015JB011886.

APPENDIX C

SUPPLEMENTAL MATERIAL: COSEISMIC EXTENSION FROM SURFACE CRACKS REOPENED BY THE 2014 PISAGUA, NORTHERN CHILE, EARTHQUAKE SEQUENCE

C.1 GPS Methods

We calculate the daily time series for 12 continuous GPS stations that are part of the Central Andean Tectonic Observatory Geodetic Array (Simons et al., 2010) or an array operated by the Chilean government, and are all processed by Blewitt (2015). From the time series of station positions, we calculate the coseismic displacement during the April 1 M_w8.1 earthquake by subtracting the station position on March 31 from that on April 2, 2014. Likewise the April 3 M_w7.7 coseismic displacements were calculated by subtracting the position on April 2 from the position on April 4, 2014. We solve for the distance-weighted infinitesimal displacement gradient tensor (Allmendinger et al., 2009; Cardozo and Allmendinger, 2009) by independently inverting the two sets of GPS displacement vectors. We test a range of distance weighting parameters from 35 to 150 km, and select the one that produces the most consistent fit between the mean crack orientations and the GPS-inferred maximum horizontal shortening axes. We find 50 km to be the optimal distance weighting parameter.

Transect	**Start Lat (^{o}), Long (^{o})**	**End Lat (^{o}), Long (^{o})**	**Start Elev. (m)**	**End Elev. (m)**	**Length (m)**	**Opening (cm)**	**Date**
Pisagua	-19.6934, -70.1336	-19.6908, -70.1253	765	812	915	10.5	July 5, 2014
CB	-20.0225, -70.0777	-20.0223, -70.0721	584	600	591	32.4	April 7, 2014
PdL 1	-21.0380, -70.1275	-21.0349, -70.1225	629	583	625	3.0	July 8, 2014
PdL 2	-21.0404, -70.1272	-21.0400, -70.1223	632	595	511	6.5	July 8, 2014
PdL 3	-21.0389, -70.1226	-21.0375, -70.1220	620	590	500	1.0	July 8, 2014

Table C.1: Location of transects. CB: Caleta Buena, PdL: Punta de Lobos

Transect		**Cumulative Opening (cm)**	**Transect length (m)**	**Apparent Co-seismic strain**	**Orientation**
Pisagua	Cracks	10.5	915	$1.15\text{x}10^{-4}$	350.9 ± 11.8^o
Pisagua	GPS	0.19	915	$2.07\text{x}10^{-6}$	354^o
CB	Cracks	32.4	591	$5.48\text{x}10^{-4}$	019.4 ± 13.7^o
CB	GPS	0.21	591	$3.52\text{x}10^{-6}$	008.4^o
PdL	Cracks (average of 3 transects)	3.5	545	$6.42\text{x}10^{-5}$	006.9 ± 9.2^o
PdL	Baker et al. (2013); 150 year event	0.39	545	$7.1\pm2.3\text{x}10^{-6}$	N/A
PdL	Baker et al. (2013); 300 year event	0.78	545	$14.2\pm2.3\text{x}10^{-6}$	N/A

Table C.2: Summary of strain magnitude and orientation calculations. GPS openings are the strain values multiplied by the transect length. The 150 and 300 year events at Punta de Lobos refer to the expected strain release from great earthquakes with recurrence intervals of 150 and 300 years, respectively. The per event strain magnitudes are inferred from the permanent extension recorded in a suite of cracks within surfaces that date from 0.8 to1.1 Ma (Baker et al., 2013).

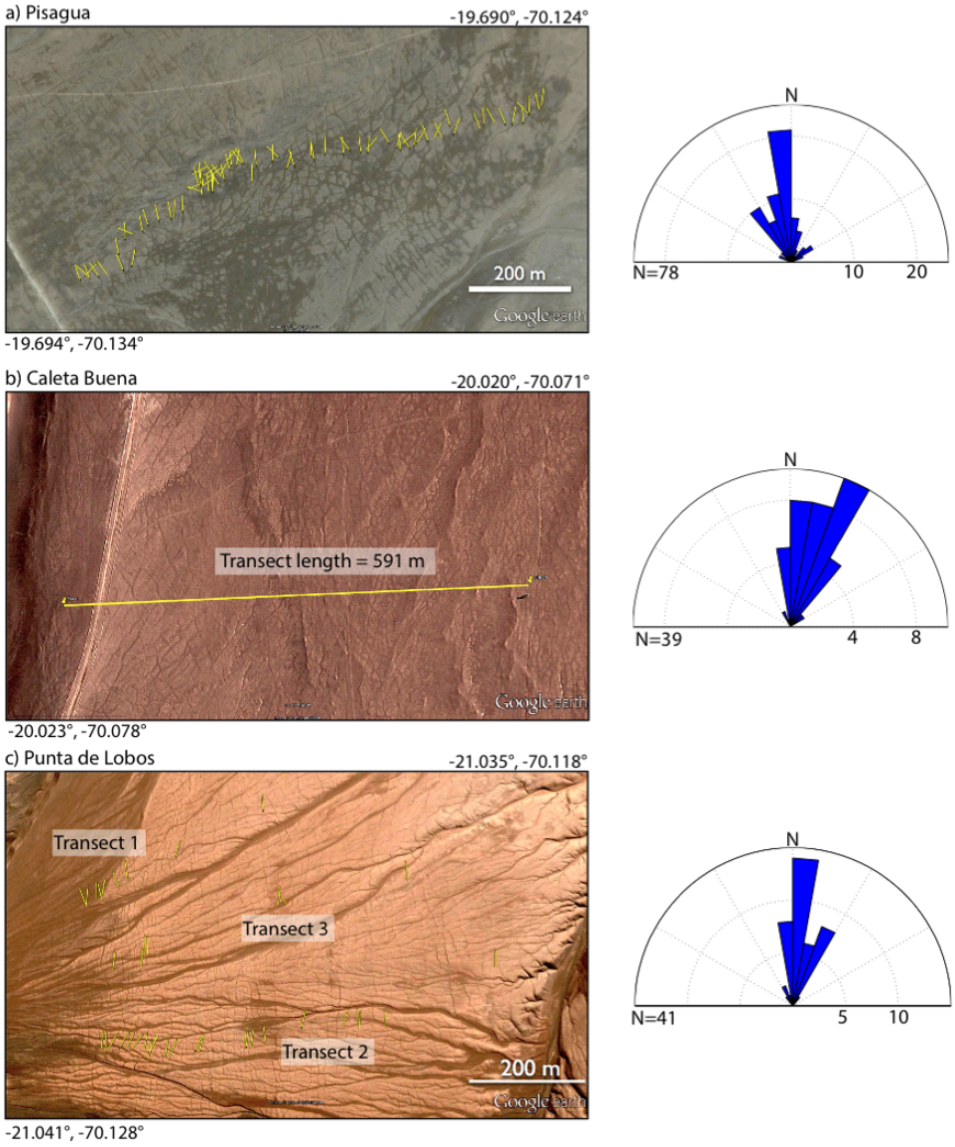

Figure C.1: Google Earth imagery of the measured transects near the Pisagua (a), Caleta Buena (b), and Punta de Lobos (c) sites. Yellow lines represent fresh coseismic cracks. Rose diagrams show the fresh crack orientations. At the Caleta Buena site, there are two old crack sets, NNE and NW-striking but, as shown in the rose diagram, only the NNE set was reactivated in 2014.

C.2 Interferometric Synthetic Aperture Radar (InSAR) methods

We generate a coseismic ascending interferogram using X-band SAR imagery with a wavelength of 3.1 cm from the TerraSAR-X satellite shown in Figure C.6. We process the interfer-

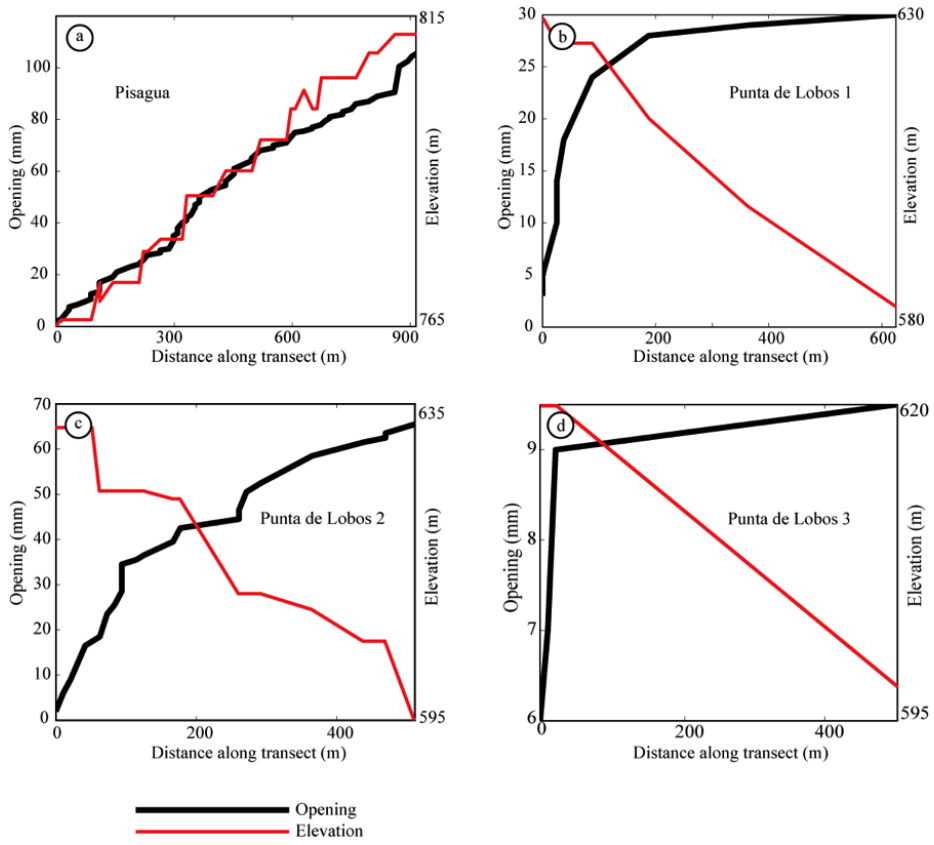

Figure C.2: Opening and elevation vs. distance along transects at the Pisagua and Punta de Lobos sites.

ogram with precise scientific orbits (Yoon et al., 2009) using the Repeat Orbit Interferometry PACkage (ROI_PAC) produced by Rosen et al. (2004). We remove the topographic phase using a 90 m digital elevation model (DEM) from the Shuttle Radar Topography Mission (SRTM, Farr et al., 2007).

C.3 InSAR analysis

We use InSAR data to characterize potential gradients in the displacement field over spatial scales that are too short to be well-sampled by the GPS data. We produce maps of the InSAR

displacement field at a spatial resolution of 30 m. This is a sufficient spatial resolution to detect if the large crack openings measured in the field are indicative of anomalous strain concentrated within the crack transects. The satellite line-of-sight direction oriented at 29^o from vertical results in a combined sensitivity to horizontal and vertical deformation.

The interferogram shows no strain concentrated over the Pisagua transect (Figure C.7a). We dismiss atmospheric effects as a noise source that could significantly contaminate the strain signal over the transect. Atmospheric artifacts in InSAR data are largely caused by differences in humidity at the timing of the SAR acquisitions and result in spatially coherent noise signals that approximately scale with elevation. Because elevation is relatively smooth over the transect length (Figure C.7b), atmospheric noise is unlikely to have significantly contaminated the InSAR signal. The summed crack apertures of 10.5 cm measured in the field at the Pisagua transect project to 5 cm of displacement in the SAR line-of-sight. Had the cracks concentrated this amount of deformation, we would expect to see almost two fringes of displacement localized to the 1 km transect (Figure C.7c & C.7d). The fact that the interferometric phase is not disrupted across the cracked area suggests that the cracks do not accommodate enhanced coseismic strain relative to the immediately surrounding areas.

C.4 Topographic control on crack orientations

Cracks commonly form along or near topographic scarps with opening vectors aligned with the direction of maximum relief even when the orientation is poorly aligned with the static strain field. This suggests that the focusing of seismic waves across underlying faults and local gravitational instabilities influence crack formation and orientation.

We assess the dominant trends of topographic scarps over the rupture area from a slope

map (Figure C.4). NS-striking topographic scarps largely outline normal faults and the Coastal Escarpment. Margin perpendicular structures include EW to ENE striking reverse faults and several large canyons. North of the Quebrada de Camarones, fault scarps rotate to a dominant NE orientation (Figure C.4). We separate scarps by azimuth and show a higher than average concentration of scarps with NS and ENE/EW orientations (Figure C.5).

We consider two approaches of accounting for the topographic control in the comparison of the strain axes inferred from the crack orientations and geodetic datasets. In the first, we simply include all mean crack orientations in the comparison calculation (Figure 4.3a). This approach benefits from including all data, irrespective of any topographic control. In the second, we remove cracks with orientations that deviate by more than 50^o from the GPS inferred strain axes for both the M_w8.8 and M_w7.7 earthquakes from our statistical analysis (Figure 4.3b & 4.3c). ∼75% of the removed field sites lie along or near EW to ENE striking structures.

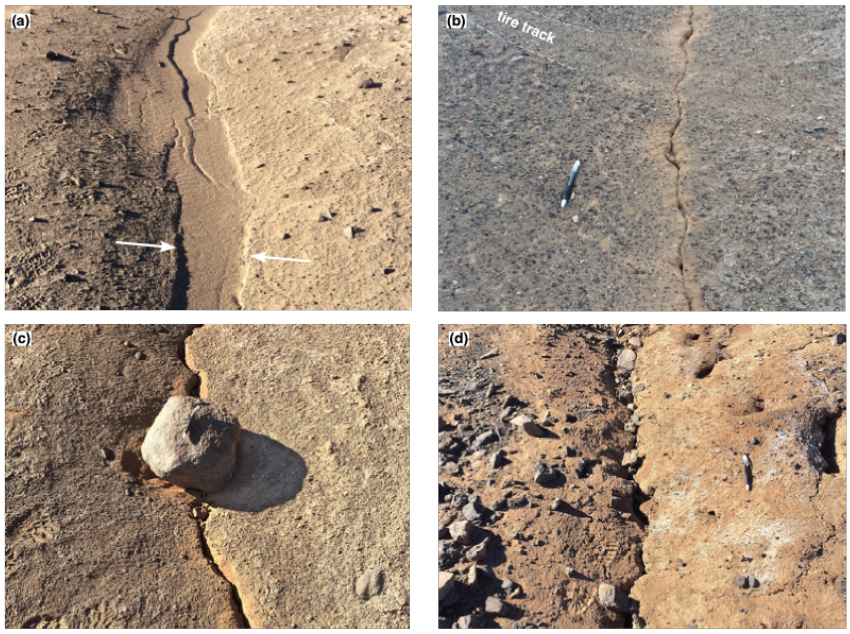

Figure C.3: Color version of field photos. Photos by Richard Allmendinger.

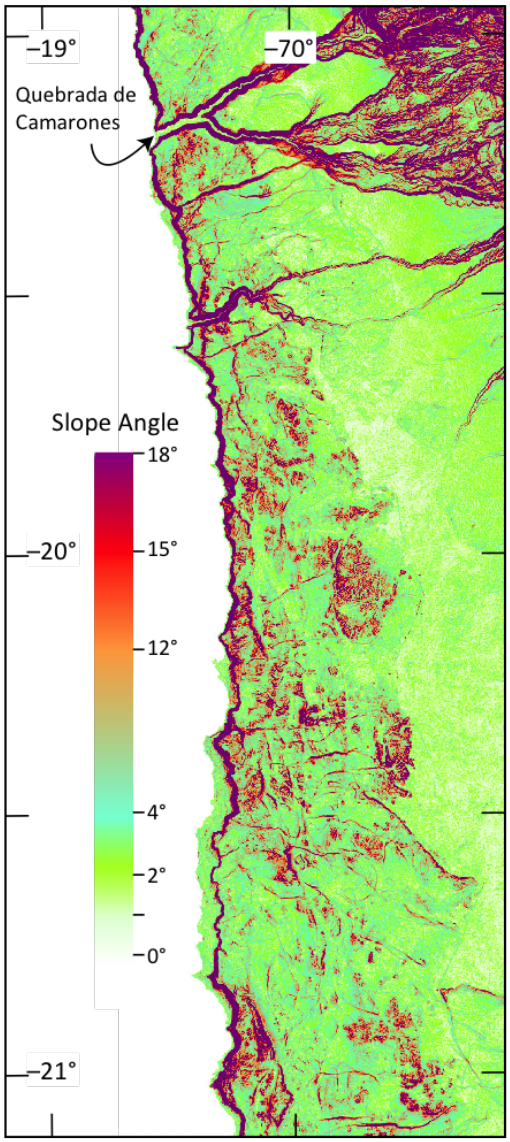

Figure C.4: Map of slope angles in the Coastal Cordillera of northern Chile.

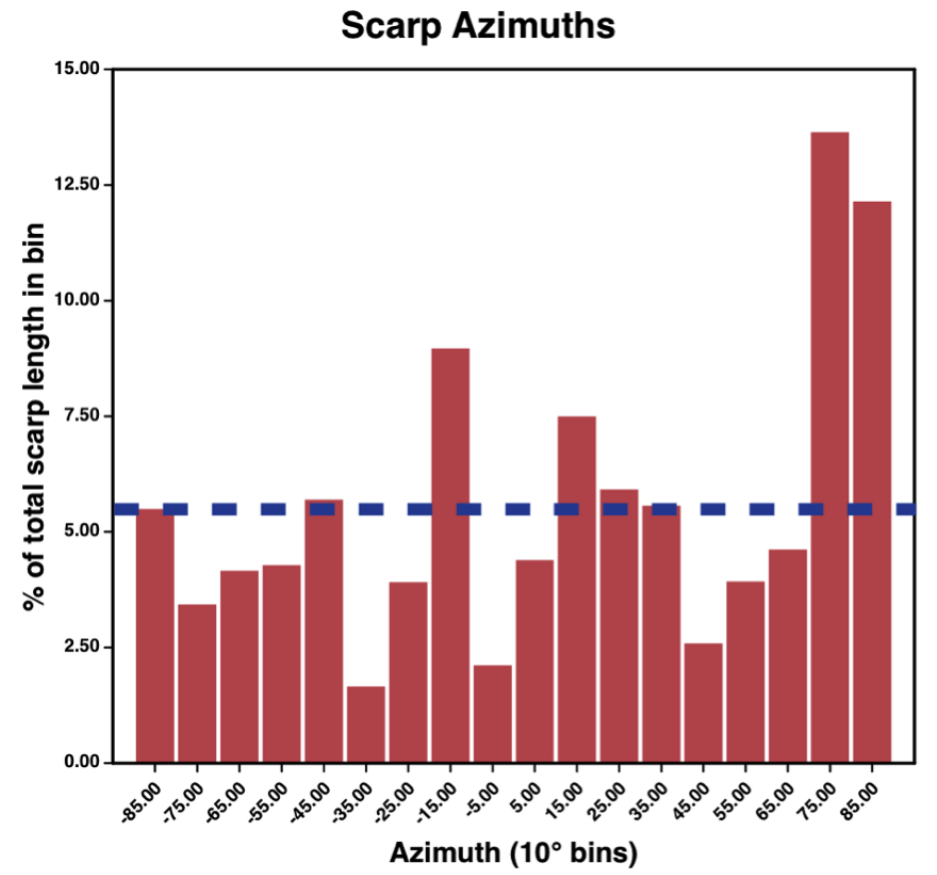

Figure C.5: Percent of total scarp length in 10^o azimuthal bins between -90^o (270^o) and 90^o scarp azimuth. The dashed blue line indicates the expected percentage of total scarp length given a uniform distribution of topographic scarps.

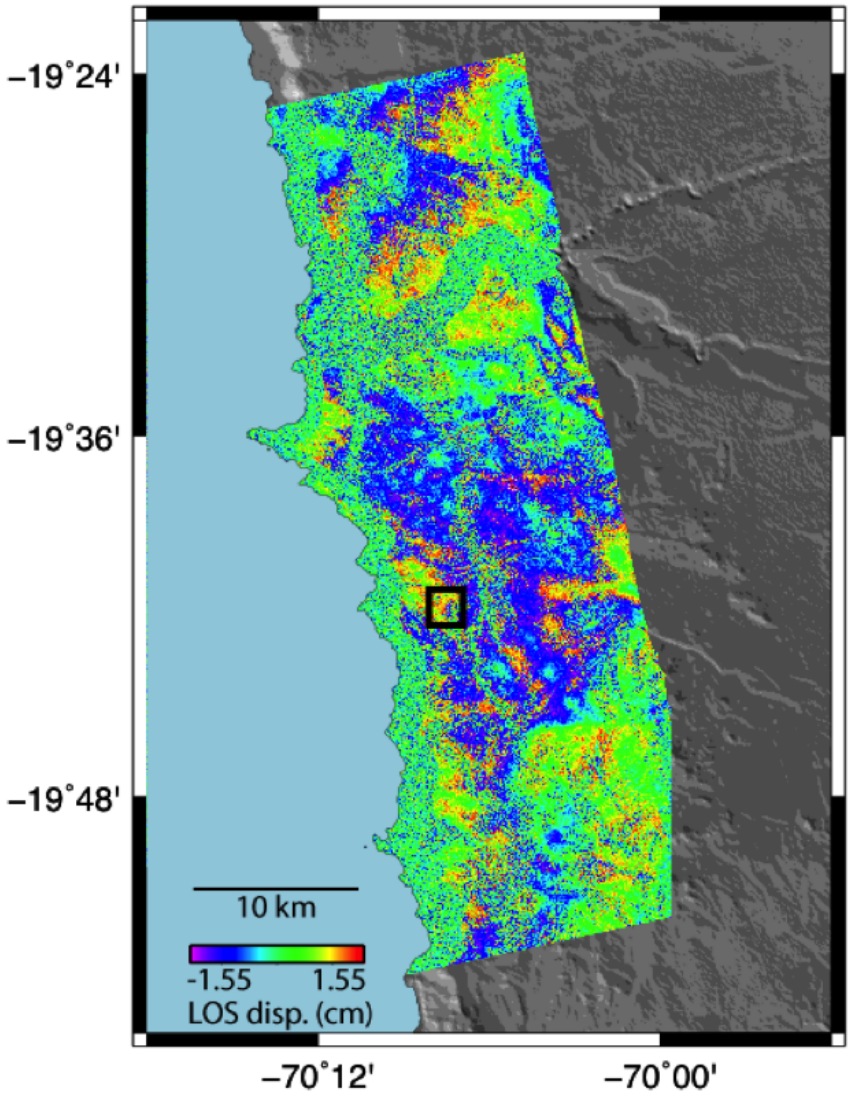

Figure C.6: Coseismic ascending TerraSAR-X imagery. The wrapped, unfiltered interferogram spans December 18, 2011- April 2, 2014. The black box outlines the Pisagua site and the zoomed area in Figure C.7.

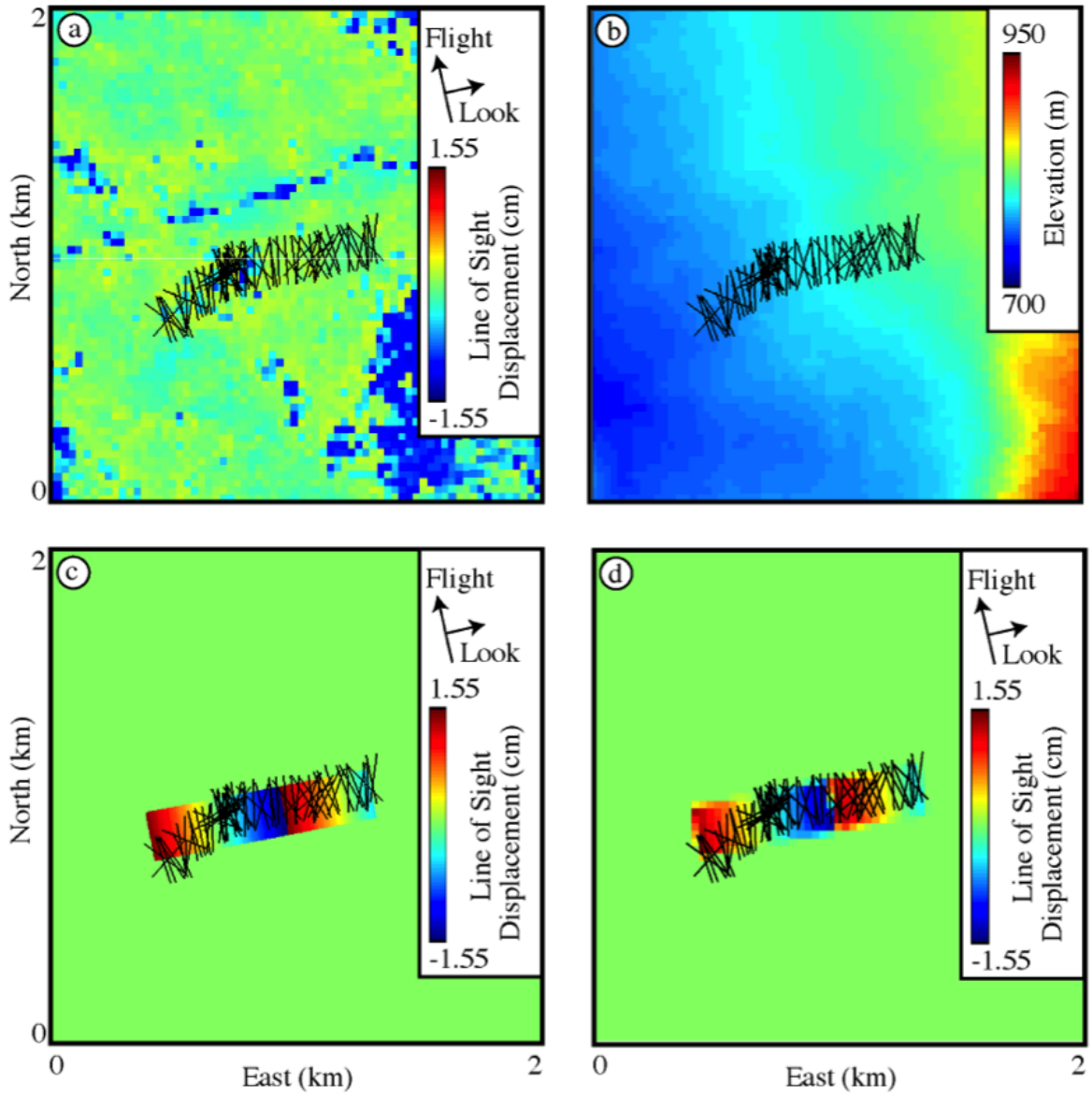

Figure C.7: InSAR-derived line-of-site displacements over the Pisagua site. (a) TerraSAR-X interferogram shown in Figure C.6 zoomed to the area outlined by the black box. The black lines represent measured cracks plotted at a uniform length of 200m. (b) SRTM Digital Elevation Model. Atmospheric noise in the InSAR data, which approximately scales with elevation, is unlikely to significantly contaminate the displacement field across the transect. (c) Predicted line-of-sight displacements across the transect assuming the crack opening field measurements represent static extension accommodated over the transect, shown at a 1 m resolution. (d) results in (c) resampled to the 30 m resolution of the interferogram in (a).

Figure C.8: Excavated crack profile showing that walls degrade near the surface. This photo is of a crack opening produced during the 2007 Mw 7.7 Tocopilla earthquake. Crack opening in the more competent material at the depth of the scale may better reflect the coseismic strain than the apparent crack opening in the looser sand. Loose eolian sand accumulated in an old surface crack depression has enhanced the new crack opening, which overlies a very fine crack in gypsum fill (lighter material where the scale is located).

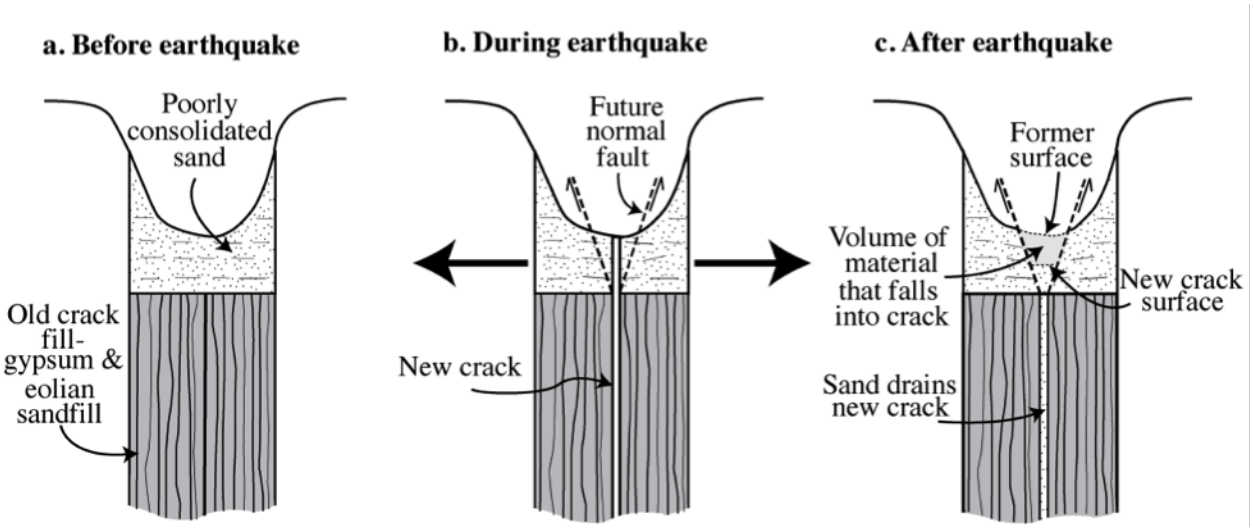

Figure C.9: Schematic illustration of crack opening before, during, and after an earthquake. Where exposes are adequate, cracks can be seen to extend meters to tens of meters into bedrock. The volume of unconsolidated sand that erodes near the surface expression of the crack drains to fill some of the volume created as the pre-existing crack grew during the earthquake. Illustration is not drawn to scale.

C.5 References

Allmendinger, R.W., Loveless, J.P., Pritchard, M.E., and Meade, B., 2009, From decades to epochs: Spanning the gap between geodesy and structural geology of active mountain belts: Journal of Structural Geology, v. 31, no. 11, p. 1409-1422, doi: 10.1016/j.jsg.2009.08.008.

Baker, A., Allmendinger, R.W., Owen, L.A., and Rech, J.A., 2013, Permanent deformation caused by subduction earthquakes in northern Chile: Nature Geoscience, v. 6, no. 6, p. 492-496, doi: 10.1038/ngeo1789.

Blewitt, G., 2015, Nevada geodetic laboratory: http://geodesy.unr.edu/billhammond/gpsnetmap/GPSNetMap.html.

Cardozo, N., and Allmendinger, R.W., 2009, SSPX: A program to compute strain from displacement/velocity data: Computers & Geosciences, v. 35, no. 6, p. 1343-1357, doi: 10.1016/j.cageo.2008.05.008.

Farr, T.G., Rosen, P.A., Caro, E., Crippen, R., Duren, R., Hensley, S., Kobrick, M., Paller, M., Rodriguez, E., Roth, L., Seal, D., Shaffer, S., Shimada, J., Umland, J., et al., 2007, The Shuttle Radar Topography Mission: Reviews of Geophysics, v. 45, no. 2, doi: 10.1029/2005RG000183.

Rosen, P.A., Hensley, S., Peltzer, G., and Simons, M., 2004, Updated repeat orbit interferometry package released: Eos, Transactions American Geophysical Union, v. 85, no. 5, p. 47-47, doi: 10.1029/2004EO050004.

Simons, M., Galetzka, J., Genrich, J., Ortega, F., Comte, D., Glass, B., Gonález, G., and Norabuena, E., 2010, Central Andean Tectonic Observatory Geodetic Array.

Yoon, Y.T., Eineder, M., Yague-Martinez, N., and Montenbruck, O., 2009, TerraSAR-X Precise Trajectory Estimation and Quality Assessment: IEEE Transactions on Geoscience and Remote Sensing, v. 47, no. 6, p. 1859-1868, doi: 10.1109/TGRS.2008.2006983.

APPENDIX D

INTERFEROMETRIC COHERENCE AND FRESH COSEISMIC CRACKS

D.1 Introduction

Surface rupture patterns and earthquake slip distributions inform studies focused on the mechanics of faulting [e.g., Wells and Coppersmith, 1994], the partition of deformation along neighboring faults [e.g., Haeussler et al., 2004], and the interpretation of paleoseismic events [e.g., Biasi and Weldon, 2006]. When an earthquake significantly disturbs reflective ground characteristics, InSAR coherence may decrease or be lost [e.g., Fielding et al., 2005]. In these cases, the use of the remotely acquired InSAR coherence imagery can support the examination of fault deformation characteristics over the entire strike length and may inform subsequent field studies. Here, I show that the reactivation of surface strain features may not necessarily decrease the coherence of InSAR imagery. Knowledge of the sensitivity of InSAR data to the formation of surface structures informs interpretations of faulting patterns from coherence InSAR imagery.

D.2 Interferometric coherence

Interferometric correlation is a measure of the similarity of reflective ground properties at the timing of different SAR acquisitions [Zebker and Villasenor, 1992]. When ground scatterers are completely coherent between the two acquisitions used to generate an interferogram, the correlation (Γ) is equal to 1. Coherence values lower than 1 indicate changes in the reflective ground characteristics. While coherence is often used as a metric for data quality

[Wei and Sandwell, 2010], variations in coherence in space and time are also indicative of changes in ground surface characteristics.

SAR instrument noise, spatial baseline, time between SAR acquisitions, and changes in ground characteristics impact coherence [Zebker and Villasenor, 1992]. For example, vegetation growth [e.g., Wegmuller and Werner, 1997] as well as changes in snow volume or soil moisture [e.g., Nolan and Fatland, 2003] decrease coherence. Further, scientists use maps of coherence changes to infer areas of likely damage following natural disasters such as earthquakes and flooding events [e.g., Fielding et al., 2005; Schepanski et al., 2012; Plank, 2014]. Mapping damage effectively requires knowledge of the behavior of different surface types in the absence of a natural disaster and the sensitivity of SAR imagery to different damage signatures.

D.3 Coseismic surface deformation & coherence

SAR imagery may be sensitive to co- and post- seismic surface disruption associated with ground motion, soil liquefaction, and the formation or reactivation of surface ruptures [e.g., Simons et al., 2002; Talebian, 2004; Fielding et al., 2005]. Observations of decreased coherence following an earthquake may direct field studies and ultimately result in more complete observations of surface rupture characteristics [e.g., Fielding et al., 2005].

The 2003 M_w 6.6 Bam, Iran, earthquake ruptured a sub-vertical fault with primarily right-lateral motion and moment release concentrated between depths of 2 and 10 km [Talebian, 2004]. Fielding et al. [2005] showed that ruptures activated in the 2003 event spatially overlap with areas of decreased coherence in coseismic Envisat imagery (C-band; $\lambda = 5.6$ cm). For example, a 40 m band of decreased coherence lies along a surface rupture that

offset a cemented gravel surface by up to 13 cm and 25 cm in the vertical and horizontal directions, respectively, as observed in the field [Fielding et al., 2005; Talebian, 2004]. Cracks with millimeter-scale openings are also associated with decreased coherence. Fielding et al. [2005] suggest that because the bands of decreased coherence are narrow, coseismic changes to the ground surface are concentrated near the rupture zone.

The 2014 Pisagua earthquake sequence offers opportunity to examine the relationship between the reopening of brittle surface cracks and coherence along a subduction zone plate boundary. Similar to Iran, the dry climate in Chile results in high coherence where surface features can be well-imaged. Unlike in Iran, the main South America- Nazca plate boundary thrust fault lies ∼50 km below the Chilean Coastal Cordillera, implying that surficial deformation features form far from the main fault that was active in the 2014 earthquake sequence.

D.4 Methods

I generate coseismic and postseismic interferograms (Table D.1) using data acquired along a TerraSAR-X ascending orbit. I process the X-band data (λ = 3.1 cm) using the Repeat Orbit Interferometry PACkage (ROI_PAC) produced by Rosen et al. [2004]. At full resolution, the pixel size is ∼1.9 m in both azimuth and range. I calculate coherence over a window of size of 5 x 5 pixels using a triangular weighting function.

When the coseismic and postseismic imagery span similar time- lengths and are acquired with similar satellite geometries, differences in coherence are likely indicative of coseismic processes in the absence of any other event. Because the postseismic interferogram has shorter temporal and spatial baselines, the difference in coherence in this set of imagery is

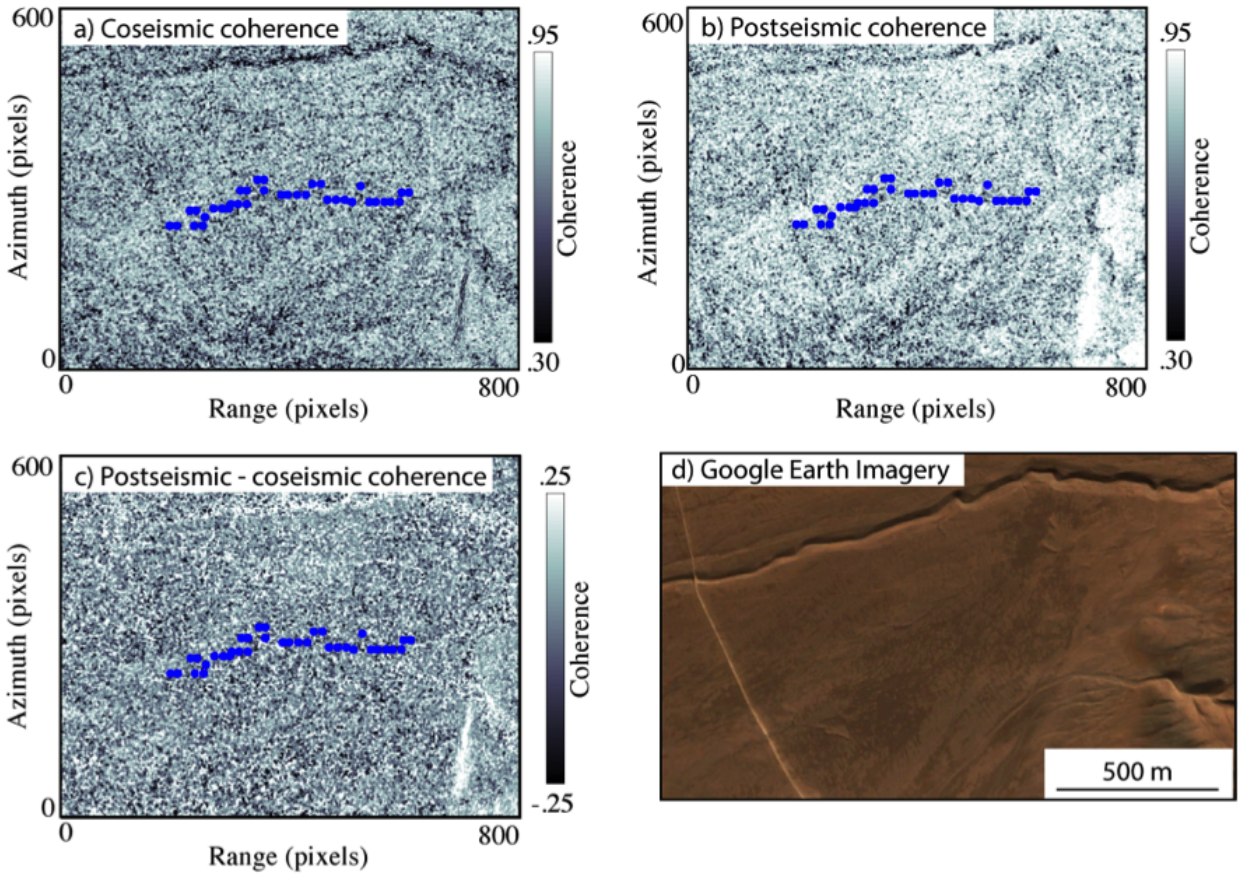

Figure D.1: Interferometric coherence at the Pisagua field site. (a) Coseismic coherence. (b) Post-seismic coherence. (c) Difference between the coseismic and the postseismic coherence. Positive values correspond to higher postseismic coherence. The pixel size for the TerraSAR-X imagery at full resolution is ∼1.9 m in azimuth and range. (d) Google Earth optical imagery covers the approximate area of panels a-c.

likely to contain artifacts that reflect differences in viewing geometry and small changes in ground characteristics that are not related to the earthquake.

Type	Date 1	Date 2	Perpendicular baseline (m)
Coseismic	November 12, 2011	April 2, 2014	157
Postseismic	April 2, 2014	June 18, 2014	41

Table D.1: Interferograms used in this study. Note the 2014 M_w 8.1 Pisagua occurred on April 1.

D.5 2014 Pisagua earthquake sequence

Figure D.1a shows the coseismic coherence surrounding the Pisagua field site described in Chapter 4 and Appendix C. The coherence remains high everywhere, including across the transect of cracks reactivated in 2014. A dried stream to the north and a dirt road to the west of the transect show decreased coseismic coherence. The shorter timespan and spatial baseline associated with the postseismic interferogram will mitigate the impact of the topographic relief surrounding these features and very minor traffic along the dirt road. The lack of signal localized to the crack transect in the imagery showing the difference between the coseismic and postseismic coherence (Figure D.1c) is consistent with the maintenance of high coherence during the 2014 earthquake.

D.6 Discussion

The correlation behavior of coseismic SAR imagery may indicate high ground shaking associated with the disruption of unconsolidated sand, the rocking of boulders, and the encouragement of crack development. While no strong motion seismic stations exist along the reactivated structures in the 2003 Bam and 2014 Pisagua earthquakes, nearby stations facilitate the placement of constraints on the minimum peak ground acceleration (PGA) likely required for crack development. A station located 400m from the fault activated in the 2003 Bam earthquake recorded a vertical PGA of 1.0 g [Fielding et al., 2005]. The USGS

event page for the 2014 Pisagua mainshock shows a maximum PGA of 0.6 g recorded at the T03A station located in Iquique, Chile, and Ruiz et al. [2015] show similarly high PGA at several sites in the Coastal Cordillera. While the maximum PGA recorded in Iran exceeds that in Chile, the PGA is likely higher near the reactivated structures in both locations. For example, Karabulut and Bouchon [2007] show that PGA varies by a factor of 3 within 1.5 km of the North Anatolian Fault likely due to an impedance contrast between the fault zone and the surrounding rocks. Lee et al. [2009] illustrate that the simulated PGA can be a factor of 5 higher along a ridge than in an adjacent valley. Ultimately, additional observations and modeling of dynamic wave propagation are likely required to understand the relationship between the formation of coseismic cracks, ground shaking, and InSAR coherence.

The different coherence behavior may also represent variable static strain concentrations in the recent Bam and Pisagua earthquakes. The resolution limit of InSAR data constrains the maximum gradients in the line-of-sight displacement where the InSAR signal remains coherent. The resolution limit is $\lambda/2\Delta R$, where λ is the wavelength and ΔR is the pixel size in range. For full resolution Envisat and TerraSAR-X data, the resolution limit is 0.2 cm/m and 0.8 cm/m, respectively. The 40 m band surrounding the Bam earthquake could accommodate up to 8 cm of relative displacement before the SAR signal becomes decorrelated. The large measured fault offsets alone exceed this value, and any off-fault deformation would only increase gradients in the surface displacement. In Chile, the cracking is relatively diffuse as many cracks with sub-parallel orientations reopen over a larger area ($\leq$1 km^2). Because the cracked areas do not accommodate enhanced strain relative to the adjacent areas where cracks appear to not develop, the strain gradient at the crack sites can be approximated from a distance- weighted inversion of the coseismic GPS displacements. This calculation suggests a coseismic strain of 2x10^{-4}cm/m at the Pisagua site, which is far below the resolution limit of either satellite.

D.7 Conclusions and future work

Here, I have shown that the reopening of brittle surface strain features does not always decorrelate InSAR imagery. The different coherence behaviors likely reflect differing proximity to the main fault. The higher static strain and potentially elevated seismic shaking associated with the 2003 Bam earthquake are likely responsible for the decreased coherence along the activated fault trace.

A range of factors including surface cover, earthquake focal mechanism, and subsurface structure impact the sensitivity of InSAR imagery to coseismic processes. In the absence of an earthquake, coherence varies over sand, gravel, hard rock, forested, and vegetated surfaces. Subsurface structures may focus seismic waves and locally enhance seismic shaking, which may lead to larger changes in reflective ground characteristics. Different earthquake geometries that result in varying extensional and contractional surface strains will likely produce a range of strain markers (e.g., cracks, faults, folds, pop-up structures) that may be recorded differently in InSAR imagery.

The Bam and Pisagua earthquakes may represent two end-member cases for the sensitivity of InSAR imagery to the activation (or reactivation) of brittle surface strain markers. Additional examinations of coseismic surface displacements and coherence imagery will support stronger constraints on the sensitivity of InSAR imagery to the formation of surface structures. This will contribute to knowledge of the cases when coherence imagery provides reliable constraints on the location of activated surface structures.

D.8 References

Biasi, G. P., and R. J. Weldon (2006), Estimating Surface Rupture Length and Magnitude of Paleoearthquakes from Point Measurements of Rupture Displacement, Bulletin of the Seismological Society of America, 96(5), 1612-1623, doi:10.1785/0120040172.

Fielding, E. J., M. Talebian, P. A. Rosen, H. Nazari, J. A. Jackson, M. Ghorashi, and R. Walker (2005), Surface ruptures and building damage of the 2003 Bam, Iran, earthquake mapped by satellite synthetic aperture radar interferometric correlation, Journal of Geophysical Research, 110(B3), doi:10.1029/2004JB003299.

Haeussler, P. J. et al. (2004), Surface Rupture and Slip Distribution of the Denali and Totschunda Faults in the 3 November 2002 M 7.9 Earthquake, Alaska, Bulletin of the Seismological Society of America, 94(6B), S23-S52, doi:10.1785/0120040626.

Karabulut, H., and M. Bouchon (2007), Spatial variability and non-linearity of strong ground motion near a fault, Geophysical Journal International, 170(1), 262-274, doi:10.1111/j.1365-246X.2007.03406.x.

Lee, S.-J., Y.-C. Chan, D. Komatitsch, B.-S. Huang, and J. Tromp (2009), Effects of Realistic Surface Topography on Seismic Ground Motion in the Yangminshan Region of Taiwan Based Upon the Spectral-Element Method and LiDAR DTM, Bulletin of the Seismological Society of America, 99(2A), 681-693, doi:10.1785/0120080264.

Nolan, M., and D. R. Fatland (2003), Penetration depth as a DInSAR observable and proxy for soil moisture, IEEE Transactions on Geoscience and Remote Sensing, 41(3), 532-537, doi:10.1109/TGRS.2003.809931.

Plank, S. (2014), Rapid Damage Assessment by Means of Multi-Temporal SAR - A Comprehensive Review and Outlook to Sentinel-1, Remote Sensing, 6(6), 4870-4906, doi: 10.3390 /rs6064870.

Ruiz, S. et al. (2015), Los Terremotos de Iquique 2014, I Congreso Chileno de Sismología e Ingeniería Sísmica Achisina 2015.

Schepanski, K., T. J. Wright, and P. Knippertz (2012), Evidence for flash floods over deserts from loss of coherence in InSAR imagery, Journal of Geophysical Research: Atmospheres, 117(D20), doi:10.1029/2012JD017580.

Simons, M., Y. Fialko, and L. Rivera (2002), Coseismic Deformation from the 1999 Mw 7.1 Hector Mine, California, Earthquake as Inferred from InSAR and GPS Observations, Bulletin of the Seismological Society of America, 92(4), 1390-1402, doi:10.1785/0120000933.

Talebian, M. (2004), The 2003 Bam (Iran) earthquake: Rupture of a blind strike-slip fault, Geophysical Research Letters, 31(11), doi:10.1029/2004GL020058.

Wegmuller, U., and C. L. Werner (1997), Retrieval of Vegetation Parameters with SAR Interferometry, IEEE Transactions on Geoscience and Remote Sensing, 35, 18-24.

Wei, M., and D. Sandwell (2010), Decorrelation of L-Band and C-Band Interferometry Over Vegetated Areas in California, IEEE Transactions on Geoscience and Remote Sensing, 48(7), 2942-2952, doi:10.1109/TGRS.2010.2043442.

Wells, D., and K. Coppersmith (1994), New Empirical Relationships among Magnitude, Rupture Length, Rupture Width, Rupture Area, and Surface Displacement, Bulletin of the Seismological Society of America, 84, 974-1002.

Zebker, H. A., and J. Villasenor (1992), Decorrelation in Interferometric Radar Echoes, IEEE Transactions on Geoscience and Remote Sensing, 30, 950-959.